De Florio, Sergio (2013) *Precise autonomous orbit control in low earth orbit: from design to flight validation.* PhD thesis.

http://theses.gla.ac.uk/4502/

Copyright and moral rights for this thesis are retained by the author

A copy can be downloaded for personal non-commercial research or study, without prior permission or charge

This thesis cannot be reproduced or quoted extensively from without first obtaining permission in writing from the Author

The content must not be changed in any way or sold commercially in any format or medium without the formal permission of the Author

When referring to this work, full bibliographic details including the author, title, awarding institution and date of the thesis must be given

Glasgow Theses Service
http://theses.gla.ac.uk/
theses@gla.ac.uk

Precise Autonomous Orbit Control in Low Earth Orbit: from Design to Flight Validation

Sergio De Florio

Submitted in the fulfillment of the requirements for the
Degree of Doctor of Philosophy

Division of Aerospace Sciences
School of Engineering
University of Glasgow

© Sergio De Florio, May 2013

Abstract

The main purpose of this research is the analysis, development and implementation of a precise autonomous orbit control system for a spacecraft in low Earth orbit. This thesis work represents a step forward in the theoretical formalization and implementation of an on-board orbit maintenance system. Two main approaches are identified for the realization of an on-board orbit control system. The first is the reconsideration and further development of state-of-the-art orbit control methods from the perspective of autonomy. A step forward is then taken in the direction of the definition of a general and rigorous formalization of the autonomous orbit control problem. The problem of the autonomous absolute orbit control is considered as a specific case of two spacecraft in formation in which one, the reference, is virtual and affected only by the Earth's gravitational field. A new parametrization, the relative Earth-Fixed elements, analogous to the relative orbital elements used for formation control, is introduced to describe the relative motion of the real and reference sub-satellite points on the Earth surface.

An extensive discussion is dedicated to the reference orbit selection and generation process and the analysis of the free motion of a spacecraft in low Earth orbit. The reference orbit defines the spacecraft's nominal trajectory designed to satisfy the mission requirements. The actual orbit is kept within certain bounds defined with respect to the reference orbit. The generation process of the reference orbit is dealt in detail as it is the fundamental starting point of the orbit control chain. The free motion analysis is essential to understand the orbit perturbation environment which causes the deviation of the actual from the nominal trajectory. The use of the precise orbit determination data of the missions PRISMA and TerraSAR-X guarantee the reliability of the results of this analysis and the understanding of the orbit's perturbation environments at an altitude of 700 and 500 km. This study helps the definition of a proper

control strategy.

The control algorithms developed in the thesis can be divided into the two broad categories of analytical and numerical. An analytical algorithm for the maintenance of a repeat-track orbit is developed from the state-of-the-art methods and new analytical formulations for the reference orbit acquisition under different constraints and requirements are presented. The virtual formation method for the absolute orbit control is formalized by means of the relative Earth-fixed elements described previously. The state-space representation is used for the mathematical formulation of the problem. A linear and a quadratic optimal regulators, based on this model, are designed for the in-plane and out-of-plane absolute orbit control.

Numerical simulations are performed for the validation of the control methods. The test platform includes a very accurate orbit propagator, the flight software and allows the simulation of actuators and navigation errors. The simulation results are evaluated from a performance and operational point of view in order to formulate a first conclusion about the advantages and disadvantages of the different control techniques. The main differences between the considered analytical and numerical control methods are outlined.

The practical implementation of a precise autonomous orbit control system for a spacecraft in low Earth orbit is then described in detail. The on-board guidance, navigation and control software development, implementation and testing of the PRISMA mission, to which the author of this thesis contributed, is described. The attention is focused on the technological aspects implied by the realization of the autonomous orbit control system tested in-flight with the autonomous orbit keeping experiment on PRISMA. Among the several innovative aspects of the flight software development, some space is dedicated to the advanced software validation and testing realized on the formation flying test-bed at DLR, the German Aerospace Center, which played a fundamental role in the realization of the PRISMA mission and its experiments.

Finally, the flight results of the autonomous orbit keeping experiment on the PRISMA mission, a fundamental milestone of this research work, are presented. This in-flight experiment took place in the summer of 2011 and demonstrated the capability of autonomous precise absolute orbit control using the analytical control method developed in this thesis.

Contents

to Paride, may he rest in peace

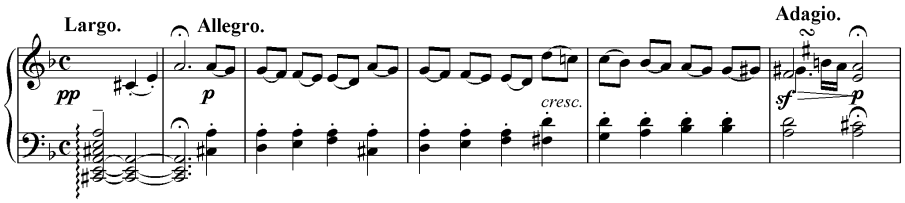

Beethoven Op. 31 No. 2

Acknowledgments

I would like to express my gratitude to my supervisors Gianmarco Radice and Simone D'Amico. Gianmarco gave me the trust and freedom I needed to accomplish this research. Simone is the scientist who taught me the art of flight dynamics in which he is a real master. I owe special thanks also to Oliver Montenbruck from whom I learned the importance of realising concretely ideas conceived during research. Thanks to Jean-Sebastian and Gabriella for their invaluable support during the AOK experiment operations and to the PRISMA mission design and operations team in Sweden.

Thanks to

My parents and my sister for their constant support and patience

My grandmother who guards my roots in Milano

Giangi for the excellent dinners and Whisky

Gianni and Paride who visited me in Glasgow and joined us in the Burns night

Elisa, Ettore, Fabrizio, Giuseppe, Lorenzo, Luca, Marcel.la, Matteo, Michele, Miguel, Paola, Saika, Serena, Yago and Yamagen for everything in the daily life in München

My theatre and athletics groups because they are also families

Dieter, my athletics trainer, for telling me that rests are as important as trainings

Claire, Filiep, Franz, Markus, Matthias, Paul and Stefan for the running trainings together

Thomas for showing me new paths in music

Carlo because the future is in space

Claudia so far but so close

Paola, Maura, Daniela and Fabio for their determined daily commitment

Guido, Lamberto and Giovanni who are like brothers

Eli for she exists

Sergio De Florio

Author’s Declaration

I hereby declare that this submission is my own work and that, to the best of my knowledge and belief, it contains no material previously published or written by another person nor material which to a substantial extent has been accepted for the award of any other degree or diploma of the university or other institute of higher learning, except where due acknowledgment has been made in the text.

Glasgow, Scotland, June 26, 2013, Sergio De Florio

Nomenclature

Symbols

a	=	semi-major axis [m]
a_{ij}	=	element ij of matrix $\mathbf{A}$
A	=	spacecraft reference area [m^2]
$\mathbf{A}$	=	dynamic model matrix [s^{-1}]
b_{ij}	=	element ij of matrix $\mathbf{B}$
B	=	ballistic coefficient of the spacecraft [kg/m^2]
$\mathbf{B}$	=	control matrix [-]
c	=	cost [€]
c_{ij}	=	element ij of matrix $\mathbf{C}$
$\mathbf{C}$	=	output matrix [-]
C_D	=	drag coefficient [-]
da/dt	=	decay rate of the semi-major axis [m/s]
dt	=	time difference [s]
e	=	eccentricity [-]
$\mathbf{e}$	=	eccentricity vector [-]
e_c	=	orbit control accuracy [m]
e_d	=	dynamic model uncertainties [m]
e_j	=	eccentricity vector component [-]
e_M	=	maneuvers error [m]
e_N	=	navigation error [m]

$F10.7$	=	solar radio flux index [sfu = 10^{-22} W m^{-2} Hz^{-1}]
g_j	=	gain
$\mathbf{G}$	=	gain matrix
$\mathbf{G_d}$	=	disturbance gain matrix
Kp	=	geomagnetic activity index [-]
i	=	inclination [rad]
i_j	=	inclination vector component [rad]
$\mathbf{J_A}$	=	Jacobian of matrix $\mathbf{A}$
J_2	=	geopotential second-order zonal coefficient [-]
m	=	spacecraft mass [kg]
M	=	mean anomaly [rad]
n	=	mean motion [rad/s]
n_N	=	nodal frequency [1/s]
R_E	=	Earth's equatorial radius [m]
s_j	=	characteristic root
t	=	time [s]
t_c	=	time required for reference orbit acquisition [s]
t_e	=	exploitation time [s]
t_{smooth}	=	time required for *smooth* reference orbit acquisition [s]
T	=	maneuver cycle [s]
$\mathbf{T}$	=	coordinates transformation matrix [-]
T_{du}	=	maneuver duty cycle [d]
T_E	=	mean period of solar day [s]
T_N	=	nodal period [s]
T_{Su}	=	Sun period [s]
u	=	argument of latitude [rad]
$\overline{u}$	=	constant value of argument of latitude [rad]
v	=	spacecraft velocity [m/s]
δa	=	relative semi-major axis [-]

Δa_{AN}	=	difference between real and reference semi-major axis at the ascending node [m]
Δa_c	=	maneuver semi-major axis increment [m]
δe	=	relative eccentricity vector amplitude [-]
δe_j	=	relative eccentricity vector component [-]
$\boldsymbol{\delta F}$	=	relative Earth-fixed elements vector [-]
δh	=	normalized altitude difference [-]
Δh	=	altitude difference [m]
δi	=	relative inclination vector amplitude [rad]
δi_j	=	relative inclination vector component [rad]
$\boldsymbol{\delta\kappa}$	=	relative orbital elements vector
δL_j	=	phase difference vector component [m]
ΔL	=	phase difference [m]
ΔL_{AN}	=	phase difference at the ascending node [m]
ΔL_{MAX}	=	LAN control window [m]
$\delta\mathbf{r}$	=	normalized relative position vector [-]
δr_j	=	component of normalized relative position vector[-]
δu	=	relative argument of latitude [rad]
$\delta\mathbf{v}$	=	normalized relative velocity vector [-]
δv_j	=	component of normalized relative velocity vector[-]
Δv_j	=	impulsive maneuver velocity increment component [m/s]
Δv_{MAX}	=	largest value allowed for a maneuver [m/s]
$\mathbb{R}^-$	=	set of negative real numbers
$\mathbb{R}^+$	=	set of positive real numbers
$\mathbb{Z}$	=	set of integer numbers
$\mathbb{Z}^+$	=	set of positive integer numbers

Greek Symbols

$\boldsymbol{\epsilon}$	=	normalized relative orbital elements vector [m]
η	=	normalized altitude [-]
ϕ	=	relative perigee [rad]
φ	=	latitude [rad]
$\boldsymbol{\kappa}$	=	mean orbital elements vector
$\boldsymbol{\kappa_o}$	=	osculating orbital elements vector
λ	=	longitude [rad]
μ	=	Earth's gravitational coefficient [m^3/s^2]
ω	=	argument of periapsis [rad]
ω_E	=	Earth rotation rate [rad/s]
Ω	=	right ascension of the ascending node [rad]
$\dot{\Omega}$	=	secular rotation of the line of nodes [rad/s]
ρ	=	atmospheric density [kg/m^3]
τ	=	time constraint for reference orbit acquisitions [s]
θ	=	relative ascending node [rad]
ξ	=	thrusters execution error [%]

Indices

Subscripts

c	=	closed-loop
CMD	=	commanded
d	=	disturbance
$\mathcal{D}$	=	discrete
du	=	duty cycle
E	=	Earth
EXE	=	executed

g	=	gravity
i	=	implementation
m	=	maneuver
n	=	navigation
N	=	cross-track
onb	=	on-board
ong	=	on-ground
OPS	=	operations
p	=	performance
r	=	reduced
$\mathcal{R}$	=	reference orbit
R	=	radial
sy	=	Sun-synchronous
sth	=	smoothed
T	=	along-track
TOT	=	total

Superscripts

T	=	vector transpose

Acronyms

ACC	Accelerometer
AFC	Autonomous formation control
AMS	Asynchronous monotonic scheduler
AOC	Autonomous orbit control
AOCS	Attitude and orbit control system
AOK	Autonomous Orbit Keeping
BSW	Basic software
CDTI	Spanish Centre for the Development of Industrial Technology
CNES	French Space Agency
COTS	Commercial off the shelf
CPU	Central processing unit
DEM	Digital elevation model
DLR	German aerospace center
DTU	Technical University of Denmark
DVS	Digital video system
ECI	Earth-centred inertial
EF	Earth-fixed
EGSE	Electrical Ground Support Equipment
EM	Engineering model
FDIR	Failure detection isolation and recovery
FF	Formation flying
FFRF	Formation flying radio frequency sensors
FM	Flight model
GIF	GPS interface
GNC	Guidance, navigation and control
GOD	GPS-based Orbit Determination
GOP	GPS-based Orbit Prediction

GS	Ground station
GSOC	German space operations center
IRF	Institute of Space Physics
ISL	Inter-satellite-link
LEO	Low Earth Orbit
LPO	Longitudinal phase of the orbit
MBD	Model-based design
MM	Magnetometer
OBC	On-board computer
OCK	Orbit Control Kit
ONB	On-board
PC	Personal computer
POD	Precise Orbit Determination
RAMSES	Rocket And Multi Satellite EGSE System
REFE	Relative Earth-Fixed elements
RCC	RTEMS cross-compilation
RMS	Root mean square
RO	Reference Orbit
ROE	Relative orbital elements
RTEMS	Real-time executive for multiprocessor systems
RTOS	Real time operating system
RTU	Remote terminal unit
RTW	Real time workshop
SAFE	Spaceborne autonomous formation flying experiment
SAR	Synthetic aperture radar
SCA	star camera
SCET	Spacecraft Elapsed Time
S/C	Spacecraft
SEU	Singular event upset

SNSB	Swedish National Space Board
SRP	Solar radiation pressure
SS	Sun sensor
SSC	Swedish space corporation
SSP	Sub-satellite point
SSTL	Surrey Satellite Technology Limited
S/W	Software
TAFF	TanDEM-X autonomous formation flying
TAN	Time at ascending node
TBC	To be confirmed
TC	Telecommand
TDX	TanDEM-X
THR	Thrusters
TM	Telemetry
TSX	TerraSAR-X
TTTC	Time-tagged-telecommand
UV	Ultra Violet
VBS	Vision based sensor

Publications

Journal Papers

- S. De Florio, S. D'Amico, G. Radice, **The Virtual Formation Method for Precise Autonomous Absolute Orbit Control**, *Journal of Guidance, Control and Dynamics*, doi:10.2514/1.61575.
- S. De Florio, S. D'Amico, G. Radice, **Flight Results of the Precise Autonomous Orbit Keeping Experiment on the Prisma Mission**, *Journal of Spacecraft and Rockets*, Vol. 50, No. 3, pp. 662-674, May 2013, doi:10.2514/1.A32347.
- S. De Florio, S. D'Amico, **The Precise Autonomous Orbit Keeping Experiment on the Prisma Mission**, *The Journal of the Astronautical Sciences*, Vol. 56, No. 4, Oct.-Dec. 2008, pp. 477-494.
- S. D'Amico, J.-S. Ardaens, and S. De Florio, **Autonomous Formation Flying based on GPS - PRISMA Flight Results**, *Acta Astronautica*, Vol. 82, No. 1, pp. 69.79, Jan. 2013, doi:10.1016/j.actaastro.2012.04.033.

Conference Papers

- S. De Florio, S. D'Amico, G. Radice G., **Combined Autonomous Absolute and Relative Orbit Control in Low Earth Orbit**, Proceedings of the 5^{th} *International Conference on Spacecraft Formation Flying Missions and Technologies*, No. 40096, 29-31 May, 2013, Munich, Germany.
- S. D'Amico, J.-S. Ardaens, G. Gaias, and S. De Florio, **Space Flight Technology Demon-**

strations of DLR within the PRISMA Mission, Proceedings of the *5th International Conference on Spacecraft Formation Flying Missions and Technologies*, 29-31 May, 2013, Munich, Germany.

- S. De Florio, S. D'Amico, G. Radice G., **Precise Autonomous Orbit Control in Low Earth Orbit**, Proceedings of the *AIAA/AAS Astrodynamics Specialist Conference*, Minneapolis, MN, USA, 13 - 16 August 2012.
- S. De Florio, S. D'Amico, and G. Radice, **Flight Results of the Precise Autonomous Orbit Keeping Experiment on the PRISMA Mission**, AAS 12-179, Proceedings of the *22nd AAS/AIAA Space Flight Mechanics Meeting*, 29 Jan. - 2 Feb. 2012, Charleston, SC, USA.
- S. De Florio, S. D'Amico, G. Radice G., **Operations Concept of the Precise Autonomous Orbit Keeping Experiment on the PRISMA Mission**, Proceedings of the *8th IAA Symposium on Small Satellites for Earth Observation*, 4-8 April 2011, Berlin.
- S. De Florio, S. D'Amico and J.S. Ardaens, **Autonomous Navigation and Control of Formation Fliyng Spacecraft on the PRISMA Mission**, IAC-10.C1.5.12, Proceedings of the *61st International Astronautical Congress*, 27 Sep - 1 Oct 2010, Prague, CZ. (2010).
- S. D'Amico, J.S. Ardaens, S. De Florio, O. Montenbruck, S. Persson, R. Noteborn R., **GPS-Based Spaceborne Autonomous Formation Flying Experiment (SAFE) on PRISMA: Initial Commissioning**, Proceedings of the *AIAA/AAS Astrodynamics Specialist Conference*, 2-5 August 2010, Toronto, Canada.
- S. D'Amico, J.-S. Ardaens and S. De Florio, **Autonomous Formation Flying based on GPS - PRISMA Flight Results**, Proceedings of the *6th International Workshop on Satellite Constellations and Formation Flying, IWSCFF*, November 1-3, 2010, Howard International House, Taipei, Taiwan
- S. De Florio, S. D'Amico, **Optimal Autonomous Orbit Control of Remote Sensing Spacecraft**, Proceedings of the *19th AAS/AIAA Space Flight Mechanics Meeting*, 8-12 Feb 2009, Savannah, USA.
- S. De Florio, E. Gill, S. D'Amico, **Performance Comparison of Microprocessors for Space-based Navigation Applications**, Proceedings of the *7th IAA Symposium on Small*

Satellite for Earth Observation, 4-8 May 2009, Berlin, Germany.

- S. D'Amico, S. De Florio, R. Larsson, M. Nylund, **Autonomous Formation Keeping and Reconfiguration for Remote Sensing Spacecraft**, Proceedings of the *21st International Symposium on Space Flight Dynamics*, 28 Sep. - 2 Oct. 2009, Toulouse, France.
- S. De Florio, S. D'Amico, M. Garcia-Fernandez, **The Precise Autonomous Orbit Keeping Experiment on the PRISMA Formation Flying Mission**, AAS 08-212, Proceedings of the *18th AAS/AIAA Space Flight Mechanics Meeting*, 28-31 Jan. 2008, Galveston, Texas, USA.
- S. De Florio, **Reduction of the Response Time of Earth Observation Satellite Constellations using Inter-satellite Links**, AIAA-2008-3281, Proceedings of the *SpaceOps Conference*, 12-16 May 2008, Heidelberg, Germany.
- S. D'Amico, J.-S. Ardaens, S. De Florio, O. Montenbruck, **Autonomous Formation Flying - TanDEM-X, PRISMA and Beyond**, Proceedings of the *5th International Workshop on Satellite Constellations and Formation Flying*, 2-4 July 08, Evpatoria, Crimea, Ukraine.
- S. D'Amico, S. De Florio, J. S. Ardaens, T. Yamamoto, **Offline and Hardware-in-the-loop Validation of the GPS-based Real-Time Navigation System for the PRISMA Formation Flying Mission**, Proceedings of the *3rd International Symposium on Formation Flying, Missions and Technology*, 23-25 April 2008, ESA/ESTEC, Noordwijk, The Netherlands.

Technical Documentation

- S. De Florio, **Flight Results of the Precise Autonomous Orbit Keeping Experiment on the PRISMA Mission**, PRISMA-DLR-OPS-56, 2011, DLR/GSOC, Deutsches Zentrum für Luft und Raumfahrt, Oberpfaffenhofen, Germany.
- S. De Florio, **Operation Concept of the Precise Autonomous Orbit Keeping Experiment on the PRISMA Mission**, PRISMA-DLR-OPS-55, 2011, DLR/GSOC, Deutsches Zentrum für Luft und Raumfahrt, Oberpfaffenhofen, Germany.
- S. De Florio, S. D'Amico, **Collision Risk Assessment for Co-orbiting Spacecraft**, DEOS-

DLR-TN-02, 2011, DLR/GSOC, Deutsches Zentrum für Luft und Raumfahrt, Oberpfaffenhofen, Germany.

- S. De Florio, **DLR's Experiment Control Center for the PRISMA Mission Interface Control Document**, PRISMA-DLR-OPS-52, DLR/GSOC, Deutsches Zentrum für Luft und Raumfahrt, Oberpfaffenhofen, Germany.
- S. De Florio, S. D'Amico, **Real-Time Satellite Laboratory Tests of DLR's Flight Software: Third SATLAB Campaign (v. 6.2.0)**, PRISMA-DLR-TST-45, DLR/GSOC, Deutsches Zentrum für Luft und Raumfahrt, Oberpfaffenhofen, Germany.
- S. De Florio, S. D'Amico, **DLR's Satellite Laboratory Test Results for the PRISMA Flight Software**, PRISMA-DLR-TST-44, DLR/GSOC, Deutsches Zentrum für Luft und Raumfahrt, Oberpfaffenhofen, Germany.
- S. De Florio, S. D'Amico, **Comparison of Scalar and Vectorial Implementation of the Extended Kalman Filter**, PRISMA-DLR-TN-19, DLR/GSOC, Deutsches Zentrum für Luft und Raumfahrt, Oberpfaffenhofen, Germany.
- S. De Florio, S. D'Amico, **Max-Path Unit Tests of the PRISMA Flight Software**, PRISMA-DLR-TN-17, DLR/GSOC, Deutsches Zentrum für Luft und Raumfahrt, Oberpfaffenhofen, Germany.

1. Introduction

1.1. Absolute Orbit Control

In the last two decades the development and exploitation of very high resolution optical systems mounted on satellites in Low Earth Orbit (LEO) was a major driver for the commercialisation of Earth observation data. The global political security situation, environmental awareness and updated legislative frameworks are pushing for the realization of new high resolution remote sensing missions. The European Global Monitoring for Environment and Security (GMES) programme now renamed Copernicus is a major example of this trend. Fig. 1.1 [81] shows a list of significant Earth observation missions in orbit or planned for the near future. These kind of missions demand specialized orbits. Remote sensing satellites are generally placed on so-called sun-synchronous orbits where they cross the true of date Earth equator at the ascending node at the same local time. This is necessary to ensure similar illumination conditions when making images of the same parts of the Earth's surface with the exploitation of different orbits. In addition, orbits of remote sensing satellites are often designed to repeat their ground track after a certain number of days. These are the so called phased orbits. Finally, it may be useful to minimize or even avoid the secular motion of the argument of perigee of the orbit. This is again achieved by a proper choice of the orbital parameters and the resulting orbit is called frozen. Orbits of remote sensing satellites are, in general, sun-synchronous, phased, and frozen simultaneously. A collection of typical orbital elements and of phasing parameters for remote sensing satellites is given in Table 1.1. The design of such orbits is based on the required characteristics of the motion of the spacecraft with respect to the Earth surface. The three-dimensional position of the spacecraft in an Earth-fixed (EF) frame is completely defined

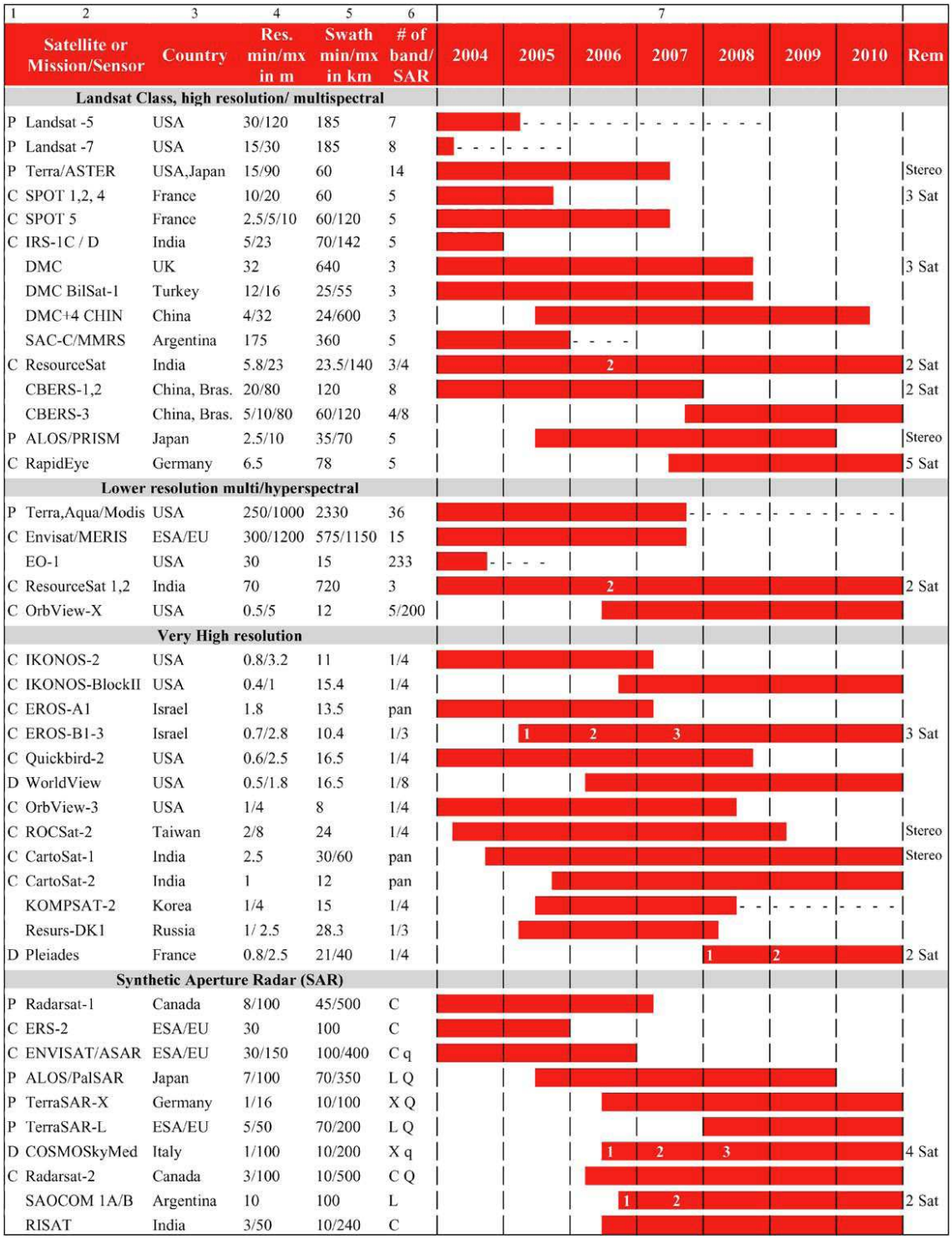

1	2	3	4	5	6	7							
	Satellite or Mission/Sensor	Country	Res. min/mx in m	Swath min/mx in km	# of band/ SAR	2004	2005	2006	2007	2008	2009	2010	Rem
	Landsat Class, high resolution/ multispectral												
P	Landsat -5	USA	30/120	185	7								
P	Landsat -7	USA	15/30	185	8								
P	Terra/ASTER	USA,Japan	15/90	60	14								Stereo
C	SPOT 1,2, 4	France	10/20	60	5								3 Sat
C	SPOT 5	France	2.5/5/10	60/120	5								
C	IRS-1C / D	India	5/23	70/142	5								
	DMC	UK	32	640	3								3 Sat
	DMC BilSat-1	Turkey	12/16	25/55	3								
	DMC+4 CHIN	China	4/32	24/600	3								
	SAC-C/MMRS	Argentina	175	360	5								
C	ResourceSat	India	5.8/23	23.5/140	3/4			2					2 Sat
	CBERS-1,2	China, Bras.	20/80	120	8								2 Sat
	CBERS-3	China, Bras.	5/10/80	60/120	4/8								
P	ALOS/PRISM	Japan	2.5/10	35/70	5								Stereo
C	RapidEye	Germany	6.5	78	5								5 Sat
	Lower resolution multi/hyperspectral												
P	Terra,Aqua/Modis	USA	250/1000	2330	36								
C	Envisat/MERIS	ESA/EU	300/1200	575/1150	15								
	EO-1	USA	30	15	233								
C	ResourceSat 1,2	India	70	720	3			2					2 Sat
C	OrbView-X	USA	0.5/5	12	5/200								
	Very High resolution												
C	IKONOS-2	USA	0.8/3.2	11	1/4								
C	IKONOS-BlockII	USA	0.4/1	15.4	1/4								
C	EROS-A1	Israel	1.8	13.5	pan								
C	EROS-B1-3	Israel	0.7/2.8	10.4	1/3		1	2	3				3 Sat
C	Quickbird-2	USA	0.6/2.5	16.5	1/4								
D	WorldView	USA	0.5/1.8	16.5	1/8								
C	OrbView-3	USA	1/4	8	1/4								
C	ROCSat-2	Taiwan	2/8	24	1/4								Stereo
C	CartoSat-1	India	2.5	30/60	pan								Stereo
C	CartoSat-2	India	1	12	pan								
	KOMPSAT-2	Korea	1/4	15	1/4								
	Resurs-DK1	Russia	1/ 2.5	28.3	1/3								
D	Pleiades	France	0.8/2.5	21/40	1/4					1	2		2 Sat
	Synthetic Aperture Radar (SAR)												
P	Radarsat-1	Canada	8/100	45/500	C								
C	ERS-2	ESA/EU	30	100	C								
C	ENVISAT/ASAR	ESA/EU	30/150	100/400	C q								
P	ALOS/PalSAR	Japan	7/100	70/350	L Q								
P	TerraSAR-X	Germany	1/16	10/100	X Q								
P	TerraSAR-L	ESA/EU	5/50	70/200	L Q								
D	COSMOSkyMed	Italy	1/100	10/200	X q			1	2	3			4 Sat
C	Radarsat-2	Canada	3/100	10/500	C Q								
	SAOCOM 1A/B	Argentina	10	100	L			1	2				2 Sat
	RISAT	India	3/50	10/240	C								

Figure 1.1.: Major Earth observation satellites in orbit or in planning (from [81])

Table 1.1.: Overview of mission parameters for some remote sensing satellites

Mission	ERS 1	SPOT 4	Envisat 1	TerraSAR	Sentinel-1
Agency	ESA	CNES	ESA	DLR	ESA
Launch date	July 1991	March 1998	June 2001	June 2007	2013 (TBC)
Mean altitude [km]	775	822	800	514	693
a [km]	7153	7200	7178	6786	7064
e [-]	0.001	0.001	0.025	0.0013	
i [deg]	98.5	98.7	98.6	97.4	98.2
Phasing [days/orbits]	3/43	26/369	35/501	11/167	12/175

by its projection on the ground track and its altitude with respect to the Earth's surface. The design of the orbit will thus define a nominal EF trajectory to be maintained during the entire mission lifetime. Specific orbit control requirements can be expressed by means of constraints on certain quantities, the operational parameters, which define the maximum allowed deviation of the real from the nominal ground track and altitude of the spacecraft. The orbit control is based on the maintenance of these operational parameters within prescribed limits which represent the dead-bands for the orbit control. The operational parameters depend on the deviation of the orbital elements from their nominal values under the action of perturbing forces. Once the mission requirements have been translated into orbit control margins, it is necessary to compute the corrections to be applied to the orbital elements to keep the value of the operational parameters within their control windows. Fig. 1.2 shows the basic block diagram of the orbit control process and in which chapters of this thesis the relevant topics are treated. The requirements which determine the reference orbit (RO) can change in some cases during the course of the mission. From the RO the nominal EF parameters to be controlled can be computed by means of a coordinates transformation represented by block T_{in} in Fig. 1.2. A similar transformation process T_{out} is used to obtain the actual EF parameters from the actual orbit of the spacecraft which varies under the actions of the natural forces determining the motion of the spacecraft. The difference between the nominal and the actual values of the EF parameters are the input to the orbit regulator. The control actions computed by the orbit regulator are then executed by the spacecraft's thrusters. The feedback control scheme of Fig. 1.2 [76-80] is valid for a ground-based or on-board orbit control system the differences being in the single blocks and in the way in which the control process is operated.

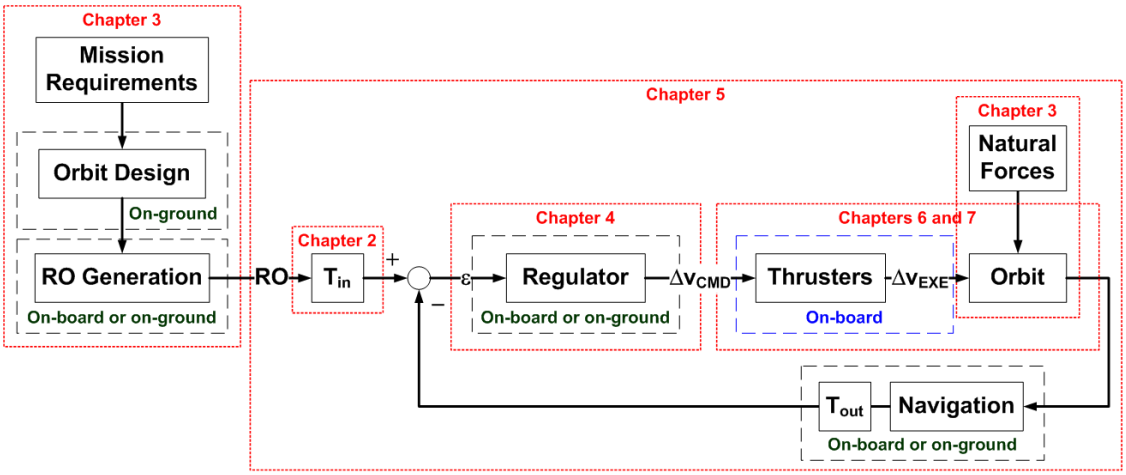

Figure 1.2.: Orbit control process

1.2. Precise Autonomous Absolute Orbit Control

Autonomous on-board orbit control means the automatic maintenance by the spacecraft itself of different operational parameters within their control dead-bands. Increasing the autonomy of spacecraft is often considered an additional unnecessary risk conflicting with the optimal planning of the payload activities. Nevertheless the exploitation of an autonomous on-board orbit control system brings some fundamental advantages and enables some specific mission features. The principal roadblock to introducing the autonomous orbit control technology is simply tradition. Orbit control has always been done from the ground and new programs do not want to risk change for what is perceived as a marginal benefit for that flight.

1.2.1. Potential Advantages and Costs Reduction

Table 1.2 [62] resumes some advantages and costs reduction resulting by the use of an autonomous on-board orbit control system. The fulfilment of very strict control requirements on different orbit parameters can be achieved in real time and with a significant reduction of flight dynamics ground operations [62]. With a fine on-board orbit control system the spacecraft follows a fully predictable RO pattern, such that the position of the spacecraft at all future times is known as far in advance as desirable and there is a longer planning horizon for all future

activities.

The scheduling and planning burden can thus be reduced. With a ground-based orbit control system, planning is done as far in advance as feasible in terms of future orbit propagation. If preliminary plans are done then an updated plan will be created several days in advance, and final updates will be made as close to the event as possible so that the predicted positions can be as accurate as possible. An autonomous on-board fine orbit control eliminates all of the replanning and rescheduling process and allows these activities to be done on a convenient business basis rather than dictated by the orbit prediction capability. Long-term planning can be done on a time lapse basis as convenient for the user group. These plans are updated as the needs of the users change and the detailed schedule of events is prepared in a manner convenient for operations and dissemination [65].

This technology provides a new and unique capability in that even very simple ground equipment that remains out of contact for extended periods can know where a satellite autonomously controlled is and when they will next be within contact. This reduces the cost and complexity of providing needed ephemeris information to the user community.

A tighter control is generally associated with additional propellant usage. For LEO satellites the dominant in-track secular perturbation is the atmospheric drag. The requirement on the orbit control system is to put back what drag takes out. By timing the thruster burns correctly this negative velocity increment can be put back so as to maintain the in-track position with no additional propellant usage over that required to overcome the drag force. Since the orbit is continuously maintained at its highest level rather than being allowed to decay and then brought

Table 1.2.: Costs Reduction

Cost reduction	**Rationale**
Operations	Eliminating the need for ground-based orbit maintenance
Planning and scheduling	By knowing the precise future positions of the spacecraft (or all of the spacecraft in a constellation)
Ephemerides transmission	The cost and complexity of transmitting spacecraft ephemerides to various users is eliminated
Lower propellant usage	The orbit is continuously maintained at its highest level

back up, the effect of drag is minimized and the required propellant usage is also minimized [58]. By increasing the required control accuracy the number of smaller thruster firings will increase. This provides a much finer granularity of control and has the secondary advantage of minimizing the orbital maneuvers disturbance torque. Generally, the largest thruster firing for a fine orbit control is a few times the minimum impulse bit of the thrusters being used. This is, by definition, the smallest level of thrust the propulsion system can efficiently provide and, therefore, the smallest orbital maneuvers disturbance torque. In some cases it may even be possible to do the thruster firings while the payload is operating.

1.2.2. In-flight Demonstrations

In the last two decades different studies have been done for the autonomous orbit control of satellites in LEO [49-64]. Some of these theoretical works were validated in the in-flight demonstrations listed in Table 1.3. All these experiments have in common the GPS-based on-board navigation which is nowadays the only means to obtain a continuous accurate on-board orbit estimation and thus an accurate orbit control. The time at ascending node (TAN) and the longitude of ascending node (LAN) are the parameters controlled by means of along-track velocity increments whereas the longitudinal phase of the orbit (LPO) is controlled by means of cross-track maneuvers. The RO is propagated using only the Earth's gravitational field model and this means that the orbit controller has to keep the gravitational perturbations and correct all the others which are no-conservative forces. Indeed the gravitational perturbations do not cause

Table 1.3.: Autonomous absolute orbit contol in-flight demonstrations

Year	1999	2005	2007	2011
Mission	UoSAT-12	Demeter	TacSat-2	PRISMA
Orbit	650 km sun-sync.	700 km sun-sync.	410 km sun-sync.	710 km sun-sync.
Exp. duration [days]	29	150	15	30
Ctrl type	TAN/LPO/e	LAN/TAN/e	TAN	LAN/TAN
Ctrl accuracy [m]	930	100	750	10
Total Δv [m/s]	0.0733	0.12	0.27	0.13
Propulsion	Cold gas	Hydrazine	Hall Effect Thruster	Hydrazine
Navigation	GPS	GPS	GPS	GPS
Ctrl system developer	Microcosm, Inc.	CNES	Microcosm, Inc.	DLR/SSC

Exp. = experiment, Ctrl = control, TAN = Time at Ascending Node, LAN = Longitude of Ascending Node

orbit decay and can be modeled precisely enough by numerical means to enable prediction of the satellite position far into the future.

The Microcosm Inc. Orbit Control Kit (OCK) software [77] was flown the first time on the Surrey Satellite Technology Limited (SSTL) UoSAT-12 [65] spacecraft, where it co-resides on a customized 386 onboard computer, developed by SSTL, with their attitude determination and control system software. The inputs for OCK are generated by the SSTL-built 12-channel L1-code GPS receiver (SSTL model SGAR 20) with an output frequency of 1 Hz. Microcosm demonstrated in flight two different high-accuracy in-track orbit controllers and one cross-track controller. In the implementation of the in-track controllers, the basic measurement to be controlled, by means of along-track velocity increments, is the TAN i.e. the deviation from the expected value in the crossing time from South to North of the Earth's equator. The actual and reference crossing times are compared for the computation of the required maneuver [58]. On-board targeting of frozen orbit conditions is used to better control the orbit average performance. A proprietary method is used to continually move the orbit toward frozen conditions and, once achieved, hold it there. Orbit-averaged mean elements are also calculated on board. An analogous process to in-track control has been implemented for the cross track control. The cross-track error is determined by comparing the longitude measured at the ascending node to a pre-determined longitude. However, the LPO and not the inclination is controlled by means of cross-track maneuvers. This means that any secular drift in the placement of the orbit plane are removed over time until the desired longitudinal position and drift rate are maintained. An updated and enhanced version of OCK was validated in-flight on TacSat-2 [66] which carried the IGOR GPS receiver developed by Broad Reach Engineering. The goal of this experiment was controlling autonomously the TAN and validating new functionalities of OCK. A series of three short validation tests, lasting up to several days, were performed. These short duration tests were followed by a fourth extended test that lasted two weeks. Similar to the experiment on UoSat-12, OCK managed to maintain the in-track position with an accuracy of 750 m over an extended period of time on TacSat-2, in spite of a variety of off-nominal events.

The main objective of the autonomous orbit control (AOC) experiment on Demeter [67-71] was to control, autonomously and securely in an operational context, the TAN, the LAN

and the mean eccentricity vector of the satellite by means of along-track velocity increments. The control algorithms used are similar to those presented in Sec. 4.1.2. The on-board orbit determination for the experiment was based on a Thales Alenia Space TOPSTAR 3000 GPS receiver [67]. The AOC software was installed in the GPS receiver and used the time, position, velocity plus other indicators as supplied by the GPS receiver for its computations. Time slots for the orbital maneuvers were defined since one of the main constraints was that AOC could not interfere with the scientific mission operations. These time slots, consisting of one orbital period close to a ground station pass, were defined on-ground and uploaded regularly. Only one orbital maneuver per slot was allowed and the size of the velocity increments which could be executed autonomously was also bounded. The ground segment made use of a RO defined consistently with the reference parameters used by the AOC. One of the most interesting aspects of Demeter is that the AOC system was used routinely after its validation and its operations were coordinated with the scientific payload activities.

The autonomous orbit keeping (AOK) experiment on the PRISMA mission [72-75] is described in detail in Chapter 7. The AOK experiment has demonstrated the nowadays most accurate absolute orbit control in full autonomy and with simple operational procedures. The guidance, navigation and control (GNC) architecture of PRISMA (Chapter 6) is structured with orbit control software modules separated from the navigation modules and installed in the spacecraft's on-board computer whereas in the Demeter satellite the control software is installed directly in the GPS receiver [67,69]. The LAN (Chapter 2) and the TAN, as for Demeter, was controlled at the same time by means of along-track velocity increments

These in-flight experiments represent milestones in demonstrating that this technology has now reached a sufficient level of maturity to be applied routinely in LEO missions.

1.3. Ground-based vs Autonomous Orbit Control

As explained in detail by the qualitative cost analysis of Sec. 8.1.1, by increasing the control accuracy requirements, thus reducing the maneuver cycle, the choice of using an autonomous orbit control system can be more convenient. The ratio between the maneuver cycle and the

maximum time between two consecutive ground station contacts is one of the most important drivers in the choice for a ground-based or on-board orbit control system. There is indeed a minimum value of the maneuver cycle for which an autonomous orbit control system is the only feasible option as the latency between the ground station contacts is too large for the exploitation of a ground-based control.

1.3.1. Mission Features Enabled by a Precise Orbit Control

Table 1.4 [62] resumes some specific mission features which are enabled by a precise orbit control. With autonomous orbit keeping, planning and scheduling are done on a business basis, not as astrodynamics dictates. Thus a detailed plan can be put out well in advance to allow time for convenient distribution and potential coordination and input among the mission users. User

Table 1.4.: Enabled Mission Features

Feature	**Rationale**
Mission scheduling in advance	The customer of the mission can plan data-take far in advance and for long period of times
Mission planning in advance	The mission control team knows well in advance when and where the spacecraft will be
Simple user terminals	User terminals with very simple ground equipments for data reception have the entire spacecraft ephemeris in advance
Collision avoidance	Space situational awareness teams have an accurate information on the position of the autonomous spacecraft at any time
Rendezvous	Rendezvous operations are simplified by a target autonomous spacecraft as its trajectory is well known
Coverage analysis for constellations	All users know where all of the satellites are all of the time with no comm link
Eliminate constellation rephasing	All satellites in the constellation are maintained in phase with each other at all times
Use of electric propulsion in LEO	The reduced size of the maneuvers allows the use of a low thrust propulsion system
Use in planetary missions	Costs are lowered due to the possibility of automating data retrieval from the surface

terminals, such as remote weather stations or bookstore computers with daily receipts, can be delivered to the user with the entire spacecraft ephemeris already in memory. Consequently, data can be transmitted autonomously when the satellite is overhead. Similarly, worldwide science groups can do observation planning based on advance knowledge of where the satellite will be and the detailed lighting and viewing conditions then. All of this provides a new level of utility while substantially reducing the cost and complexity of providing needed ephemeris information to the user community.

The fundamental problem with avoiding both collisions and RF interference is to know about it as far in advance as possible. This allows coordination with other system operators and, as discussed above, allows avoidance maneuvers to be done as fuel efficiently as possible. A system using autonomous orbit control may choose to make the future positions of its satellites public. This allows any other satellite users or potential users to calculate as far in advance as possible when potential collisions or interference could occur. This provides the maximum possible warning and permits advance coordination.

For a satellite constellation [64-50] retaining the structure at minimum cost and risk is fundamental. An autonomous orbit control system on-board each satellite can maintain the orbital period such that the mean period will be the same for all satellites in the constellation over its lifetime. This maintains all the satellites synchronized with each other and ensures that the constellation structure will be fully maintained over the lifetime of the satellites without periodic rephasing or readjustment.

The combined use of new low-power electric propulsion technologies and autonomous guidance, navigation, and control techniques provides an effective way to reduce the costs of the orbit maintenance of a satellite in LEO. The use of a suitable electric propulsion system allows for significant savings on propellant mass and a consequent increase of the spacecraft lifetime [56].

The use of a satellite with an autonomous on-board orbit control system around a planet of the solar system to be explored (e.g. Mars) could lower the mission costs due to the possibility of automating data retrieval from the surface [51].

1.3.2. Systems Comparison

The advantages brought by an autonomous orbit control system explained in Sec. 1.2.1 can be afforded indeed by a ground-based control system (except of course for the reduction of the on-ground operations costs) at the condition of a high control accuracy. A routine orbit maintenance with an accuracy of 250 m, at an altitude of 500 km, in the directions perpendicular to the reference ground track has been demonstrated by the TerraSAR-X mission [44,114]. Future missions like Sentinel-1 [118-121] are planned to have a control accuracy requirement of 50 m at an altitude of 700 km. It is necessary to track the main differences, advantages and disadvantages of the two options and identify in which cases one method is more convenient than the other. Fig. 1.2 shows which operations of the orbit control process can be executed on-ground or on-board. Table 1.5 resumes schematically the points of confrontation between ground-based and on-board orbit control systems.

If the orbit control system is ground-based, the only operation executed on-board is the thrusters activation by means of time-tagged-telecommands (TTTC) uploaded to the spacecraft during a ground station contact and the complementary activities (e.g. attitude maneuvers, computation and correction of thruster activation times, etc.). The ground-based orbit determination process needs eventually data downloaded from the spacecraft (e.g. GPS, attitude and maneuvers data). The value of the orbital maneuvers computed on-ground is typically the output of an optimization process which have the availability of space environment data collected on the long period, the most precise navigation data and practically no constraints on the computational resources. The ground station contacts with the spacecraft provide navigation and housekeeping data to the ground segment. These data are filtered and used for an orbit determination to get the best possible knowledge of the satellite status and motion. The operational parameters are computed and handed over to the orbit control software. Inputs for the orbit determination and controller software are also external data, consisting of up-to-date solar flux data, Earth rotation parameters, eventual navigation payload (e.g. GPS) auxiliary data and propulsion system information. The controller compares the predicted operational parameters over a certain period of time with the control dead-bands and computes a time-tagged maneuver which is uploaded to the spacecraft in the next ground station contact. The main operational

Table 1.5.: Comparison between ground-based and on-board orbit control systems

Element	On-ground	On-board
RO	Best available	Best available if uploaded or less accurate if generated on-board
Navigation (GPS)	POD	10 times less accurate
Orbit perturbations	Long period accurate data	On-board estimation or uploaded
Computing resources	Virtually unlimited	Limited
Control software	Optimization process with no hardware or time constraints	Designed considering CPU resources constraints
Man. computation	Optimized	Including on-board navigation errors and limited information about space environment
GS contacts	Necessary for control	Verification only
Reaction time	GS contacts latency time	In real time
Thrusters	Thrusters performance limitations	
Attitude control	Errors included in the computation of the maneuvers	

Man. = maneuver, GS = ground station

constraint is related with the satellite visibility to the available network of ground stations. In fact a minimum lapse of time is required for the upload of the orbital maneuver instructions to the spacecraft and the verification that they have been correctly stored on-board. The ground station contacts are limited due to geographic position of the station and the costs for contact time. Only with a polar ground station a contact visibility is possible every orbit for LEO satellites whereas a ground station at middle latitudes allows typically two scheduled contact per day meaning that the satellite conditions can be checked with an interval of 12 hours. The reaction time of the orbit control system is then commensurate to the latency time of the ground station contacts. An adequate number of post-maneuver passes out of the normal mission schedule, and involving ground station not pertaining to the ground segment, may be required to verify that the maneuver has been executed correctly and that the desired effect on the operational parameters has been obtained.

If the orbit control system is on-board, one of the operations which can be optionally executed

on-ground is the RO generation which can be uploaded to the spacecraft in form of TTTC during a ground station contact (Chapter 7). Other operations which are executed on-ground to support the on-board orbit control system are the calibration of the controller's parameters and the atmospheric density modelling. The major limitation for the generation of the RO on-board is due to the available computational resources of the spacecraft's on-board computer (OBC) which determines the quality of the orbit propagation model that can be used. The initial state of the RO on-board propagation can be a state of the precise orbit determination (POD) ephemerides generated on-ground or a state generated by the on-board navigation system. In the latter case the propagation of the on-board orbit estimation error has to be considered carefully (Sec. 3.2.2). Once the RO is available, all the operations of the control chain are executed on-board the spacecraft. The main advantage of an on-board with respect to ground-based control system is that it reacts in real time to the deviations from the nominal trajectory of the spacecraft. The ground station contacts are included in the orbit control chain only to verify that the system is working properly and no additional contacts have to be scheduled. Some major limitations concerning the inputs and the software have to be considered in designing an autonomous on-board orbit maintenance system. The on-board navigation data will include an error which can be ten times that of a ground-based POD (for a GPS-based orbit estimation process) [73]. This error will impact on the accuracy of the computed orbital maneuver. The information about the orbital environment is also very limited. An on-board estimation of the atmospheric drag, the main non-gravitational perturbation in LEO, required for the computation of the maneuvers can be done using the navigation data filtered and fitted (Sec. 4.1.4). The orbit environment data required by the on-board orbit propagation model can be eventually updated periodically by means of a data upload. The regulator software design has to be compliant with the constraints dictated by the computational and data storage resources of the spacecraft's OBC. A long period optimization process is thus generally not available on-board.

The satellite-bus constraints regarding both control systems, concern mainly the performance of the spacecraft's attitude control and thrusters accuracy. The accuracy of the attitude control system and of the on-board thrusters influence the effectiveness of the orbital maneuvers. The location of the thrusters on-board the spacecraft determines the attitude maneuver profile re-

quired before and after an orbit control maneuver. Besides, the correct operation of certain attitude sensors (e.g. star sensors) may impose time-slots during which the orbital maneuvers cannot be executed. Another important operational issue is that often the science payload cannot work during the orbital maneuvers and the orbit maintenance and payload schedules have to be integrated together. If the control chain is ground-based the scheduling of the payload and orbit maintenance operations can be optimized. If the orbit control system is on-board, the eventual orbital maneuvers are input as a constraint in the scheduling problem.

1.4. The PRISMA Mission

A substantial part of this research is motivated and finds its application in the frame of the PRISMA mission and was realized at the German Space Operations Center (GSOC) of the German Aerospace Center (DLR). PRISMA [82-109] is a micro-satellite formation mission created by the Swedish National Space Board (SNSB) and Swedish Space Corporation (SSC) [168], which serves as a platform for autonomous formation flying and rendezvous of spacecraft. The formation comprises a fully maneuverable micro-satellite (MANGO) as well as a smaller satellite (TANGO) which were successfully launched aboard a Dnepr launcher from Yasny, Russia, on June 15^{th} 2010 into a nominal dawn-dusk orbit at a mean altitude of 757 km, 0.004 eccentricity and 98.28° inclination. The PRISMA mission primary objective is to demonstrate in-flight technology experiments related to autonomous formation flying, homing and rendezvous scenarios, precision close range 3D proximity operations, soft and smooth final approach and recede maneuvers, as well as to test instruments and unit developments related to formation flying. Key sensors and actuators comprise a GPS receiver system, two vision based sensors (VBS), two formation flying radio frequency sensors (FFRF), and a hydrazine monopropellant thruster system (THR). These support and enable the demonstration of autonomous spacecraft formation flying, homing, and rendezvous scenarios, as well as close-range proximity operations. The experiments can be divided in Guidance, Navigation and Control (GNC) experiments and sensor/actuator experiments. The GNC experiment sets consist of closed loop orbit control experiments conducted by SSC and the project partners which are the German

Aerospace Center (DLR/GSOC), the French Space Agency (CNES) in partnership with the Spanish Centre for the Development of Industrial Technology (CDTI), the Technical University of Denmark (DTU), ECAPS (a subsidiary company to SSC), Nanospace (a subsidiary company to SSC), Techno Systems (TSD) and Institute of Space Physics (IRF) in Kiruna. Table 1.6 collects the GNC primary and secondary objectives and the involvement of the different project partners. Table 1.7 resumes the sensor/actuator primary and secondary experiments and the involvement of the different project partners. In addition to the GPS-based absolute and relative navigation system, which is the baseline navigation sensor for the on-board GNC functionalities, DLR contributes two dedicated orbit control experiments. The primary experiment, named Spaceborne Autonomous Formation Flying Experiment (SAFE) [92,143], was executed successfully in two parts, the first one in 2010 and the second one in 2011. SAFE implements autonomous formation keeping and reconfiguration for typical separations below 1 km based on GPS navigation. The secondary experiment of the DLR's contributions to PRISMA is AOK which implements the autonomous absolute orbit keeping of a single spacecraft. The MANGO spacecraft (Fig. 1.3.a) has a wet mass of 150 kg and a size of 80 x 83 x 130 cm in launch configuration, has a three-axis, reaction-wheel based attitude control and three-axis delta-v capability. The GNC sensors equipment comprises two three-axes magnetometers, one pyramid sun acquisition sensors and five sun-presence sensors, five single-axis angular-rate sensors, five single-axis accelerometers, two star-tracker camera heads for inertial pointing, two GPS receivers, two vision-based sensors and two formation flying radio frequency sensors. Three magnetic torque rods, four reaction wheels and six thrusters are the actuators employed. Electrical power for the

Table 1.6.: PRISMA GNC experiments

Primary GNC related tests			
Type of control	**Distance [m]**	**Sensor**	**Prime**
Autonomous formation flying	20-5000	GPS	SSC
Proximity operations [101]	5-100	VBS/GPS	SSC
Collision avoidance and autonomous rendezvous	10-100000	VBS/GPS	SSC
Autonomous formation control (SAFE) [92,143]	50-1000	GPS	DLR
RF-based FF and forced RF-based motion [100,109]	20-5000	FFRF	CNES
Secondary GNC related tests			
Autonomous Orbit Keeping (AOK) of a single spacecraft [72-75]		GPS	DLR

Table 1.7.: PRISMA sensor/actuator experiments

Primary Hardware Related Tests	
Experiment	**Prime**
Flight demo of GPS Phoenix receiver	DLR
Flight demo of HPGP motor [82]	SSC
Flight demo of micro-thrusters motor [99]	Nanospace
Validation of RF sensor (FFRF)	CNES
Validation of Vision Based Sensor (VBS)	DTU
Secondary hardware related tests	
Flight demo of a digital video system	Techno System
Flight demo of a MEMS-based particle mass spectrometer	IRF

operation of the spacecraft bus and payload is provided by two deployable solar panels delivering a maximum of 300 W. In contrast to the highly maneuverable MANGO satellite, TANGO (Fig. 1.3.b) is a passive and much simpler spacecraft, with a mass of 40 kg at a size of 80 x 80 x 31 cm with a coarse three-axes attitude control based on magnetometers, sun sensors, and GPS receivers (similar to MANGO), with three magnetic torque rods as actuators and no orbit control capability. The nominal attitude profile for TANGO will be sun or zenith pointing. Required power is produced by one body-mounted solar panel providing a maximum of 90 W. The communication between the ground segment and the TANGO spacecraft is only provided through MANGO acting as a relay and making use of a MANGO-TANGO inter-satellite link (ISL) in the ultra-high-frequency band with a data rate of 19.2 kbps. DLR/GSOC, besides designing and conducting his own experiments, has assumed responsibility for providing the GPS-based navigation functionality which comprises the provision of Phoenix GPS receivers [103-105], the GPS based on-board navigation system for absolute/relative orbit determination and the ground-based POD [83-85]. In fact the on-board navigation system includes two Phoenix-S GPS receivers and the real-time orbit estimation software with an absolute (relative) position accuracy capability of 2 (0.2) m (3D, RMS) in nominal conditions under the provision of sufficient GPS data. The ground-based POD provides absolute (relative) position accuracies better than 0.1 (0.05) m (3D, RMS). The GPS measurements collected on TANGO are transferred to MANGO via the ISL. The navigation system provides absolute position and velocity of the participating spacecraft to be used by the MANGO GNC system as well as the other PRISMA

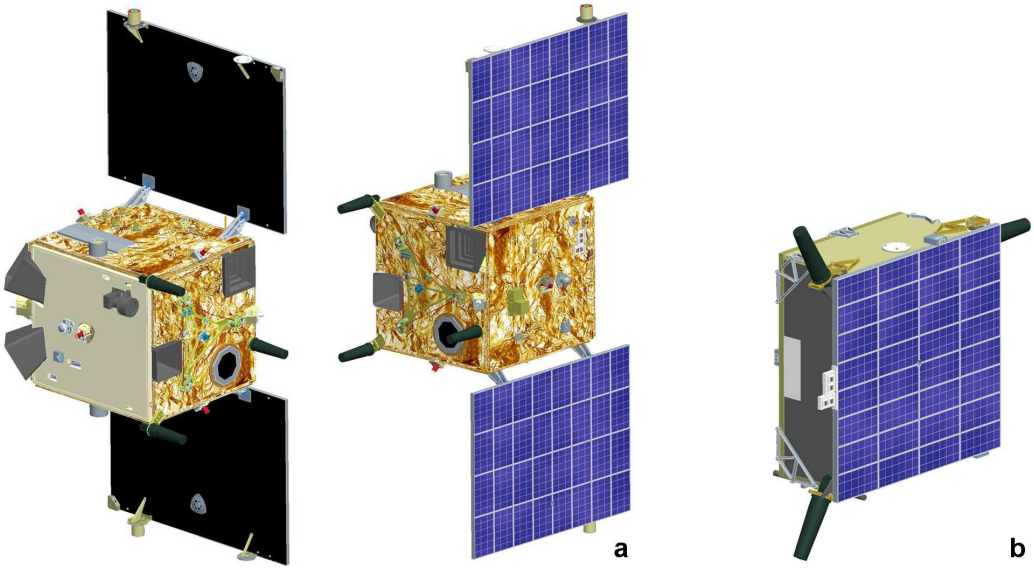

Figure 1.3.: MANGO (a) and TANGO (b) spacecraft

experiments. The GPS system provides also timing information for on-board synchronization. The physical architecture of the GPS system is identical on MANGO and TANGO. For redundancy, two Phoenix-S GPS receivers are available, which are connected to two GPS antennas via a coaxial switch. The dual antenna system provides increased flexibility for handling non-zenith pointing attitudes and antennas may be selected by ground command or autonomously on-board. Only one receiver will be active at any time. Continuous orbit information is important for autonomous on-board GNC applications. As a consequence, orbit prediction is a mandatory function of the navigation system and provides continuous absolute and relative position and velocity information of the co-orbiting satellites. Furthermore the navigation system provides an accuracy measure indicating the expected quality of the orbit results.

1.4.1. The AOK Experiment

The AOK experiment on the PRISMA mission was executed successfully from the 18th of July to the 16th of August 2011 and has demonstrated the capability of autonomous absolute orbit control with an unprecedented accuracy. The main scientific goal of the experiment was to demonstrate the accuracy, robustness and reliability of an autonomous GPS-based on-board

orbit control for its possible routine exploitation in future scientific missions. The main differences with respect to similar experiments conducted in the past (Sec. 1.2.2) are the extremely tight requirements on control accuracy and the full autonomy also enhanced by the possibility of on-board RO propagation. The AOK controller adopts a guidance law for the orbital Longitude of the Ascending Node (LAN) and implements the analytical feedback control algorithm presented in Sec. 4.1. Using GPS-based absolute navigation data, the on-board controller commanded thruster activations in the orbital frame to autonomously control the orbit within a predefined window. The main performance requirement of the experiment was a control accuracy of the osculating ascending node of 10 m (1 σ standard deviation) with a maneuver velocity increment-decrement (Δv) available budget of 0.5 m/s. The AOK software was first developed and tested using the offline and hardware-in-the-loop test facilities at DLR (Chapter 6). After the integration in the PRISMA flight-software, AOK was thoroughly tested at OHB Sweden by means of the Real-Time Satellite Laboratory (SATLAB), a hardware-in-the-loop test facility [87]. The experiment operations were executed at the DLR's PRISMA experiment control centre while the mission was operated at DLR/GSOC. A commissioning phase of 4 days was required to verify that the control software was working properly in all its functionalities. During this phase MANGO flew in free motion as the controller was in open-loop and the orbital maneuvers were computed on-board but not executed. The closed-loop phase of 26 days included RO acquisition, controller tuning and fine control phases. In the last four days of the experiment the possibility of exploiting a RO generated on-board the spacecraft was tested in closed-loop. The 10 m control accuracy requirement was fulfilled. The mean value of the longitude of ascending node deviation was -3.6 m with a standard deviation of 9.5 m during the fine control phase. The on-board controller demonstrated also to be very accurate in computing and executing RO acquisitions. The total Δv spent during the entire experiment was 0.1347 m/s corresponding to 27% of the allocated maneuvers budget. The mean maneuver cycle was 11 hours with a standard deviation of 8.3 hours. The position accuracy available on-board was about 2 m (1 σ) during the entire experiment whereas the accuracy of the on-board estimation of the semi-major axis was 4 m (1 σ) as it comes from a combination of the accuracies of position and velocity.

1.5. The TerraSAR-X/TanDEM-X Missions

TerraSAR-X/TanDEM-X represents the typical remote sensing mission which could take advantage of a precise autonomous orbit control system. TerraSAR-X (TSX) [110-117] is a German Earth-observation satellite realized in a public-private partnership between the German Federal Ministry of Education and Research (BMBF), DLR and EADS Astrium GmbH. The primary goal of the TSX mission (Fig. 1.4) is the provision of high-resolution Synthetic Aperture Radar (SAR) data to both science and commercial users. Its primary payload is an X-band radar sensor with a range of different modes of operation, allowing it to record images with different swath widths, resolutions and polarisations. TSX thus offers space-based observation capabilities that were previously unavailable. The objective of the mission is to provide value-added SAR data in the X-band, for research and development purposes as well as scientific and commercial applications. The successful launch of TSX on 15th June 2007 from the Russian Baikonur Cosmodrome in Kazakhstan marked the start of a campaign to map the Earth at an unprecedented level of accuracy. The aim is to create new, high-quality radar images of the Earth's surface. The satellite has a size of 4.88 x 2.4 m, a mass of 1230 kg and flies in a 514

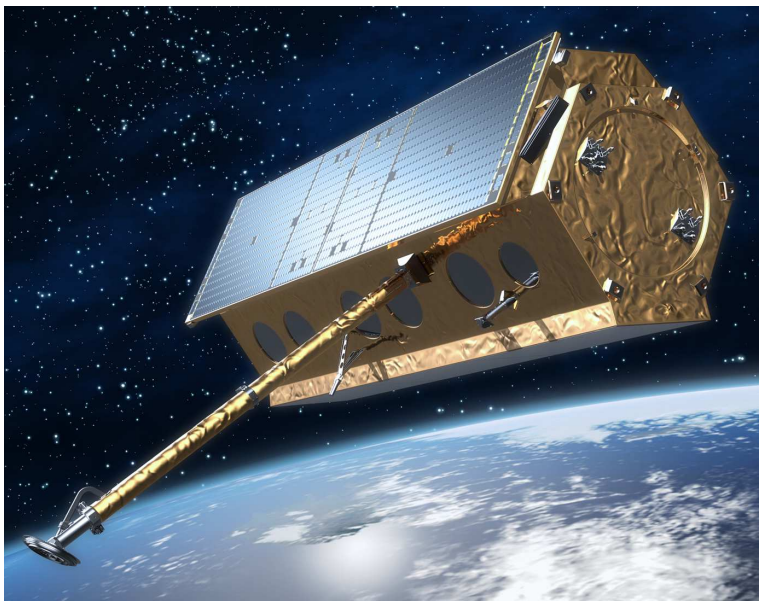

Figure 1.4.: TerraSAR-X

km sun-synchronous dusk-dawn orbit with an inclination of 97.4° and an 11 day repeat period. Using its active radar antenna, TSX it is able to produce image data with a resolution of down to 1 m, regardless of weather conditions, cloud cover or absence of daylight. TSX [171] has been fully operational since 7 January 2008. The radar beam can be electronically tilted within a range of 20 to 60 degrees perpendicular to the flight direction, without having to move the satellite itself. This allows the radar to zoom in on many more ground targets from the satellite's orbit than would be possible using a non-steerable radar. In order to support the spacecraft AOCS and to enable high-precision orbit reconstruction the satellite bus is equipped with a single frequency GPS receiver and the secondary payload features a dual frequency GPS receiver. Due to the objectives of the interferometric campaigns the satellite has to comply to tight orbit control requirements, which are formulated in the form of a toroidal tube with a radius of 250 m around a pre-flight determined reference trajectory [32]. To minimize both the interruption of SAR data takes and the total amount of thruster firings, the maintenance of semi-major axis and eccentricity is simultaneously achieved by a single maneuver at an optimized location [44,110]. The orbit maintenance maneuvers are executed by the mono-propellant (Hydrazine) 4 x 1 N propulsion system.

TanDEM-X (TDX) was built to form the first configurable SAR interferometer employing formation flying with TSX. The main objective of the common TerraSAR-X/TanDEM-X mission (Fig. 1.5) is to generate a global digital elevation model (DEM) with unprecedented accuracy as the basis for a wide range of scientific research as well as for commercial DEM production. TDX [172] was launched on 21th June 2010 and acquired an initial formation with 20 km along-track separation for commissioning purposes roughly one month later. The close formation flight with separations of a few hundred meters was finally established in October 2010. TSX/TDX is the first operational mission requiring a post-facto baseline reconstruction with an accuracy of 1 mm. The TDX/TSX relative orbit control concept is based on the relative eccentricity/inclination vector separation method [143,144]. TDX is equipped with an Autonomous Formation Flying (TAFF) system [111,112] developed at DLR/GSOC. The implementation of autonomous formation flying functionalities on the TDX spacecraft is considered to be a key driver for a more efficient use of the available on-board resources. The objective of TAFF is to

Figure 1.5.: TerraSAR-X and TanDEM-X in formation

enable a simple and robust formation control in order to ease the on-ground operations. TAFF is implemented as part as the attitude and orbit control system on-board TDX and is intended to take over the in-plane formation keeping activities throughout the mission, with a control accuracy of a few meters. A short closed-loop test campaign of TAFF, during which all the functionalities of the autonomous software could be successfully tested, was performed at the end of March 2011.

1.6. Contributions of this Research

The main research topic of this thesis is the autonomous orbit control of a single spacecraft. A fundamental achievement is the rigorous formalization of the absolute orbit control problem as

a special case of formation keeping. For this reason this work can found its collocation in the research dedicated to the spacecraft formation flying [143]. The AOK and SAFE experiments on the PRISMA mission are two complementary in-flight realistic demonstrations of a complete GNC system respectively for autonomous absolute and relative orbit control in a LEO orbit.

1.6.1. Theory

The first step of this research is the reconsideration of state-of-the-art orbit control methods [3,42-48] from the perspective of autonomy. Starting from an analytical algorithm for the maintenance of a repeat-track orbit, the control chain of Fig. 1.2 is developed and implemented under the assumption of the availability of a GPS-based on-board navigation. An algorithm is developed for the on-board estimation, by means of navigation data, of the semi-major axis decay caused by the atmospheric drag. New analytical formulations for the RO acquisition under different constraints and requirements are developed.

Particular emphasis is given to the analysis of the RO generation process which can be ground-based or on-board. The main achievement of this analysis is the definition of constraints on the minimal accuracy of the orbit model used and of the initial state for the propagation. An extensive study of the orbit perturbation environment in LEO is carried on. The results of this study have the added value, with respect to similar analyses performed in the past, of the availability of a large amount of POD data from the missions PRISMA and TerraSAR-X which have near circular orbit at respectively 700 and 500 km. These POD data have an accuracy better than 10 cm (1 σ) and have also been used for the calibration of the orbit models used for all the numerical simulations performed during this research work.

The state-of-the-art orbit control methods are based on a formalization of the problem which is dependent on the particular mission and its orbit maintenance requirements. A step forward is then taken in the direction of the definition of a general and rigorous formalization of the autonomous orbit control problem and the exploration of new control methods. The problem of the autonomous absolute orbit control is considered as a specific case of two spacecraft in formation in which one, the reference, is virtual and affected only by the Earth's gravitational field. A new parametrization, the relative Earth-Fixed elements (REFE), analogous to the rela-

tive orbital elements (ROE) [137,159], is introduced to describe the relative motion of the real and reference sub-satellite points on the Earth surface. The REFE allow the general formalization of the absolute orbit control requirements which are usually expressed through specific Earth-fixed operational parameters such as altitude deviation, phase difference, etc. [3]. A direct mapping between REFE and ROE enables the direct translation of absolute into relative orbit control requirements. By means of this new formalization, the deviation between the actual and the reference nominal orbit [32] can be defined in an Earth-fixed coordinate system analogous to the orbital frame [4]. This approach allows moreover the straightforward use of modern control theory techniques for orbit control. A linear and a quadratic optimal regulators are designed and compared, by means of numerical simulations, with the analytical algorithms. The goal is to show a method rather than some specific simulation results. The particular absolute and relative orbit control problem with its requirements can be formalized using every time the same parametrization given by the REFE and the ROE.

1.6.2. Transfer of Technologies from Ground to On-board Computer

The innovation and originality of this thesis derives also from the design and practical implementation of the control chain of Fig. 1.2 in the frame of the PRISMA mission. This research work has led to the full development, testing and validation of the autonomous absolute orbit control flight code embedded in the OBC of the MANGO spacecraft of the PRISMA technology demonstration. The design and validation of the GPS-based flight software throughout its complete development process, up to the spacecraft launch, is described. The innovative approach of model-based software design (MBD) is addressed. The MBD allows the implementation and execution of the GNC software on different platforms in a fully consistent manner. The GNC system was first tested as a standalone unit in a dedicated software development environment at DLR [170] and later validated after its full integration into the PRISMA spacecraft on-board computer. This allows first to develop the software simulations off-line on a PC and then to reproduce them consistently as real-time and hardware-in-the-loop tests during the validation

phase. In the off-line tests, the flight software is stimulated through different sources of GPS data with an increasing level of realism. The complete application is then ported to a Real-Time Executive for Multiprocessor Systems (RTEMS) environment in the LEON3 PRISMA on-board computer by means of MATLAB/Simulink Real Time Workshop. Overall the test and validation process shows the compliance of the navigation and control software to the challenging requirements of the PRISMA mission in terms of functionality, data interface, GNC accuracy, on-board memory and CPU load.

The flight data of the AOK [72-75] experiment on the PRISMA mission [167] are displayed and commented. The main scientific goal of the experiment, successfully executed in the summer of 2011, was to demonstrate the accuracy, robustness and reliability of an autonomous GPS-based on-board orbit control for its possible routine exploitation in future scientific missions. Autonomous precise orbit maintenance, RO acquisition and on-board RO generation have been successfully demonstrated in orbit.

1.7. Thesis Outline

This thesis is structured in seven chapters complemented by an appendix section. Referring to Fig. 1.2, after an extensive theoretical dissertation of the different blocks composing the orbit control chain, the attention is focused on the practical implementation, validation and testing of the considered autonomous orbit control methods.

The thesis starts with an extended general discussion about orbit control requirements and the state of the art of its implementation. The attention is focused on the advantages brought by the exploitation of an autonomous orbit maintenance system in terms of costs reduction and enabled mission features. A statistical comparison between ground-based and on-board orbit control is not possible because only few autonomous orbit control in-flight experiments have been performed so far. Nevertheless a qualitative discussion and cost analysis can be made based on the available literature and on the author's practical experience. A fundamental statement is that a major driver to the development of on-board autonomous orbit control is the increasing accuracy demand due to the steady development and exploitation of very high res-

olution optical and synthetic aperture radars systems in the last two decades. A description of two missions, PRISMA and TerraSAR-X/TanDEM-X, is also given in the introduction since a substantial part of this research is motivated and finds its application in the frame of those projects. The PRISMA mission gave the possibility to perform an autonomous orbit keeping experiment which validated successfully one of the orbit control methods proposed in this thesis. The TerraSAR-X/TanDEM-X formation represents the typical remote sensing mission which can take advantage of a precise autonomous orbit control system.

After the introduction, the thesis proceeds explaining, in Chapter 2, the parametrizations used, the basic mathematical means on which the different orbit control methods proposed are based. Two main approaches are identified for the realization of an on-board orbit control system. The first is the reconsideration and further development of state-of-the-art orbit control methods from the perspective of autonomy. A step forward is then taken in the direction of the definition of a general and rigorous formalization of the autonomous orbit control problem. The problem of the autonomous absolute orbit control is considered as a specific case of two spacecraft in formation in which one, the reference, is virtual and affected only by the Earth's gravitational field. A new parametrization, the relative Earth-Fixed elements (REFE), analogous to the relative orbital elements used for formation control, is introduced to describe the relative motion of the real and reference sub-satellite points on the Earth surface. The relative Earth-Fixed elements allow the general formalization of the absolute orbit control requirements which are usually expressed, with the first approach, through specific Earth-fixed operational parameters (e.g. altitude deviation, phase difference, etc.).

An extensive discussion is dedicated in Chapter 3 to the RO selection and generation process and the analysis of the free motion of a spacecraft in low Earth orbit. The RO defines the spacecraft's nominal trajectory designed to satisfy the mission requirements. The actual orbit is kept within certain bounds defined with respect to the RO. The RO selection process based on the mission requirements is briefly described as well as the typical orbits used for remote sensing. The link between the operational parameters and the requirements is explained. The generation process of the RO is dealt in detail as it is the fundamental starting point of the orbit control chain. The free motion analysis is essential to understand the orbit perturbation

environment which causes the deviation of the actual from the nominal trajectory. The use of the precise orbit determination data of the missions PRISMA and TerraSAR-X guarantee the reliability of the results of this analysis and the understanding of the orbit's perturbation environments at an altitude of 700 and 500 km. This study helps the definition of a proper control strategy. The conclusions drawn in this chapter about the RO generation process are also based on the experience gained with the realization of the AOK in-flight experiment described in Chapter 7.

The control algorithms, explained in Chapter 4, can be divided into the two broad categories of analytical and numerical. An analytical algorithm for the maintenance of a repeat-track orbit is developed from the state-of-the-art methods and implemented under the assumption of the availability of a GPS-based on-board navigation. A complementary algorithm for the on-board estimation of the semi-major axis decay caused by the atmospheric drag is developed. New analytical formulations for the RO acquisition under different constraints and requirements are presented. The virtual formation method for the absolute orbit control is formalized by means of the relative Earth-fixed elements described previously in the chapter dedicated to the parametrization. The state-space representation is used for the mathematical formulation of the problem. The system to be controlled is described by means of a linear dynamic model including the J_2 zonal coefficient of the Earth's gravitational field and the atmospheric drag perturbation force. A linear and a quadratic optimal regulators, based on this model, are designed for the in-plane and out-of-plane absolute orbit control. Among the control methods presented in this chapter, only the analytical algorithm was validated in-flight with the AOK experiment on the PRISMA mission because it had a most advanced implementation status at the moment of its selection.

The entire Chapter 5 deals with the results of the numerical simulations performed for the validation of the control methods explained in Chapter 4. The high degree of realism of the simulations' results is guaranteed by a calibration of the orbit propagator model by means of the comparison between the propagated and the actual orbit data given by the POD process of the PRISMA and TerraSAR-X missions. The mission parameters of these two formations are also used as simulation scenarios. The test platform includes a very accurate orbit propagator,

the flight software and allows the simulation of actuators and navigation errors. The simulation results are evaluated from a performance and operational point of view in order to formulate a first conclusion about the advantages and disadvantages of the different control techniques. The main differences between the considered analytical and numerical control methods are outlined. Though the main topics of the thesis is the orbit maintenance of a single spacecraft, some simulation results of a combined autonomous absolute and formation maintenance system are shown. This is a practical way to indicate one of the possible ways forward.

Once the theory has been explained extensively, the practical implementation of a precise autonomous orbit control system for a spacecraft in low Earth orbit is described in detail in Chapter 6. The on-board guidance, navigation and control software development, implementation and testing of the PRISMA mission, to which the author of this thesis contributed, is described. The attention is focused on the technological aspects implied by the realization of the autonomous orbit control system tested in-flight with the autonomous orbit keeping experiment on PRISMA. The development of the control system is driven by a compromise between control performance requirements, on-board computer resources limitation and mission operational constraints. The model-based-design approach, used for the realization of the PRISMA flight software, is described as well as the basic layout of the on-board software architecture. Among the several innovative aspects of the flight software development, some space is dedicated to the advanced software validation and testing realized on the formation flying test-bed at DLR, the German Aerospace Center, which played a fundamental role in the realization of the PRISMA mission and its experiments.

Finally, the flight results of the AOK experiment on the PRISMA mission, a fundamental milestone of this research work, are presented in Chapter 7. This experiment took place in the summer of 2011 and demonstrated the capability of autonomous precise absolute orbit control using the analytical control method explained in Sec. 4.1. The 30-day experiment is described in all its phases with the presentation of the control performance results and the operational issues.

Chapter 8 provides a summary of the achieved results, draws the main conclusions and gives some recommendations for future study.

Appendix A contains the linear dynamic model used in Sec. 4.2.1, Appendix B gives some further details about the numerical simulations and Appendix D points out some aspects of the AOK experiment.

The Bibliography is structured in sub-sections each one grouping references dealing about the same argument and listed in alphabetical order of the authors' surnames.

2. Parametrizations

2.1. Overview

A parametrization is defined by the parameters which describe both the absolute motion of a spacecraft orbiting around the Earth and the relative motion with respect to a nominal orbit. The set of orbital elements chosen for the absolute state representation and shown in Eq. (2.1) are the semi-major axis a, the components of the eccentricity vector $\mathbf{e}$, the orbital plane inclination i, the mean argument of latitude Ω sum of the argument of perigee ω and the mean anomaly M.

$$\boldsymbol{\kappa} = \begin{pmatrix} a \\ e_x \\ e_y \\ i \\ \Omega \\ u \end{pmatrix} = \begin{pmatrix} a \\ e\cos\omega \\ e\sin\omega \\ i \\ \Omega \\ \omega + M \end{pmatrix} \tag{2.1}$$

The choice of this parametrization of the state is dictated by the fact that it does not lead to singular equations if the eccentricity value tends to zero. Nevertheless this set of orbital elements leads to singular equations if the inclination angle tends to zero but this case is out of interest in this study. The components of vector $\boldsymbol{\kappa}$ are the mean orbital elements obtained from the osculating elements $\boldsymbol{\kappa_o}$ using Brouwer's analytical transformation [12]

$$\boldsymbol{\kappa} = \boldsymbol{\xi}(\boldsymbol{\kappa}_o) \tag{2.2}$$

The mean orbital elements are indeed the most appropriate in the representation of the secular evolution of the motion subjected to perturbations. Indeed the orbital elements of a spacecraft deviate from their nominal values under the action of perturbing forces. The mission requirements are translated into control margins to be applied to the orbital elements to keep the value of specific parameters, which define the maximum allowed deviation of the actual from the nominal trajectory of the spacecraft, within their control windows. Two different set of parameters, function of the difference between the actual and reference orbital elements, are introduced in this chapter for the description of the motion of a spacecraft with respect to its RO.

First, specific mission requirements are expressed by means of operational parameters [3] which define the maximum allowed deviation of the real from the nominal trajectory of the spacecraft. Typical operational parameters as the altitude deviation and phase difference at a certain latitude, local time deviation, in-orbit phasing, specify the nominal position of the spacecraft's sub-satellite point in relation to a reference ground track on the Earth's surface [44]. The operational parameters are used by the algorithms developed for the state-of-the-art ground based orbit control systems. Secondly, a new parametrization, the relative Earth-Fixed elements (REFE), is derived by considering the problem of the autonomous absolute orbit control as a specific case of two spacecraft in formation in which one, the reference, is virtual and affected only by the Earth's gravitational field. The REFE, analogous to the ROE [137,159] for the description of the in-orbit relative motion of two spacecraft, are introduced to describe the relative motion of the real and reference sub-satellite points on the Earth surface. This parametrization allows a more general and rigourous mathematical formalization of the absolute orbit control problem.

2.2. Operational Parameters

2.2.1. Phase Difference

The phase difference ΔL is the difference, measured along a parallel of latitude, between the actual ground track and the track pertaining to a RO. The phase difference at the ascending node

ΔL_{AN} is most commonly used as operational parameter for maintenance of phased orbits. In fact if the inclination remains equal to its nominal value, the monitoring of the phasing at the equator will be sufficient to monitor the entire phasing grid formed by the network of reference tracks on Earth. ΔL_{AN} can be written in terms of relative orbital elements between the real satellite and a virtual satellite whose orbit is the RO. By assuming that the real and virtual satellites pass the equator respectively at times t and $t_{\mathcal{R}}$ with in-orbit angular velocities $\dot{u}$ and $\dot{u}_{\mathcal{R}}$, and neglecting any differences in the eccentricity of the real and the RO, the differential of ΔL_{AN} is given by:

$$\frac{1}{R_E} d(\Delta L_{AN}) = \frac{1}{R_E} d(\Delta L_{AN_\Omega} + \Delta L_{AN_u}) = (\dot{\Omega} - \dot{\Omega}_{\mathcal{R}})dt - d(|\omega_E - \dot{\Omega}_{\mathcal{R}}|\Delta t) \tag{2.3}$$

where R_E is the Earth's equatorial radius, $\dot{\Omega}$ and $\dot{\Omega}_{\mathcal{R}}$ are the secular rotations of the real and reference line of nodes respectively , $\omega_E = 7.292115 \times 10^{-5}\ rad\ s^{-1}$ is the Earth rotation rate and $\Delta t = t - t_{\mathcal{R}}$.

Eq. (2.3) expresses the fact that the difference of longitude of the two tracks at the equator is due to the superposition of two effects. The differential $d\Delta L_{AN_\Omega}$ is due to the different time-change rates $\dot{\Omega}$ and $\dot{\Omega}_{\mathcal{R}}$ of the right ascension of ascending node during time interval dt. The term $d\Delta L_{AN_u}$, positive if Δt is negative, is due to the fact that the real and reference satellites pass the equator at different times while the Earth is rotating. Since $|\omega_E - \dot{\Omega}_{\mathcal{R}}|$ is constant, $d(|\omega_E - \dot{\Omega}_{\mathcal{R}}|\Delta t) = |\omega_E - \dot{\Omega}_{\mathcal{R}}| d(\Delta t)$. The differential $d(\Delta t)$ can be written as

$$d(\Delta t) = dt - dt_{\mathcal{R}} = \frac{du}{\dot{u}} - \frac{du}{\dot{u}_{\mathcal{R}}} \qquad \text{with} \qquad \dot{u} = \frac{du}{dt} \qquad \text{and} \qquad \dot{u}_{\mathcal{R}} = \frac{du_{\mathcal{R}}}{dt} = n \tag{2.4}$$

where $n = \sqrt{\mu / a_{\mathcal{R}}^3}$ is the mean motion (with $\mu = 3.9860064 \times 10^{14}\ m^3\ s^{-2}$). As $du = \dot{u}dt$, from Eq. (2.4) it results

$$d(\Delta t) = \frac{\dot{u}_{\mathcal{R}} - \dot{u}}{\dot{u}_{\mathcal{R}}} dt \tag{2.5}$$

Using Eq. (2.5) in Eq. (2.3)

$$\frac{1}{R_E} d(\Delta L_{AN}) = (\dot{\Omega} - \dot{\Omega}_{\mathcal{R}})dt + \frac{|\omega_E - \dot{\Omega}_{\mathcal{R}}|}{n} (\dot{u} - \dot{u}_{\mathcal{R}})dt \tag{2.6}$$

The first derivative of Ω and u expanded as function of J_2 [2,21] and of the mean orbital elements in the first-order truncation of Brouwer's analytical satellite solution [12] when the orbit is nearly circular ($e \approx 0$) are $\dot{\Omega} = -3\gamma n \cos i$ and $\dot{u} = n + 3\gamma n(4\cos^2 i - 1)$ [3]. The second derivatives $d^2\Omega/dt^2$ and d^2u/dt^2 are then

$$\frac{d^2\Omega}{dt^2} = 3\gamma n \left(\frac{7}{2a}\cos i \frac{da}{dt} + \sin i \frac{di}{dt}\right) \qquad \frac{d^2\Omega_{\mathcal{R}}}{dt^2} = 0 \tag{2.7}$$

$$\frac{d^2u}{dt^2} = -\frac{3n}{2a}\left[1 + 7\gamma(4\cos^2 i - 1)\right]\frac{da}{dt} - 12\gamma n \sin 2i \frac{di}{dt} \qquad \frac{d^2u_{\mathcal{R}}}{dt^2} = 0 \tag{2.8}$$

where $\gamma = (J_2/2)(R_E/a)^2$ and the derivatives $d\gamma/dt$ and dn/dt have been written as

$$\frac{d\gamma}{dt} = -\frac{2\gamma}{a}\frac{da}{dt} \qquad \frac{dn}{dt} = -\frac{3n}{2a}\frac{da}{dt} \tag{2.9}$$

Using Eqs. (2.7)-(2.8) and substituting $3\gamma n \sin i = -\dot{\Omega}\tan i$ and $7\gamma\cos i = -7\dot{\Omega}/(3n)$, the time derivative of Eq. (2.6) yields

$$\begin{aligned}\frac{d^2(\Delta L_{AN})}{dt^2} = &-\frac{3}{2}|\omega_E - \dot{\Omega}_{\mathcal{R}}|\left(\frac{R_E}{a}\right)\left[1 + \frac{7}{3}\frac{\dot{\Omega}}{|\omega_E - \dot{\Omega}_{\mathcal{R}}|} + 7\gamma(4\cos^2 i - 1)\right]\frac{da}{dt} + \\ &-R_E\left[\dot{\Omega}\tan i + 12\gamma|\omega_E - \dot{\Omega}_{\mathcal{R}}|\sin 2i\right]\frac{di}{dt}\end{aligned} \tag{2.10}$$

Imposing that the orbit is sun synchronous or near sun-synchronous with $\dot{\Omega} = \dot{\Omega}_{\mathcal{R}} = \dot{\Omega}_{sy}$, Eq. (2.10) becomes

$$\frac{d^2(\Delta L_{AN})}{dt^2} \approx -\frac{3\pi}{T_E}\left(\frac{R_E}{a}\right)(1 + \epsilon_L)\left[\frac{da}{dt} - \xi_L\frac{di}{dt}\right] \tag{2.11}$$

where ϵ_L has been approximated as

$$\epsilon_L \approx \frac{7}{3}\left(\frac{T_E}{T_{Su}}\right) + 7\gamma(4\cos^2 i - 1) \tag{2.12}$$

and

$$\xi_L = -\frac{2}{3} a \left(\frac{T_E}{T_{Su}}\right) \left(\frac{1+\eta_L}{1+\epsilon_L}\right) \tan i \qquad \eta_L = 24\gamma \left(\frac{T_{Su}}{T_E}\right) \cos^2 i \tag{2.13}$$

and where T_{Su} is the Sun period (1 year), T_E is the mean period of solar day (86400 s) and $\eta_L \ll 1$ and $\epsilon_L \ll 1$ for near polar orbits.

The evolution of ΔL, the phase difference at non-zero latitude, in terms of relative and absolute orbital elements is [3]

$$\Delta L = \Delta L_{AN} \sqrt{1 - (\sin u \sin i)^2} \pm R_E \, \delta i_x \sin u \left[\frac{(\cos u \sin i)^2}{1 - (\sin u \sin i)^2}\right]^{-1/2} \tag{2.14}$$

where in the second term the $+$ sign has to be used in ascending orbit and the $-$ in descending orbit, ΔL_{AN} is given by Eq. (2.6), u is the argument of latitude and $\delta i_x = i - i_{\mathcal{R}}$ is the difference between the real and the nominal inclination.

2.2.2. Local Time Deviation

The local time deviation ΔLT is directly equivalent to the deviation of the right ascension of the ascending node Ω from its nominal value.

$$\Delta LT = T_E \frac{\Delta\Omega}{2\pi} \tag{2.15}$$

where: $\Delta\Omega = \Omega - \Omega_{\mathcal{R}}$

The general analytical expression for the evolution of ΔLT with the orbital elements [3] is

$$\frac{d^2(\Delta LT)}{dt^2} = -\frac{T_E}{T_{Su}} \left(\tan i \frac{di}{dt} + \frac{7}{2a} \frac{da}{dt}\right) \tag{2.16}$$

2.2.3. Altitude Deviation at Latitude

The altitude deviation Δh is the difference between the actual and the nominal altitude at latitude θ. The general analytical expression for the evolution of Δh with the orbital elements [3]

is

$$\Delta h(u) = (1+\epsilon_h)\Delta a - a(\cos u \Delta e_x + \sin u \Delta e_y) + \eta_h \Delta i \tag{2.17}$$

with

$$\epsilon_h = \frac{J_2}{6}\left(\frac{R_E}{a}\right)^2 \left[9\left(1-\frac{3}{2}\sin^2 i\right) - \sin^2 i \cos 2u\right] - e\cos(u-\omega)$$

$$\eta_h = R_E\left[\frac{J_2}{6}\frac{R_E}{a}\left(\frac{27}{2}\sin 2i + \sin 2i \cos 2u\right) + (u-\omega)\sin 2i \sin^2 u\right]$$

2.2.4. In Orbit Position Deviation

The in orbit position deviation Δu is the difference between the argument of latitude of the real satellite and that of a virtual satellite moving on the RO affected only by the force model used to the generation of the reference trajectory. The general analytical expression for the evolution of Δu with the orbital elements [3] is

$$\frac{d^2(\Delta u)}{dt^2} = -\frac{3}{2a}n\left[1+\frac{7}{2}J_2\left(\frac{R_E}{a}\right)^2(4\cos^2 i - 1)\right]\Delta a - 6nJ_2\left(\frac{R_E}{a}\right)^2 \sin 2i \Delta i \tag{2.18}$$

2.3. Virtual Formation Parametrization

The definition of the operational parameters in Sec. 2.2 is based on the description of the motion of a spacecraft with respect to a reference ground track specified by the nominal absolute orbital elements. The relative Earth-fixed elements are instead defined in this section formulating the absolute orbit control system design as a formation keeping problem of two spacecraft in which one is virtual and not affected by non-gravitational orbit perturbations. Both these parametrizations will be used in the development of this thesis for the realization of an autonomous orbit control system. The use of the operational parameters allows the straightforward reconsideration of state-of-the-art orbit control methods from the perspective of autonomy. The on-board control system used for the AOK experiment (Chapter 7) is based on an analytical method to control the phase difference at the equator (Sec. 4.1). With this approach, the control perfor-

mance of an on-board and ground-based system can be compared more easily.

The use of the REFE parametrization is a step forward in the direction of the definition of a general and rigorous formalization of the autonomous orbit control problem and the exploration of new control methods or the exploitation of algorithm already developed for the formation keeping. Since this approach allows the straightforward use of modern control theory techniques for orbit control a linear and a quadratic optimum regulators are developed in Sec. 4.2 and validated by means of numerical simulations Chapter 5.

2.3.1. Relative Orbital Elements

The most appropriate parametrization to represent the relative motion of the real spacecraft with respect to the reference is the set of ROE [92,150,159] shown in Eq. (2.19) (where the subscript $\mathcal{R}$ refers to the RO).

$$\boldsymbol{\delta\kappa} = \begin{pmatrix} \delta a \\ \delta e_x \\ \delta e_y \\ \delta i_x \\ \delta i_y \\ \delta u \end{pmatrix} = \begin{pmatrix} (a - a_{\mathcal{R}})/a_{\mathcal{R}} \\ e_x - e_{x\mathcal{R}} \\ e_y - e_{y\mathcal{R}} \\ i - i_{\mathcal{R}} \\ (\Omega - \Omega_{\mathcal{R}}) \sin i \\ u - u_{\mathcal{R}} \end{pmatrix} \tag{2.19}$$

These parameters are obtained as a non-linear combination of the mean orbital elements $\boldsymbol{\kappa} = (a, e_x, e_y, i, \Omega, u)$ [12,22]. The relative orbit representation of Eq. (2.19) is based on the relative eccentricity and inclination vectors [144] defined in Cartesian and polar notations as

$$\boldsymbol{\delta e} = \begin{pmatrix} \delta e_x \\ \delta e_y \end{pmatrix} = \delta e \begin{pmatrix} \cos\phi \\ \sin\phi \end{pmatrix} \qquad \boldsymbol{\delta i} = \begin{pmatrix} \delta i_x \\ \delta i_y \end{pmatrix} = \delta i \begin{pmatrix} \cos\theta \\ \sin\theta \end{pmatrix} \tag{2.20}$$

The phases of the relative $\mathbf{e}/\mathbf{i}$ vectors are termed relative perigee ϕ and relative ascending node θ because they characterize the relative geometry and determine the angular locations of the perigee and ascending node of the relative orbit. The normalized position $\boldsymbol{\delta r} = (\delta r_R\, \delta r_T\, \delta r_N)^T/a_{\mathcal{R}}$ and velocity $\boldsymbol{\delta v} = (\delta v_R\, \delta v_T\, \delta v_N)^T/(n a_{\mathcal{R}})$ vectors of the spacecraft relative to the RO in the

RTN orbital frame (**R** pointing along the orbit's radius, **N** pointing along the angular momentum vector and $\mathbf{T} = \mathbf{N} \times \mathbf{R}$ pointing in the direction of motion for a circular orbit) can be described through the relative orbital elements [144] as

$$\begin{pmatrix} \boldsymbol{\delta r} \\ \hline \boldsymbol{\delta v} \end{pmatrix} = \begin{pmatrix} \mathbf{T_p} \\ \hline \mathbf{T_v} \end{pmatrix} \boldsymbol{\delta\kappa} = \left(\begin{array}{cccccc} 1 & -\cos u & -\sin u & 0 & 0 & 0 \\ -(3/2)u & 2\sin u & -2\cos u & 0 & 1/\tan i & 1 \\ 0 & 0 & 0 & \sin u & -\cos u & 0 \\ \hline 0 & \sin u & -\cos u & 0 & 0 & 0 \\ -(3/2) & 2\cos u & 2\sin u & 0 & 0 & 0 \\ 0 & 0 & 0 & \cos u & \sin u & 0 \end{array}\right) \begin{pmatrix} \delta a \\ \delta e_x \\ \delta e_y \\ \delta i_x \\ \delta i_y \\ \delta u \end{pmatrix} \tag{2.21}$$

Eq. (2.21) represents the first order solution of the Clohessy-Wiltshire equations [142] expressed in terms of relative orbital elements.

2.3.2. Relative Earth-fixed elements

The constraints on the relative position of the sub-satellite points (SSPs) of the real and reference spacecraft and on the difference of their altitudes, determine the virtual formation's geometry to be maintained in the **RTN** orbital frame. The SSP is here defined as the intersection between a sphere of radius a, centred in the Earth's centre and tied to its rotation, and the line through the centre of the Earth and the satellite. Referring to Fig. 2.1 the $(\lambda\varphi\eta)$ reference frame has the origin in the SSP, the λ-axis tangent to the local circle of latitude and pointing eastward, the φ-axis tangent to the local meridian and pointing northward and the η-axis pointing along the orbit radius. The relative position of the real and reference SSPs is defined in the $(\lambda_{\mathcal{R}}\varphi_{\mathcal{R}}\eta_{\mathcal{R}})$ frame of the reference spacecraft by the phase difference vector $\delta\mathbf{L} = (\delta L_\lambda, \delta L_\varphi)^T$ and by $\delta h = \Delta h / a_{\mathcal{R}}$ the altitude difference normalized to $a_{\mathcal{R}}$. Considering the actual spacecraft at the ascending pass over latitude φ, the REFE vector $\boldsymbol{\delta f} = (\delta L_\lambda \; \delta L_\varphi \; \delta h)^T$ components are defined

as

$$\delta L_\lambda = \delta\lambda_{\delta t=0} + \delta\lambda_{\delta t} = (\delta\lambda - \delta\varphi\cot i_{\mathcal{R}}) - \cos\varphi|\omega_E - \dot{\Omega}_{\mathcal{R}}|\delta t \tag{2.22}$$

$$\delta L_\varphi = \delta\varphi \tag{2.23}$$

$$\delta h = \delta\eta \tag{2.24}$$

where $(\delta\lambda, \delta\varphi, \delta\eta) = (\lambda - \lambda_{\mathcal{R}}, \varphi - \varphi_{\mathcal{R}}, \eta - \eta_{\mathcal{R}})$, $i_{\mathcal{R}}$ is the RO inclination, φ is the real spacecraft's latitude at time t, $\delta t = t - t_{\mathcal{R}}$ and $t_{\mathcal{R}}$ is the time at which the reference spacecraft passes at latitude φ. Fig. 2.1 depicts the case in which $t > t_{\mathcal{R}}$. The phase difference vector's component $\delta L_\lambda = \delta L_\lambda(\varphi, \delta\lambda, \delta\varphi, \delta t)$ is the distance, normalized to $a_{\mathcal{R}}$, of the real and reference ground tracks measured along the λ-axis at latitude φ. δL_λ is also function of δt because the real and reference spacecraft pass at latitude φ at different times and the coordinate systems $(\lambda_{\mathcal{R}}\varphi_{\mathcal{R}}\eta_{\mathcal{R}})$ and $(\lambda\varphi\eta)$ move with the SSPs while the Earth is rotating. The quantity $\delta\lambda_{\delta t=0}$ is the normalized distance, measured along the λ-axis, between the intersection points S and R_1 of the real and RO projections with the circle of latitude φ at time t (Figures 2.1 and 2.2.a). Referring to Fig. 2.2.a, approximating the spherical triangles as planar, since in the plane $(\lambda_{\mathcal{R}}\varphi_{\mathcal{R}})$ is $R_1 \approx (\delta\varphi\cot(\pi - i_{\mathcal{R}}), -\delta\varphi)$, and $S = (-\delta\lambda, -\delta\varphi)$, it results $\delta\lambda_{\delta t=0} = R_1 - S \approx \delta\lambda - \delta\varphi\cot i_{\mathcal{R}}$. The quantity $\delta\lambda_{\delta t}$ is the normalized distance measured along the λ-axis between the intersection points R_1 and $R(t_{\mathcal{R}})$ of the RO projection with the circle of latitude φ at times t and $t_{\mathcal{R}}$ (Fig. 2.1). The minus sign in the second member of Eq. (2.22) is due to the convention that $\delta\lambda_{\delta t}$ is positive when δt is negative and vice-versa. The time difference δt can be written as $\delta t = -\delta\varphi\, n\sin i_{\mathcal{R}}$ where $n\sin i_{\mathcal{R}} = v_\varphi$ is the φ-component of the velocity of the reference sub-satellite point moving on the Earth's surface. Hence Eq. (2.22) can be written as

$$\delta L_\lambda = \delta\lambda + \left(\frac{|\omega_E - \dot{\Omega}_{\mathcal{R}}|\cos\varphi}{n\sin i_{\mathcal{R}}} - \cot i_{\mathcal{R}}\right)\delta\varphi \tag{2.25}$$

As the absolute orbit control requirements are formulated in terms of REFE (Eqs. (2.22)-(2.24)) but the control is realized in terms of ROE (Eq. (2.19)), a direct mapping between the two systems is required. Referring to Figures 2.2.b and 2.2.c for the transformation from **RTN** to

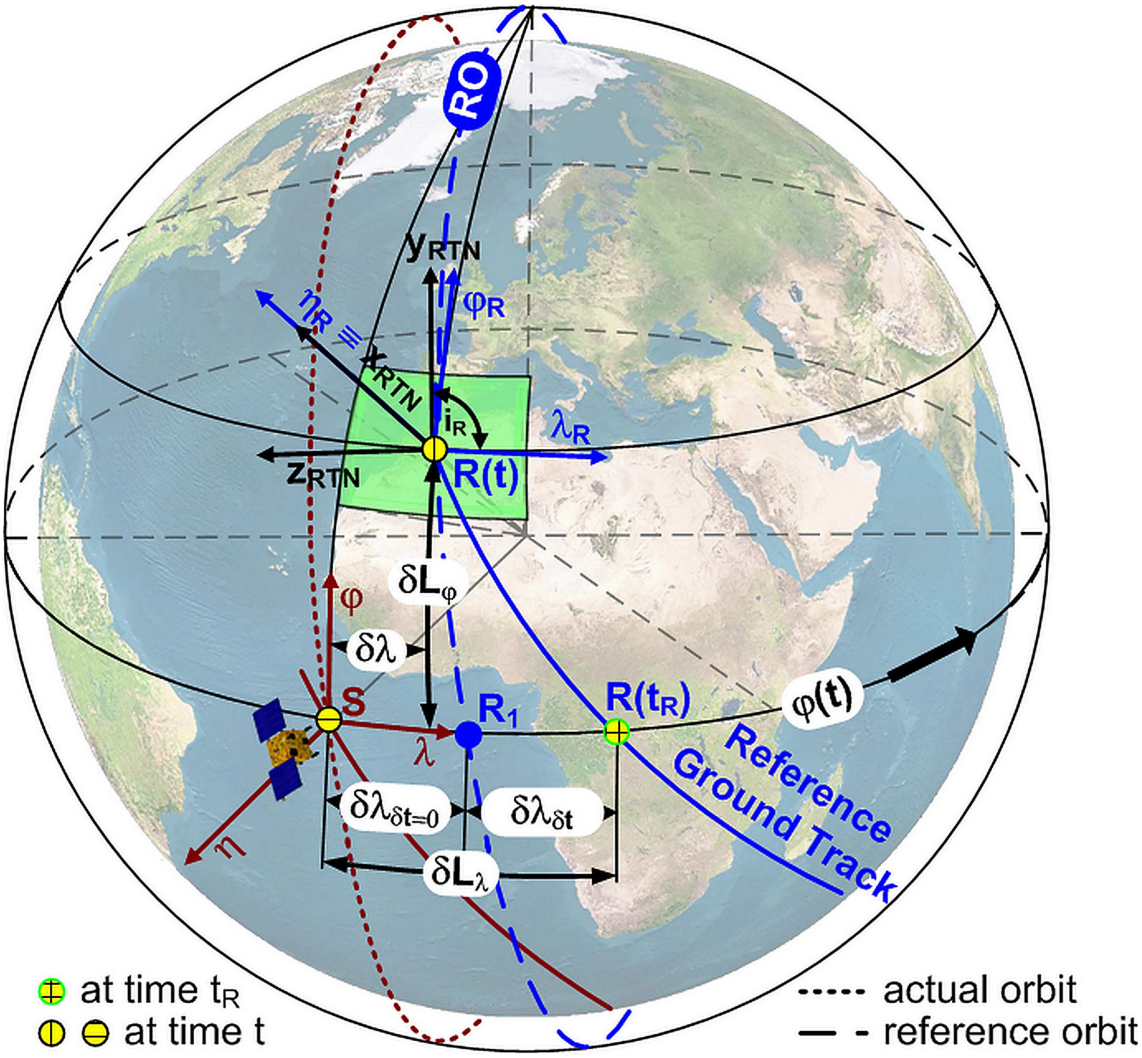

Figure 2.1.: Geometry of the relative Earth-fixed elements

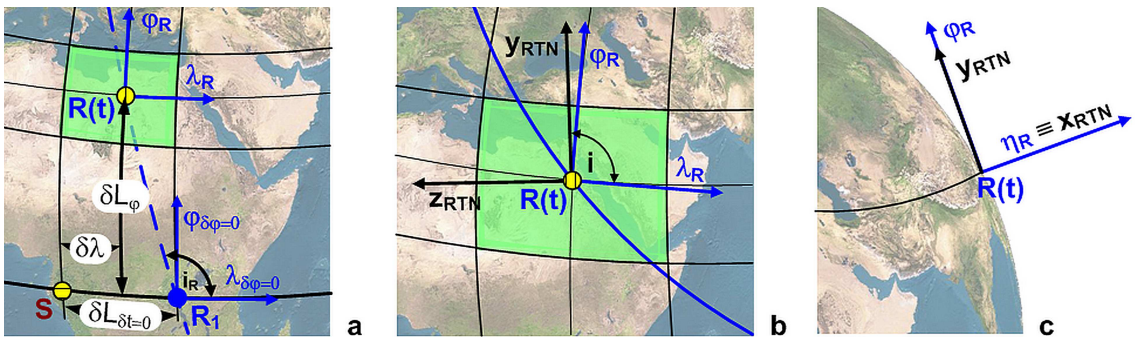

Figure 2.2.: Detail of Earth-fixed reference frame (a) and transformation from orbital to Earth-fixed reference frame (b,c)

$(\lambda\varphi\eta)$ and using Eqs. (2.23), (2.24) and (2.25), the REFE vector $\boldsymbol{\delta F} = (\delta L_\lambda \; \delta L_\varphi \; \delta h)^T$ can be mapped into **RTN** coordinates with the transformation

$$\boldsymbol{\delta F} = \mathbf{T_{EF}} \boldsymbol{\delta r} \tag{2.26}$$

$$\mathbf{T_{EF}} = \begin{pmatrix} 0 & \dfrac{|\omega_E - \dot{\Omega}_\mathcal{R}|}{n} \cos\varphi & \left(\dfrac{|\omega_E - \dot{\Omega}_\mathcal{R}|}{n} \cos\varphi \cos i_\mathcal{R} - 1 \right) \dfrac{1}{\sin i_\mathcal{R}} \\ 0 & \sin i_\mathcal{R} & \cos i_\mathcal{R} \\ 1 & 0 & 0 \end{pmatrix} \tag{2.27}$$

Eq. (2.25) is singular for $i_\mathcal{R} = 0 + k\pi$ (with $k \in \mathbb{Z}$) as for those values of $i_\mathcal{R}$ the orbital and equatorial planes are parallel. It is interesting to remark that the term $\delta\lambda_{\delta t=0}$ of Eq. (2.22) can be written directly in the **RTN** coordinate system by imposing $\delta\varphi = \delta r_T \sin i_\mathcal{R} + \delta r_N \cos i_\mathcal{R} = 0$, and substituting the solution $\delta r_T = -\delta r_N \cos i_\mathcal{R} / \sin i_\mathcal{R}$, singular for $i_\mathcal{R} = 0 + k\pi$, in equation $\delta\lambda = \delta r_T \cos i_\mathcal{R} - \delta r_N \sin i_\mathcal{R}$. Finally, from Eqs. (2.21) and (2.26) and substituting $\cos\varphi = \sqrt{1 - (\sin u \sin i)^2}$ ($\sin\varphi = \sin u \sin i$ from the sine formula of spherical trigonometry), vector $\boldsymbol{\delta F}$ and its time derivative $d(\boldsymbol{\delta F})/dt$, evaluated fixing $u = \overline{u}$, can be written in terms of relative orbital elements using the transformation matrix $\mathbf{T} = \mathbf{T_{EF}} \mathbf{T_p}$ ($\mathbf{T_p}$ defined in Eq. (2.21)):

$$\boldsymbol{\delta F}(\overline{u}, \boldsymbol{\delta\kappa}) = \mathbf{T}(\overline{u}) \boldsymbol{\delta\kappa} \tag{2.28}$$

$$\frac{d(\boldsymbol{\delta F})}{dt} = \mathbf{T}(\overline{u}) \frac{d(\boldsymbol{\delta\kappa})}{dt} \tag{2.29}$$

$$\mathbf{T}(u) = \begin{pmatrix} -\dfrac{3}{2}u\tau & 2\tau su & -2\tau cu & \dfrac{su}{si_\mathcal{R}}(\tau ci_\mathcal{R} - 1) & \left[\dfrac{\tau(1-cu)ci_\mathcal{R}}{cu} + 1 \right] \dfrac{cu}{si_\mathcal{R}} & \tau \\ -\dfrac{3}{2}usi_\mathcal{R} & 2susi_\mathcal{R} & -2cusi_\mathcal{R} & suci_\mathcal{R} & (1-cu)ci_\mathcal{R} & si_\mathcal{R} \\ 1 & -cu & -su & 0 & 0 & 0 \end{pmatrix} \tag{2.30}$$

with $\tau = (|\omega_E - \dot{\Omega}_\mathcal{R}|/n)\sqrt{1 - (\sin u \sin i)^2}$, $su = \sin u$, $cu = \cos u$, $si_\mathcal{R} = \sin i_\mathcal{R}$ and $ci_\mathcal{R} = \cos i_\mathcal{R}$. Since $u(t)$ is periodic, the vectorial function $\boldsymbol{\delta F}(\overline{u}, \boldsymbol{\delta\kappa}(t))$ is obtained from function $\boldsymbol{\delta F}(u(t), \boldsymbol{\delta\kappa}(t))$ by considering only the subset $(\overline{u}, \boldsymbol{\delta\kappa}(t))$ of the function's domain $(u(t), \boldsymbol{\delta\kappa}(t))$. This is why the term $(d\mathbf{T}/dt)\boldsymbol{\delta\kappa} = (d\mathbf{T}/d\overline{u})(d\overline{u}/dt)\boldsymbol{\delta\kappa} = 0$ does not compare in Eq. (2.29) (if the variation of i is considered negligible). This procedure is justified by the control design approach explained at the end of Sec. 4.2.1. Eqs. (2.28) and (2.29) are valid

under the assumptions of near circular orbits and separations between the real and reference spacecraft small when compared to the RO radius (see Eq. (2.21)). The following equations show the form assumed by the relative Earth-fixed elements of Eq. (2.28) when evaluated at the ascending node ($\overline{u} = 0$).

$$\delta L_\lambda = \frac{\delta i_y}{\sin i_\mathcal{R}} + \frac{|\omega_E - \dot{\Omega}_\mathcal{R}|}{n}(\delta u - 2\delta e_y) \tag{2.31}$$

$$\delta L_\varphi = (\delta u - 2\delta e_y)\sin i_\mathcal{R} \tag{2.32}$$

$$\delta h = \delta a - \delta e_x \tag{2.33}$$

The phase difference vector component δL_λ at the ascending node is commonly used as operational parameter for the maintenance of phased orbits. If the inclination remains equal to its nominal value, the control of the phase difference at the equator will be the most effective way to monitor the displacement between real and reference ground tracks. It can also be noticed that the maintenance of the altitude deviation δh requires the control of the semi-major axis as well as the eccentricity vector.

3. Reference Orbit and Free Motion Analysis

As seen in Chapter 1 the nominal orbit specifications as well as the orbit keeping accuracy depend on the type of mission and payload considered. The specification of a target trajectory, a RO based on the nominal orbit parameters, is fundamental for the definition of the orbit control strategy. The orbit control is based on the maintenance of pre-defined operational parameters within prescribed limits which represent the dead-band for the orbit control. The real and RO are compared in order to quantify the error of the operational parameters. Thus the actual orbit will be kept within certain bounds defined with respect to the RO in order to fulfil the mission requirements. This chapter deals with the RO selection and generation and the orbit perturbation environment which causes the deviation of the actual from the nominal trajectory.

3.1. Reference Orbit Selection

Fig. 3.1 shows the detailed view of the subsystem of Fig. 1.2 representing the RO selection. A RO is an orbit representing the mean nominal motion of the satellite over a long time interval. The RO design is based on the orbit's specifications dictated by the mission requirements on the local altitude, local time, phasing an coverage. The requirements define the nominal value of the orbital elements (Eq. (2.1)). The RO's propagation model has to be as complete as possible because the controlled spacecraft's actual orbit has to be as close as possible to the reference. On the other hand it should not include non-conservative perturbation forces because usually the RO has to be completely periodic. Thus the RO model should at least consider the

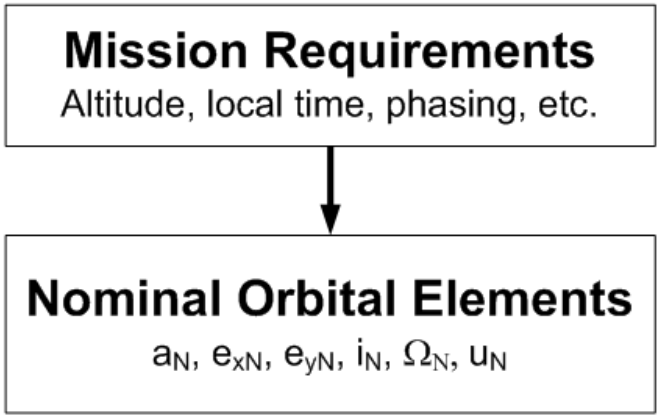

Figure 3.1.: Reference orbit selection process

non-spherical terms of the Earth gravitational potential so that the RO is an ideal orbit whose mean orbital elements are periodical functions with invariant maximum and minimum amplitudes. The nominal value of the orbital elements, which meet the operational requirements, are obtained [3] by solving the orbital equations of motion including only secular perturbations (in the case of sun synchronicity, phasing and altitude) and long period perturbations (for the altitude) which are related to the geopotential. The result is a defined relationship, dependent on the requirements, between different orbital elements as shown in Table 3.1. The level of accuracy of the nominal orbital elements' numerical value is related to the gravitational field model and the number of terms used. Only the zonal harmonics of even value are considered for the secular variations and odd value for long-period variations. The elements a, e_x, e_y determine the size, shape and orientation of the orbit within its plane whereas i and Ω characterize the orientation of the orbital plane. The value of the argument of latitude u does not require any

Table 3.1.: Orbit specification in terms of nominal mean orbital elements

Orbit specification	**Related orbital elements**
Space fluctuations of altitude	$e_{x_\mathcal{R}}(a_\mathcal{R})$, $e_{y_\mathcal{R}}(a_\mathcal{R})$
Time fluctuations of altitude	$e_{x_\mathcal{R}}(a_\mathcal{R}, i_\mathcal{R})$, $e_{y_\mathcal{R}}(a_\mathcal{R}, i_\mathcal{R})$
Local time	$a_\mathcal{R}(i_\mathcal{R})$
Phasing	$a_\mathcal{R}(i_\mathcal{R})$
Coverage	$i_\mathcal{R}$

absolute specification as it represents the time variable. Several specifications can be grouped for the design of a RO.

3.1.1. Altitude Requirements

The altitude variation constraints can be required in terms of space by minimizing the fluctuations in relation to latitude on a given orbit segment or in terms of time by restricting the fluctuations in time over a given point of the Earth surface and can be established through a proper choice of a, e_x and e_y (e and ω).

Minimization of Spatial Fluctuations

The variation of altitude as a function of u taking into account the variations of a, e_x and e_y must be examined to carry out the spatial minimization. Considering the expansion to the first order in e of the altitude h = h(u,e) and assuming a near circular orbit, there will be a maximum deviation $\Delta h_{MAX_{e=0}}$ relative to the mean h_m at the equator and the extreme latitudes [3]

$$h(u) = h_m - e a_m \cos(u - \omega) - (\Delta h_{MAX,e\approx 0}) \cos 2u \tag{3.1}$$

$$h_m = a \left[1 - \frac{3}{2} J_2 \left(\frac{R_E}{a} \right)^2 \left(1 - \frac{3}{2} \sin^2 i \right) \right] - R_E \left[1 - \frac{f}{2} \sin^2 i \right] \tag{3.2}$$

$$\Delta h_{MAX,e\approx 0} = R_E \left[\frac{f}{2} - \frac{J_2}{6} \left(\frac{R_E}{a} \right) \right] \sin^2 i \tag{3.3}$$

where $f = 1 - a_p/a_e$ is the flattening parameter of the Earth ellipsoid [8] if a_e and a_p are respectively its semi-major and semi-minor axes.

The minimization of altitude variations in the orbital quadrants $q = 1, 2, 3, 4$ corresponding to $u = [0, \pi/2], [\pi/2, \pi], [\pi, (3/2)\pi], [(3/2)\pi, 2\pi]$ leads to

$$\omega = \frac{3}{4}\pi - (q-1)\frac{\pi}{2} \quad , \quad e \approx 1.57 \, \frac{\Delta h_{MAX,e\approx 0}}{a} \tag{3.4}$$

$$\Delta h_{MAX,q} = \left(\frac{1.57}{\sqrt{2}} - 1 \right) \Delta h_{MAX,e\approx 0} \tag{3.5}$$

Minimization of Time Fluctuations

For the minimization of the altitude fluctuations in time, the variations of the mean orbital elements e and ω have to be cancelled out [3]

$$\frac{de}{dt} = f(a, e, \omega, i) = 0 \tag{3.6}$$

$$\frac{d\omega}{dt} = g(a, e, \omega, i) = 0 \tag{3.7}$$

If the low frequency portion of the spectrum of perturbations of the geopotential is considered (periods much longer than the orbital period) then the long-period variations affecting e and ω are due to the odd number zonal terms of the geopotential whereas the secular variations affect only ω and are related to the even number zonal terms. Adding these two effects, the solution of Eq. (3.6) yields the frozen orbit conditions [23-28]. If only an expansion limited to J_3 is used, the approximate solution of Eq. (3.6) is

$$\omega = \pm\frac{\pi}{2} \tag{3.8}$$

$$e \approx -\frac{J_3}{2J_2}\frac{R_E}{a}\sin i \tag{3.9}$$

The majority of frozen orbits have $\omega = \pi/2$. In both cases of $\omega = \pm\pi/2$ the altitude at a given latitude is the same in the ascending and descending orbits disregarding the influence of longitude via the tesseral terms of the potential.

3.1.2. Local Time Requirements

Sun synchronism is imposed through the relationship between a and i obtained by setting the secular angular rotation of the line of nodes, due to the non-sphericity of the Earth, equal to the known angular rotation of the meridian plane containing the mean Sun. The sun synchronism condition [29,30] is thus represented by Eq. (3.10) where the averaged variation of Ω due to the first three zonal terms J_2, J_3 and J_4 [21] is represented by Eq. (3.10).

$$\dot{\Omega} = \omega_{sy} \tag{3.10}$$

$$\dot{\Omega} = -\frac{3}{2} n J_2 \left(\frac{R_E}{p}\right)^2 \cos i - \frac{3}{2} n J_2^2 \left(\frac{R_E}{p}\right)^4 \cos i \left[\frac{9}{4} + \frac{3}{2}\sqrt{1-e^2} - \sin^2 i \left(\frac{5}{2} + \frac{9}{4}\sqrt{1-e^2}\right) + \right.$$
$$\left. + \frac{e^2}{4}\left(1 + \frac{5}{4}\sin^2 i\right) + \frac{e^2}{8}(7 - 15\sin^2 i)\cos 2\omega \right] - \frac{3}{8} n J_3 \left(\frac{R_E}{p}\right)^3 (15\sin^2 i - 4) e \cot i \sin\omega +$$
$$+ \frac{15}{16} n J_4 \left(\frac{R_E}{p}\right)^4 \cos i \left[(4 - 7\sin^2 i)\left(1 + \frac{3}{2}e^2\right) - (3 - 7\sin^2 i) e^2 \cos 2\omega \right] \tag{3.11}$$

where $\omega_{sy} = 1.99099299 \times 10^{-7}\ rad\ s^{-1}$ is the mean apparent revolution speed of the Sun around the Earth, $R_E = 6378140\, m$ is the equatorial radius of the terrestrial spheroid, $p = a(1-e^2)$ is the parameter of the orbit and $n = \sqrt{\mu/a^3}$ is the mean motion (with $\mu = 3.9860064 \times 10^{14}\ m^3\ s^{-2}$).

Eq. (3.10) imposes the constraints that the nominal drift of the line of nodes is frozen in relation to the Earth-Sun direction and thus provides one of the two orbital element (a, i) as function of the other. The semi-major axis of a sun-synchronous orbit has its upper boundary at $12.35 \cdot 10^6$ m for an inclination which tends to 180 deg. The inclination of a sun synchronous orbit is always more than 90 deg

3.1.3. Phasing Requirements

A repeat-ground-track orbit [31-38] is obtained when there is a commensurability between the satellite's nodal frequency and the Earth's rotation rate i.e. the time required by the satellite to complete an integer number of orbits is equal to the total time required by the Earth to complete an integer number of rotations. If $T_{\mathcal{R}}$ and $n_{\mathcal{R}} = 2\pi/T_{\mathcal{R}}$ are respectively the nodal period and the nodal frequency, the condition for the ground track to repeat every k orbits in d days can be formulated as [31]

$$\frac{\omega_E - \dot{\Omega}}{n_{\mathcal{R}}} = \frac{d}{k} \tag{3.12}$$

where $\omega_E = 7.292115 \times 10^{-5}\ rad\ s^{-1}$ is the Earth rotation rate, $\dot{\Omega}$ is the secular rotations of the line of nodes.

If the zonal coefficients J_2 and J_4 of the geopotential are considered, the repeat-ground-track

condition of Eq. (3.12) can be explicitly formulated as [31]

$$\begin{aligned}
\frac{N}{D} =& \frac{d}{k} \\
N =& \frac{\omega_E}{nJ_2}\left(\frac{a}{R_E}\right)^2 + \frac{3}{2}\cos i - \frac{15}{16}\frac{J_4}{J_2}\left(\frac{R_E}{a}\right)^2 \cos i(4 - 7\sin^2 i) + \\
&+ \frac{3}{8}J_2\left(\frac{R_E}{a}\right)^2 \cos i(11 - 20\sin^2 i) \\
D =& 1 + 3 - \frac{15}{4}\sin^2 i - \frac{15}{16}\frac{J_4}{J_2}\left(\frac{R_E}{a}\right)^2 \left(\frac{34}{5} - 25\sin^2 i + \frac{77}{4}\sin^4 i\right) + \\
&+ \frac{3}{16}J_2\left(\frac{R_E}{a}\right)^2 (14 + 17\sin^2 i - 35\sin^4 i)
\end{aligned}$$

The phasing of the orbit then define a relationship between a and i. With a defined repeat-ground-track pattern and the operational inclination given, the corresponding mean semi-major axis a can be found by using any standard numerical method.

3.1.4. Coverage Requirements

The payload access to targets observation is a key requirement in the design of an orbit. The target can be one location, specified by a latitude or longitude, or a region of interest on the Earth's surface. To this end, the design of the orbit must satisfy performance metrics that are specified by the end user as the total time of coverage over a region, the access to daytime and nighttime coverage, or the time required to access a different region, among others. The requirement for coverage [39-41] of a terrestrial zone extending to a given latitude φ will determine, among other parameters, an acceptable range of values for the inclination i between φ and $\pi - \varphi$ if the lateral field of view of the payload is not taken into account.

3.2. Reference Orbit Generation

Fig. 3.2 shows the detailed view of the block of Fig. 1.2 representing the RO generation process. The deviations of the real from the reference orbital elements are defined by means of the operational parameters (Sec. 2.2) or equivalently by means of the relative Earth-fixed elements

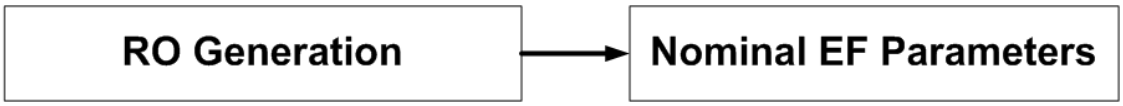

Figure 3.2.: Reference orbit generation process

(Sec. 2.3.2). Table 3.2 collects the relationship between the orbit specifications, the operational parameters, the REFE and the deviation of the real from the nominal orbital elements expressed by means of relative orbital elements. The dependence of Δh on $\delta i_x \equiv \delta i$ (Eq. (2.17)) has not be considered as it is negligible on the short time scale. In Sections 3.2.1 and 3.2.2 the fundamental issues regarding the RO generation will be analysed in detail. As a case study the PRISMA mission (Sec. 1.4) is used since the analyses carried on in this section are strictly related to the design and implementation of the on-board orbit control system validated in-flight with the AOK experiment (Chap. 7).

Table 3.2.: Control specifications

Orbit specification	**Op. Parameter**	**Rel. EF Element**	**Rel. Orbital Element**
Space fluctuations of altitude	Δh	δh	δa, δe_x, δe_y
Time fluctuations of altitude	Δh	δh	δa, δe_x, δe_y
Local time	ΔLT	$\delta L_\lambda(0)$ - $\delta L_\varphi(0)\alpha$*	δi_y
Phasing	ΔL_{AN}	$\delta L_\lambda(0)$	δe_y, δi_y, δu
Coverage	-	-	δi_x
*$\alpha = \lvert\omega_E - \dot{\Omega}_\mathcal{R}\rvert/(n \sin i_\mathcal{R})$			

3.2.1. Reference Orbit Propagation Model

As explained in Sec. 3.1, the RO is generated by an orbit propagator which includes in the forces model only the Earth gravitational field. The actual orbit of a spacecraft deviates from the RO under the action of non-conservative perturbing forces. The goal of this section is to quantify the contribution of the accuracy of the Earth's gravitational field model used for the RO generation to the deviation of the actual from the reference values of the operational parameters controlled. To this end numerical simulations have been performed. In each simulation a propagated orbit representing the actual trajectory of the MANGO spacecraft in free motion, has been compared

Table 3.3.: PRISMA spacecraft physical properties

Spacecraft Physical Property	**MANGO**	**TANGO**
Mass [kg]	155.12	38.45
Drag area [m^2]	0.5625	0.2183
Drag coefficient [-]	2.5	2.5
SRP effective area [-]	0.5625	0.2183
SRP [4] coefficient [-]	5.5	3.13

with a RO generated using a gravitational field model each time including a higher order and degree number of harmonics (20x20, 30x30, 40x40, 50x50, 60x60 and 70x70). Tables 3.3 and 3.4 collect respectively the spacecraft physical properties and the force models used for the propagation of the simulated actual and reference trajectories. The initial state used for the orbit propagation is shown in Table 3.5 and the run time is one month (duration of the AOK experiment). The POD ephemerides of the spacecraft TANGO, the PRISMA formation's target satellite which flies in free motion, have been exploited to calibrate the atmospheric density model used for the simulations in order to have a high degree of realism. Fig. 3.3 shows the difference between TANGO's orbit as estimated by the POD process with an accuracy at the sub-decimetre level and an orbit propagated with the calibrated model of Table 5.1.

Table 3.4.: Propagation parameters

Orbit Propagation	**Model**
Earth gravitational field	GRACE GGM01S 70x70
Atmospheric density	Harris-Priester
Sun and Moon ephemerides	Analytical formulas [4]
Solid Earth, polar and ocean tides	IERS
Relativity effects	First order effects
Numerical integration method	Dormand-Prince, fixed step 1 s
RO Propagation	**Model**
Earth gravitational field	GRACE GGM01S nxn

Table 3.5.: Initial state - POD state on 20-06-2011 at 06:00:00 UTC

ECI state	$\mathbf{r_R}[\mathbf{m}]$	$\mathbf{r_T}[\mathbf{m}]$	$\mathbf{r_N}[\mathbf{m}]$	$\mathbf{v_R}[\mathbf{m/s}]$	$\mathbf{v_T}[\mathbf{m/s}]$	$\mathbf{v_N}[\mathbf{m/s}]$
	-3967394.8566	-289822.105	5883191.2151	-6126.365	1487.7675	-4071.5062
Mean orb. el.	$\mathbf{a}[\mathbf{m}]$	$\mathbf{e_x}[-]$	$\mathbf{e_y}[-]$	$\mathbf{i}[\mathbf{deg}]$	$\mathbf{\Omega}[\mathbf{deg}]$	$\mathbf{u}[\mathbf{deg}]$
	7130522.2961	-0.004058	0.002774	98.28	351.74	123.38

Figures 3.4-3.8 show the comparison between the actual and the RO propagated with different models.

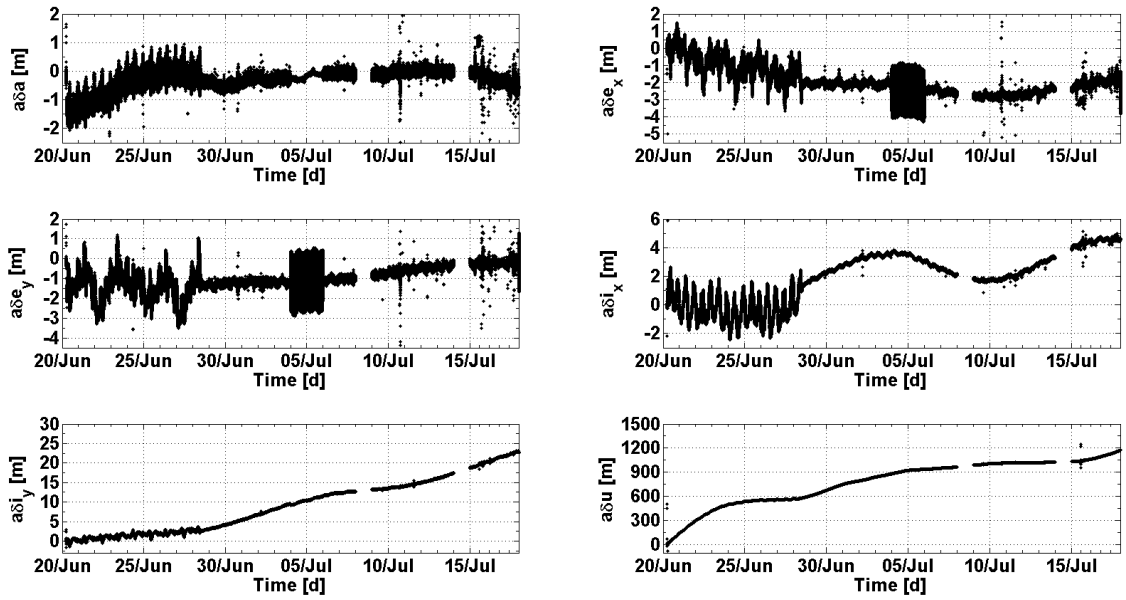

Figure 3.3.: Difference between TANGO's actual (POD) and propagated orbital elements

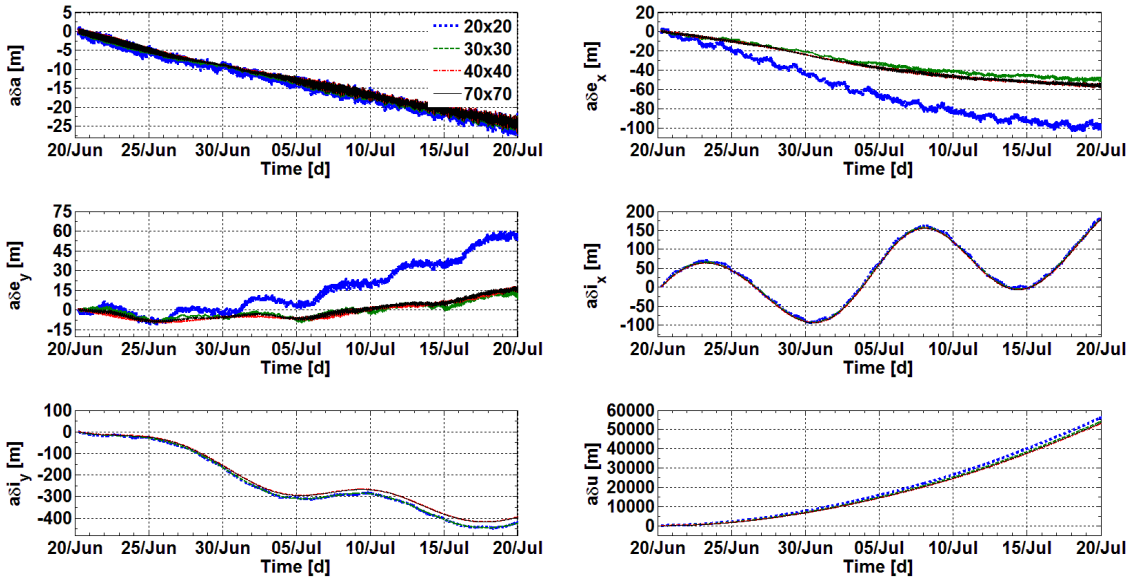

Figure 3.4.: MANGO's ROE (Actual-RO)

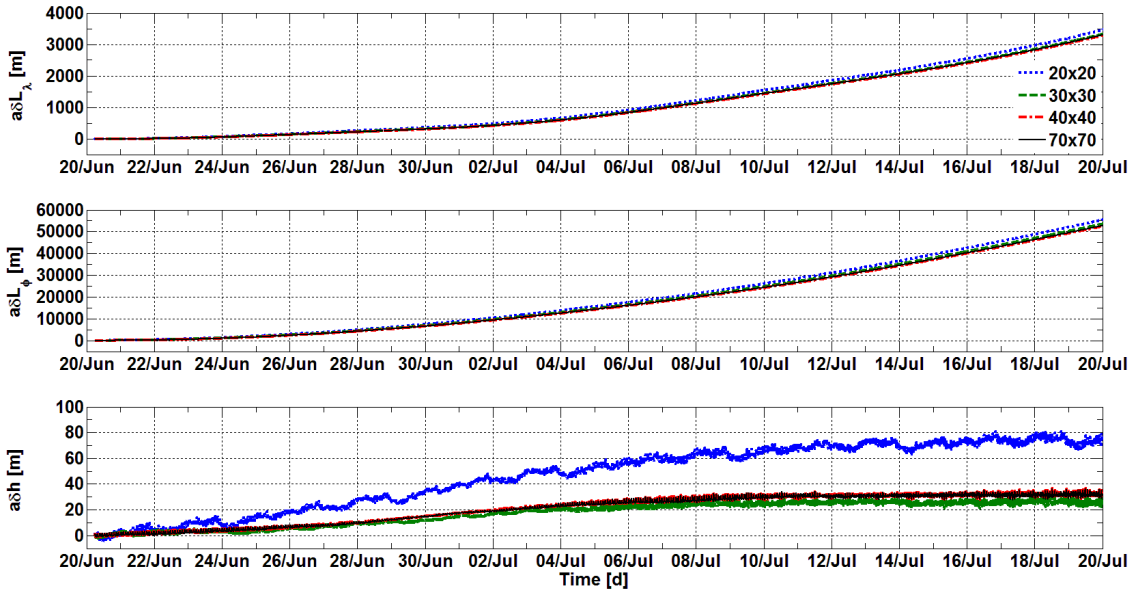

Figure 3.5.: MANGO's REFE at the ascending node (Actual-RO)

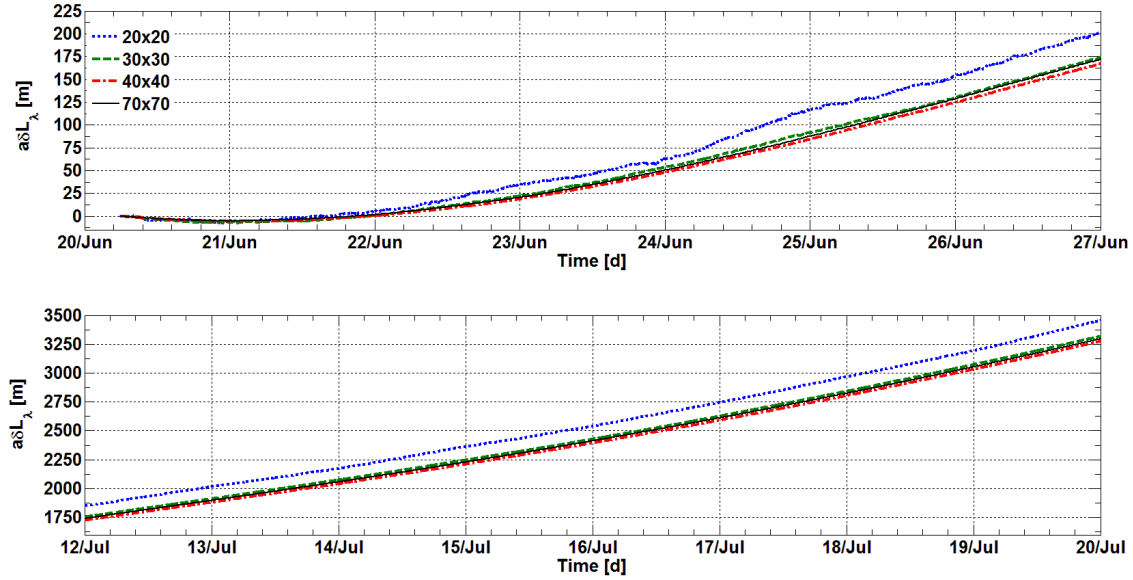

Figure 3.6.: MANGO's δL_λ at the ascending node (Actual-RO) - Details

In Fig. 3.4 the comparison is done by means of relative orbital elements, whereas in Figures 3.6-3.8 the evolution in time of the REFE is shown. It can be noted that in the RO generation process, the use of a gravitational field model including an order and degree of harmonics

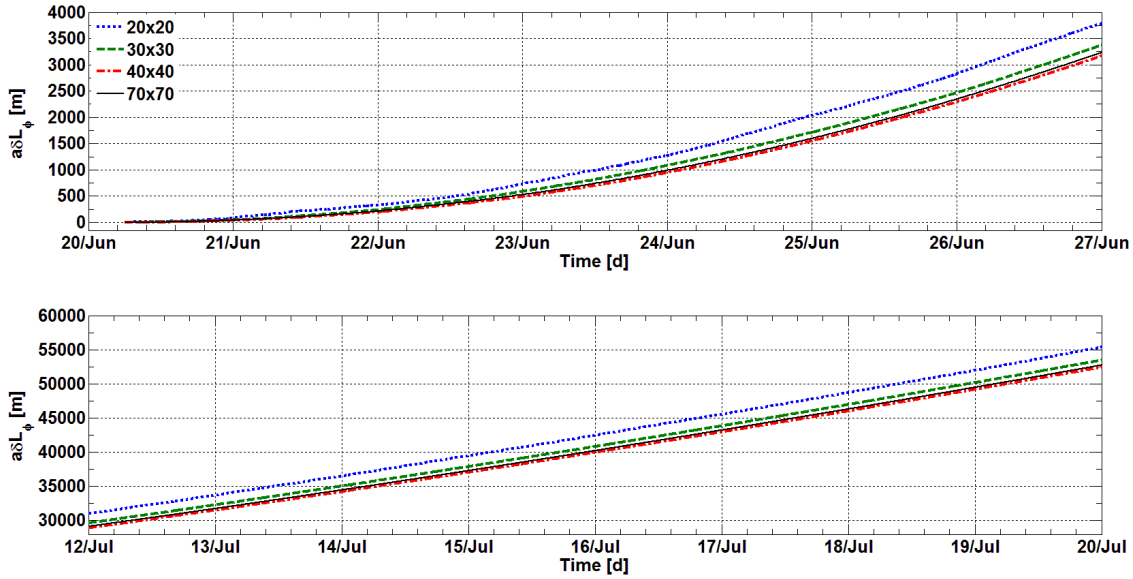

Figure 3.7.: MANGO's δL_φ at the ascending node (Actual-RO) - Details

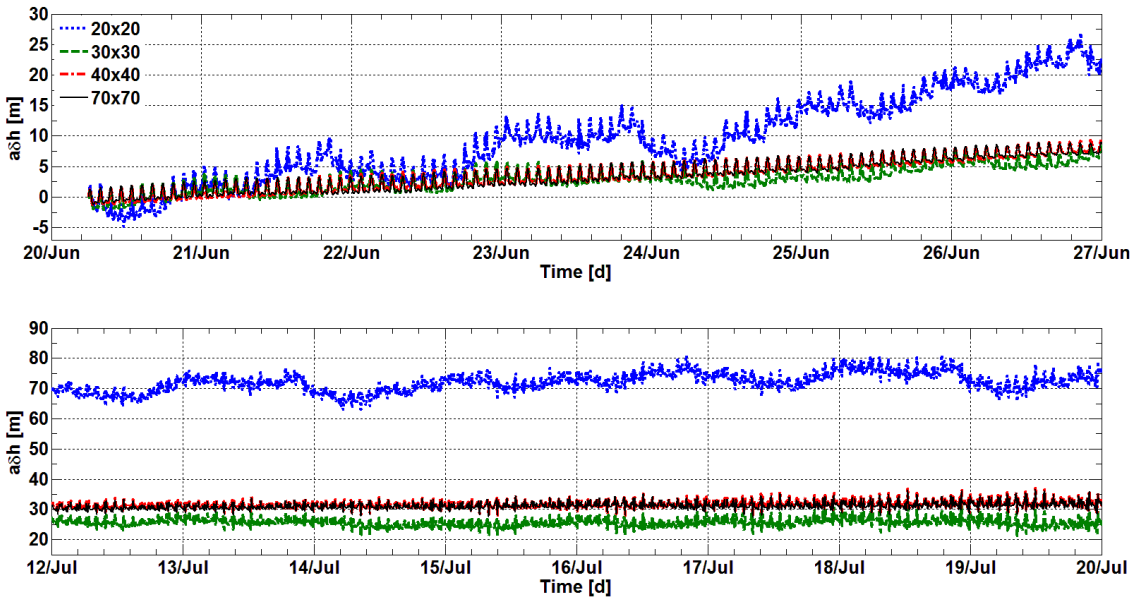

Figure 3.8.: MANGO's δh at the ascending node (Actual-RO) - Details

lower than 40x40 causes a propagation error. It can be stated therefore that a gravitational field model including at least an harmonics order and degree of 40 should be used to avoid the inclusion of orbit's model errors in the generation of the RO. If the RO is generated on-board, the

quality of the gravitational field which can be used may be limited by the available computational resources (see Chapter 7) and the errors introduced by the RO propagation model has to be evaluated in relation to the control accuracy requirements.

3.2.2. Accuracy Requirements of the Reference Orbit's Initial State

This section is dedicated to the evaluation of the propagation error introduced by a bias in the initial state used for the RO generation. The results of this analysis are relevant for the case in which the RO is generated on-board using an actual state of the spacecraft (see Chapter 7). The most accurate satellite state vectors available are those contained in the POD ephemerides which, for the PRISMA spacecraft, are accurate at the sub-decimetre level. An alternative source of absolute orbit information is the navigation filter integrated in the spacecraft on-board computer. The values collected in Table 3.6 are representative of the spacecraft state estimation errors on-board the MANGO spacecraft. Numerical simulations have been run to understand the impact of the errors of the initial state on the propagation of the RO. Figures 3.9 and 3.10 show the difference between the actual orbit and a RO propagated using initial states with different accuracies. The different initial states used for the propagation of the RO are obtained from that of Table 3.5 by adding the navigation error of Table 3.6 multiplied by 1, 2 and 3. All the orbits, the actual and the reference, have been propagated using a 70x70 gravitational field model in order to exclude oscillations due to different gravitational field harmonics modelling. From the results shown in Figures 3.9 and 3.10 it can be stated that if the RO is generated on-board using an actual state of the spacecraft, it is recommendable to use an uploaded POD state vector.

Table 3.6.: On-board navigation error

RTN_ECI state	$\mathbf{x[m]}$	$\mathbf{y[m]}$	$\mathbf{z[m]}$	$\mathbf{v_x[m/s]}$	$\mathbf{v_y[m/s]}$	$\mathbf{v_z[m/s]}$
	-3.0	-2.5	-1.0	-0.005	0.006	-0.002

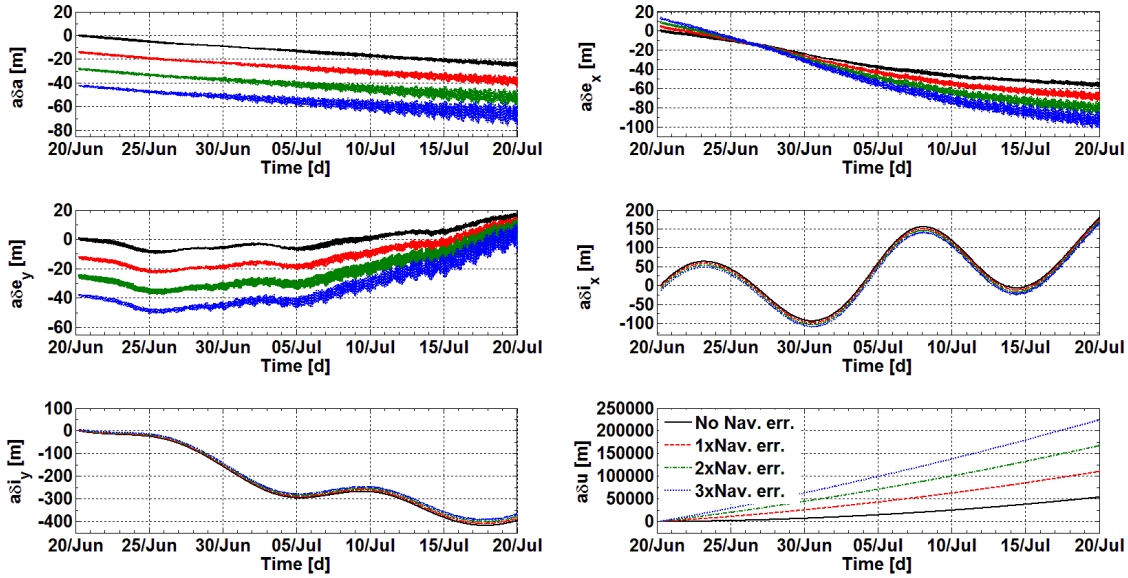

Figure 3.9.: MANGO's ROE (POD-RO)

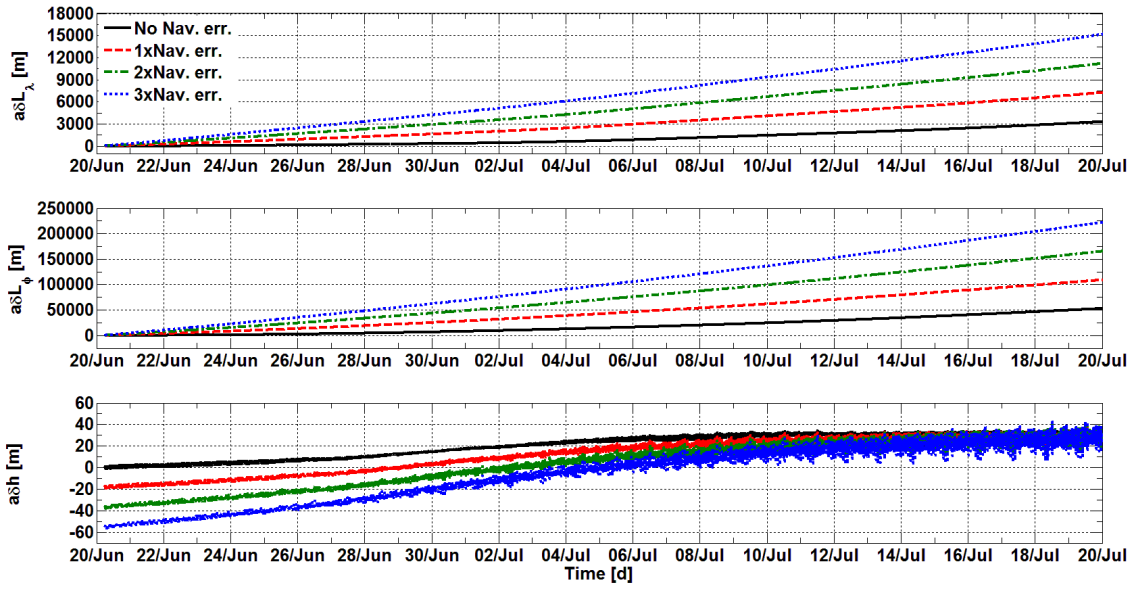

Figure 3.10.: MANGO's REFE (POD-RO)

3.3. Free Motion Analysis

A study of the orbital variations induced by the natural forces only [12-21], a free motion analysis, shows that the real orbital elements will tend to diverge from their nominal values.

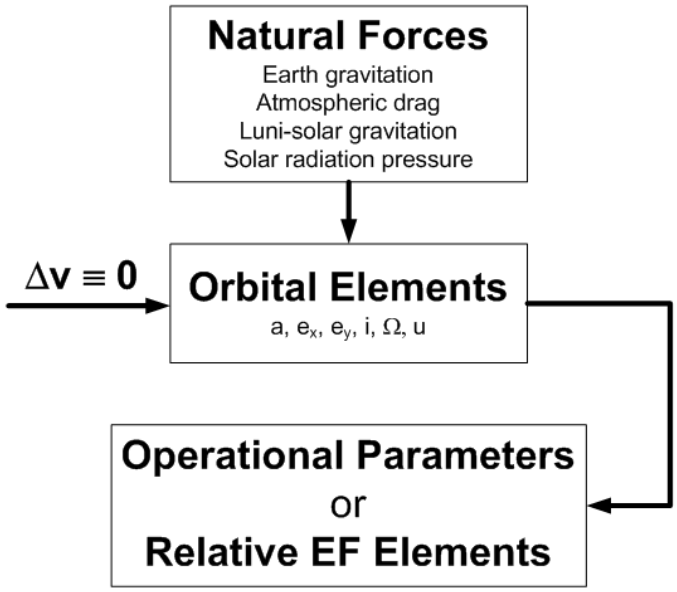

Figure 3.11.: Free motion

This leads to a violation of the flight control requirements defined by means of the operational parameters (Table 3.2). Fig. 3.11 shows the detailed view of the subsystem of Fig. 1.2 representing the dynamics of the system when the control input Δv is zero, i.e. when the system is in open-loop. From an analysis of the system in open-loop the evolution in time of mission characteristics may be predicted and an orbit control strategy defined. The main natural forces perturbing the ideal Keplerian spacecraft orbit are the non-spherical Earth gravitation field, the Luni-solar gravitation, the atmospheric drag and the solar radiation pressure. The Earth and Luni-solar gravitation are derived from a potential and may be treated analytically by means of the Lagrange equations [8] whereas the other perturbations have to be treated with the Gauss equations [5,2]. The evolution in time of each orbital element κ_i can be modelled [3] as

$$\kappa_i(t) = \kappa_0 + \sum_{1}^{m} A_j \sin\left(2\pi \frac{t}{T_j} + \phi_j\right) + \sum_{1}^{n} B_i (t - t_0)^i \tag{3.13}$$

The first term of Eq. (3.13) represents the mean element associated with κ_i. The second term is the periodic evolution of the orbital element with its period T_j, amplitude A_j and phase ϕ_j. The third term represents the secular evolution of κ_i, which is an expansion in powers of the

time difference. It expresses the long-term trend of the orbital element at the time at which the periodic effect becomes negligible in relation to the secular effect. The perturbations are classified in Table 3.7 according to the value of their period T. The natural evolution of the orbit causes the operational parameters or the REFE to diverge from their nominal value (Table 3.2).

The free motion analyses carried on in the next sections, are based on the POD data of PRISMA (Sec. 1.4) and TerraSAR-X/TanDEM-X (Sec. 1.5) which are representative of missions flying in LEO at respectively 700 and 500 km altitude. Main goal of these analyses is the study of the orbital perturbation forces environment which is fundamental for the design of an on-board orbit control system.

Table 3.7.: Influence of orbit perturbation forces on the orbital elements

Perturbation	**Short period** $\mathbf{T_j \leq T_{orb}}$	**Mean period** $\mathbf{T_{orb} < T_j \leq T_E}$	**Long period** $\mathbf{T_E < T_j}$	**Secular**
Geo-potential	a, e_x, e_y, i, Ω	a, e_x, e_y, i, Ω	e_x, e_y	e_x, e_y
Atmospheric drag	a, e_x, e_y		a	a, e_x, e_y
Luni-solar			i, Ω	i, Ω
Solar radiation			e_x, e_y, i	e_x, e_y, i
T_{orb} = orbital period, T_E = Earth rotation period				

3.3.1. Free Motion of the MANGO Satellite

The first step of this analysis was the calibration (Sec. 3.2.1) of the propagator's parameters in order to obtain a computed orbit as near as possible to the real one over a long simulation period. The POD ephemerides of the spacecraft TANGO of the PRISMA mission, the formation's target satellite which flies in free motion, have been exploited to calibrate the atmospheric density model used for the orbit propagations. Fig. 3.12 shows the evolution of the relative orbital elements between the POD ephemerides and the RO (generated with the parameters of Tables 3.4-3.6) and between the propagated orbit and the RO. As one can see the orbit's propagation obtained over one month is very representative of the reality considering that the PRISMA POD ephemerides [83-85] have an accuracy at the sub-decimetre level. Figures 3.13-3.15 highlight the contributions of each orbital perturbation force to the deviation of the real

from the RO for the satellite MANGO flying in a near sun synchronous orbit at an altitude of about 700 km.

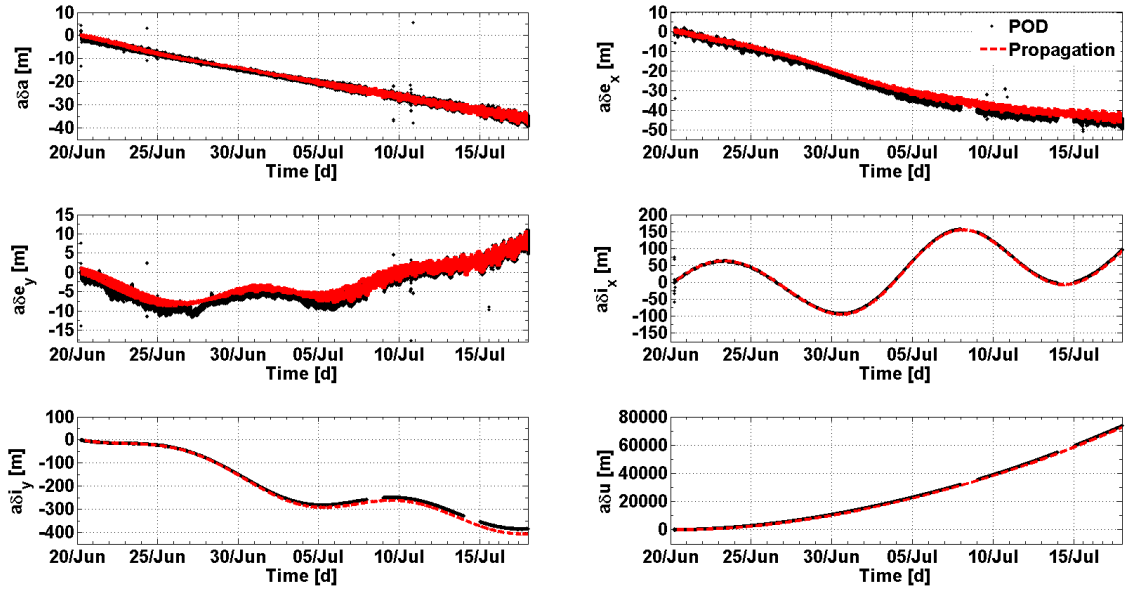

Figure 3.12.: TANGO's ROE (POD-RO) - Propagator calibration

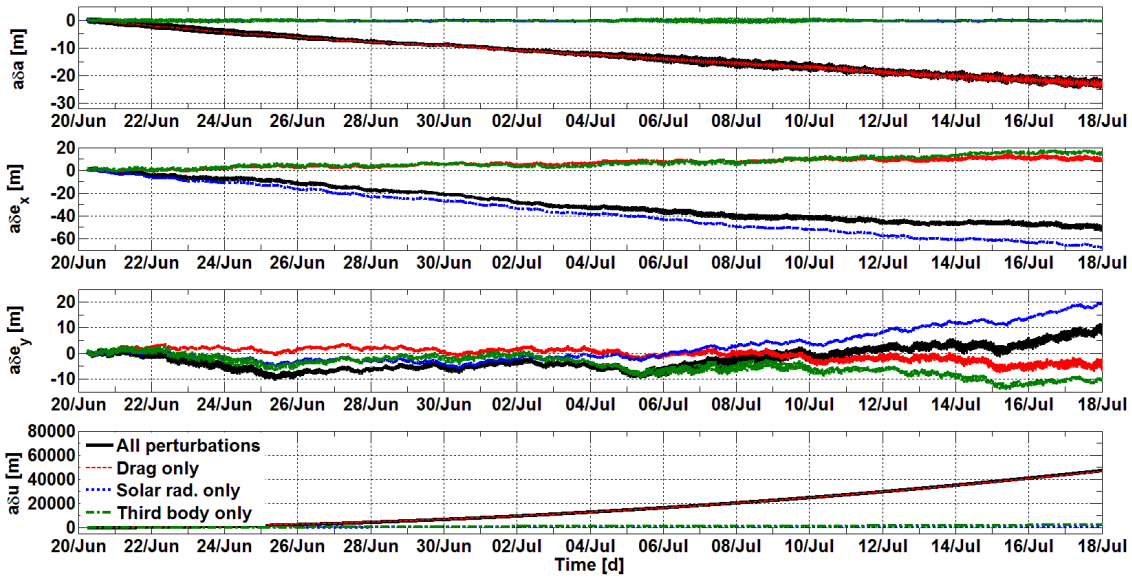

Figure 3.13.: MANGO's in-plane ROE (Propagated-RO)

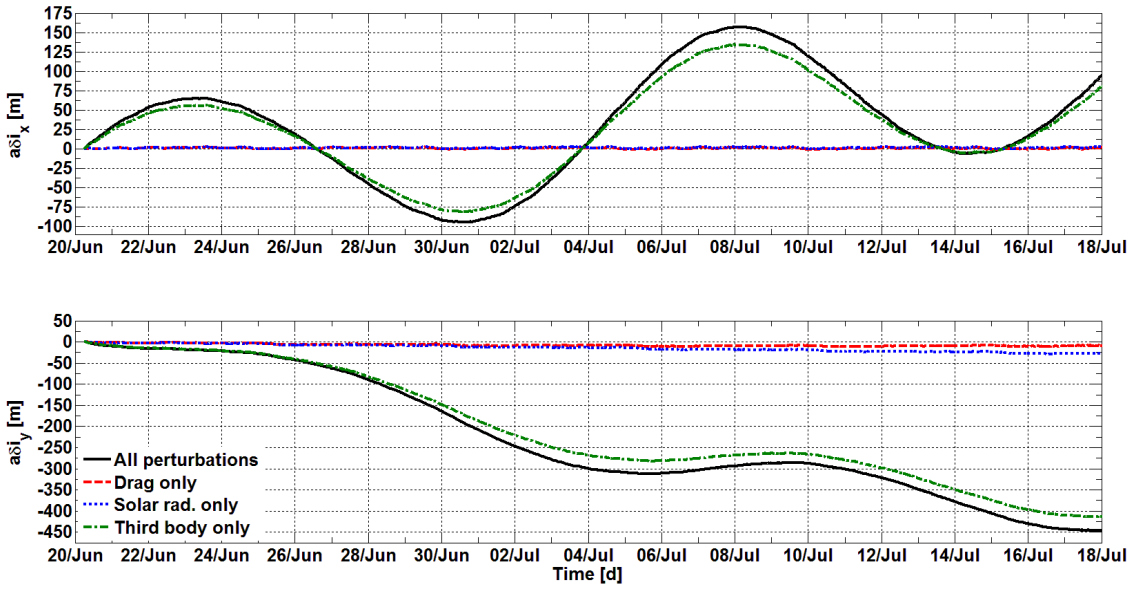

Figure 3.14.: MANGO's out-of-plane ROE (Propagated-RO)

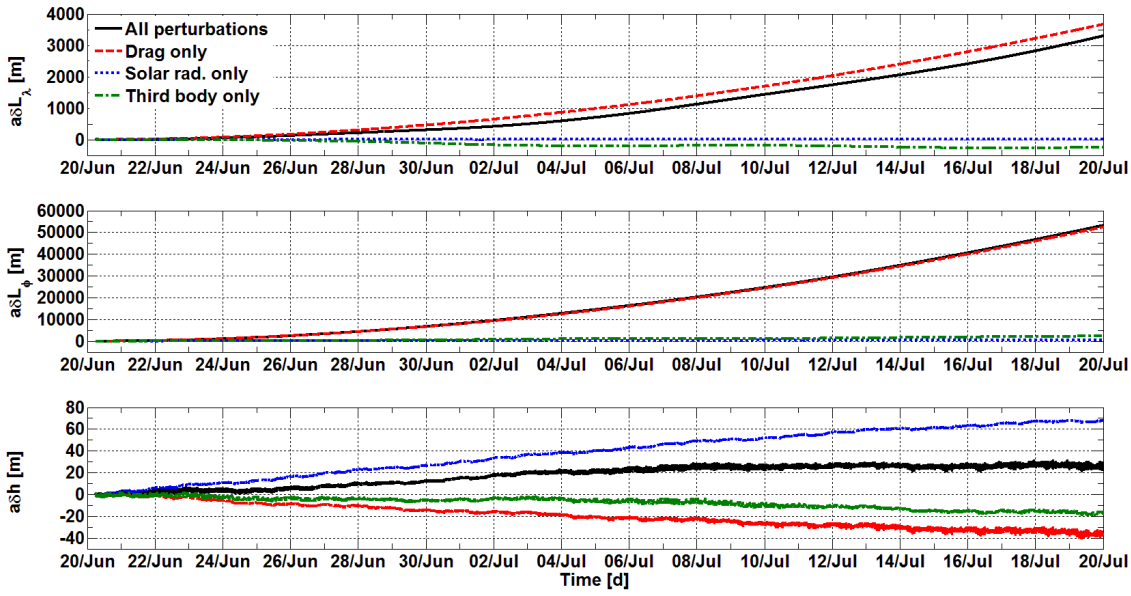

Figure 3.15.: MANGO's REFE at the ascending node (Propagated-RO)

The perturbation forces (Table 3.4) are the atmospheric drag, the solar radiation pressure and the luni-solar third body gravitational field. As shown in Figures 3.13 and 3.14 the atmospheric drag and the solar radiation pressure affect the in-plane (δa, δe_x, δe_y, δu) relative motion of the

real from the RO and give a negligible contribution to the out-of-plane motion (δi_x, δi_y). On the other hand the contribution of the third body perturbation is relevant in the out-of-plane relative motion and negligible in the in-plane. Considering the REFE computed at the orbit's ascending node (Equations (2.28)-(2.29) and Equations (2.31)-(2.33)) the atmospheric drag has the major influence on the evolution in time of δL_λ and δL_φ whereas the solar radiation pressure give the main contribution to the evolution of δh.

3.3.2. Free Motion of the TerraSAR-X Satellite

The calibration of the propagator's parameters for the case of the TerraSAR-X satellite is shown in Fig. 3.16 which shows the evolution of the relative orbital elements between the POD ephemerides and the RO and between the propagated orbit and the RO. In this case a free motion orbit arc of 7 days has been used as this is the maneuver cycle of TSX. The modelled forces used for the propagation are the same of Table 3.4 whereas TSX's physical propierties and the propagation initial state are collected respectively in Tables 3.8 and 3.9. The initial state is the POD state of TSX on 03-07-2011 at 06:00:00 UTC and the solar radiation pressure reference area is the same as the drag area. Figures 3.17-3.19 highlight the contributions of each orbital perturbation force to the evolution in time of the ROE and REFE. The same considerations of the previous section are valid here. Despite the fact that the mass of TSX (Table 3.9) is about ten times larger than the mass of MANGO (Table 3.4) the orbital decay rate of TSX is much larger. This is due to the fact that as TSX flies at an altitude 200 km lower than MANGO the atmospheric drag is stronger, and of course also to the larger drag area.

Table 3.8.: Physical properties of the TerraSAR-X spacecraft

TSX	**Mass [kg]**	**Drag and SRP area [m^2]**	**Drag coefficient [-]**	**SRP coefficient [-]**
	1341.17	3.2	3.0	3.0

Table 3.9.: Propagation initial state

RTN_ECI state	$\mathbf{r_R}[\mathbf{m}]$	$\mathbf{r_T}[\mathbf{m}]$	$\mathbf{r_N}[\mathbf{m}]$	$\mathbf{v_R}[\mathbf{m/s}]$	$\mathbf{v_T}[\mathbf{m/s}]$	$\mathbf{v_N}[\mathbf{m/s}]$
	4888898.0844	289059.4988	-4852522.5771	-5165.0722	-1691.6329	-5308.9558
Mean orb. el.	$\mathbf{a}[\mathbf{m}]$	$\mathbf{e_x}[-]$	$\mathbf{e_y}[-]$	$\mathbf{i}[\mathbf{deg}]$	$\mathbf{\Omega}[\mathbf{deg}]$	$\mathbf{u}[\mathbf{deg}]$
	6883553.0003	0.000026	0.001251	97.43	190.82	225.11

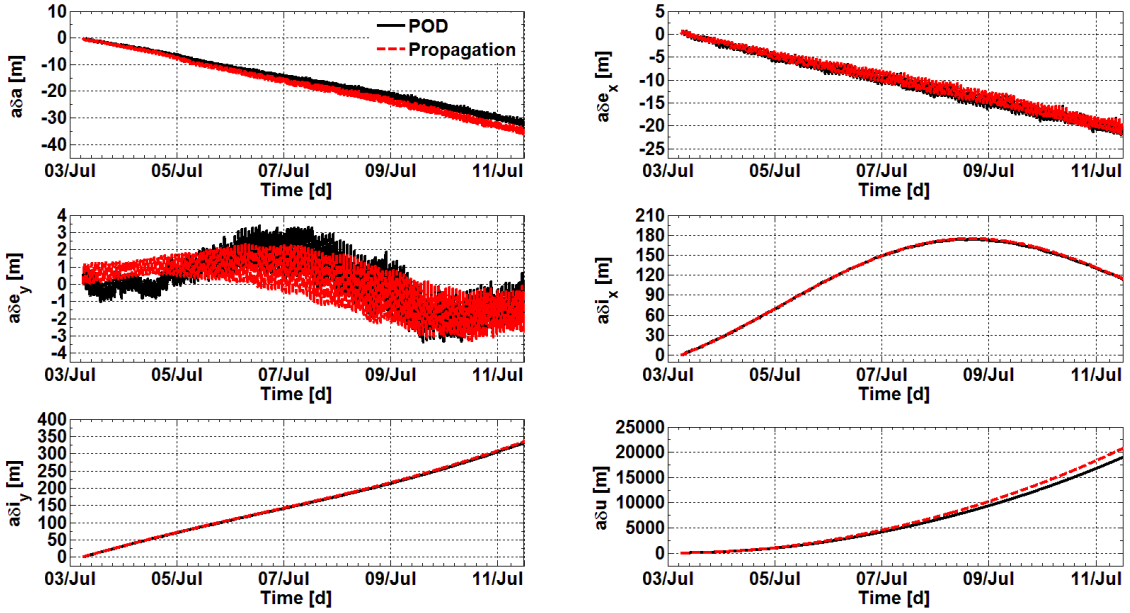

Figure 3.16.: TSX's ROE (POD-RO) - Propagator calibration

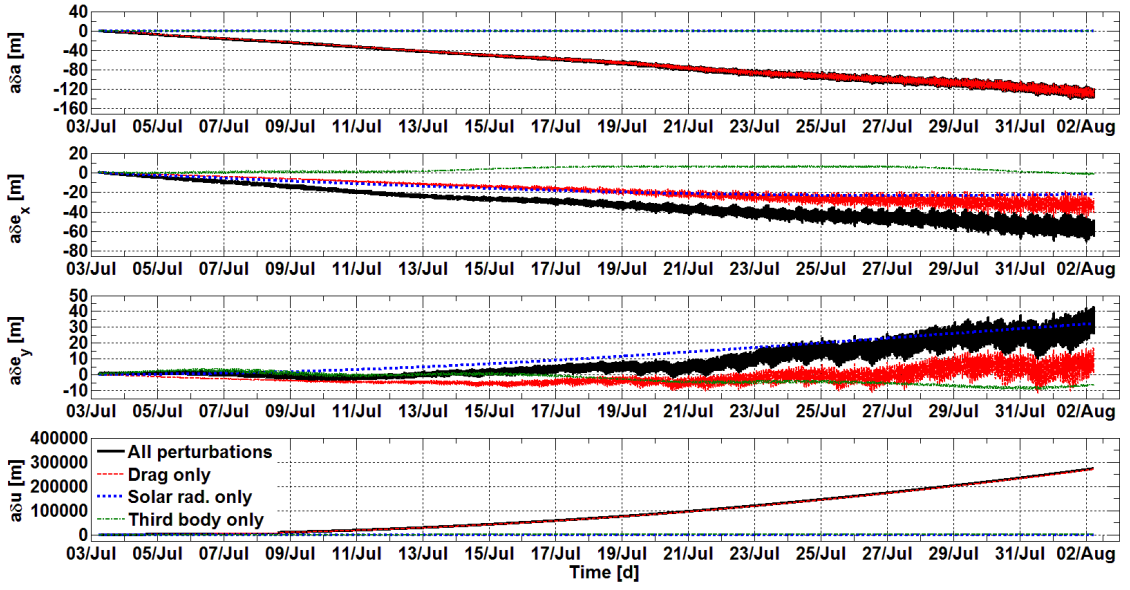

Figure 3.17.: TSX's in-plane ROE (Propagated-RO)

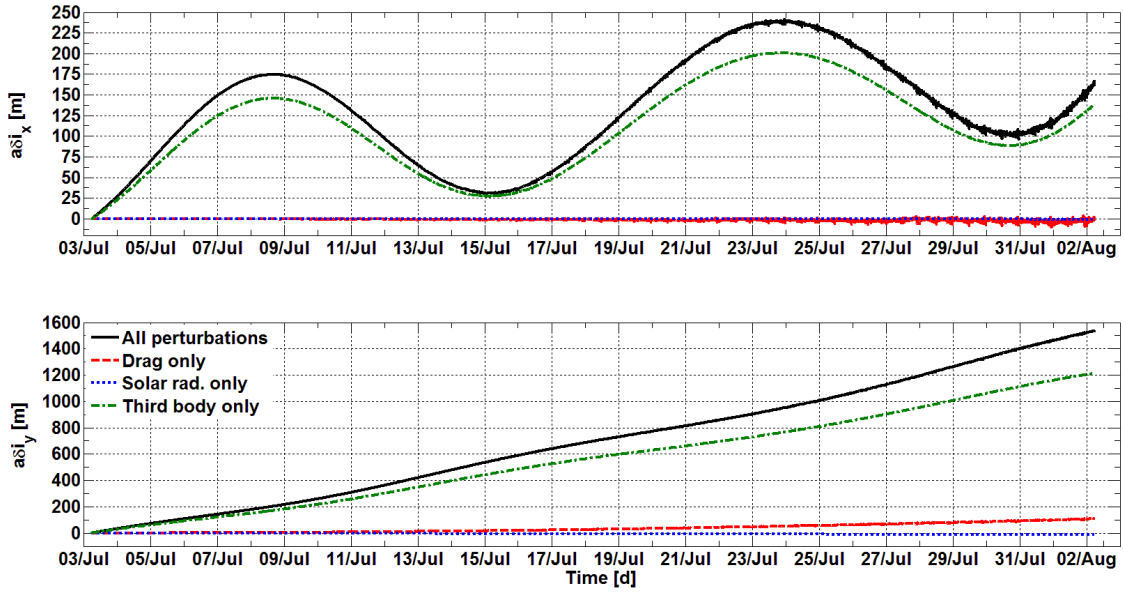

Figure 3.18.: TSX's out-of-plane ROE (Propagated-RO)

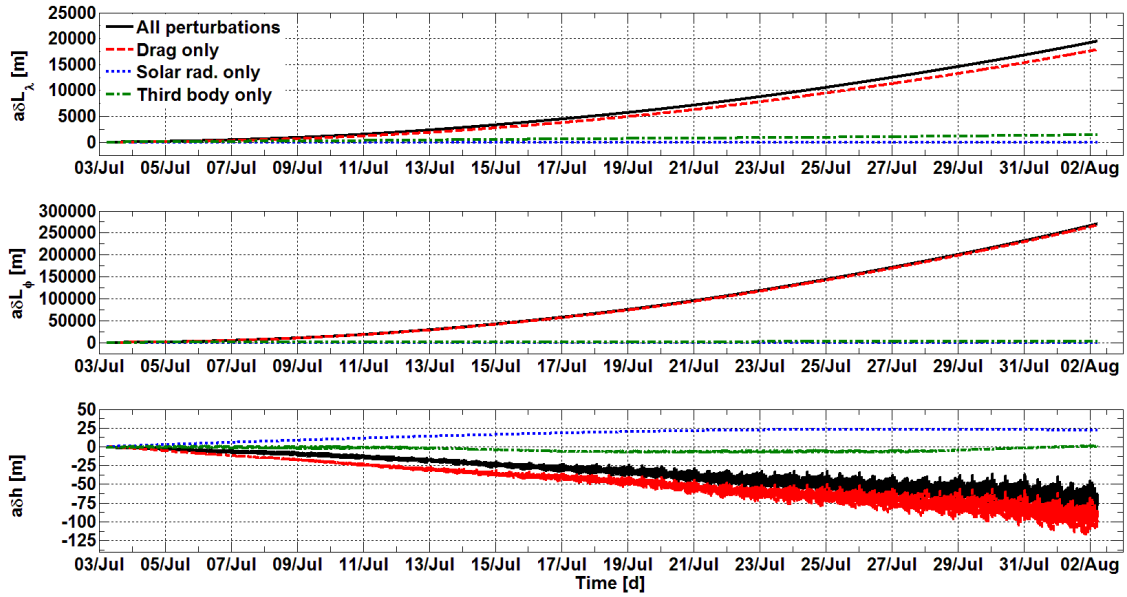

Figure 3.19.: TSX's REFE at the ascending node (Propagated-RO)

4. Control Methods

This chapter deals with the regulator block of Fig. 1.2. As shown in Fig. 3.1, the regulator receives as input the difference between the actual and nominal parameters to be controlled and issues an orbital maneuver computed with a specific algorithm. Three types of control algorithms are presented. The first is the one used in the AOK experiment (Chapter 7) on the PRISMA mission. The AOK controller adopts a guidance law for the orbital longitude of the ascending node and implements an analytical feedback control algorithm using along- and anti-along-track velocity increments. The second and third controllers are the linear and the quadratic optimal regulators from modern control theory. In the case of the analytical methods the mission dependent orbit's requirements are translated into thresholds applied on some operational parameters (Sec. 2.2) which specify the main features of the orbit's ground track geometry. The analytical model which describes the evolution of each operational parameter in relation to the orbital elements allows then the definition of a control cycle. In the case of the numerical feedback methods the problem is defined as a virtual formation control design

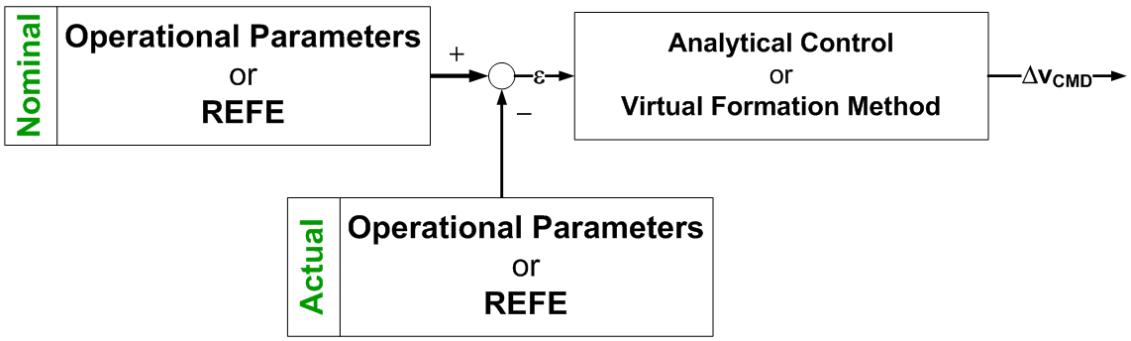

Figure 4.1.: Orbit regulator

by means of the relative Earth-fixed elements (Sec. 2.3) and solved with the techniques of the modern control theory. The analytical and numerical feedback control methods will be compared by means of numerical simulations in Chapter 5 where some conclusions will be drawn about the advantages and drawbacks in using and operating each type of orbit controller.

4.1. Analytical Control of Phase Difference

Remote sensing satellites in LEO are often required to carry out repeat Earth coverage in order to ensure identical geometric conditions of observation. If the orbit's inclination can be assumed to remain equal to its nominal value, controlling the phase difference at the equator will suffice to keep the phasing of the orbit. This section is dedicated to an analytical method for the control of the phase difference. Among the control methods presented in this chapter, only this algorithm was validated in-flight with the AOK experiment on the PRISMA mission because it had a most advanced implementation status at the moment of its selection.

4.1.1. Control Concept

Specific mission requirements are expressed by means of operational parameters [3] functions of the orbital elements, which define the maximum allowed deviation of the actual from the nominal trajectory of the spacecraft. Typical operational parameters (Sec. 2.2) are the altitude deviation and phase difference at a certain latitude, local time deviation and in-orbit phasing which specify the nominal position of the sub-satellite point in relation to a reference ground track on the Earth's surface [44]. The orbital elements of a spacecraft deviate from their nominal values under the action of perturbing forces. Once the mission requirements have been translated into orbit control margins, it is necessary to compute the corrections to be applied to the orbital elements to keep the value of the operational parameters within their control windows. The following equations in the mean elements are the Gauss variational equations of motion adapted for near-circular, non-equatorial orbits [3] and provide the relationships between the

velocity increments in the **RTN** orbital frame and the increments in the orbital elements.

$$\begin{pmatrix} \Delta a \\ \Delta e_x \\ \Delta e_y \\ \Delta i \\ \Delta \Omega \\ \Delta u \end{pmatrix} = \frac{1}{v} \begin{pmatrix} 0 & 2a & 0 \\ \sin u & 2\cos u & 0 \\ -\cos u & 2\sin u & 0 \\ 0 & 0 & \cos u \\ 0 & 0 & \sin u / \sin i \\ -2 & 0 & -\sin u / \tan i \end{pmatrix} \begin{pmatrix} \Delta v_R \\ \Delta v_T \\ \Delta v_N \end{pmatrix} \tag{4.1}$$

where v is the spacecraft's velocity magnitude. The implementation of an orbit control strategy implies the specification not only of the magnitude of the corrective maneuvers but also the geometric and time characteristics which maximize their efficiency. The choice of the less expensive maneuvers' in-orbit location depends on the operational parameter that has to be controlled. An out-of-plane maneuver Δv_N to change the orbit's inclination, for example, according to the Gauss equations (Eq. (4.1)) is most effective if placed at the node ($\overline{u} = 0$) while at the orbit's highest latitude ($\overline{u} = \pi/2$) if Ω has to be changed. On the other hand, while the semi-major axis can be changed with an along-track maneuver Δv_T with the same effectiveness anywhere along the orbit, the Δv_T most effective [74] to control δL_λ (Eqs. (2.31)-(2.33)) has to be computed at the equator (ascending or descending node) for reasons of symmetry.

4.1.2. Basic Orbit Keeping Strategy

Referring to Eq. (2.10) if da/dt and di/dt are taken as constants, ΔL_{AN} is found to have a near parabolic variation as its second derivative is constant. A positive ΔL_{AN} means that the ground track of the satellite at the equator lies eastwards with respect to the reference track. This means that if it is assumed that the semi-major axis has a linear decay under the influence of the atmospheric drag, the real orbit LAN will move parabolically eastwards of the reference LAN. Based on this consideration a simple control cycle can be imposed [3]. When the deviation between the real and nominal LAN exceeds a pre-defined upper bound ΔL_{MAX} a correcting impulse in the along-track direction of the satellite's orbit is applied as much as twice as would be neces-

sary in order to return to the initial semi-major axis' value. As a result, just after the impulse the satellite's LAN begins to move westward, reaches the lower bound of the allowable band and drifts back to the upper limit where the next correction maneuver is made. The theoretical maneuver cycle T and the semi-major axis increments Δa_c to be applied (Fig. 4.2) can thus be obtained from Eq. (2.10) assuming also that di/dt is negligible compared to da/dt [3].

$$\Delta a_c = \frac{1}{2}\sqrt{K\left|\frac{da}{dt}\right|\Delta L_c} \tag{4.2}$$

$$T = \sqrt{K\left|\frac{da}{dt}\right|^{-1}\Delta L_c} \tag{4.3}$$

$$K = \frac{16}{3\pi}\left(\frac{a}{R_E}\right)T_E \tag{4.4}$$

with $\Delta L_c = \Delta L_{MAX}$ in steady state phase (no RO acquisition). From the Gauss equations adapted for circular orbits, the velocity increment to be applied is

$$\Delta v = \left(\frac{\Delta a_c}{2a}\right)v \tag{4.5}$$

where v is the satellite velocity. By considering Eqs. (4.2) and (4.5) it is straightforward to conclude that a correct and fine estimation of the maneuver is strictly connected to a correct estimation of da/dt which is mainly determined by the atmospheric drag. Fig. 4.2 shows the possible evolutions of the LAN deviation after a maneuver based on different estimated values of da/dt. It is evident that if da/dt has been underestimated the Δv applied results in a Δa_c that is smaller than necessary to impose an optimal maneuver cycle period. On the other hand if da/dt has been overestimated the Δv applied results in a Δa that is too large and the negative LAN deviation exceeds the lower dead-band $-\Delta L_{MAX}$ resulting in requiring an anti-along-track maneuver to keep the LAN value within the control window. The better the estimation of da/dt, the closer the realized maneuver cycle will be to the ideal one thus minimizing the number of required maneuvers (Fig. 4.2).

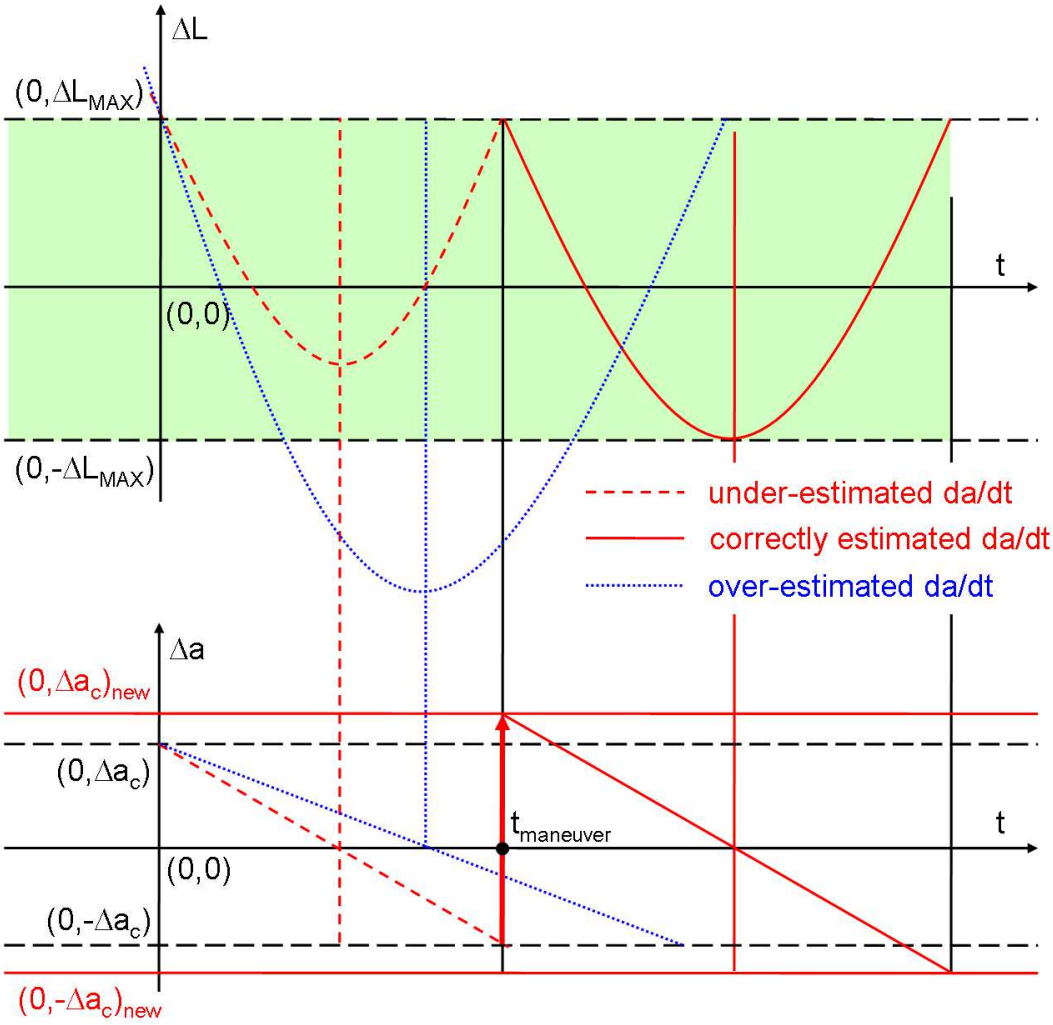

Figure 4.2.: Maneuver with estimated da/dt

4.1.3. Reference Orbit Acquisition

A fundamental requirement of an autonomous orbit control is to bring back the LAN deviation within the control window limits $\pm\Delta L_{MAX}$ starting from an error which has a magnitude greater than the allowed threshold. This type of maneuver can be requested to be optimal in the sense that it minimizes the amount of fuel required and can be required to be performed within certain time constraints. If no time requirements are enforced, an optimal maneuver will impose a Δa_c that will let the LAN to drift in free motion, with respect to the reference, along a parabola whose vertex lays on the minimum threshold of the control window. Referring to Fig. 4.3 in

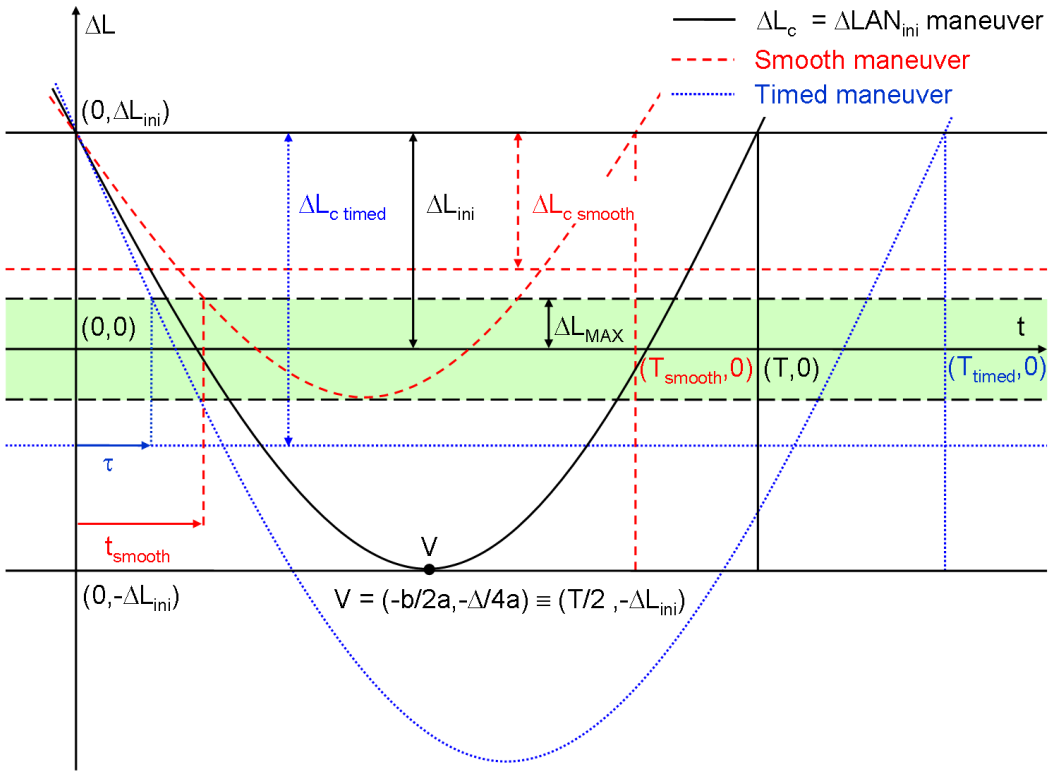

Figure 4.3.: Smooth and timed RO acquisition from positive LAN deviation values

general the maneuver's Δa_c for a RO acquisition is given by Eq. (4.2) where the proper ΔL_c can be computed given an initial phase difference ΔL_{ini} and a time constraint. Imposing an initial semi-major axis displacement Δa_c with an along-track maneuver, the evolution of the LAN error can be represented in the plane $t - \Delta L$ by a parabola of equation

$$\Delta L = \frac{8\Delta L_c}{T^2}t^2 - \frac{8\Delta L_c}{T}t + \Delta L_{ini} \tag{4.6}$$

with T given by Eq. (4.3). The time required for the return of the LAN error within the control window limits is then the intersection of parabola of Eq. (4.6) with line of equation $\Delta L = \Delta L_{MAX}$

$$t_c = \frac{T}{2}\left[1 - \frac{1}{2}\sqrt{4 + \frac{2(\Delta L_{MAX} - \Delta L_{ini})}{\Delta L_c}}\right] \tag{4.7}$$

Imposing that $t_c \in \Re$ and $t_c \geq 0$, the following conditions on ΔL_c and ΔL_{ini} are obtained

$$\Delta L_c \geq \frac{\Delta L_{ini} - \Delta L_{MAX}}{2} \quad \text{and} \quad \Delta L_{ini} \geq \Delta L_{MAX} \tag{4.8}$$

Smooth Maneuver

If the RO acquisition has to be performed with the only requirement of minimizing the maneuver size with no time constraints, the vertex ordinate of the parabola of Eq. (4.6) will be imposed to be equal to $-\Delta L_{MAX}$ i.e. placed on the lower threshold of the control window. In the ideal case this kind of maneuver, indicated as *smooth* in Fig. 4.3, does not require any further correction to the initial Δv. The resulting ΔL_c is then

$$\Delta L_c = \frac{\Delta L_{ini} + \Delta L_{MAX}}{2} \tag{4.9}$$

and the acquisition time is

$$t_{smooth} = \frac{T}{2}\left(1 - \sqrt{\frac{\Delta L_{MAX}}{\Delta L_c}}\right) = \frac{1}{2}\sqrt{K\left|\frac{da}{dt}\right|^{-1}\Delta L_c}\left(1 - \sqrt{\frac{2\Delta L_{MAX}}{\Delta L_{MAX} + \Delta L_{ini}}}\right) \tag{4.10}$$

with K given by Eq. (4.2). The RO acquisition maneuver is computed with Eqs. (4.2) and (4.5) using ΔL_c given by Eq. (4.9).

Timed Maneuver from positive deviation

If a time constraint $t_c \leq \tau$ is imposed and $t_{smooth} > \tau$, where τ is a fixed time interval, a *timed* maneuver is required as indicated in Fig. 4.3. If the initial phase difference deviation ΔL_{ini} has a positive value, Eq. (4.7) can be solved for ΔL_c imposing $t_c = \tau$ and T given by Eq. (4.3) and yields

$$\Delta L_c = \frac{1}{K}\left|\frac{da}{dt}\right|\left[K\left|\frac{da}{dt}\right|^{-1}\frac{(\Delta L_{ini} - \Delta L_{MAX})}{8\tau} + \tau\right]^2 \tag{4.11}$$

where K is given by Eq. (4.2). The RO acquisition maneuver is computed with Eqs. (4.2) and (4.5) using ΔL_c given by Eq. (4.11). This kind of maneuver requires an anti-along-track

counter-maneuver when the negative LAN deviation reaches the lower deadband $-\Delta L_{MAX}$.

Timed Maneuver from negative deviation

If the initial phase difference deviation has a negative value, the problem can be solved by considering Fig. 4.4. The value of $-\Delta a_c$ has to be found such that starting from an initial value $-\Delta L_{ini}$, ΔL will evolve in time on the timed maneuver parabola of Eq. (4.12) thus fulfilling the RO acquisition time constraint.

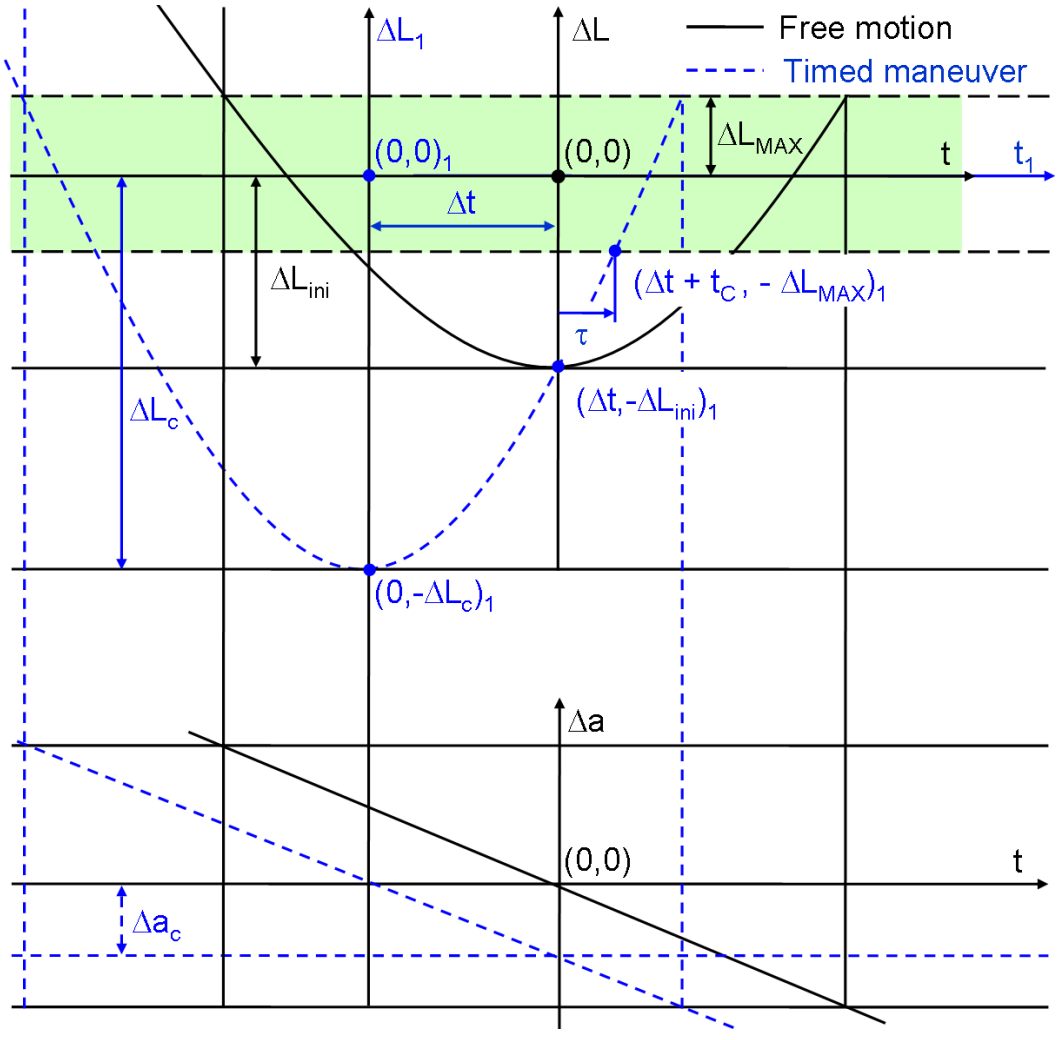

Figure 4.4.: Timed RO acquisition from negative LAN deviation values

$$\Delta L_1 = \frac{8\Delta L_c}{T^2} t_1^2 - \Delta L_c = \frac{8}{K}\left(\frac{da}{dt}\right) t_1^2 - \Delta L_c \tag{4.12}$$

The parabola of Eq. (4.12) is written in coordinates $t_1, \Delta L_1$ obtained from $t, \Delta L$ with the coordinates transformation $t_1 = t + \Delta t$, $\Delta L_1 = \Delta L$. Imposing that points of coordinates $(\Delta t, -\Delta L_{ini})_1$ and $(\Delta t + \tau, -\Delta L_{MAX})_1$ belong to the parabola of Eq. (4.12) it results

$$\Delta t = \frac{\tau}{2}\left[K\left|\frac{da}{dt}\right|^{-1}\frac{(\Delta L_{ini} - \Delta L_{MAX})}{8\tau^2} - 1\right] \tag{4.13}$$

$$\Delta L_c = \frac{(\Delta L_{ini} - \Delta L_{MAX})}{2}\left[K\left|\frac{da}{dt}\right|^{-1}\frac{(\Delta L_{ini} - \Delta L_{MAX})}{16\tau^2} - 1\right] + \frac{2\tau^2}{K}\left|\frac{da}{dt}\right| + \Delta L_{ini} \tag{4.14}$$

where K is given by Eq. (4.2). The anti-along-track RO acquisition maneuver is computed with Eqs. (4.2) and (4.5) using ΔL_c given by Eq. (4.14).

4.1.4. On-board Atmospheric Drag Estimation

As atmospheric density has a remarkable variability over time mainly due to fluctuations in the solar flux (see Appendix D) an atmospheric model cannot provide the necessary accuracy for strict LAN control requirements. On the other hand, as in case of the MANGO satellite, it is not always possible to have on-board accelerometers accurate enough ($< 10^{-5}\ m/s^2$) to extrapolate the drag acceleration from their measurements. Nevertheless da/dt can be estimated on-board using the actual orbit's semi-major axis estimated by the navigation filter with an accuracy of 4 m 1σ (see Sec. 7.1.8) and the RO. The value of da/dt is then found with the following procedure explained with the help of Fig. 4.5.

The actual and reference semi-major axis data are first filtered by taking their values at the ascending node and smoothed if required. The difference Δa_{AN} between the actual and reference semi-major axis values is computed. The value of da/dt is finally found as the slope of the line representing the linear fit over the time of a sample of Δa_{AN} data. A smoothing process of the on-board estimated values of Δa_{AN} is required in the computation of da/dt in presence of noise due to short period harmonics not included in the gravitational field model used for the

RO propagation or errors in the on-board estimation of Δa_{AN}. Fig. 4.5 shows the comparison of the Δa_{AN} curves obtained with a RO generated with a 70x70 gravitational field model and one generated with a 5x5 model. The real orbit is generated by numerical orbit propagation including the aspherical Earth gravitational field (GGM01S model) through an expansion in spherical harmonics up to degree and order 70, tides and relativity gravitational field perturbations, the Sun and Moon third body forces, the atmospheric drag (atmospheric density model Harris-Priester) and solar radiation pressure. It can be noticed in Fig. 4.5 that in the case of the 5x5 orbit model a short period (for example 10 points) linear fitting without data smoothing is totally unreliable for estimating the atmospheric drag. A long period (50 points) linear fitting would allow an accurate estimation of da/dt, but requires a minimum maneuver cycle period of 50 orbits (i.e. more than 3 days) which could be too long as in the case of the AOK controller (Chapter 7). Nevertheless an efficient estimation of da/dt is still possible using samples of 10 Δa_{AN} values with a proper smoothing process. The smoothing filter takes as input the points marked by circles in Fig. 4.5 and flattens them on a line λ keeping unaltered the ratios of their distances from it. Line λ is defined by point $(x_1, \overline{y})$ and angular coefficient m where x_1 is the x-coordinate of the first point, $\overline{y}$ is the mean of the y-coordinates of all the points of the sample and m is the estimated da/dt. The smoothed points $y_{k_{sth}}$ are computed with the following equations

$$y_{k_{sth}} = mx_k + q \pm \frac{d\sqrt{1+m^2}}{f} \tag{4.15}$$

$$d = \frac{|y_k - (mx_k + q)|}{\sqrt{1+m^2}} \qquad q = \overline{y} - mx_1 \tag{4.16}$$

where in the second term of Eq. (4.15) the $+$ sign has to be used if $y_k \geq mx_k + q$, the $-$ sign if $y_k < mx_k + q$ and $f \geq 1$ is a flattening coefficient uploaded by TC. An initial value of da/dt, estimated on-ground and uploaded to the spacecraft, is used for the very first smoothing process. The output points $y_{k_{sth}}$ of the smooth filter are marked by triangles in Fig. 4.5. If the RO is generated with a 70x70 gravitational field model no data smoothing is required.

The AOK controller uses a GRACE GGM01S 20x20 gravitational field model for the on-board RO generation (Sec. 7.1.2) and a sample buffer of 10 Δa_{AN}'s which is renewed at each

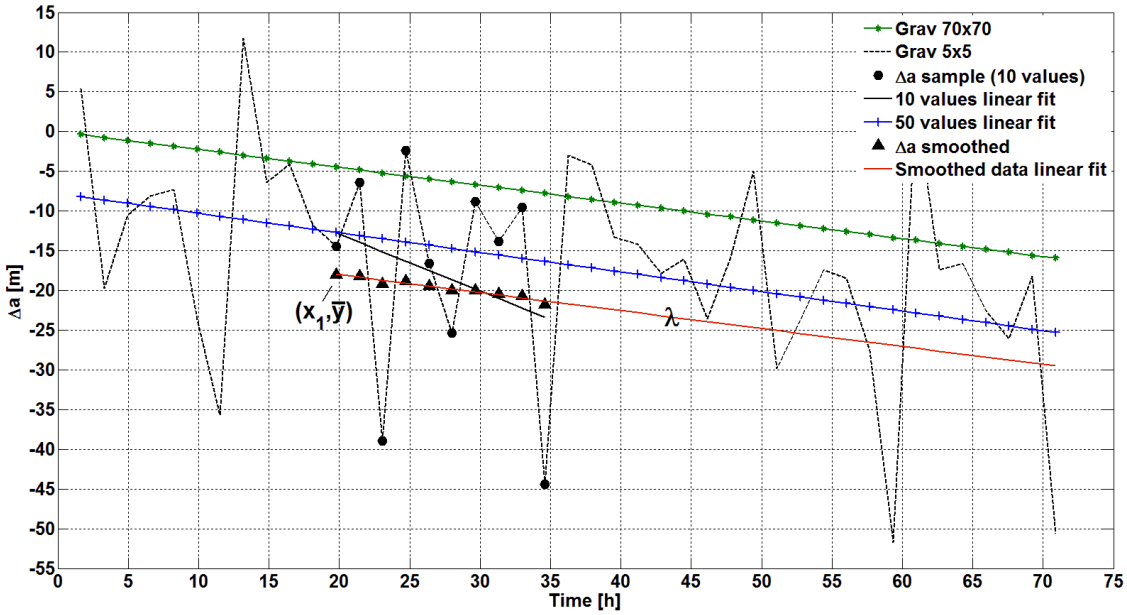

Figure 4.5.: On-board estimation process of da/dt

ascending node passage with a first-in-last-out logic so thus the last 10 orbits data are always stored in the buffer. The buffer is reset after each maneuver. In case no fitting is possible because there isn't a sufficient number of samples in the buffer, the da/dt is estimated using the first of the Gauss equations (Eq. (4.1)) approximated for circular orbits [3]

$$\frac{da}{dt} = -\frac{\rho}{B}\sqrt{\mu a} \tag{4.17}$$

where ρ is the atmospheric density from the Harris-Priester model, $B = m/(AC_D)$ is the ballistic coefficient of the satellite and $\mu = 3.9860064 \times 10^{14}\ m^3\ s^{-2}$.

4.2. Virtual Formation Model

This section analyses the problem of the autonomous orbit control of a satellite in LEO using the linear and the quadratic optimal regulators from the classical control theory [9, 10]. For the implementation of the linear regulators the problem has been formulated as a specific case of two spacecraft in formation in which one, the reference, is virtual and affected only by the

Earth's gravitational field. The control action is realized by means of in-plane and out-of-plane velocity increments. The state-space representation approach is used here for the realization of the autonomous orbit control with techniques from modern control theory. In general, the linear model used has state-space representation form

$$\dot{\boldsymbol{\epsilon}} = \mathbf{A}\boldsymbol{\epsilon} + \mathbf{B}\Delta\mathbf{v} + \mathbf{x_d} \tag{4.18}$$

$$\mathbf{y} = \mathbf{C}\boldsymbol{\epsilon} \tag{4.19}$$

$$\Delta\mathbf{v} = -\mathbf{G}\mathbf{y} - \mathbf{G_d}\mathbf{x_d} \tag{4.20}$$

where $\boldsymbol{\epsilon}$ is the state vector, $\mathbf{A}$ and $\mathbf{B}$ are respectively the dynamic model and control input matrix, $\mathbf{x_d}$ is the modelled state perturbation, $\Delta\mathbf{v}$ is the impulsive velocity increment vector, and $\mathbf{G}$ and $\mathbf{G_d}$ are, respectively, the output and disturbance gain matrices. The output vector $\mathbf{y}$ is comprised of relative Earth-fixed elements introduced by Eq. (2.28).

4.2.1. Linear Dynamic Model

The state-space model of the orbital motion of the real and reference spacecraft is given by

$$\dot{\boldsymbol{\kappa}} = \tilde{\mathbf{A}}_\mathbf{g}(\boldsymbol{\kappa}) + \tilde{\mathbf{A}}_\mathbf{d}(\boldsymbol{\kappa}) \tag{4.21}$$

$$\dot{\boldsymbol{\kappa}}_\mathcal{R} = \tilde{\mathbf{A}}_\mathbf{g}(\boldsymbol{\kappa}_\mathcal{R}) \tag{4.22}$$

where $\boldsymbol{\kappa} = (a, e_x, e_y, i, \Omega, u)$ is the mean orbital elements vector.

Vector functions $\tilde{\mathbf{A}}_\mathbf{g}$ and $\tilde{\mathbf{A}}_\mathbf{d}$ (Eqs. (A.1) and (A.3) in Appendix A) describe the behaviour of the mean orbital elements $\boldsymbol{\kappa}$ under the influence of the J_2 gravitational perturbation and atmospheric drag [5,21]. The mean orbital elements $\boldsymbol{\kappa}_\mathcal{R}$ of the reference spacecraft are affected only by the Earth's gravitational field as they define the nominal trajectory [3,32]. The linearization around $\boldsymbol{\kappa}_\mathcal{R}$ of the difference between Eqs. (4.21) and (4.22) yields

$$\frac{d(\boldsymbol{\delta\kappa})}{dt} = \tilde{\mathbf{A}}(\boldsymbol{\kappa}_\mathcal{R})\boldsymbol{\delta\kappa} + \tilde{\mathbf{A}}_\mathbf{d}(\boldsymbol{\kappa}_\mathcal{R}) \tag{4.23}$$

where

$$\tilde{\mathbf{A}}(\boldsymbol{\kappa}_{\mathcal{R}}) = \left.\frac{\partial[\tilde{\mathbf{A}}_{\mathbf{g}}(\boldsymbol{\kappa}) + \tilde{\mathbf{A}}_{\mathbf{d}}(\boldsymbol{\kappa})]}{\partial \boldsymbol{\kappa}}\right|_{\boldsymbol{\kappa}_{\mathcal{R}}} \tag{4.24}$$

is the Jacobian evaluated at $\boldsymbol{\kappa}_{\mathcal{R}}$ of the vectors sum $\tilde{\mathbf{A}}_{\mathbf{g}}(\boldsymbol{\kappa})+\tilde{\mathbf{A}}_{\mathbf{d}}(\boldsymbol{\kappa})$, and $\boldsymbol{\delta\kappa}$ is the relative orbital elements vector. Making the proper modifications to matrix $\tilde{\mathbf{A}}(\boldsymbol{\kappa}_{\mathcal{R}})$ for the normalization in $a_{\mathcal{R}}$ and the introduction of δi_y (Eq. (2.19)), and adding the control term $\mathbf{B}(\boldsymbol{\kappa})\Delta\mathbf{v}$:

$$\dot{\boldsymbol{\epsilon}} = \mathbf{A}(\boldsymbol{\kappa}_{\mathcal{R}})\boldsymbol{\epsilon} + \mathbf{x_d} + \mathbf{B}(\boldsymbol{\kappa})\Delta\mathbf{v} \tag{4.25}$$

where $\mathbf{A}(\boldsymbol{\kappa}_{\mathcal{R}}) = \mathbf{A_g}(\boldsymbol{\kappa}_{\mathcal{R}}) + \mathbf{A_d}(\boldsymbol{\kappa}_{\mathcal{R}})$ (Eqs. (A.2) and (A.4)), $\boldsymbol{\epsilon} = a_{\mathcal{R}}\boldsymbol{\delta\kappa}$ is the relative orbital elements vector (Eq. (2.19)) normalized to the semi-major axis, $\mathbf{x_d}$ results from the direct (dyadic) vectors product $(\tilde{\mathbf{A}}_{\mathbf{d}}(\boldsymbol{\kappa}_{\mathcal{R}}))(1, a_{\mathcal{R}}, a_{\mathcal{R}}, 1, 1, 1)^T$ and $\Delta\mathbf{v} = (\Delta v_R, \Delta v_T, \Delta v_N)^T$ is the vector of impulsive velocity increments in the **RTN** orbital frame.

Matrix $\mathbf{B}(\boldsymbol{\kappa})$ (Eq. (A.5)) represents the Gauss variational equations of motion adapted for near-circular non-equatorial orbits [3]. The elements of matrix $\mathbf{B}(\boldsymbol{\kappa})$ are computed with good approximation [5] using the mean orbital elements. The Gauss equations provide the relationships between the impulsive velocity increments Δvs in the **RTN** orbital frame and the increments of the orbital elements. Eq. (4.25) can be written in the general form

$$\begin{pmatrix} \dot{\boldsymbol{\epsilon}} \\ \dot{\mathbf{x}}_{\mathbf{d}} \end{pmatrix} = \begin{pmatrix} \mathbf{A} & \mathbf{I} \\ \mathbf{0} & \mathbf{A_0} \end{pmatrix} \begin{pmatrix} \boldsymbol{\epsilon} \\ \mathbf{x_d} \end{pmatrix} + \begin{pmatrix} \mathbf{B} \\ \mathbf{0} \end{pmatrix} \Delta\mathbf{v} \tag{4.26}$$

Eq. (4.26) is the representation of a tracking system [9] in which the atmospheric drag perturbation vector $\mathbf{x_d}$ is represented as an additional state variable, the disturbance input, which is assumed to satisfy the model $\dot{\mathbf{x}}_{\mathbf{d}} = \mathbf{A_0}\mathbf{x_d}$ and $\mathbf{I}$ is the 6x6 identity matrix. If the feedback controller is designed to compute the control inputs Δv_j always in the same place of the orbit ($u = \overline{u}$), $\mathbf{x_d}$ can be assumed as constant (Eq. (A.3)) i.e. $\mathbf{A_0} \equiv 0$. This design approach stems from the consideration that the implementation of an orbit control strategy implies the specification not only of the magnitude of the corrective maneuvers but also the in-orbit location which maximizes their efficiency (Sec. 4.1.1).

4.2.2. Reduced Model

In case no eccentricity or inclination are to be actively controlled, the model can be reduced by considering only the states δa, δi_y and δu. The elements $a_{ij} = a_{gij} + a_{dij}$ are given by Eqs. (A.2) and (A.4). The use of this model allows the design of a linear controller for the relative Earth-fixed elements δL_λ and δL_φ. The passive control of δh can be achieved by a proper in-orbit placement of the along-track maneuvers as explained in the next section.

$$\begin{aligned} \mathbf{A_r} &= \frac{3}{4}\left(\frac{a}{R_E}\right)^2 \frac{nJ_2}{(1-e^2)^2}\begin{pmatrix} a_{11} & 0 & 0 \\ a_{51} & 0 & 0 \\ a_{61} & 0 & 0 \end{pmatrix} \qquad \boldsymbol{\epsilon_r} = a_{\mathcal{R}}\begin{pmatrix} \delta a \\ \delta i_y \\ \delta u \end{pmatrix} \\ \mathbf{B_r} &= \frac{1}{n}\begin{pmatrix} 0 & 2 & 0 \\ 0 & 0 & \sin u \\ -2 & 0 & -\sin u/\tan i \end{pmatrix} \qquad \mathbf{x_{dr}} = -\frac{A}{m}C_D\rho\begin{pmatrix} \sqrt{\mu a} \\ 0 \\ 0 \end{pmatrix} \end{aligned} \tag{4.27}$$

If the reduced model of Eq. (4.27) is used, Eqs. (2.28)-(2.30) can be written, considering only the states δa, δi_y and δu, as

$$\boldsymbol{\delta F}(\overline{u}, \boldsymbol{\epsilon_r})a_{\mathcal{R}} = \mathbf{T_r}(\overline{u})\boldsymbol{\epsilon_r} \qquad \frac{d(\boldsymbol{\delta F})}{dt}a_{\mathcal{R}} = \mathbf{T_r}(\overline{u})\mathbf{A_r}\boldsymbol{\epsilon_r} \tag{4.28}$$

$$\mathbf{T_r}(u) = \begin{pmatrix} -\frac{3}{2}u\tau & \left[\frac{\tau(1-cu)ci_{\mathcal{R}}}{cu}+1\right]\frac{cu}{si_{\mathcal{R}}} & \tau \\ -\frac{3}{2}usi_{\mathcal{R}} & (1-cu)ci_{\mathcal{R}} & si_{\mathcal{R}} \\ 1 & 0 & 0 \end{pmatrix} \tag{4.29}$$

4.2.3. Characteristic Polynomial

The characteristic polynomial of matrix $\mathbf{A}$ of Eq. (4.25) has the form

$$|s\mathbf{I} - \mathbf{A}| = s^2(s - a_{11})(s^3 + bs^2 + cs + d) \tag{4.30}$$

$$b = -(a_{22} + a_{33}) \qquad c = a_{22}a_{33} - a_{26}a_{62} - a_{36}a_{63} - a_{23}a_{32} \tag{4.31}$$

$$d = a_{26}(a_{62}a_{33} - a_{63}a_{32}) + a_{36}(a_{63}a_{22} - a_{23}a_{62}) \tag{4.32}$$

and the elements a_{ij} of matrix $\mathbf{A}$ are given by the summation of Eqs. (A.2) and (A.4).

Table 4.1 collects the analytic expressions of the roots of Eq. (4.30), the poles of the system [9], in the general case with non-zero (I) and zero (II) eccentricity and in the case in which $\mathbf{A} \equiv \mathbf{A_g}$ (III) (no drag).

Table 4.1.: Analytic expressions of the poles

Case	$\mathbf{s_1}$	$\mathbf{s_2}$	$\mathbf{s_3}$	$\mathbf{s_4}$	$\mathbf{s_5}$	$\mathbf{s_6}$
I.	0	0	a_{11}	$v+z-\frac{b}{3}$	$-\frac{1}{2}(v+z)-\frac{b}{3}+\frac{\sqrt{3}}{2}(v-z)j$	$-\frac{1}{2}(v+z)-\frac{b}{3}-\frac{\sqrt{3}}{2}(v-z)j$
II.	0	0	0	a_{11}	$-\alpha\sqrt{\frac{\mu}{a}}-\beta(5\cos^2 i-1)j$	$-\alpha\sqrt{\frac{\mu}{a}}+\beta(5\cos^2 i-1)j$
III.	0	0	0	0	$-\beta(5\cos^2 i-1)\sqrt{\frac{3e^2+1}{e^2-1}}j$	$\beta(5\cos^2 i-1)\sqrt{\frac{3e^2+1}{e^2-1}}j$
	I. $\mathbf{A}=\mathbf{A_g}+\mathbf{A_d}$				II. $\mathbf{A}=\mathbf{A_g}+\mathbf{A_d}$ and $e=0$	III. $\mathbf{A}=\mathbf{A_g}$

with

$$\alpha = \frac{A}{m}C_D \qquad \beta = \frac{3}{4}\left(\frac{R_E}{a}\right)^2 nJ_2$$

$$v = \sqrt[3]{\frac{r}{2}+\sqrt{\frac{q^3}{27}+\frac{r^2}{4}}} \qquad z = \sqrt[3]{\frac{r}{2}-\sqrt{\frac{q^3}{27}+\frac{r^2}{4}}}$$

$$q = \frac{3c-b^2}{9} \qquad r = \frac{9bc-27d-2b^3}{54}$$

and b, c and d given by Eqs. (4.31)-(4.32).

The poles in the origin have multiplicity 2 in case I, multiplicity 3 in case II and 4 in case III. Thus, in every case the system is not stable in the sense that at least one initial state $\boldsymbol{\epsilon}(0)$ exists for which $\boldsymbol{\epsilon}$ will diverge over time. It is worthwhile to point out that in case III, the poles are representative of the solutions of the system dynamics unforced by external non-conservative forces. In cases I and II the system is in fact rendered non-homogeneous by the atmospheric drag perturbation force ($\dot{\boldsymbol{\epsilon}} = \mathbf{A}\boldsymbol{\epsilon} + \tilde{\mathbf{A}}_\mathbf{d}$). In case III where the Earth's gravity is the only force modelled, the unique initial condition for which the system is stable is $\boldsymbol{\epsilon}(0) = \mathbf{0}$. In case III with an initial condition $\boldsymbol{\epsilon}(0) \neq \mathbf{0}$, δa will remain constant, δu will diverge and all the other

states, the components of the eccentricity and inclination vectors, will be affected by long period perturbations due to the Earth's gravitational field zonal coefficient J_2. The poles of the reduced system of Eq. (4.27) are $s_1 = 0$, $s_2 = 0$ and $s_3 = a_{11}$.

4.2.4. Model Validation

The POD ephemerides [83,85] of the spacecraft TANGO [92], the target spacecraft of the PRISMA formation, have been used for the validation of the linear dynamic models of Eqs. (4.25) and (4.27). TANGO is in free motion not having any orbit control capability and has an orbit almost identical to MANGO's. The POD positions of TANGO provide a picture of the real orbit perturbation forces environment. In Fig. 4.6 the lines noted as POD are the evolution over 3 days of the difference between TANGO's orbital elements and a RO. The RO [73, 74] has been generated using a gravitational field model (GRACE GGM01S, 70x70 degree-order) as the only modelled force. The initial state of the RO is the first state of the POD ephemerides considered and is given in Table 4.2. The propagated relative elements with respect to the RO are obtained from the dynamic models of Eqs. (4.25) (full) and (4.27) (reduced) with a null initial error. The

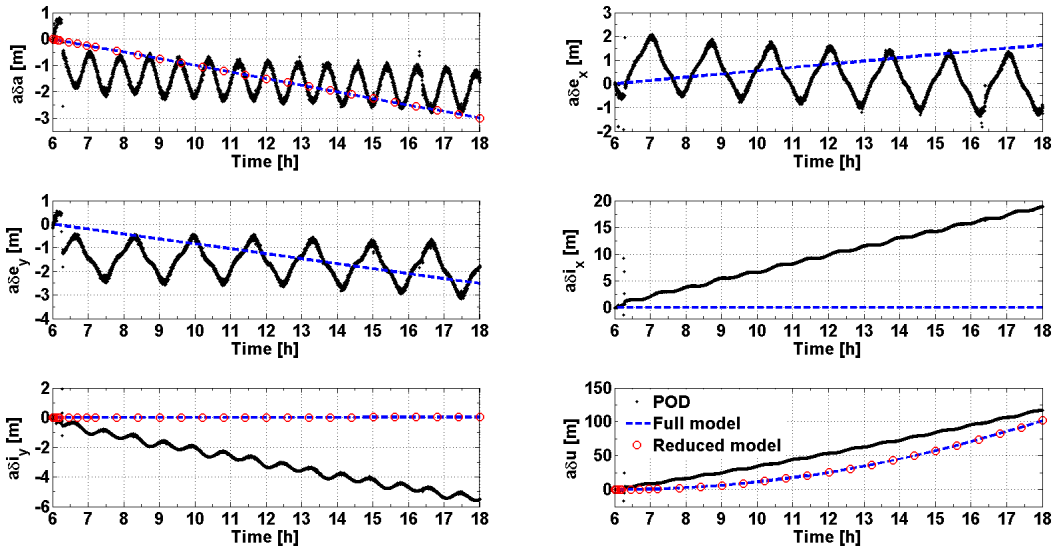

Figure 4.6.: Evolution in time of TANGO's real (POD) and propagated orbital elements with respect to the RO

Table 4.2.: Propagation parameters

ECI state	$\mathbf{r_R}[\mathbf{m}]$	$\mathbf{r_T}[\mathbf{m}]$	$\mathbf{r_N}[\mathbf{m}]$	$\mathbf{v_R}[\mathbf{m/s}]$	$\mathbf{v_T}[\mathbf{m/s}]$	$\mathbf{v_N}[\mathbf{m/s}]$
	-3967394.8566	-289822.105	5883191.2151	-6126.365	1487.7675	-4071.5062
Mean orb. el.	$\mathbf{a}[\mathbf{m}]$	$\mathbf{e_x}[-]$	$\mathbf{e_y}[-]$	$\mathbf{i}[\mathbf{deg}]$	$\mathbf{\Omega}[\mathbf{deg}]$	$\mathbf{u}[\mathbf{deg}]$
	7130522.2961	-0.004058	0.002774	98.28	351.74	123.38

spacecraft's physical properties are collected in Table 3.3 and the initial state, in Earth centred inertial coordinates (ECI), shown by Table 4.2. The propagation is over 12 hours, a reasonable duration for the validation of such a linear rough model. The two linear dynamic models give identical results in the propagation. This means that if only the control variables δa, δi_y and δu are used for the design of the orbit control system, the reduced model of Eq. (4.27) can be used without any loss of accuracy with respect to the full model. The comparison of the propagation with the POD data highlights the lack of accuracy of the model in the out-of-plane (δi_x, δi_y) motion prediction as the gravitational field is modelled only by the J_2 zonal coefficient and neither the third body gravitational perturbation nor the solar radiation pressure are included in the model. Table 4.3 collects the values of the poles of system Eq. (4.25) computed in the state of Table 4.2. Fig. 4.7 shows the non-zero real and imaginary parts of the poles computed at the ascending nodes of the RO. The poles have been computed from the entries of matrix $\mathbf{A}$

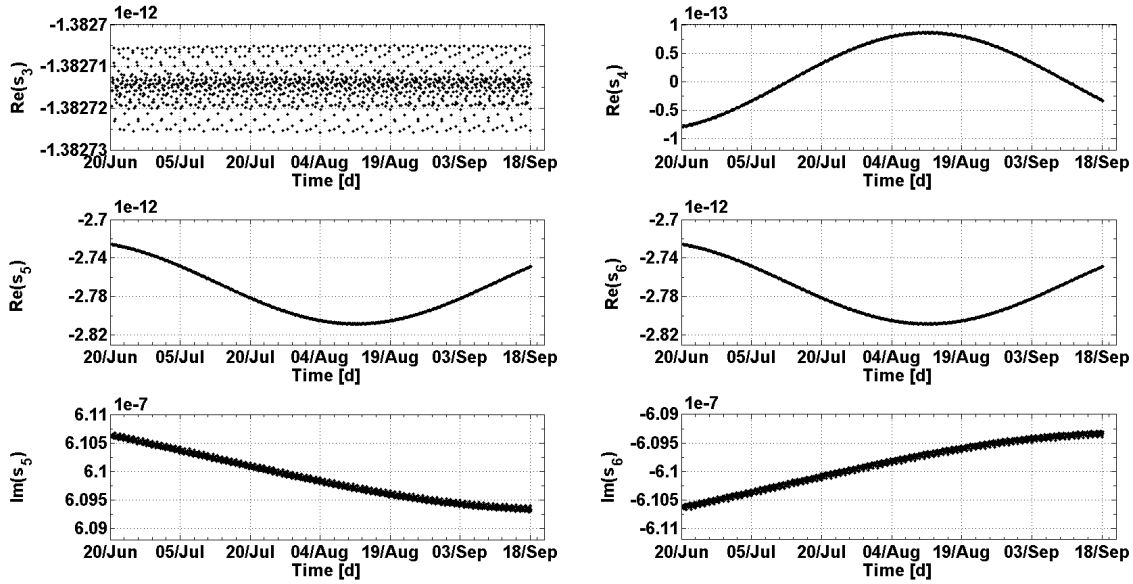

Figure 4.7.: Poles computed with the RO states

(Eq. (4.25)) after converting each state in orbital elements. Considering the order of magnitude of the real and imaginary parts of the poles displayed in Table 4.3 it can be concluded that on the short period the dynamic of the system is mainly determined by the zonal coefficient J_2 only (case III).

Table 4.3.: Poles computed in the initial state

Case	$\mathbf{s_1}$	$\mathbf{s_2}$	$\mathbf{s_3}$	$\mathbf{s_4}$	$\mathbf{s_5}$	$\mathbf{s_6}$
I.	0	0	-1.38·10^{-12}	-7.95·10^{-14}	-2.73·10^{-12} + 6.106·10^{-7}j	-2.73·10^{-12} - 6.106·10^{-7}j
II.	0	0	-1.38·10^{-12}	0	-2.73·10^{-12} + 6.106·10^{-7}j	-2.73·10^{-12} - 6.106·10^{-7}j
III.	0	0	0	0	6.106·10^{-7}j	-6.106·10^{-7}j
I. $\mathbf{A} = \mathbf{A_g} + \mathbf{A_d}$			II. $\mathbf{A} = \mathbf{A_g} + \mathbf{A_d}$ and $e = 0$		III. $\mathbf{A} = \mathbf{A_g}$	

4.3. Virtual Formation Control

4.3.1. Linear Control

The linear control law for the system Eq. (4.26) has the general form [9] of Eq. (4.20). $\mathbf{G}$ and $\mathbf{G_d}$ are the gain matrices and $\mathbf{y} = \mathbf{C}\boldsymbol{\epsilon}$ is the system's output. The terms of matrix $\mathbf{C}$ will be computed from Eq. (2.30) as the goal of the proposed absolute orbit controller is the maintenance of one or more relative Earth-fixed elements within their control windows. In order for the closed-loop system to be asymptotically stable, the characteristic roots [9] of the closed-loop dynamics matrix $\mathbf{A_c} = \mathbf{A} - \mathbf{BGC}$ must have negative real parts. This can be accomplished by a suitable choice of the gain matrix $\mathbf{G}$ if the system is controllable. Once the gains and thus the poles of matrix $\mathbf{A_c}$ have been set, matrix $\mathbf{G_d}$ is obtained substituting Eq. (4.20) in Eq. (4.25), imposing $\mathbf{y} = \mathbf{C}\boldsymbol{\epsilon}$ and the steady state condition $\dot{\boldsymbol{\epsilon}} = \mathbf{0}$:

$$\mathbf{G_d} = (\mathbf{C}\mathbf{A_c^{-1}}\mathbf{B})^{-1}\mathbf{C}\mathbf{A_c^{-1}}\mathbf{I} \tag{4.33}$$

The linear control system is designed by means of poles placement. The choice of which relative EF has to be controlled is dictated by the mission requirements, whereas the best place and direction of the orbital maneuvers is determined both by which relative EF is controlled and by

the Gauss equations (Eq. (A.5)). First, an in-plane orbit control system will be considered with the single control input Δv_T and two outputs δL_λ, $d(\delta L_\lambda)/dt$ computed at the orbit's ascending node. This is the basic control required for the maintenance of a repeat-track orbit [3]. Secondly, an in-plane/out-of-plane controller with two control inputs Δv_T, Δv_N and three outputs δL_λ, $d(\delta L_\lambda)/dt$, δi_y is designed. In this case the in-orbit phasing δL_φ can be restrained in a control window as well. The design of these regulators will be based on the reduced model Eq. (4.27).

In-plane control with one input ($\Delta \mathrm{v_T}$) and two outputs ($\delta \mathrm{L_\lambda}$, $\mathrm{d}(\delta \mathrm{L_\lambda})/\mathrm{dt}$)

In this case, the design of the feedback system is finalized to control δL_λ and $d(\delta L_\lambda)/dt$, computed at the ascending node (Eqs. (2.31)-(2.33)), by means of along-track velocity increments. This means that the orbit controller is designed to work only once per orbit at most. The system components are

$$\mathbf{A_r} = \begin{pmatrix} a_{r_{11}} & 0 & 0 \\ a_{r_{21}} & 0 & 0 \\ a_{r_{31}} & 0 & 0 \end{pmatrix} \qquad \boldsymbol{\epsilon_r} = a_{\mathcal{R}} \begin{pmatrix} \delta a \\ \delta i_y \\ \delta u \end{pmatrix} \qquad \mathbf{B_r} = \begin{pmatrix} b_1 \\ 0 \\ 0 \end{pmatrix}$$

$$\mathbf{G} = \begin{pmatrix} g_1 & g_2 \end{pmatrix} \qquad \mathbf{G_d} = \begin{pmatrix} g_0 & 0 & 0 \end{pmatrix} \qquad \mathbf{x_{dr}} = \begin{pmatrix} x_{d1} \\ 0 \\ 0 \end{pmatrix} \tag{4.34}$$

with $a_{r_{11}}$, $a_{r_{21}}$, $a_{r_{31}}$, $b_1 = 2/n$, x_{d1} given by Eq. (4.27) and $g_1, g_2 \in \mathbb{R}$. The output $\mathbf{y} = \mathbf{C}\boldsymbol{\epsilon_r}$ is

$$a_{\mathcal{R}} \begin{pmatrix} \delta L_\lambda \\ \dfrac{d(\delta L_\lambda)}{dt} \end{pmatrix} = a_{\mathcal{R}} \begin{pmatrix} 0 & c_{12} & c_{13} \\ c_{21} & 0 & 0 \end{pmatrix} \begin{pmatrix} \delta a \\ \delta i_y \\ \delta u \end{pmatrix} \tag{4.35}$$

where the terms $c_{12} = 1/\sin i_{\mathcal{R}}$, $c_{13} = |\omega_E - \dot{\Omega}_{\mathcal{R}}|/n$ and $c_{21} = a_{r_{21}}/\sin i_{\mathcal{R}} + a_{r_{31}}|\omega_E - \dot{\Omega}_{\mathcal{R}}|/n$ are obtained from Eqs. (4.28)-(4.29) imposing $\overline{u} = 0$.

The control input is given by $\Delta v_T = -(g_1 \delta L_\lambda + g_2 d(\delta L_\lambda)/dt) a_{\mathcal{R}}$. The objective here is

to find the gains g_1 and g_2 which place the poles of the closed-loop dynamic matrix $\mathbf{A_c} = \mathbf{A_r} - \mathbf{B_r G C}$ at the locations desired. The characteristic polynomial of $\mathbf{A_c}$ is

$$|s\mathbf{I} - \mathbf{A_c}| = s[s^2 + (b_1 c_{21} g_2 - a_{r_{11}})s + b_1(a_{r_{21}} c_{12} + a_{r_{31}} c_{13})g_1] = s[s^2 + \hat{a}_1 s + \hat{a}_2] \quad (4.36)$$

$$\hat{a}_1(g_2) = b_1 c_{21} g_2 - a_{r_{11}} \qquad \hat{a}_2(g_1) = b_1(a_{r_{21}} c_{12} + a_{r_{31}} c_{13})g_1 \quad (4.37)$$

One of the three poles of $\mathbf{A_c}$ is placed in the origin regardless of the value of the gains. This is due to the fact that the part of the system depending on δi_y is not controllable by Δv_T. Indeed the controllability test matrix

$$\mathbf{Q_{ctr}} = \begin{pmatrix} \mathbf{B} & \mathbf{A_r B_r} & \mathbf{A_r^2 B_r} \end{pmatrix} = \begin{pmatrix} b_1 & a_{r_{11}} b_1 & a_{r_{11}}^2 b_1 \\ 0 & a_{r_{21}} b_1 & a_{r_{11}} a_{r_{21}} b_1 \\ 0 & a_{r_{31}} b_1 & a_{r_{11}} a_{r_{31}} b_1 \end{pmatrix} \quad (4.38)$$

has rank 2, smaller than the maximum rank 3. Nevertheless at the ascending node $\delta L_\lambda = k_1 \delta i_y + k_2 \delta e + k_3 \delta u$ ((Eqs. (2.31)-(2.33))) can be controlled by means of variations of δu which compensate the variations of δi_y and δe. The closed-loop poles $s = (-\hat{a}_1 \pm \sqrt{\hat{a}_1^2 - 4\hat{a}_2})/2$ of Eq. (4.36) are real (complex-conjugate) if $|\hat{a}_1| >= 2\sqrt{\hat{a}_2}$ ($|\hat{a}_1| < 2\sqrt{\hat{a}_2}$) and $\hat{a}_2 = b_1 c_{21} g_1 > 0$. If $\hat{a}_1 > 0$ the poles are placed on the left of the imaginary axis of the complex plane and the closed-loop system is stable. If If $\hat{a}_1 < 0$ the system is not stable. These stability conditions impose constraints on the value of the gains as resumed by Table 4.4 where $\hat{a}_2$ is given by Eq. (4.37). If the poles chosen are complex-conjugate, the contribution of the term

Table 4.4.: Gain constraints

Pole type	$\mathbf{c_{21}(i) > 0}$ **and** $\mathbf{g_1 > 0}$	$\mathbf{c_{21}(i) < 0}$ **and** $\mathbf{g_1 < 0}$
Real	$g_2 > \dfrac{a_{r_{11}} + 2\sqrt{\hat{a}_2}}{b_1 c_{21}}$	$g_2 < \dfrac{a_{r_{11}} + 2\sqrt{\hat{a}_2}}{b_1 c_{21}}$
Complex	$\dfrac{a_{r_{11}}}{b_1 c_{21}} < g_2 < \dfrac{a_{r_{11}} + 2\sqrt{\hat{a}_2}}{b_1 c_{21}}$	$\dfrac{a_{r_{11}} + 2\sqrt{\hat{a}_2}}{b_1 c_{21}} < g_2 < \dfrac{a_{r_{11}}}{b_1 c_{21}}$

$-g_2(d(\delta L_\lambda)/dt)a_\mathcal{R}$ to the control action Δv_T will be negligible as $a_\mathcal{R} d(\delta L_\lambda)/dt$ has an order of magnitude of 30/86400 m s^{-1} [74] and the value of g_2 is limited in the range indicated in the second row of Table 4.4. This means that in order to control also $d(\delta L_\lambda)/dt$ the poles have to be on the negative real axis since in this way a suitably large value of g_2 can be obtained. The gains are related to the poles by the following equation

$$g_1 = \frac{s_1 s_2}{b_1(a_{r_{21}} c_{12} + a_{r_{31}} c_{13})} \qquad g_2 = \frac{s_1 + s_2 + a_{r_{11}}}{b_1 c_{21}} \tag{4.39}$$

with $s_1, s_2 \in \mathbb{R}^-$. The gain values chosen as a first guess are $g_1 = \text{sgn}(c_{21})\Delta v_{T_{\delta L}}/(a_\mathcal{R}\delta L_{\lambda_{MAX}})$ and $g_2 = \text{sgn}(c_{21})\Delta v_{T_{d\delta L}}/(a_\mathcal{R} d(\delta L_\lambda)/dt)_{MAX}$ where $\Delta v_{T_{\delta L}}, \Delta v_{T_{d\delta L}}, a_\mathcal{R}\delta L_{\lambda_{MAX}}, (a_\mathcal{R} d(\delta L_\lambda)/dt)_{MAX} \in \mathbb{R}^+$ are limits imposed by design and $\text{sgn}(c_{21})$ is the sign of c_{21}. The dynamics of the closed-loop system can be verified and adjusted by computing the poles with Eq. (4.39), adjusting their placement and iterating the process.

The control input is

$$\Delta v_T = -\mathbf{G}\mathbf{C}\boldsymbol{\epsilon_r} = -(g_2 c_{21}\delta a + g_1 c_{12}\delta i_y + g_1 c_{13}\delta u)a_\mathcal{R} \tag{4.40}$$

The following subsystem of Eq. (4.34) is considered for the determination of the disturbance gain matrix $\mathbf{G_d}$ (Eq. (4.20))

$$\frac{d(\delta a)}{dt} a_\mathcal{R} = (a_{r_{11}}\delta a)a_\mathcal{R} + b_1\Delta v_T + x_{d1} \qquad y = a_\mathcal{R}\delta a \tag{4.41}$$

for which Eq. (4.33) yields $g_0 = 1/b_1$ and then

$$\mathbf{G_d} = \begin{pmatrix} \frac{1}{b_1} & 0 & 0 \end{pmatrix} \tag{4.42}$$

The term x_{d1}/b_1 for a small satellite in low Earth orbit has an order of magnitude of 10^{-8} m/s and is absolutely negligible in the computation of Δv_T. This is not surprising since $\mathbf{G_d}$ represents the instantaneous effect of the drag and not its integration over time.

The maneuvers have to be computed at the ascending node but can be executed with the

same effectiveness in any place along the orbit as they have to change δu by means of semi-major axis increments (first row of Eq. (A.5)). Nevertheless the along-track maneuvers can be located [92] in order to be the most effective on the control of the relative eccentricity vector components δe_x and δe_y. Solving the second and third of the Gauss equations $\dot{\boldsymbol{\epsilon}} = \mathbf{B}(\boldsymbol{\kappa})\Delta\mathbf{v}$ in u and imposing that the effect of the velocity increment Δv_T is decreasing the magnitude of δe_x and δe_y, the eccentricity vector can be passively controlled with a proper in-orbit location [44] of the along-track maneuver:

$$u_M = \arctan\left(\frac{\delta e_y}{\delta e_x}\right) + k\pi \tag{4.43}$$

$$k = 0 \quad \text{if} \quad (\delta e_x \Delta v_T) < 0 \tag{4.44}$$

$$k = 1 \quad \text{if} \quad (\delta e_x \Delta v_T) > 0 \tag{4.45}$$

In-plane/out-of-plane control with two inputs ($\Delta\mathrm{v_T}$, $\Delta\mathrm{v_N}$) and three outputs ($\delta\mathrm{L_\lambda}$, $\mathrm{d}(\delta\mathrm{L_\lambda})/\mathrm{dt}$, $\delta\mathrm{i_y}$)

In this case, the design of the system is finalized to control the relative Earth-fixed elements δL_λ and δL_φ at the ascending node by means of along-track and cross-track velocity increments. At the ascending node δL_λ and δL_φ are related each other by equation $\delta L_\lambda = k_1 \delta i_y + k_2 \delta L_\varphi$ where k_1 and k_2 are the values displayed in Eqs. (2.31)-(2.33). The only chance of controlling at the same time δL_λ and δL_φ is thus selecting δi_y as one of the controlled outputs. The velocity increment Δv_N to control δi_y has to be placed at the orbit's highest latitude ($u = \pi/2$) in order to maximize its effectiveness (fifth row of Eq. (A.5)). The execution of Δv_T will be placed with the rule of Eq. (4.43). The system components are $\mathbf{A_r}$ and $\boldsymbol{\epsilon_r}$ from Eq. (4.34) and

$$\mathbf{B_r} = \begin{pmatrix} b_1 & 0 \\ 0 & b_2 \\ 0 & 0 \end{pmatrix} \qquad \mathbf{G} = \begin{pmatrix} g_1 & g_2 & 0 \\ 0 & 0 & g_N \end{pmatrix} \tag{4.46}$$

where $b_1 = 2/n$, $b_2 = \sin u/n$ are given by the first and fifth rows of matrix $\mathbf{B}$ (Eq. (A.5)) and the term of $\mathbf{B_r}$ relating Δv_N and δu has been omitted by design. The output $\mathbf{y} = \mathbf{C}\boldsymbol{\epsilon_r}$ is

$$a_{\mathcal{R}} \begin{pmatrix} \delta L_\lambda \\ \dfrac{d(\delta L_\lambda)}{dt} \\ \delta i_y \end{pmatrix} = a_{\mathcal{R}} \begin{pmatrix} 0 & c_{12} & c_{13} \\ c_{21} & 0 & 0 \\ 0 & 1 & 0 \end{pmatrix} \begin{pmatrix} \delta a \\ \delta i_y \\ \delta u \end{pmatrix} \tag{4.47}$$

where c_{12}, c_{13} and c_{21} are the same as in Eq. (4.35). The system is controllable as the rank of the controllability matrix is 3. The characteristic polynomial of $\mathbf{A_c} = \mathbf{A_r} - \mathbf{B_r G C}$ is

$$|s\mathbf{I} - \mathbf{A_c}| = s^3 + (b_1 g_2 c_{21} + b_2 g_N - a_{r_{11}})s^2 + [b_1 g_1 (a_{r_{21}} c_{12} + a_{r_{31}} c_{13}) + b_2 g_N (b_1 g_2 c_{21} - a_{r_{11}})]s$$
$$+ a_{r_{31}} c_{13} b_1 b_2 g_1 g_N = s^3 + \hat{a}_1 s^2 + \hat{a}_2 s + \hat{a}_3 \tag{4.48}$$

$$\hat{a}_1(g_2, g_N) = b_1 g_2 c_{21} + b_2 g_N - a_{r_{11}} \tag{4.49}$$

$$\hat{a}_2(g_1, g_2, g_N) = b_1 g_1 (a_{r_{21}} c_{12} + a_{r_{31}} c_{13}) + b_2 g_N (b_1 g_2 c_{21} - a_{r_{11}}) \tag{4.50}$$

$$\hat{a}_3(g_1, g_N) = a_{r_{31}} c_{13} b_1 b_2 g_1 g_N \tag{4.51}$$

The proper control gains can be found by splitting the problem in two distinct sub-problems. The first-guess values of g_1, g_2 are the same found solving the problem of the previous section. The cross-track maneuver gain is found with the relation $g_N = a_{\mathcal{R}} \delta i_{y_{MAX}} / \Delta v_{N_{MAX}}$ where $\delta i_{y_{MAX}}, \Delta v_{N_{MAX}} \in \mathbb{R}^+$ are imposed by design. The placement of the closed-loop poles and the dynamic response of the system can then be verified by finding the roots of Eq. (4.48). The control input is

$$\Delta v_T = [-g_2 c_{21} \delta a - g_1 (c_{12} \delta i_y + c_{13} \delta u)] a_{\mathcal{R}} \qquad \Delta v_N = -g_N \delta i_y a_{\mathcal{R}} \tag{4.52}$$

4.3.2. LQR Control

The linear quadratic optimal regulator (LQR) [9] is best suited for a multiple-input/multiple-output system like that here considered. Here, instead of seeking a gain matrix to achieve specified closed-loop locations of the poles, a gain is sought to minimize a specified cost function Λ expressed as the integral of a quadratic form in the state $\boldsymbol{\epsilon}$ plus a second quadratic from

in the control $\Delta\mathbf{v}$

$$\Lambda = \int_t^T \left[\boldsymbol{\epsilon}^T(\tau)\mathbf{C}^T\mathbf{Q_y}\mathbf{C}\boldsymbol{\epsilon}(\tau) + \Delta\mathbf{v}^T(\tau)\mathbf{R}\Delta\mathbf{v}(\tau)\right] d\tau \tag{4.53}$$

where $\mathbf{Q} = \mathbf{C}^T(\tau)\mathbf{Q_y}(\tau)\mathbf{C}$ is the 6×6 state weighting symmetric matrix, $\mathbf{Q_y}$ is weighting matrix of the output $\mathbf{y} = \mathbf{C}\boldsymbol{\epsilon}$ and $\mathbf{R}$ is the 3×3 control weighting symmetric matrix. The optimal steady-state ($T = \infty$ in Eq. (4.53)) gain matrix $\mathbf{G}$ for system Eq. (4.26) is

$$\mathbf{G} = -\mathbf{R}^{-1}\mathbf{B}^T\bar{\mathbf{M}} \tag{4.54}$$

where $\bar{\mathbf{M}}$ is the steady-state solution to the Riccati equation

$$-\dot{\bar{\mathbf{M}}} = \bar{\mathbf{M}}\mathbf{A} + \mathbf{A}^T\bar{\mathbf{M}} - \bar{\mathbf{M}}\mathbf{B}\mathbf{R}^{-1}\mathbf{B}^T\bar{\mathbf{M}} + \mathbf{Q} = \mathbf{0} \tag{4.55}$$

The disturbance gain matrix $\mathbf{G_d}$ for the case of Eq. (4.26) in which $\mathbf{x_d}$ is constant, is given by

$$\mathbf{G_d} = -\mathbf{R}^{-1}\mathbf{B}^T(\mathbf{A_c}^T)^{-1}\bar{\mathbf{M}}\mathbf{I} \tag{4.56}$$

where $\mathbf{A_c} = \mathbf{A} - \mathbf{B}\mathbf{G}$ is the closed-loop dynamics matrix, $\bar{\mathbf{M}}$ is given by Eq. (4.55) and $\mathbf{I}$ is the identity matrix. As already remarked in Sec. 4.3.1, the term $\mathbf{G_d}\mathbf{x_d}$ can be neglected. In the performance function defined by Eqs. (4.53) the quadratic form $\mathbf{y}^T\mathbf{Q}\mathbf{y}$ represents a penalty on the deviation of the real from the RO and the weighting matrix $\mathbf{Q}$ specifies the importance of the various components of the state vector relative to each other. The term $\Delta\mathbf{v}^T\mathbf{R}\Delta\mathbf{v}$ is instead included to limit the magnitude of the control signal $\Delta\mathbf{v}$ and to prevent saturation of the actuator. Overall the gain matrices choice is a trade-off between control action cost (i.e., small gains to limit propellant consumption and avoid thruster saturation phenomena) and control accuracy (i.e. large gains to limit the excursion of the state from its reference value). The choice of the weighting matrices is done here with the maximum size technique [10]. The aim of this method is to confine the individual states and control actions within prescribed maximum limits given respectively by $y_{i_{MAX}}$ and $\Delta v_{i_{MAX}}$. The terms of $\mathbf{Q_y}$ and $\mathbf{R}$ will be thus chosen with the rule

imposed by the following equations.

$$Q_{yii} = \frac{k_i}{y^2_{i_{MAX}}}, \;\; Q_{yij} = \frac{k_{ij}}{2y_{i_{MAX}} y_{j_{MAX}}}, \;\; k_{ij} \in \mathbb{R} \;\text{ for }\; i = 1,2,3 \;\text{ and }\; j = 1,2,3 \tag{4.57}$$

$$R_{ii} = \frac{h_i}{\Delta v^2_{i_{MAX}}}, \;\; R_{ij} = \frac{h_{ij}}{2\Delta v_{i_{MAX}} \Delta v_{j_{MAX}}}, \;\; h_{ij} \in \mathbb{R} \;\text{ for }\; i = R,T,N \;\text{ and }\; j = R,T,N \tag{4.58}$$

The choice of diagonal $\mathbf{Q_y}$ and $\mathbf{R}$ matrices is usually a good starting point in a trial-and-error design procedure aimed at obtaining the desired properties of the controller.

4.3.3. Discrete Control

The absolute orbit control problem has been solved in Sections 4.3.1-4.3.2 in the continuous time domain. Nevertheless if the regulator has to control the value of the REFE computed in one specific point of the orbit (e.g. at the ascending node), the problem is defined in the discrete domain. Fig. 4.8 helps to visualize this important concept, showing the variation with time of the REFE of the MANGO satellite flying in free motion (Sec. 3.3.1). The REFE are computed (Eqs. (2.28)-(2.30)) in $u = u(t)$ (continuous time domain) and once per orbit in $\overline{u} = 0$ (discrete time domain).

The linear regulators can be design in the continuous domain, as done in the previous sections, as long as the relation between the stability condition in the continuous and discrete domains is provided. Each closed-loop pole s_i in the continuous domain, root of the characteristic polynomial $|s\mathbf{I} - \mathbf{A_c}|$, can be mapped into a pole $s_{i_\mathcal{D}}$ in the discrete domain in a different way, depending on the discretization method used, using one of the following relations

$$s_{i_\mathcal{D}} = 1 + T_{du} s_i \qquad \text{Euler} \tag{4.59}$$

$$s_{i_\mathcal{D}} = \frac{1}{1 - T_{du} s_i} \qquad \text{Euler backward} \tag{4.60}$$

$$s_{i_\mathcal{D}} = \frac{1 + T_{du} s_i/2}{1 - T_{du} s_i/2} \qquad \text{Tustin} \tag{4.61}$$

where the control duty cycle $T_{du} = pT_N$, with $p \in \mathbb{Z}^+$, is also the discretization step multiple of the nodal period T_N.

The asymptotic stability condition in the discrete domain is $|s_{i_\mathcal{D}}| < 1$. Fig. 4.9 shows the stability region as mapped from the continuous into the discrete domain when the discretization methods of Eqs. (4.59)-(4.61) are used. Eulers's method maps part of the left half of the complex plane into points placed out of the unitary circle in the discrete domain. This means that, depending on the discretization step T_{du}, stable poles in the continuous domain may be mapped into unstable poles in the discrete domain. For this reason Euler's method is generally not used. Euler's backward method maps the stability region in the continuous domain into a subset of the discrete stability region. Finally Tustin's method maps exactly the continuous into the discrete stability region.

The linear regulator can be designed in the continuous domain with a proper choice of the poles s_i and duty cycle T_{du}, provided that the stability condition $|s_{i_\mathcal{D}}| < 1$ in the discrete domain is verified by means of Eqs. (4.59)-(4.61).

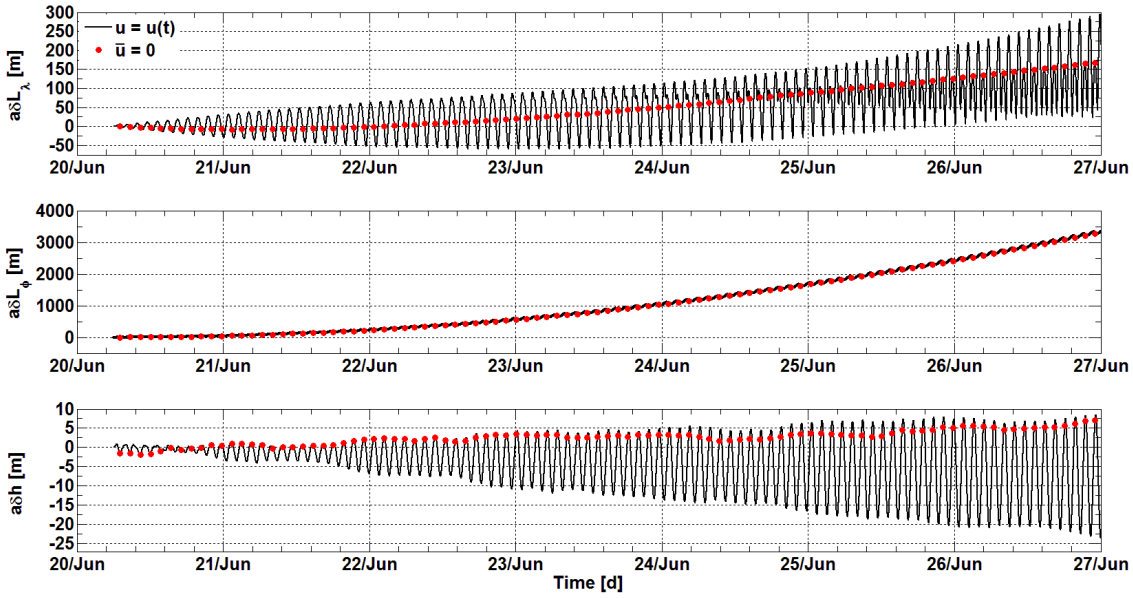

Figure 4.8.: REFE computed in u(t) and at the ascending node

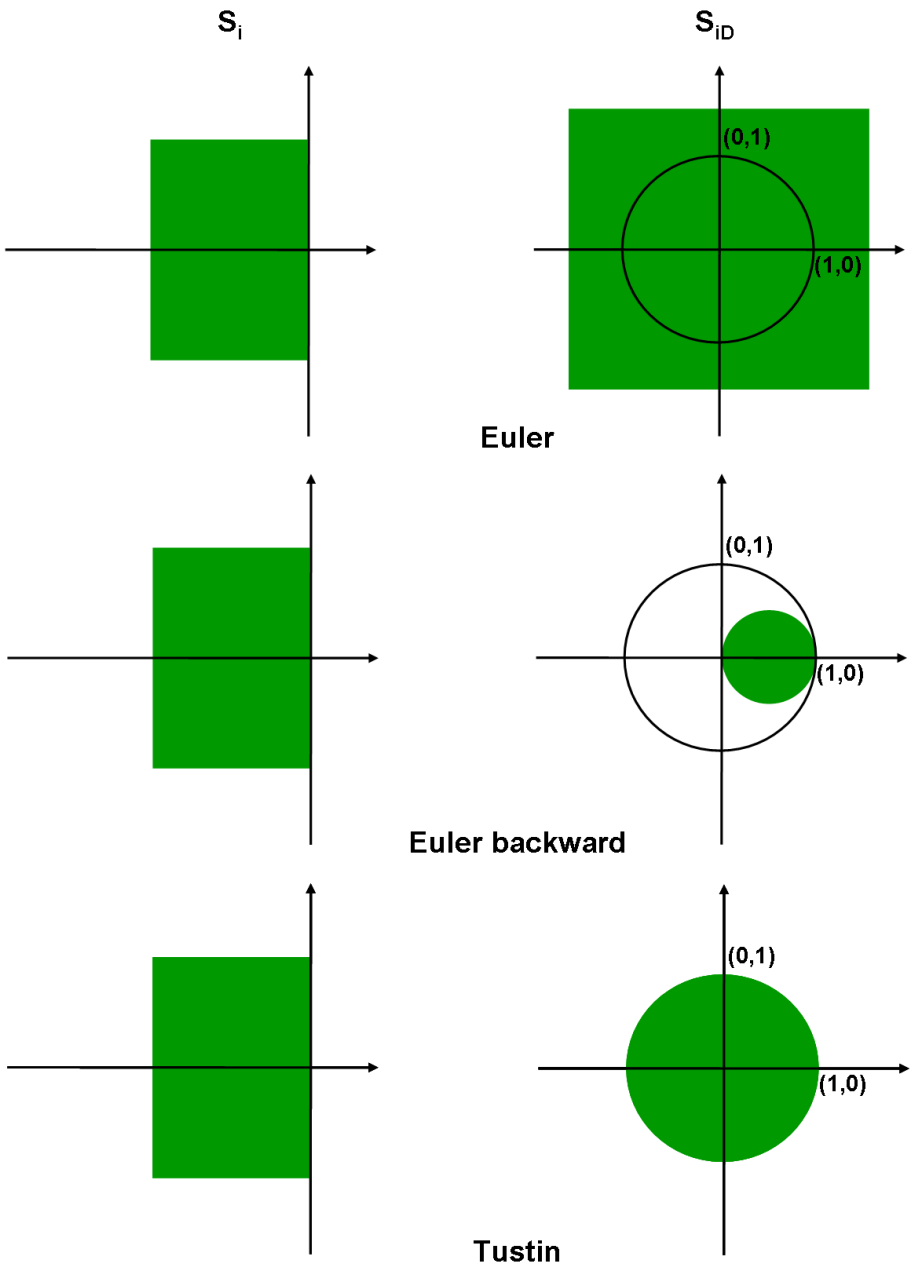

Figure 4.9.: Region of stability as mapped from the continuous to the discrete domain

5. Numerical Simulations

In Chapter 4 the problem of the autonomous absolute orbit control has been formalized using the operational parameters and the relative Earth-fixed parametrization presented respectively in Sections 2.2 and 2.3. The REFE parametrization has been used for the design of a linear and a quadratic optimal regulators for orbit maintenance. The state-space representation has been used for the mathematical formulation of the problem. The system to be controlled has been described by means of a linear dynamic model including the J_2 zonal coefficient of the Earth's gravitational field and the atmospheric drag perturbation force. An analytical algorithm based on the control of the phase difference (Sec. 2.2.1) at the equator has been developed for the RO acquisition and maintenance and validated with the AOK experiment on the PRISMA mission (Chapter 7).

This chapter is dedicated to the presentation of numerical simulations in which the different types of orbit control presented in Chapter 4 are compared. Two types of numerical simulations are carried on. A first set of simulations is based on an orbit propagation model including the gravitational field and a constant atmospheric drag as the only orbit's perturbation force. By means of these ideal simulations the performance of the different controllers can be compared in theoretical design conditions. A second set of simulations are run to compare the behaviour of the controllers in a realistic orbit environment. As a case study the PRISMA mission (Sec. 1.4) is used. The simulation results are evaluated from a performance and operational point of view in order to formulate a first conclusion about the advantages and disadvantages of the different control techniques. The DLR/GSOC simulation platform (Sec. 6.4) is used to make the analyses. This test platform includes a very accurate orbit propagator, the control software and allows the simulation of actuators and navigation errors.

5.1. Simulation Parameters

Two types of numerical simulations were run in order to validate and compare the control methods explained in the previous sections. A first set of simulations was based on an orbit propagation model with the gravitational field and a constant atmospheric drag as the only orbit's perturbation force. This is also the perturbation model on which the analytical algorithm of the AOK controller (Sec. 4.1) is based. By means of these ideal simulations the performance of the different controllers could be compared in theoretical design conditions. A second set of simulations was run to compare the behaviour of the controllers in a realistic orbit environment. Tables 5.1 and 5.2 collect respectively the orbit propagation parameters and the sensor, actuators and navigation models used for the simulations. The physical parameters of the MANGO spacecraft are shown in Table 3.3. The propulsion system is characterized by a Minimum Impulse Value (MIV) and a Minimum Impulse Bit (MIB). Consequently the thrusters can only realize Δvs which are larger than MIV and integer multiples of MIB. Furthermore, the execution error of the thrusters is quantified by the relation $\xi = |(\Delta V_{real} - \Delta V_{cmd})/\Delta V_{cmd}| \cdot 100$ where Δv_{cmd} is the velocity increment commanded by the on-board controller and Δv_{real} is the actual velocity increment executed by the propulsion system. Finally the attitude control error, which causes thrusters misalignment, is treated as Gaussian noise with zero bias and a 0.2° standard deviation in the three spacecraft's body axes. The values of the navigation accuracy refer to the magnitude of the absolute position and velocity vectors in the $\mathbf{RTN}$ frame and are typical of an on-board GPS based navigation system [83]. For further details about

Table 5.1.: Propagation parameters

Orbit Propagation	**Model**
Earth gravitational field	GRACE GGM01S 40x40
Atmospheric density	Harris-Priester
Sun and Moon ephemerides	Analytical formulas [4]
Solid Earth, polar and ocean tides	IERS
Relativity effects	First order effects
Numerical integration method	Dormand-Prince
RO Propagation	**Model**
Earth gravitational field	GRACE GGM01S 30x30

the navigation accuracy in the simulations see Appendix B. The initial state used for the orbit propagation is the same shown in Table 4.2 and the run time is one month. The RO is assumed to be generated on-ground and uploaded to the satellite. The RO has been propagated using the GRACE GGM01S 30x30 gravitational field (different than the model used for the actual orbit propagation) to simulate the inaccuracies which also the best available model has with respect to the actual Earth's gravitational field. The atmospheric density and solar radiation pressure models have been calibrated (see Sections 3.3.1 and 3.3.2) in order to have a high degree of realism.

Table 5.2.: Navigation and actuators accuracy

Propulsion System Accuracy	**Value**
MIV	$7 \cdot 10^{-4}$ [m/s]
MIB	$7 \cdot 10^{-5}$ [m/s]
ξ	5 [%]
Attitude Control Accuracy	**Value**
Mean	0 [deg]
σ	0.2 [deg]
Absolute Navigation Accuracy	**Value**
Mean	3.4 [m]
σ	1.6 [m]

5.2. In-Plane Orbit Control

5.2.1. Ideal Simulation Scenario

In these simulations a constant atmospheric drag is the only perturbation force included in the orbit propagation model and no thruster, attitude and navigation errors are included. The gravitational field model used for the orbit propagation is the GRACE GGM01S 40x40 whereas that used for the RO generation is the GRACE GGM01S 30x30. Figures 5.1 and 5.2 show respectively the ROE and the REFE of the spacecraft in case the orbit control system is designed with the analytical algorithms of the AOK experiment, Eq. (4.40) (linear) and Eq. (4.54) (LQR). The REFE are computed at the ascending node ($\overline{u} = 0$). In Fig. 5.1 only the orbital elements influ-

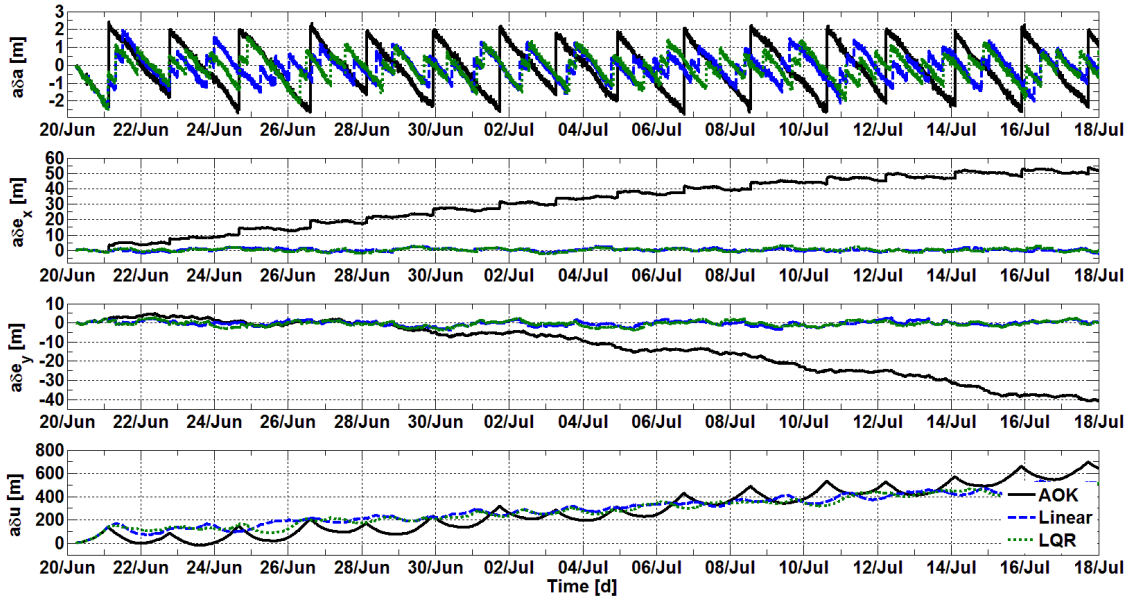

Figure 5.1.: ROE (in-plane control)

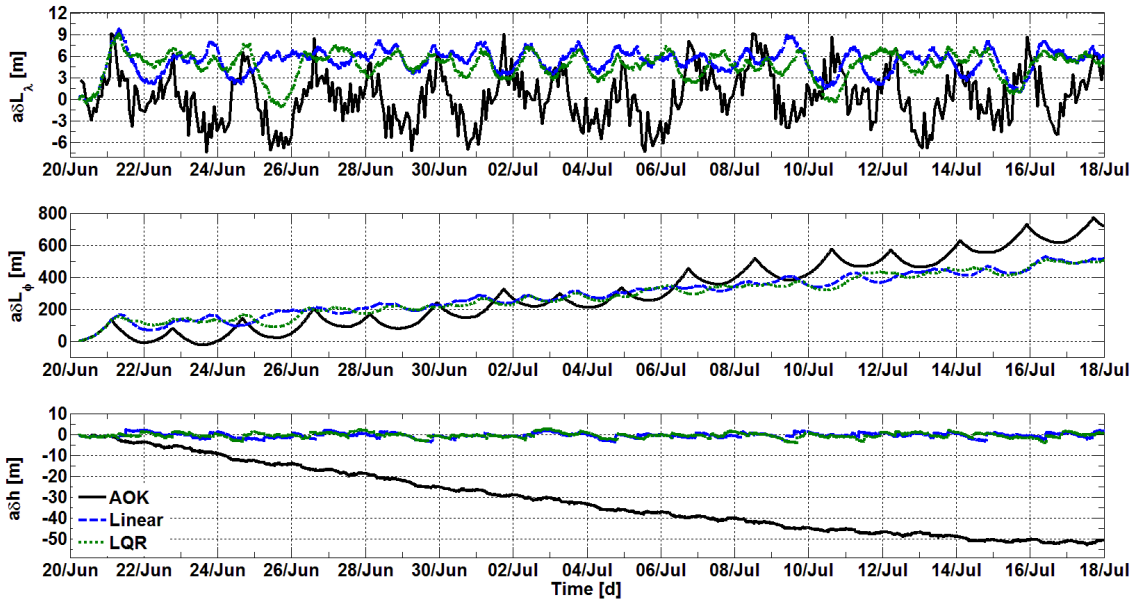

Figure 5.2.: REFE (in-plane control)

enced by Δv_T are shown. Table 5.3 collects the parameters used for the design of the linear regulators (Eqs. (4.39), (4.57) and (4.58)). The maneuver duty cycle imposed in all the simulations was two orbital periods i.e. the controllers could compute and command maneuvers once every

Table 5.3.: Regulators design parameters

	AOK	**Linear**	**LQR**
$\boldsymbol{\delta L_{\lambda_{MAX}}}$ **[m]**	5	10	10
$\boldsymbol{(d\delta L_{\lambda}/dt)_{MAX}}$ **[m/s]**	-	100/86400	200/86400
$\boldsymbol{\Delta v_{R_{MAX}}}$ **[m/s]**	-	-	10^{-6}
$\boldsymbol{\Delta v_{T_{MAX}}}$ **[m/s]**	-	10^{-3}	10^{-3}
$\boldsymbol{\Delta v_{N_{MAX}}}$ **[m/s]**	-	-	10^{-6}

third orbit. The execution of the maneuvers takes place at the ascending node for the analytical controller and is placed with the rule of Eq. (4.43) for the linear regulators. Figures 5.1 and 5.2 show how the phase difference vector component δL_{λ} is maintained in its control window by means of along-track maneuvers which change the value of the orbit's semi-major axis. The guided time evolution of δa determines that of δu and thus the timing of the real with respect to the virtual spacecraft in passing at the ascending node (Eq. (2.22)). The different time evolution of δu with respect to that in free motion can be observed comparing Figures 3.13 and 5.1. The drift of the phase difference vector component δL_{φ} is actually used to compensate the drift of δi_y in the control of δL_{λ} (Eqs. (2.31)-(2.33)). The correct placement of the maneuvers allows the control of the eccentricity vector (and thus δh) by the linear regulators whereas the analytical controller has no eccentricity vector control capability as it executes the maneuvers only at the orbit's ascending node. Fig. 5.3 shows the orbital maneuvers commanded by the on-board controllers and executed by the spacecraft thrusters. Table 5.4 collects the control performance and the maneuver budget. The goal of controlling δL_{λ} by means of along- and anti-along-track velocity increments is achieved by the three controllers with very similar performances. The main difference between the AOK analytical controller and the numerical regulators is that the AOK's maneuvers computation is based on a long term prediction of δa highly dependent on the correct estimation of the semi-major axis decay rate da/dt. On the other hand, the linear regulators compute the orbital maneuvers with a pure feedback logic based on the values of the control gains. This fundamental difference between the two control strategies is demonstrated by examining Fig. 5.3. The linear and LQR regulators command groups of equal sized consecutive maneuvers ($\approx 8 \cdot 10^{-4}$ m/s) at non-regular time intervals whereas the AOK control system commands larger maneuvers ($\approx 2.5 \cdot 10^{-3}$ m/s) at a deterministic maneuvers cycle of two days.

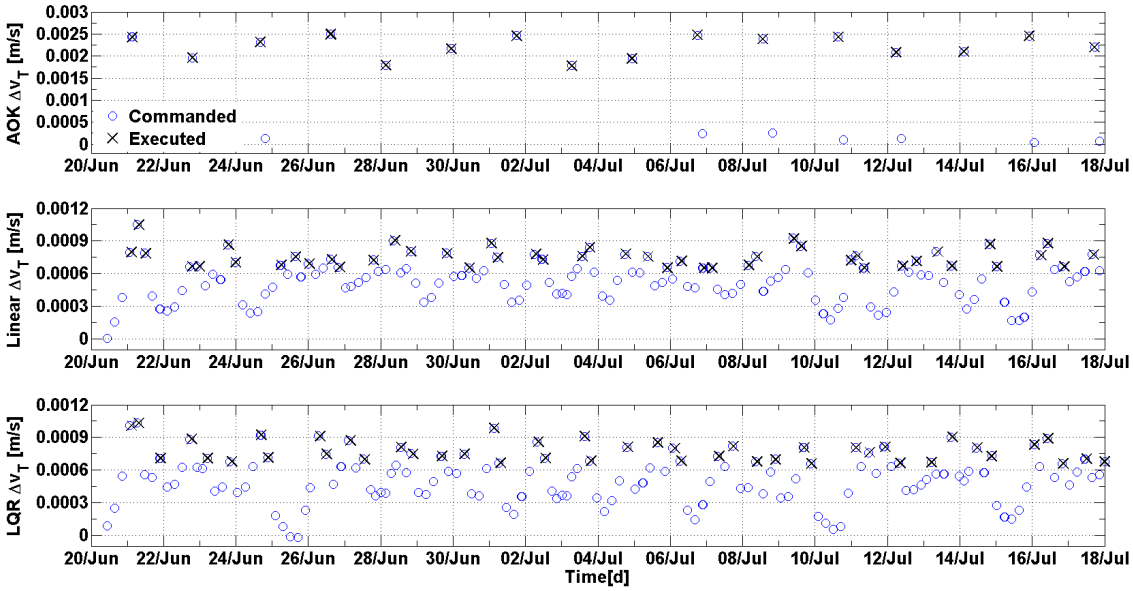

Figure 5.3.: Commanded and executed orbital maneuvers

Table 5.4.: Control performance and maneuver budget with in-plane control

δL_λ [m]	Min	Max	Mean	σ	RMS	Δv_T [m/s]	Min	Max	TOT
AOK	-7.4	9.2	0.18	3.6	3.6	**AOK**	0.0018	0.0025	0.0373
Linear	-0.6	9.9	5.3	1.7	5.6	**Linear**	0.0007	0.0011	0.0379
LQR	-1.2	9.1	4.8	1.8	5.1	**LQR**	0.0007	0.001	0.0374

The AOK algorithm has an optimal control performance, in terms of control accuracy and Δv budget, if it has an accurate knowledge of the semi-major axis decay rate as in the case of this simulation. The constant value of the atmospheric density used for the orbit propagation was in fact given as input to the AOK software to simulate a very accurate on-board estimation of the semi-major axis decay rate.

5.2.2. Realistic Simulation Scenario

These simulations were run using the parameters of Tables 5.1 and 5.2. The regulators have been designed with the same parameters of Table 5.3 with the exception of the imposition of $\delta L_{\lambda_{MAX}} = 15$ m for all the regulators. Figures 5.4 and 5.5 show respectively the ROE and the REFE of the spacecraft. A RO acquisition based on the control of δL_λ (Sec. 1.4) has also

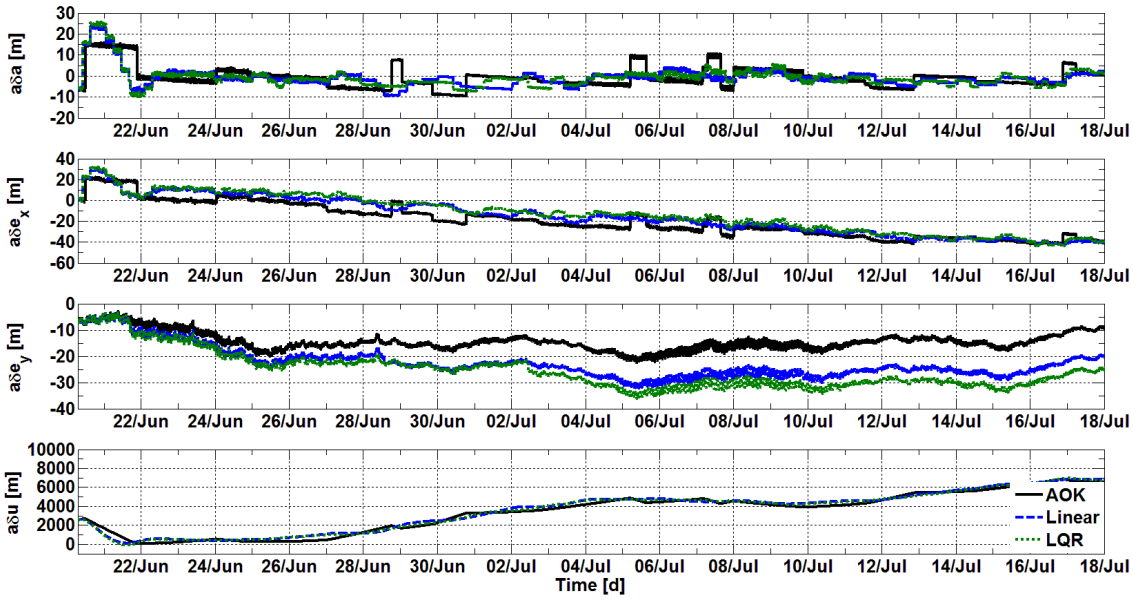

Figure 5.4.: ROE (in-plane control)

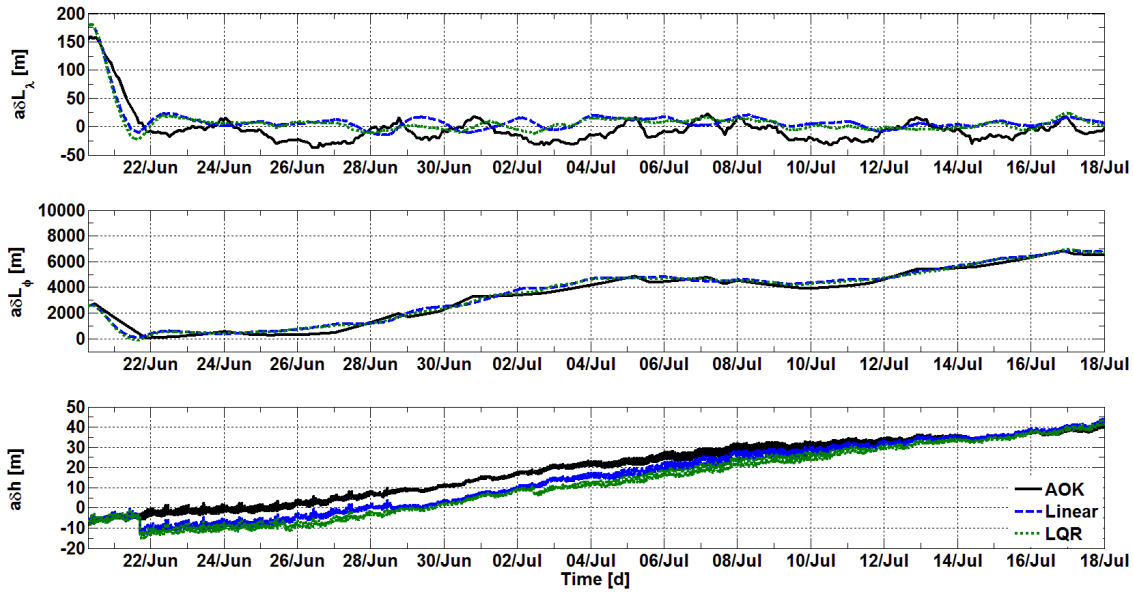

Figure 5.5.: REFE (in-plane control)

been simulated. Table 5.5 collects the control performance and the maneuver budget during the steady state phase following the RO acquisition. The degradation of the control performance with respect to the ideal case (Table 5.4) is mainly caused by the inclusion of the on-board

Table 5.5.: Control performance and maneuver budget with in-plane control

δL_λ [m]	Min	Max	Mean	σ	RMS	Δv_T [m/s]	Min	Max	TOT
AOK	-37.2	23.3	-9.8	13.5	16.7	**AOK**	-0.0078	0.0107	0.0942
Linear	-15.4	24.0	6.5	7.8	10.2	**Linear**	-0.0044	0.0112	0.0946
LQR	-13.3	24.5	3.9	7.5	8.4	**LQR**	-0.0049	0.0114	0.1228

navigation error in the simulation model. The placement of the maneuvers with the rule of Eq. (4.43), not optimized [44] from time to time, is not sufficient for a strict control of the relative eccentricity vector as the solar radiation pressure perturbing force is this time included in the orbit's perturbation forces and the orbit is not at frozen eccentricity. The AOK controller has in this case the additional disadvantage of inaccuracies in the on-board estimation of the atmospheric drag [72,74] and for this reason has a control accuracy performance slightly worse than the linear regulators. The reliance of the AOK analytical controller on a correct on-board estimation of the atmospheric drag can be noticed comparing Figures 5.3 and 5.6. The loss of accuracy in the on-board estimation of da/dt [74] entails the loss of determinism in the maneuver cycle. Table 5.6 offers an overview of the different pole placements in open- and closed-loop.

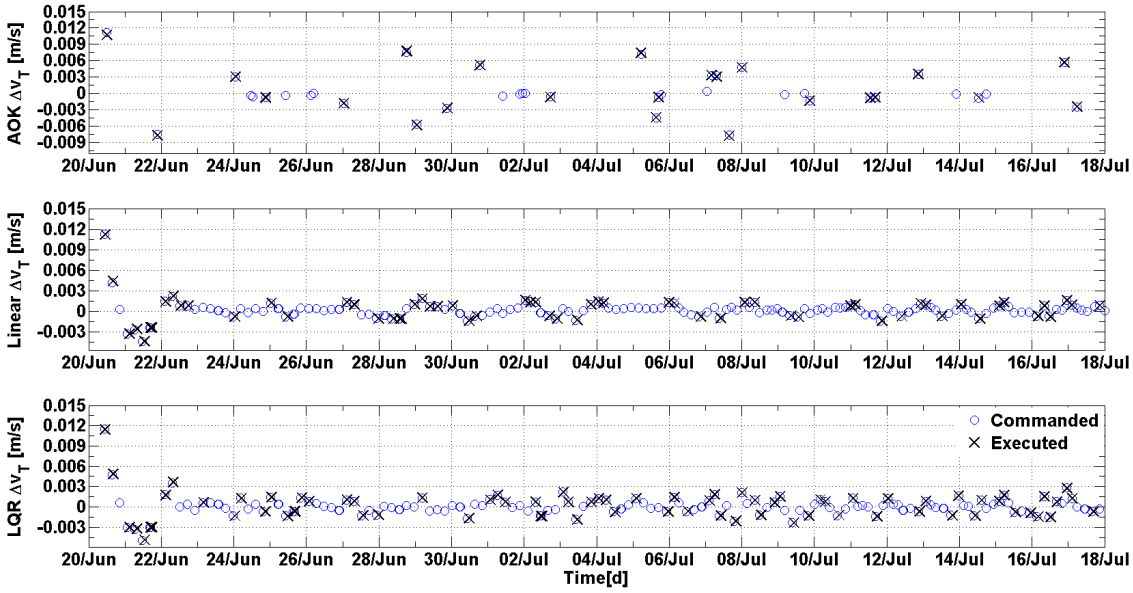

Figure 5.6.: Commanded and executed orbital maneuvers

The LQR is able to find an optimal placement for all the poles while the linear in-plane regulator can instead place two poles only. Nevertheless poles s_5 and s_6 by which depend the control of δL_λ and $d(\delta L_\lambda)/dt$ using along-track velocity increment are placed in a similar way by both methods. Fig. 5.7 shows the mapping of the poles from the continuous to the discrete domain when the Tustin discretization method (Eq. (4.61)) is used. The values of the poles used for the design of the regulators in the continuous domain guarantee the system stability also in the discrete domain. The stability in the discrete domain would not be kept with the use of the Euler discretization method.

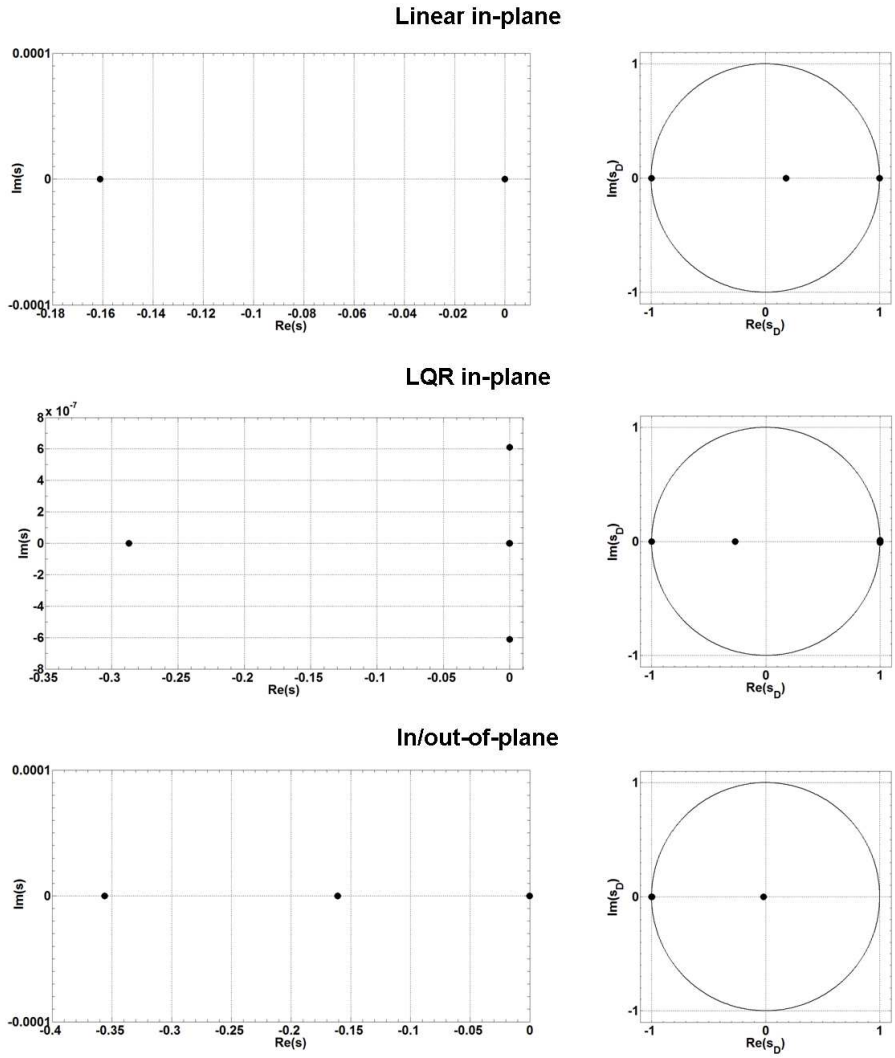

Figure 5.7.: Mapping of continuous to discrete poles with the Tustin discretization method

Table 5.6.: Poles

	Open loop	Linear in-plane	LQR in-plane	In/out-of-plane
$\mathbf{s_1}$	0	-	-8.77·10^{-10}-8.78·10^{-10}j	-
$\mathbf{s_2}$	0	-	-8.77·10^{-10}+8.78·10^{-10}j	-
$\mathbf{s_3}$	-2.38·10^{-12}	-	-3.16·10^{-12} - 6.11·10^{-7}j	-
$\mathbf{s_4}$	-5.71·10^{-7}	0	-3.16·10^{-12} + 6.11·10^{-7}j	-3.56·10^{-1}
$\mathbf{s_5}$	-1.94·10^{-5} + 4.35j	-1.61·10^{-1}	-2.87·10^{-1}	-1.61·10^{-1}
$\mathbf{s_6}$	-1.94·10^{-5} - 4.35j	-7.72·10^{-5}	-1.93·10^{-4}	-1.15·10^{-4}

5.3. In-Plane/Out-of-Plane Orbit Control

Figures 5.8 and 5.9 show respectively the ROE and the REFE of the spacecraft in case of in-plane/out-of-plane orbit control realized with the linear controller of Eq. (4.52) and in a realistic simulation scenario (Table 5.1). The gains were computed imposing the limits $\delta L_{\lambda_{MAX}}$ = 10 m, $(d\delta L_\lambda/dt)_{MAX}$ = 100/86400 m/s and $\delta i_{y_{MAX}}$ = 40 m on the outputs and $\Delta v_{T_{MAX}} = 1 \cdot 10^{-3}$ and $\Delta v_{N_{MAX}} = 1.5 \cdot 10^{-2}$ m/s on the inputs. The value of $\delta i_{y_{MAX}}$ was chosen to keep δL_φ in a control window of 1500 m. The duty cycle imposed for the in-plane maneuver at the ascending node was 4 orbital periods (6 hours) and 8 (12 hours) for the out-of-plane maneuvers placed at $u = \pi/2$. Unlike the case of the previous section, all the three states δa, δi_y and δu are controlled as all the poles are placed on the left of the imaginary axis (Table 5.6). As expected the out-of-plane velocity increments allow the control of δL_φ. The same considerations of the previous section regarding the in-plane control are valid here. In Fig. 5.8 one can also observe that δi_x is not influenced at all by Δv_N as the out-of-plane maneuvers are executed only when $u = \pi/2$ (Eq. (A.5)). Fig. 5.10 shows the orbital maneuvers commanded by the on-board controller and executed by the spacecraft thrusters. A regular maneuver cycle of the in-plane and out-of-plane maneuvers cannot be detected.

Table 5.7 collects the control performance and the maneuver budget. The in-plane control accuracy and cost is very similar to that of the simple linear controller of the previous section (Table 5.5). The out-of-plane Δv spent is 0.51 m/s, rather expensive compared to the in-plane maneuver budget. These simulations results confirm that the in-plane and out-of-plane control

problems can be treated separately in the design of the regulator.

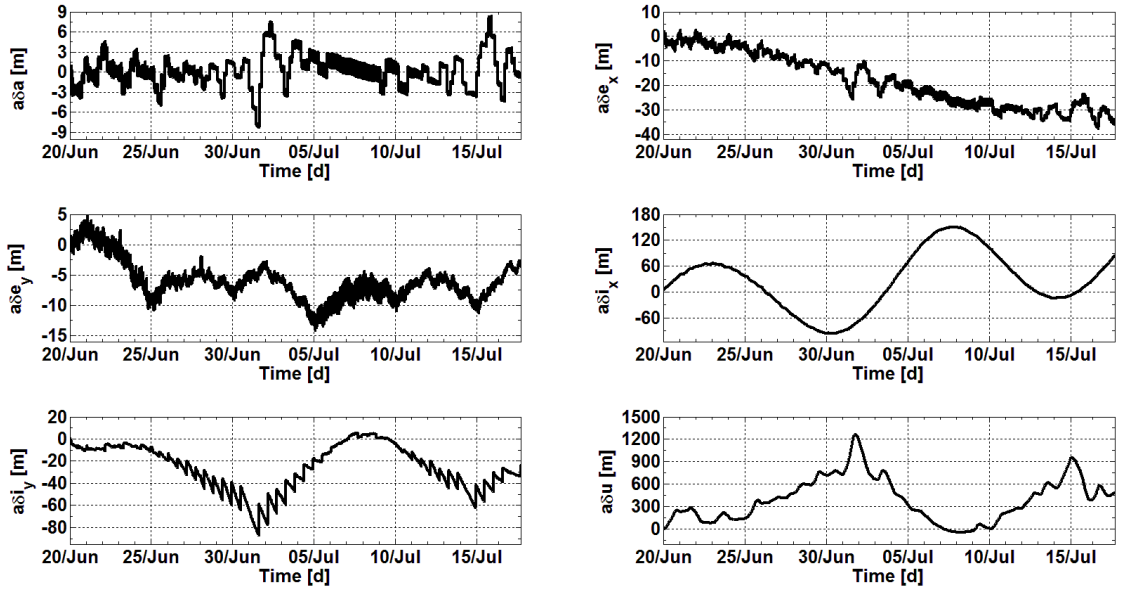

Figure 5.8.: ROE (in-plane and out-of-plane control)

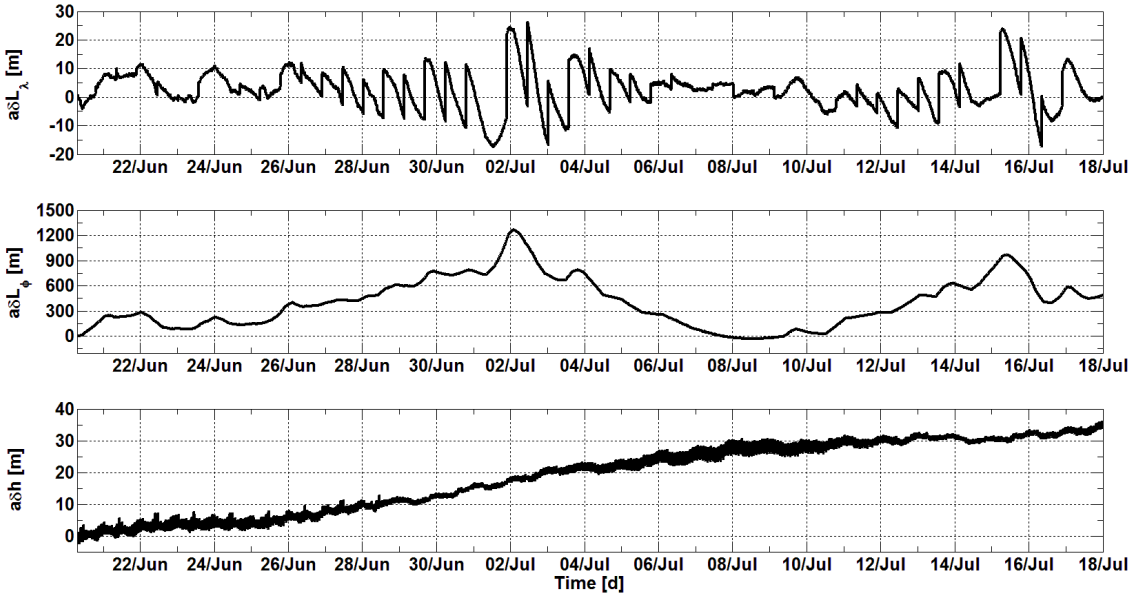

Figure 5.9.: REFE (in-plane and out-of-plane control)

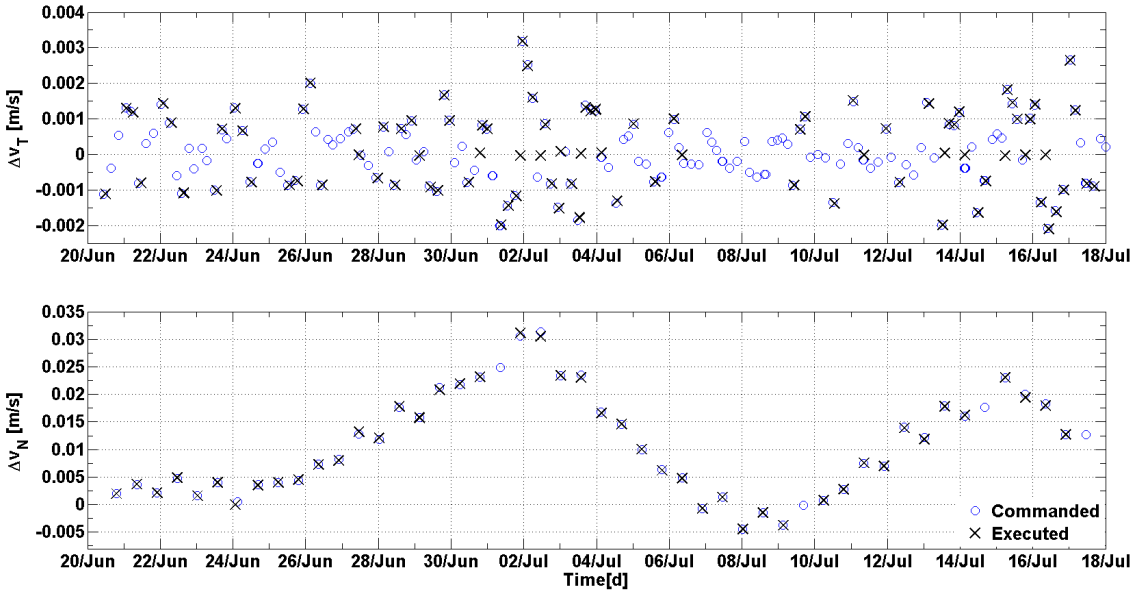

Figure 5.10.: Commanded and executed orbital maneuvers

Table 5.7.: Control performance and maneuver budget with in-plane and out-of-plane control

δL [m]	Min	Max	Mean	σ	RMS	Δv [m/s]	Min	Max	TOT
δL_λ	-17.5	26.3	2.4	6.7	7.1	Δv_T	-0.0021	0.0032	0.094
δL_φ	-153.9	1269.2	403.4	293.1	498.6	Δv_N	-0.0044	0.0312	0.51

5.4. Discussion

The control methods presented in Chapter 4 have been validated and compared by means of numerical simulations. The linear and quadratic regulator have a performance similar to the analytical (AOK) controller. Despite the fact that the linear regulators here considered can place two to three poles only on the left of the imaginary axis, their performance is comparable and in some cases better than the LQR regulator. In a realistic simulation scenario the degradation of the control performance with respect to the ideal case is mainly caused by the on-board navigation error. The AOK controller has in this case the additional disadvantage of inaccuracies in the on-board estimation of the semi-major axis decay and for this reason has a performance slightly worse than the numerical regulators. The main difference between these methods is that the maneuvers' computation by the analytical controller is based on a long term orbit pre-

diction whereas the linear regulators compute the control actions with a pure feedback logic based on the values of the control gains. The accuracy of the orbit model plays therefore a critical role in the implementation of the analytical controller. For the implementation of the numerical feedback regulators, the critical issue is not the prediction accuracy of the model but its reliability in defining the stability conditions of the closed-loop system in the determination of the gains. The PRISMA analytical controller has demonstrated in-flight to be robust, cost-effective and capable of very good control accuracies. With the on-board availability of an accurate orbit model, this type of analytical controller has an optimal control performance in terms of accuracy and costs, and a deterministic maneuvers cycle whose duration depends on the size of the control window. On the other hand, the numerical regulators have a simpler flight software implementation and an enhanced flexibility given by the possibility of varying the type of on-board controller simply by uploading to the spacecraft different gain configurations. The type of control of these feedback systems is in fact entirely determined by the type and value of the gains.

6. On-board Orbit Control System Architecture

The practical implementation of an on-board autonomous orbit control system implies the solution of problems concerned with the software development, validation and testing and its integration in the overall spacecraft flight-software. The development of the control system is driven by a compromise between control performance requirements, on-board computer resources limitation and mission operational constraints. This chapter deals with the development, testing and on-board integration of the absolute autonomous orbit control system on-board the spacecraft MANGO of the PRISMA mission (Sec. 1.4). Though this is a mission specific implementation it stems from a general approach that can be applied in any other mission in LEO. After a general description of the model-based design approach and the system architecture, the attention is focused on the PRISMA/DLR flight software development and testing to which the author of this thesis has given a fundamental contribution. The technological aspects implied by the realization of the autonomous orbit control system tested in-flight with the AOK experiment are explained.

6.1. Software Design

6.1.1. Model-based Design Approach

Model-Based Design (MBD) is a mathematical and visual method for the realization of complex engineering systems and it is also applied in designing embedded software. The MBD approach

[122-129] is considerably different from traditional design methodology. In this method, complicated systems can be created by using mathematical models representing system components and their interactions with their surrounding environment. Rather than using complex structures and extensive software code, blocks with advanced functional characteristics are defined. These blocks, assembled in a complex system model and used with simulation tools, can lead to rapid prototyping, software testing, and verification. This approach raises the abstraction level for the development in order to allow an efficient handling of ever more complex systems. Engineers can continuously test the design as it evolves, checking it against requirements and finding mistakes earlier in development when they are easier and less costly to correct. In addition, model-based design automates code generation for the embedded system by eliminating the need to hand-code the guidance, navigation and control algorithms. By introduction of advanced, automated code-generation technology these models can also be used as the input to an automatic code generation tool for embedded systems. Hardware-in-the-loop simulations are also enhanced by this approach and the testing of dynamic effects on the system can be done more quickly and efficiently than with traditional design methodology.

The MBD process consists of four main steps. The first phase involves the definition and design of the objective system and the identification of system components. The next step is the implementation part in which the system components are mathematically modelled and a suitable software code in a selected language is generated to implement the system. For embedded systems, the preferred programming language is C/C++. After the code development, the next step is validation and testing by means of simulations. If the tests show that there are mistakes in the system design, then system designer should revise his design and pass it to code developers to implement the revised system. Finally when the implemented system has been validated and extensively tested the production of embedded code generation can start.

A model-based design method is used for the complete on-board application software of the PRISMA mission. To this end, the on-board software is implemented in *MATLAB/Simulink* blocks which are then auto-coded with *Real Time Workshop* and executed under the operating system Real-Time Executive for Multiprocessor Systems (RTEMS) on the on-board LEON3 processor [129,135].

6.1.2. Design Strategy

The PRISMA on-board software main development and simulation environment was realized with *MATLAB/Simulink* by Mathworks. All high-level application software is implemented as Simulink models. Furthermore, the data acquisition and handling, the telemetry and telecommand interface as well as the application tasks scheduling is incorporated within Simulink models. Basic software, consisting of device drivers, interrupt handler etc. and other platform dependent software is programmed in handwritten C/C++ [123,128]. For the basic software, the Gaisler Research RTEMS Cross Compiling System [126] is used for development and debugging. All the hardware interfaces work via the basic software. The Application Software is as far as possible platform independent, i.e. easily ported to another hardware platform and/or using another real time operating system (RTOS). Criteria as functionality, code efficiency, predictability, verifiability and simplicity have been employed in the development strategy for the on-board software system architecture. The simplicity criterion has received special attention in the development of the PRISMA on-board software architecture.

6.1.3. System Architecture

The on-board software (OBS) architecture is structured in two main layers consisting in a Basic Software (BSW) level and an Application Software (ASW) level communicating with each other through dedicated message queues. The BSW includes basic system applications, device drivers and I/O-utilities. The ASW includes all the top-level applications like spacecraft control and telecommand (TC) and telemetry (TM). The ASW consists of a number of application components each one encapsulating a logically-grouped functionality. Each application component, with its uniform internal structure and interface, is executed via an Asynchronous Monotonic Scheduler (AMS) with a specified sample time and priority. The external data stores provide access to the Remote Terminal Unit (RTU) components. The internal data store is used for communication between the application components. Fig. 6.1 shows the internal structure of an application core. The input section includes the processing of incoming TCs, the external data e.g. from sensors, and internal data from other application components. The application core

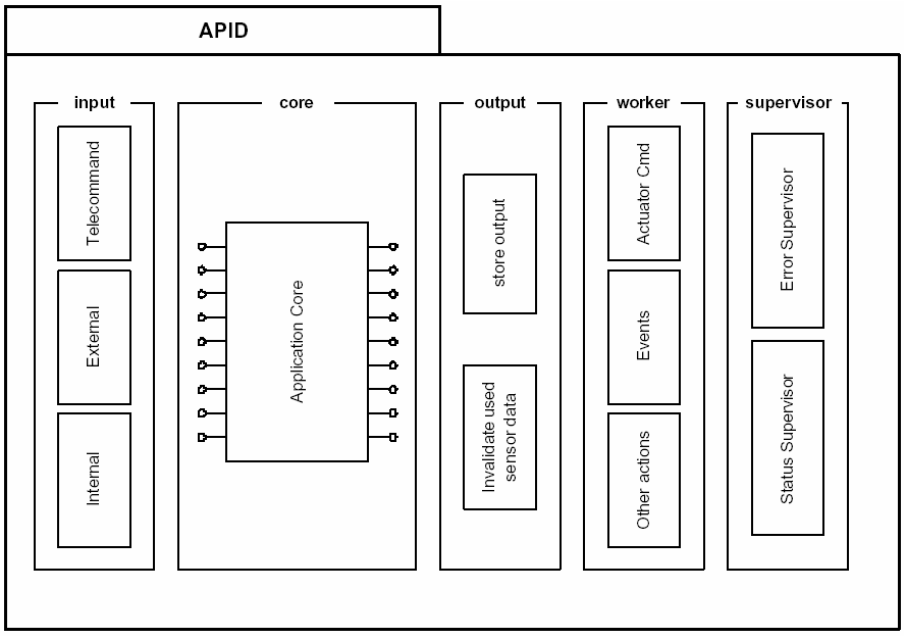

Figure 6.1.: Internal structure of an application component [128]

contains most of the components' algorithms. The output section stores the external output vector and holds a component which invalidates already exploited sensor data. The worker sends actuator commands, housekeeping data and provides other application core's services. Finally, the supervisor implements the failure detection isolation and recovery (FDIR) functions.

6.1.4. Guidance, Navigation and Control Application Cores

An application core is implemented as an input/output function. The function retrieves the input vector, executes its algorithms and delivers an output vector. Each application core runs with a basic sample time. The execution time of each algorithm in the application core has to be smaller than the basic sample time. For this reason the algorithms with a considerable computational demand cannot be executed in application cores with small sample times. Most of the guidance, navigation and control (GNC) algorithms being dedicated to sensor data processing and filtering, have limited computational requirements and can therefore be grouped into a GNC application component which runs at a rate of 1 Hz. The navigation task of absolute and relative on-board orbit determination based on GPS data is instead computationally very

Table 6.1.: Application components for GNC software

Component	Sample time [s]	Features
BSW	1	Direct interface with the GPS hardware
ORB	30	Absolute and relative on-board orbit determination
GNC	1	Majority of GNC algorithms

demanding and may thus not be integrated into the GNC application component. The ORB application component which runs with a sample time of 30 s (1/30 Hz) has been therefore defined. The ORB allows a proper separation of computational intensive GNC algorithms from less demanding ones. The software functions which interface directly the GPS hardware are located in the BSW application component which runs at a rate of 1 Hz. The software architecture for navigation, guidance and control must thus take into account the specific application components for PRISMA and associate functional tasks with the appropriate application components. Table 6.1 resumes the main features of the application components of the GPS-based flight software.

6.2. Guidance, Navigation and Control Software Architecture

6.2.1. Top-level Architectural Design

Fig. 6.2 shows the top-level architectural design of the DLR's GPS-based flight software on the MANGO and TANGO spacecraft [94,143]. The application cores BSW, ORB and GNC are implemented as tasks with different priority with sample times respectively of 1, 30 and 1 s. The software is structured into the subsystems GPS interface (GIF), GPS-based Orbit Determination (GOD), Autonomous Orbit Keeping (AOK), GPS-based Orbit Prediction (GOP) and Autonomous Formation Control (AFC), according to their functional objectives. The depicted architectural design emphasizes the flow of information which is directed from bottom to top. The sensors and actuators involved in the GPS-based GNC functionalities are represented in Fig. 6.2 by the boxes GPS, SCA (star camera), ACC (accelerometer), MM (magnetometer),

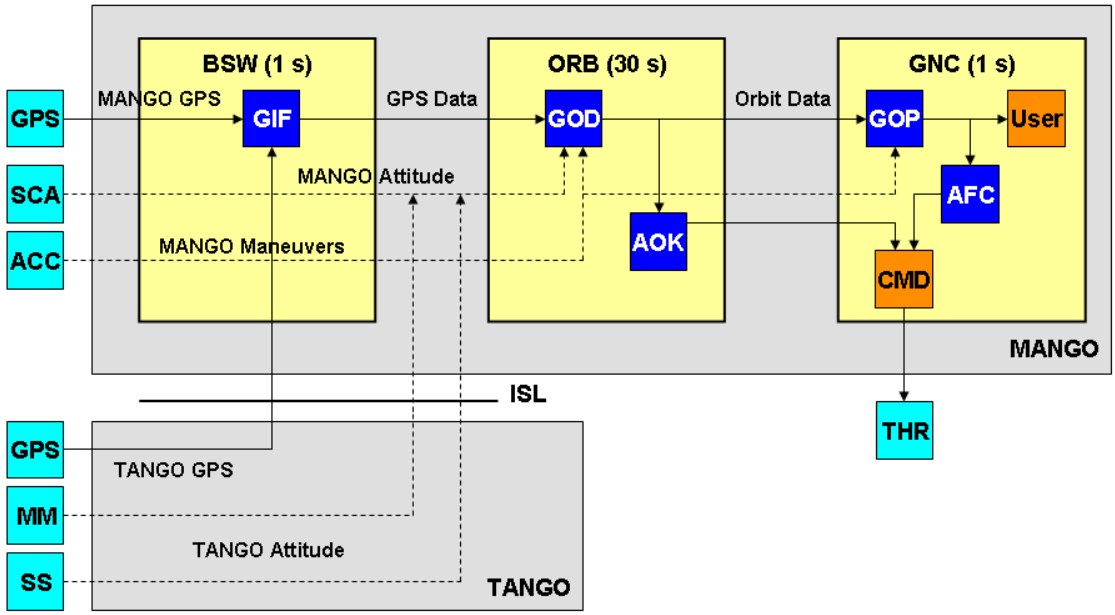

Figure 6.2.: Simplified scheme of the software architecture

SS (sun sensor) and THR (thrusters). Solid lines indicate data variables which are directly exchanged between application cores, while dashed lines represent variables which are conditioned and filtered by auxiliary on-board software modules (not indicated).

GIF is located within the BSW application core and receives the messages from the operational Phoenix-S receivers [105] on MANGO and TANGO. GIF performs message validation, editing, and extraction and stores the extracted raw GPS data for access by the orbit determination function. GIF provides to the OBS the GPS time for on-board time synchronization and writes GPS data and internal status parameters to a data buffer for further download as housekeeping data. GPS raw measurements are read as internal data by GOD which is part of the ORB application core. GOD implements an extended Kalman filter to process GRAPHIC observables as well as single difference carrier phase measurements from MANGO and TANGO. Attitude data from both spacecraft are applied to correct for the GPS receivers antenna offset with respect to the spacecraft center of mass. Furthermore, a history of maneuver data is provided to GOD and taken into account in the orbit determination task. GOD performs a numerical orbit propagation which is invoked after the measurement update and provides orbit coefficients

for interpolation to GOP for both spacecraft. As a result, GOD outputs MANGO and TANGO orbit parameters which are also stored internally. These parameters are then accessed by GOD in the next execution step to compute position/velocity at the successive measurement times and by the orbit prediction function located in the GNC core. The GOP subsystem retrieves the on-board time, or Spacecraft Elapsed Time (SCET), and the orbit coefficients which have been generated by GOD. These parameters are used to compute 1 Hz updates of the MANGO and TANGO spacecraft position and velocity at the SCET. In the case that orbit maneuvers have been executed in the past interval, GOP generates a new set of orbit coefficients which is used internally until a new set is provided by GOD. Auxiliary information provided by GOD is applied by GOP to derive accuracy related information on the MANGO and TANGO states. Due to the different data rates of the GPS-based navigation modules, orbit maneuvers data have to be taken into account in both GOD and GOP. In particular at each GNC core step, the GOP task accounts for maneuvers which have not been considered by GOD in the last orbit determination/prediction process.

Among the users of the GPS-based navigation data the AFC and AOK modules are located in the GNC and ORB cores respectively. AOK is dedicated to the precise autonomous absolute control of MANGO's orbit whereas AFC controls the two spacecraft relative motion. The required velocity increments computed by these two modules, which are activated only when the spacecraft is put in AOK or AFC mode [89], are provided to the on-board flight software for the execution.

6.2.2. Subsystems Implementation

Fig. 6.3 shows the BSW, ORB and GNC application cores as they are implemented in MATLAB/Simulink. At the lowest level, the subsystems GIF, GOD, GOP, AOK and AFC, which form the inner structure of the cores as depicted in Fig. 6.2, consist of S-functions providing a C/C++ interface to the application software [127]. These S-functions are hand-coded in C/C++ and are based on the libraries of Montenbruck and Gill [4]. In particular, C++ low level routines, which are interfaced with MATLAB/Simulink high level structures, represents the computational layer of the software system including for example numerical integrations,

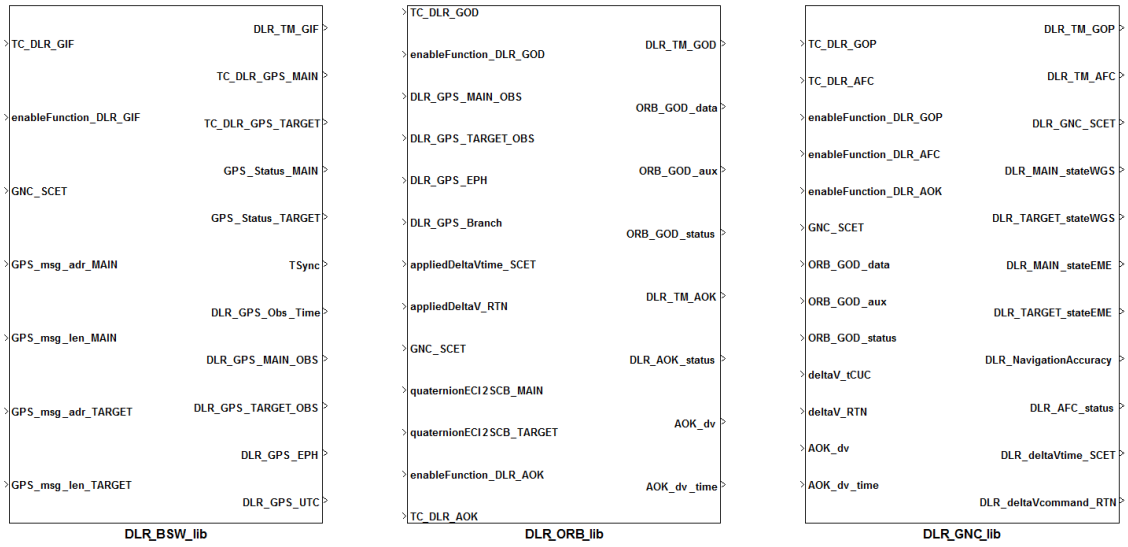

Figure 6.3.: Simulink subsystems implementing the BSW, ORB and GNC application cores

data filtering, etc. MATLAB/Simulink provides instead the communication layer, including input/output interfaces, complex logics, time synchronization. The prototyping of the software as well as the related analysis and simulations are performed first on a host standard laptop PC in a MATLAB/Simulink environment. All the functions can then be auto-coded using the MATLAB tool Real Time Workshop and executed under the operating system RTEMS on the target LEON3 processor. The full consistency of the flight software generation chain can thus been verified by comparing relevant outputs generated by the software running on the host and target computer.

6.3. Autonomous Orbit Keeping Software Module

6.3.1. Top-level Architectural Design

Fig. 6.4 shows the inner structure of the ORB core which includes the software module GOD and AOK. The AOK module is dedicated to the autonomous orbit control of spacecraft MANGO and implement the analytical algorithm presented in Sec. 4.1. When the spacecraft MANGO is put in AOK mode (Chapter 7), the GOD is put in solo navigation mode and only the GPS

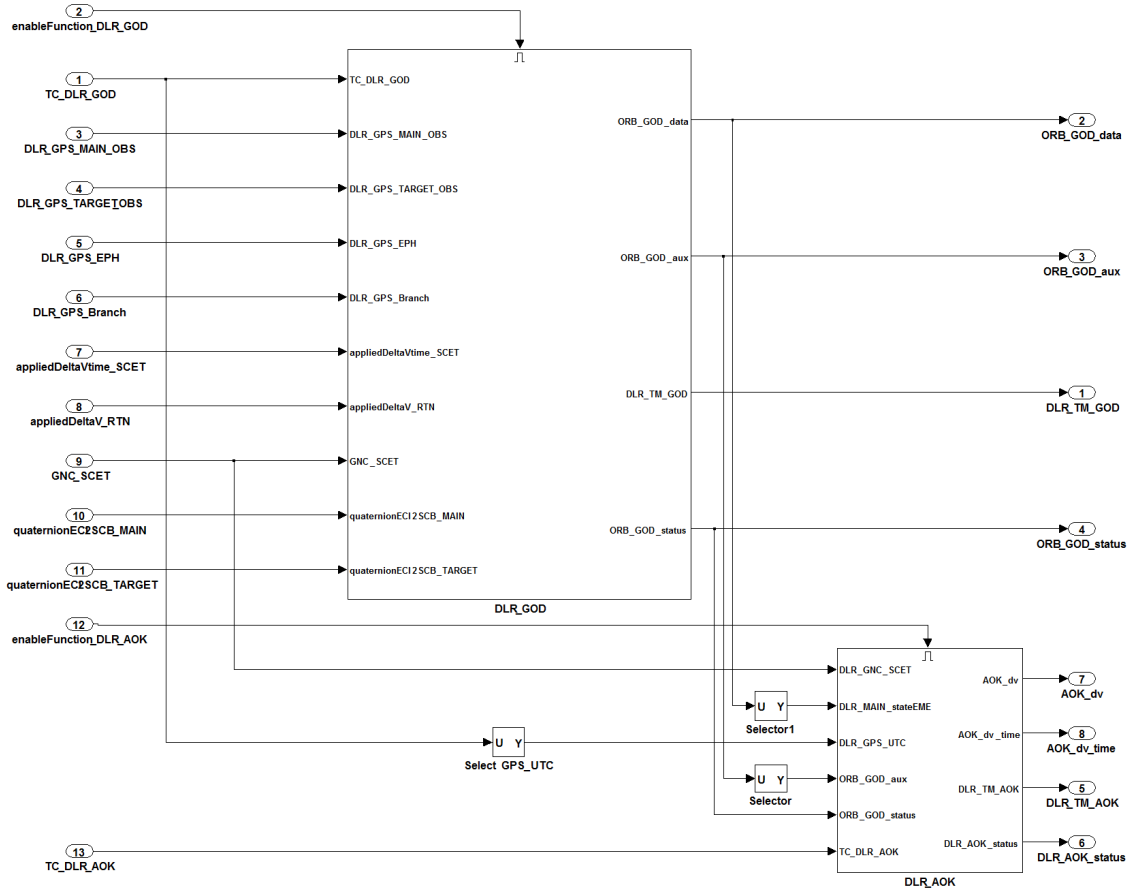

Figure 6.4.: Inner structure of the ORB application core

data of MANGO are considered by the on-board orbit estimation process. AOK receives the navigation data from GOD and at each ascending node pass computes the actual value of the LAN and compares it with the reference value. If the difference between the real and reference LAN has exceeded the imposed limit, an along-track maneuver is commanded. The inputs and outputs of AOK are listed in Tables 6.2 and 6.3. The AOK's inputs consist of navigation data and TCs. The TCs include parameters for the controller configuration and a 3.2 days segment of the RO to be stored on-board the spacecraft. The outputs include the time and value of the eventual commanded orbital maneuver, the telemetry parameters for the monitoring of the AOK module and an error diagnostics status byte. AOK, as every DLR's flight software module, outputs a status bytes indicating anomalies detected during the execution of the software instructions. This functionality provides also input to specific Fault Detection Isolation and

Table 6.2.: AOK software module input

Input variable	Type(size)	Description
enableFunction_DLR_AOK	boolean(1)	Flag for AOK activation
DLR_GNC_SCET	uint32(2)	GPS integer and fractional seconds since initial epoch GPS
DLR_MAIN_stateEME	double(8)	MANGO position and velocity in ECI frame
DLR_GPS_UTC	double(1)	Leap seconds
ORB_GOD_aux	double(11)	MANGO's ballistic coefficient and estimated position components vector standard deviation
ORB_GOD_status	uint8(1)	GOD status byte
TC_DLR_AOK	double(121)	AOK telecommands

Recovery (FDIR) algorithms implemented into the on-board software. The objective of this measure is to improve robustness and continuity of the system operations, independent from ground contacts. Table 6.4 shows the structure of the AOK status byte. If AOK is put in *idle* mode, the execution of the software breaks and the code is run normally at the next call. If a *reset* occurs, the execution of the software breaks, the value of some internal variables is put to zero and the code is run at the next call. If the input navigation data are not valid AOK is put in *idle* mode (bits 0 and 1). If one of the check on the inputs results negative, AOK is automatically put in *reset* or *idle* mode (bits 2 and 5) and recovered once the value of the inputs results valid. Illegal operations (e.g. divisions by zero or square roots of negative numbers) detected by means of checks on the variables included in a computation, can also trigger the *reset* or *idle* states. Bit 3 is set when an orbital maneuver has been issued successfully whereas bit 4 is set if the maneuver size is larger than a predefined threshold. Bit 6 indicates that the RO uploaded from ground has been correctly stored on-board. Bit 7 indicates that the RO stored on-board

Table 6.3.: AOK software module output

Output variable	Type(size)	Description
AOK_dv	double(3)	Size of commanded orbital maneuvers in RTN frame
AOK_dv_time	uint32(2)	Time of commanded maneuvers (start of thrust pulse)
DLR_TM_AOK	double(36)	AOK telemetry parameters
DLR_AOK_status	uint8(1)	AOK status byte

Table 6.4.: Structure of AOK status byte

Position in byte	Value [hex]	Description	AOK FDIR
0	0x01	Max. navigation error exceeded	Put AOK in *idle* mode
1	0x02	Invalid navigation input	Put AOK in *idle* mode
2	0x04	AOK *reset*	-
3	0x05	Maneuver successfully issued	-
4	0x10	Maneuver size is too large	Reset AOK
5	0x20	AOK in *idle* mode	-
6	0x40	RO uploaded and stored on-board	-
7	0x80	Stored RO is expired	Switch to on-board RO or AOK in *idle* mode

is expired. In this case AOK is put in *idle* mode until a new RO segment is uploaded to the spacecraft or the on-board RO generation is switched-on if this option is active.

6.3.2. Basic Logic of the AOK Controller

Top-level Logic

The flowchart of Fig. 6.5 shows the top level logic of the AOK module of the MANGO spacecraft. AOK, which runs with a sample time of 30 s, receives current navigation data directly from the GOD module. The orbit controller is activated only once per orbit at the ascending node. A fundamental process run at each AOK call is the RO management. As depicted in Fig. 6.6 this process is dedicated to extract the RO data required by the controller at the next AN pass and check their validity. The RO can be generated on-board or on-ground and then uploaded to the spacecraft. In case of on-ground generation, it is stored on-board in a buffer which contains 50 reference longitude and semi-major axis values at the ascending node and their GPS times, corresponding to a RO segment of 3.2 days. Once a new RO segment is uploaded the buffer's index is locked in the position corresponding to the next AN. In case the RO stored on-board is expired and not replaced the AOK module can go in *idle* mode or switch to on-board RO generation if this option has been activated by means of a dedicated TC. The RO is propagated on-board using a GRACE GGM01S 20x20 gravitational field model and an initial state given by the on-board navigation

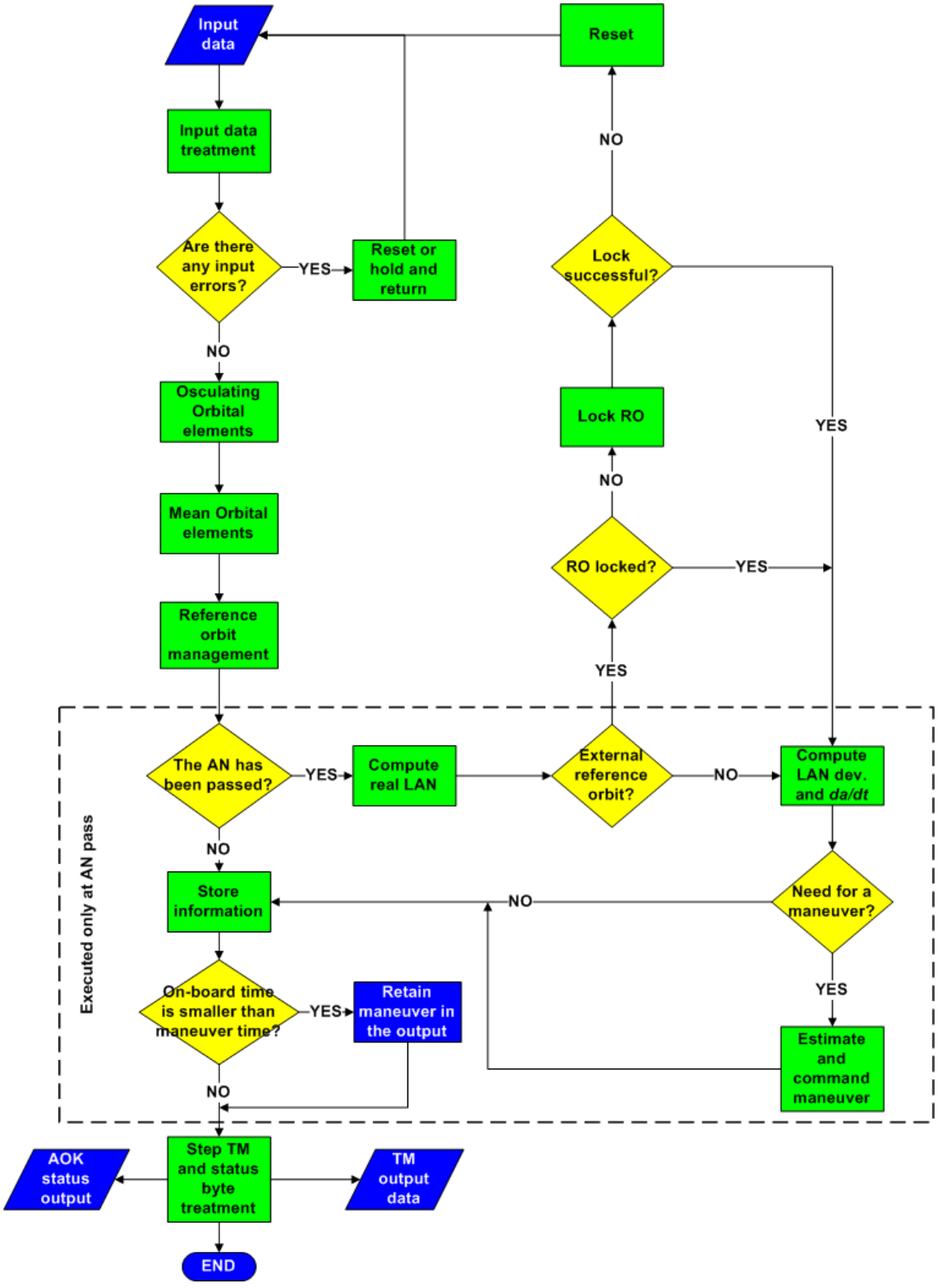

Figure 6.5.: Simplified scheme of the software architecture

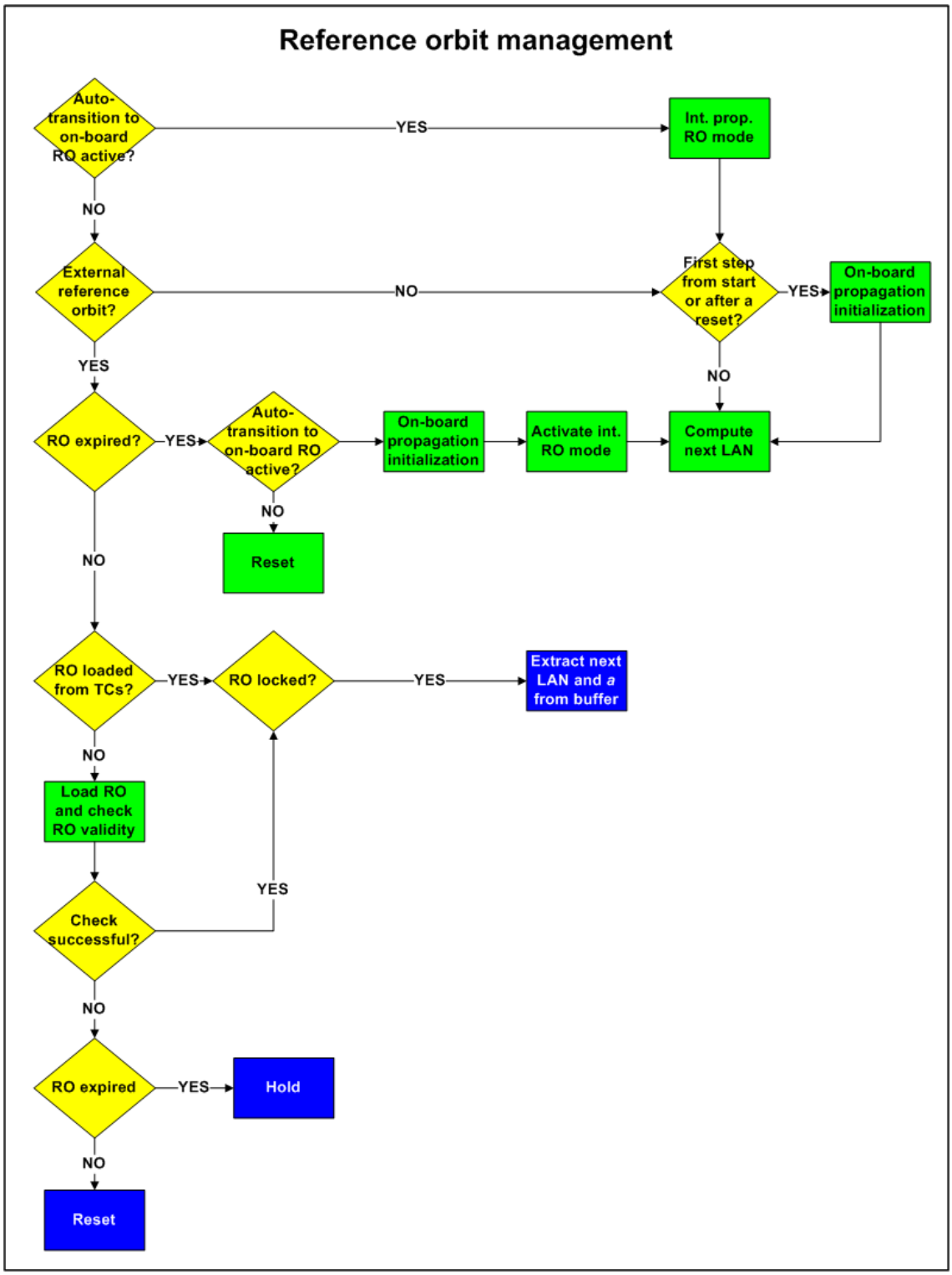

Figure 6.6.: Simplified scheme of the software architecture

Maneuvers computation

Table 6.5 collects the conditions by which a maneuver is computed and commanded by AOK and how the maneuver's Δv is computed for each condition. ΔL_{AN} is the LAN deviation, ΔL_{min} and ΔL_{MAX} are respectively the lower and upper limits of the control window, T_m is the time elapsed from the last executed maneuver, t_{smooth} and τ have the same meaning as in the previous section, T_{d-} and T_{d+} are the duty cycles imposed respectively for anti-along-track and along-track maneuvers. The need for a maneuver and its computation and execution is performed only at the ascending node. For the rest of the orbit the AOK controller performs routine state and telecommands validity checks, RO management operations if required and evaluates the satellite's position with respect to the ascending node. In cases I, III and IV of Table 6.5 the maneuver Δv is the sum of the maneuver required to bring the present Δa to null and that to obtain the Δa_c computed as in Table 6.5. In case II the value of Δa is simply brought to zero. In all cases Δv is computed by Eq. (4.5). For nominal system and environmental conditions, conditions I and II occur during the steady-state control phase. Condition I (II) implies that the absolute value of the LAN deviation exceeds the upper (lower) limit of the control window, its absolute value is increasing with time and a time greater than the imposed duty cycle is elapsed from the last executed maneuver. In case I Eq. (4.9) is used for the computation of ΔL_c as the *smooth* maneuver is the cheapest one. In case II the cheapest maneuver is bringing the value of Δa to a null value in order to invert the sign of $d\Delta L/dt$ (see Fig. 4.2). Condition III (IV) implies that the absolute value of the LAN deviation exceeds the upper (lower) limit of the control window, the LAN deviation value tends by free motion to return within the control window but too slowly as $t_{smooth} > \tau$ and an acquisition maneuver is allowed if a time greater than the imposed duty cycle is elapsed from the last executed maneuver. Condition $T_m > \tau$ imposes that

Table 6.5.: AOK maneuvers computation

Condition	$\mathbf{\Delta a_c}$	$\mathbf{\Delta L_c}$
I. $\Delta L_{AN} \geq \Delta L_{MAX}$ & $d\Delta L_{AN}/dt > 0$ & $T_m > T_{d+}$	Eq. (4.2)	Eq. (4.9)
II. $\Delta L_{AN} \leq \Delta L_{min}$ & $d\Delta L_{AN}/dt < 0$ & $T_m > T_{d-}$	Δa	-
III. $\Delta L_{AN} \geq \Delta L_{MAX}$ & $d\Delta L_{AN}/dt < 0$ & $t_{smooth} > \tau$ & $T_m > \tau$ & $T_m > T_{d+}$	Eq. (4.2)	Eq. (4.11)
IV. $\Delta L_{AN} \leq \Delta L_{min}$ & $d\Delta L_{AN}/dt > 0$ & $t_{smooth} > \tau$ & $T_m > \tau$ & $T_m > T_{d-}$	Eq. (4.2)	Eq. (4.14)

a new acquisition maneuver can be issued only after a time τ is elapsed from the last executed maneuver. The accuracy of the maneuvers' computation is dependent on the correct estimation of da/dt as can be noted considering Eqs. (4.2), (4.11) and (4.14). The semi-major axis decay rate da/dt is estimated on-board by the AOK controller using the procedure described in Sec. 4.1.4.

6.4. Software Development and Testing Environment

The GPS-based flight software described in the previous sections was tested extensively as a standalone unit prior to its full integration into the spacecraft on-board computer. Thank to the model based design of the PRISMA on-board software, the tests can be executed on different platforms in a fully consistent manner. This testing approach allows a seamless transition between offline simulations performed on a laptop PC and real-time hardware-in-loop tests comprising real Phoenix GPS receivers [105] (the GPS receivers on-board the PRISMA satellites) and a 2x12 channels Spirent GSS7700 GPS signal simulator [108]. Furthermore the complete application is ported to a RTEMS environment in a LEON-3 board, representative of the PRISMA on-board computer. Figures 6.7 (a and c) give a schematic view of the flight software development and testing environment at DLR whereas Figures 6.7 (b and d) show the integration and testing environment at SSC [131].

In a first phase, the flight software, wrapped through dedicated Simulink S-functions, is executed on a standard laptop PC (Fig. 6.7.a) and stimulated by different sources of raw GPS data. The simplest simulations make use of emulated GPS measurements generated by the Phoenix EMulator (PEM), a software which simulates GPS data. PEM allows a realistic modelling of measurements issued by a GPS receiver in LEO. More specifically, PEM emulates the output messages for raw measurements, navigation solutions and broadcast ephemerides generated by the Phoenix GPS receiver. As a next step raw single frequency GPS data (from JPL's BlackJack receivers) collected during the swap phase [155] of the GRACE satellites (on 9-10 December, 2005) are used. During this period, both the GRACE satellites were flying in close formation (baseline <10 km, minimum separation around 400 m) on two slightly different orbits. Before

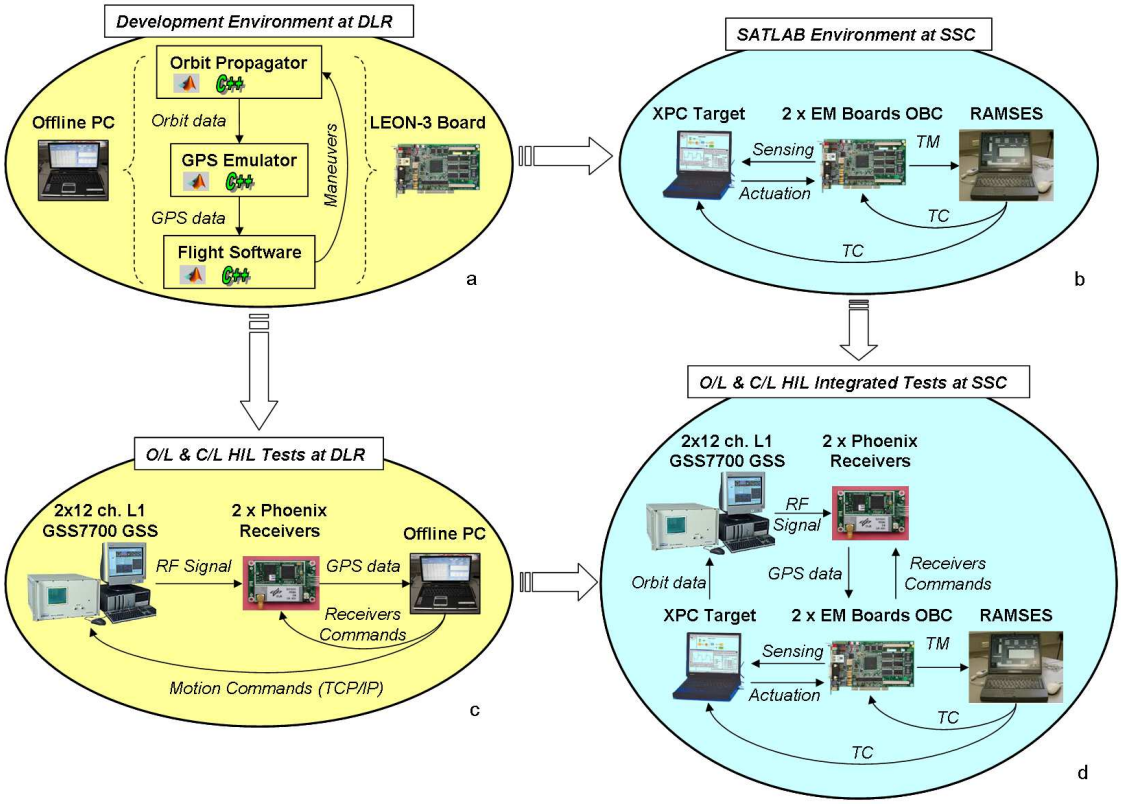

Figure 6.7.: Software development and validation at DLR (a, c) and SSC (b, d) [131]

the launch of the PRISMA satellites, this constituted the only available set of real GPS data for satellites flying in close formation.

In a second phase the flight software is validated in real-time through the inclusion of hardware in the loop. The offline software blocks in charge of numerical orbit propagation and Phoenix receiver emulation (Fig. 6.7.a) are replaced by a 2x12 channels Spirent GSS7700 GPS signal simulator and two Phoenix GPS receivers (Fig. 6.7.c) fully representative of PRISMA's flight units. The flight software is still integrated in a pure MATLAB/Simulink environment with the introduction of dedicated S-functions for data reading/writing from/to serial ports of the host PC. The preliminary evaluation of the memory usage and computational load of the DLR's flight software is performed on a LEON-3 microprocessor FPGA board which is representative of the MANGO spacecraft on-board computer. The OBC is based on a SPARC V8 processor, clocked at 24 Mhz, and is complemented by a GRFPU Floating Point Unit. All RAM blocks

(cache and register-file memory) are Single Event Upset (SEU) protected. MATLAB/Real-Time-Workshop is used to automatically generate C-code out of the MATLAB/Simulink tests previously executed on the host PC. The generated code is compiled and linked with the hand-written C++ flight software libraries (i.e., the S-function wrappers) using the RTEMS cross-compilation system (RCC).

The SCC/SATLAB (Fig. 6.7.b) is a real-time system which includes the two flight on-board computers, a Target PC and the Rocket And Multi Satellite EGSE (Electrical Ground Support Equipment) System (RAMSES). Except for the OBCs, all the hardware units are simulated by the real time Satellite simulator (SATSIM) [130]. The simulation input is the control commands received from the on-board software and the output is data from the simulated units, described by sensor, actuator, power and thermal models. Both the spacecraft and the simulator are commanded from the RAMSES software with help of procedure scripts thereby making it possible to automate the tests. Since the timing is handled by the scripts the tests can be re-run, making the timing of the tests deterministic. There is a significant advantage in using the same control environment during both test and operations: the flight procedures currently used by the operational team are the same developed and used during the test and validation of the two spacecraft. With this configuration there is also the possibility to test and attend to timing issues of the space segment on ground before it is used to command the real spacecraft pair in orbit. The test environments of Figures 6.7.b and 6.7.c were integrated to form the test platform shown in Fig. 6.7.d.

Finally, the spacecraft system level test campaign consists of a series of tests performed on the Flight Model (FM) spacecraft and on a bench test environment involving Engineering Model (EM) and FM hardware. The tests are aimed towards verifying the system level requirements. For the GNC subsystem, the tests have two main groups: open and closed-loop tests. The open loop tests must verify the sign of all different sensor-to-actuator loops. This is done by stimulating the sensors and looking at the software's response and the behavior of the actual actuators. The closed loop tests consist of a subset of the scenarios performed in SATLAB. The difference between this environment and SATLAB is that this environment uses the real interface electronics between sensors/actuators.

6.4.1. Software Tests

One of the greatest advantages of the software design and development approach described in the previous sections is that it allows the test of the flight software performance directly on the on-board spacecraft computer [132]. Different tests typologies were executed at DLR for the validation of the PRISMA's flight software.

1. Long-term runs reproducing, on the LEON3 board in a RTEMS environment, the functional tests performed on the host PC. Each MATLAB/Simulink model is used to automatically generate C-code via RTW. The C-code is then compiled and linked with the handwritten C++ code (S-function wrappers) using the RTEMS cross-compilation system.
2. Dynamic memory allocation tests to determine the usage of the heap. The dynamic memory allocation of each software module (GIF, GOD, GOP, AFC and AOK) is monitored to determine if memory leaks exist in the heap region of the LEON3 board RAM.
3. Max-path unit tests to determine the maximum CPU load of each software module. Each software module is stimulated with specific constant inputs that provides the maximum computational effort on the LEON3 board.

The analysis of the software execution times [135] has special interest because it allows to verify if the different software modules comply with the maximal allocated CPU loads. Analysis of heap and stack allocation and software profiling can also be made for the detection of eventual software execution bottlenecks. Table 6.6 resumes the main features of the LEON3 board and host PC used for the tests performed with the DLR's facility depicted in Fig. 6.7.a and the tools which were required to execute the software tests at DLR.

6.4.2. Heap and Stack Tests

The goal of the analysis of the heap memory status before and after each call of the software modules is retrieving the allocated and not released heap size and the number of allocation calls without release. The RTEMS function *malloc_info(index)*, which is a modified version of the function *malloc_dump(void)*, is used to obtain information about the heap usage during run-

Table 6.6.: LEON3 board and host laptop PC features

LEON3 microprocessor	
Component	**Description**
Board model	LEON FPGA GR-PCI-XC2V
CPU	LEON3FT SPARC V8 Processor (ver 0x0), 24 MHz, win8, hwbp 4, itrace 128, lddel 1
FPU	GRFPU-lite, icache 1x8 kbyte, 32 byte/line, dcache 1x4 kbyte, 16 byte/line
Memory Controller	FT memory controller (ver 0x1), 32-bit prom, 32-bit sdram: 1x64 Mbyte, col 9, cas 2, ref 7.7 us
Operating system	RTEMS version 4.6.5
Host Laptop PC	
Component	**Description**
CPU	2x x86 Family 6 Model 15 Stepping 6 GenuineIntel 1994 Mhz
Memory Controller	Intel(R) 82801G (ICH7 Family) USB2 Enhanced Host Controller - 27CC
Operating system	Microsoft Windows XP Professional
Host PC's tools required for the tests	
Tool	**Description**
MATLAB/Simulink	MATLAB, Simulink, RTW, RTW Embedded Coder
Debug monitor	GRMON Professional
C/C++ compiler (host)	Microsoft Visual C++ .NET
C/C++ compiler (target)	gcc
Standard C++ library	libstdc++.a
Linux emulator	Cygwin

time for each software module. As shown in Fig. 6.8, in order to verify the effectiveness and reliability of this test, it has been applied to a software module that was known to cause memory leakage problems due to an improper management of the dynamic memory (i.e. *new* operator used without *delete*). The information given by the test has been used to forecast the stuck of the software run due to memory saturation. The rightness of this forecast has demonstrated the validity of the test. Fig. 6.9 shows the results of a test run over 9 hours. The GIF, GOD, GOP and AFC (in guidance mode) software modules do not cause memory leakage by allocating and de-allocating memory in a proper way. It was also verified that GOD is the only software module which makes some allocations of the Heap without release. The Heap space allocated by GOD remains constant during the running of the flight software.

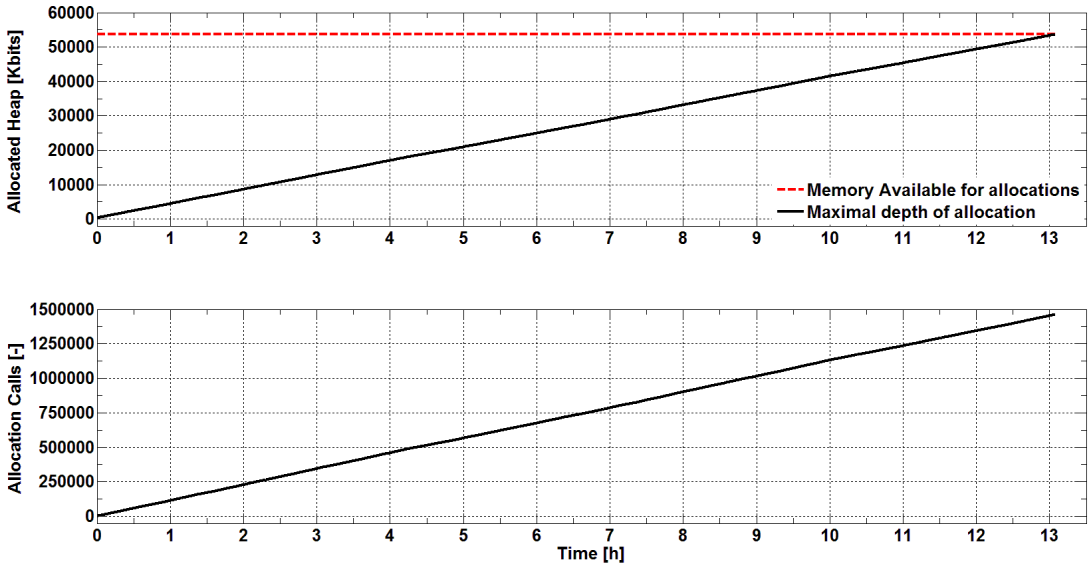

Figure 6.8.: Software development and validation environments at DLR and SSC

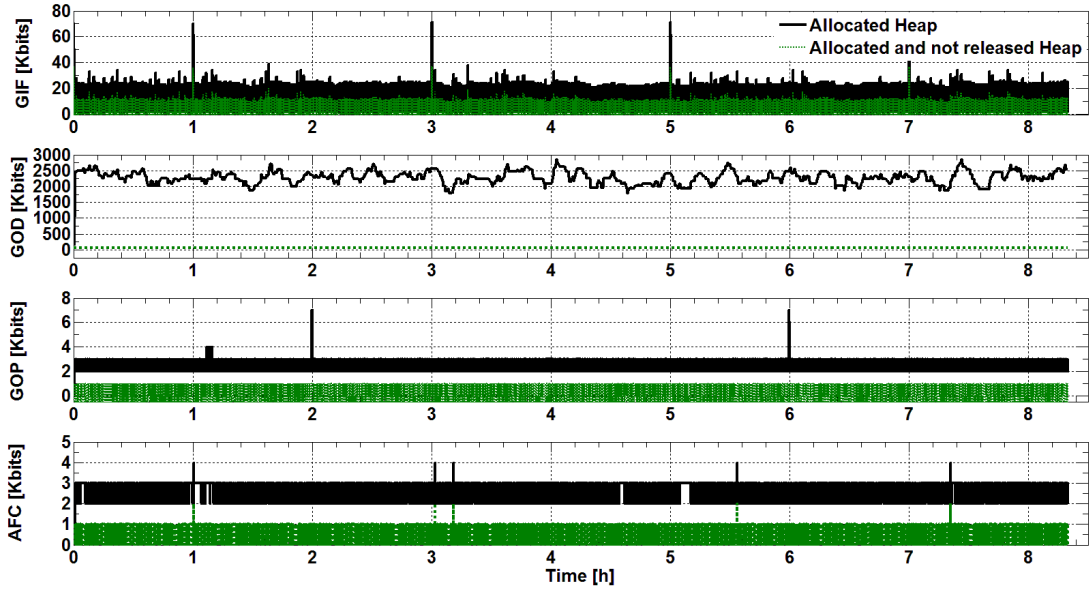

Figure 6.9.: Software development and validation environments at DLR and SSC

6.4.3. Max-Path Tests

A max-path [133] is defined as a unit test that reproduces the conditions of maximum computational load of a software module via the provision of a minimum quantity of constant inputs.

The CPU loads are computed by dividing the maximum execution time of each software module by its sample time (i.e., 1 s for the BSW and GNC cores, 30 s for the ORB core). The advantage of using a max-path unit test is given by the fact that the maximum CPU load can be assessed or reproduced through one or few calls of the software module under consideration. The maximum CPU load of a software module is obtained through the stimulation of as many sections of the code as possible at the same time. The definition of the proper inputs to obtain a max-path unit test is mainly based on a detailed knowledge of the code. Nevertheless a careful analysis of the maximum peaks in the execution times of the software during several long-term runs represents a valuable cross-check to verify the assumptions made on which the test is based. An accurate analysis of the software execution times obtained during long-term runs has enabled the definition of reliable max-path tests for each DLR's software module. The RTEMS function *rtems_clock_get (RTEMS_CLOCK_GET_TICKS_SINCE_BOOT, &Time)* is used to estimate the execution time of each module. The max-path tests have been defined in a MATLAB/Simulink environment as basic Simulink models retrieving the necessary inputs from the MATLAB workspace. In a second step, the unit tests models have been translated automatically in RTEMS applications using Real-Time Workshop and the RCC system. Fig. 6.10 shows the Simulink model of the max-path unit test for AOK.

The maximum computational load of GIF is obtained if the following conditions are valid:

1. The input buffers containing F40, F62 and F14 Mitel messages are completely filled with data coming from the MANGO and TANGO GPS receivers.
2. All the incoming messages are valid.

The max-path unit test consists of 2 simulation steps.

The maximum computational load of GOD is obtained if the following conditions are valid:

1. All the channels (i.e. 12) of the GPS receivers on-board MANGO and TANGO are allocated and raw GPS data are provided for all the tracked satellites.
2. All the incoming measurements are considered valid by GIF and GOD.
3. The maximum possible number of impulsive orbit control maneuvers (i.e. 30) is included in the navigation process.

The max-path unit test consists of 3 simulation steps.

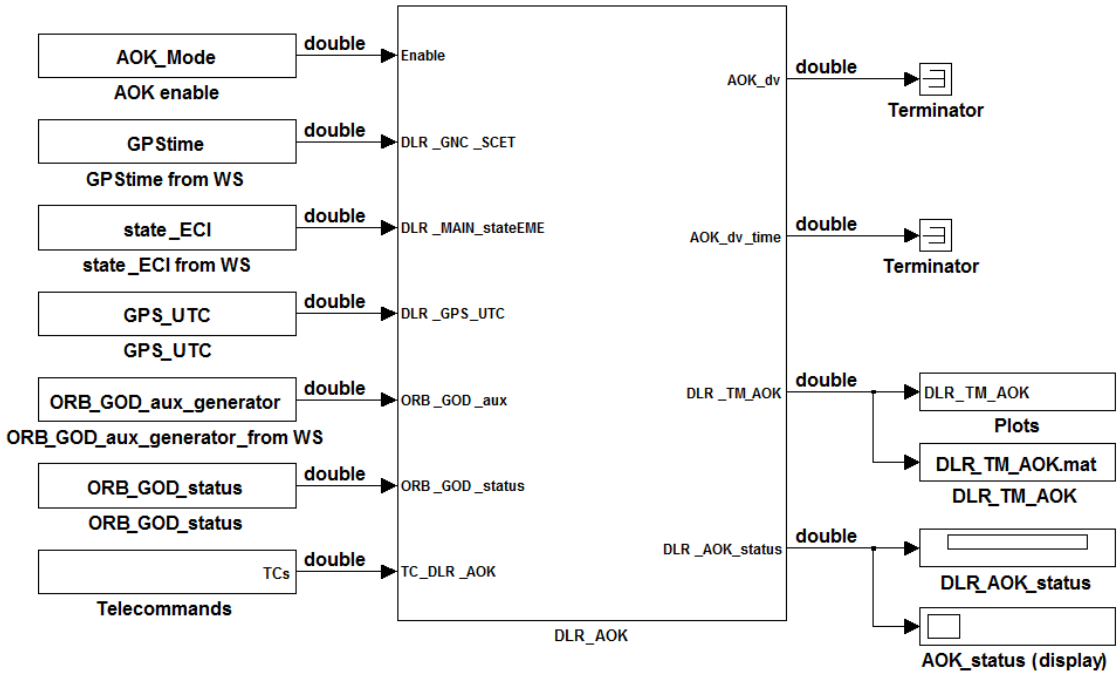

Figure 6.10.: Software development and validation environments at DLR and SSC

The maximum computational load of GOP is obtained if the following condition is valid:

1. The orbit polynomial coefficients have to be updated by GOP including two orbit control maneuvers (two is the maximum number of maneuvers that can be considered at the same time).

The max-path unit test consists of 2 simulation steps.

The maximum computational load of AOK is obtained if the following condition is valid in one of the possible RO modality (uploaded RO, multi-step internal propagated RO, one-step internal propagated RO):

1. In the same run step are computed the atmospheric drag by means of smoothing and fitting and the orbit control maneuver.

The max-path unit test consists of 64 simulation steps.

Table 6.7 collects the execution times and the CPU loads obtained from the max-paths tests on the LEON3 board for the software modules GIF, GOD, GOP and AOK. The CPU loads are obtained as the ratio between the total execution time of each module and the sample time of

Table 6.7.: Execution times and CPU loads

App. Core	S/W Module	Task	Ex. Time [ms]	CPU Load [%]
BSW (1 s)	**GIF**	Proc. inputs	2	
		Proc. messages	104	
		Proc. observations	1	
		Proc. ephemerides	2	
		Proc. outputs	2	
		Total	**111**	**11.1**
ORB (30 s)	**GOD**	Proc. inputs	9	
		Initialization	3379	
		Time update	864	
		Measurements update	6694	
		Proc. outputs	464	
		Total	**8033**	**26.8**
	AOK	Proc. inputs	1	
	Uploaded RO	Step comp.	61	
	On-board RO	Step comp.	680	
		AN comp.	1	
		Maneuver comp.	3	
		Proc. outputs	1	
	Uploaded RO	**Total**	**67**	**0.4**
	On-board RO	**Total**	**687**	**4.4**
GNC (1 s)	**GOP**	**Total**	**68**	**6.8**

the application core to which it belongs. Since GIF and GOD generate the maximum peaks of the CPU load with 26.8% and 11.1% respectively, the BSW and ORB application cores are implemented as low priority tasks on the MANGO's OBC. A net CPU load below 30%, as prescribed by the requirements, ensures that the GIF and GOD functions can be executed within the sample time of the respective cores. The most computational intensive task of GIF is shown to be the processing of Mitel messages provided by the Phoenix-S GPS receivers. The computational load of GOD is proportional to the number of measurements to be processed by the measurement update. When the initialization of the Kalman filter is required, no time and measurement updates are performed and the total GOD execution time reduces 3852 ms equivalent to 7.8 % CPU load. The maximum CPU load of AOK is determined by the RO

management task (Fig. 6.6). The RO can be uploaded from ground or propagated on-board. In case of on-board RO propagation the maximum CPU load of AOK is 4.4 %. The maximum load of GOP is dominated by the incorporation of maneuvers within the orbit coefficients.

7. The Precise Autonomous Orbit Keeping Experiment on the PRISMA Mission

This chapter presents the flight results of the AOK experiment which was executed successfully from the 18th of July to the 16th of August 2011 and has demonstrated the capability of autonomous precise absolute orbit control. The main scientific goal of the experiment was to demonstrate the accuracy, robustness and reliability of an autonomous GPS-based on-board orbit control for its possible routine exploitation in future scientific missions. The main differences with respect to similar experiments conducted in the past (Sec. 1.2.2) are the extremely tight requirements on control accuracy and the full autonomy also enhanced by the possibility of on-board RO propagation. The AOK controller adopts a guidance law for the orbital LAN and implements the analytical feedback control algorithm explained in Sec. 4.1. Using GPS-based absolute navigation data, the on-board controller commanded thruster activations in the orbital frame to autonomously control the orbit within a predefined window. The main performance requirement of the experiment was a control accuracy of the osculating ascending node of 10 m (1 σ standard deviation) with a maneuver velocity increment-decrement (Δv) available budget of 0.5 m/s. The AOK software was first developed and tested using the offline and hardware-in-the-loop test facilities at DLR (Chapter 6) which include the Phoenix GPS receivers and the satellite on-board CPU LEON3. After the integration in the PRISMA flight-software, AOK was thoroughly tested at OHB Sweden by means of the Real-Time Satellite Laboratory (SATLAB), a hardware-in-the-loop test facility [87]. The experiment operations were executed at the

DLR's PRISMA experiment control centre [74] while the mission was operated at DLR/GSOC. A commissioning phase of 4 days was required to verify that the control software was working properly in all its functionalities. During this phase MANGO flew in free motion as the controller was in open-loop and the orbital maneuvers were computed on-board but not executed. The closed-loop phase of 26 days included RO acquisition, controller tuning and fine control phases. In the last four days of the experiment the possibility of exploiting a RO generated on-board the spacecraft was tested in closed-loop. The AOK experiment operations have also included some remote sensing activities (Fig. 7.1).

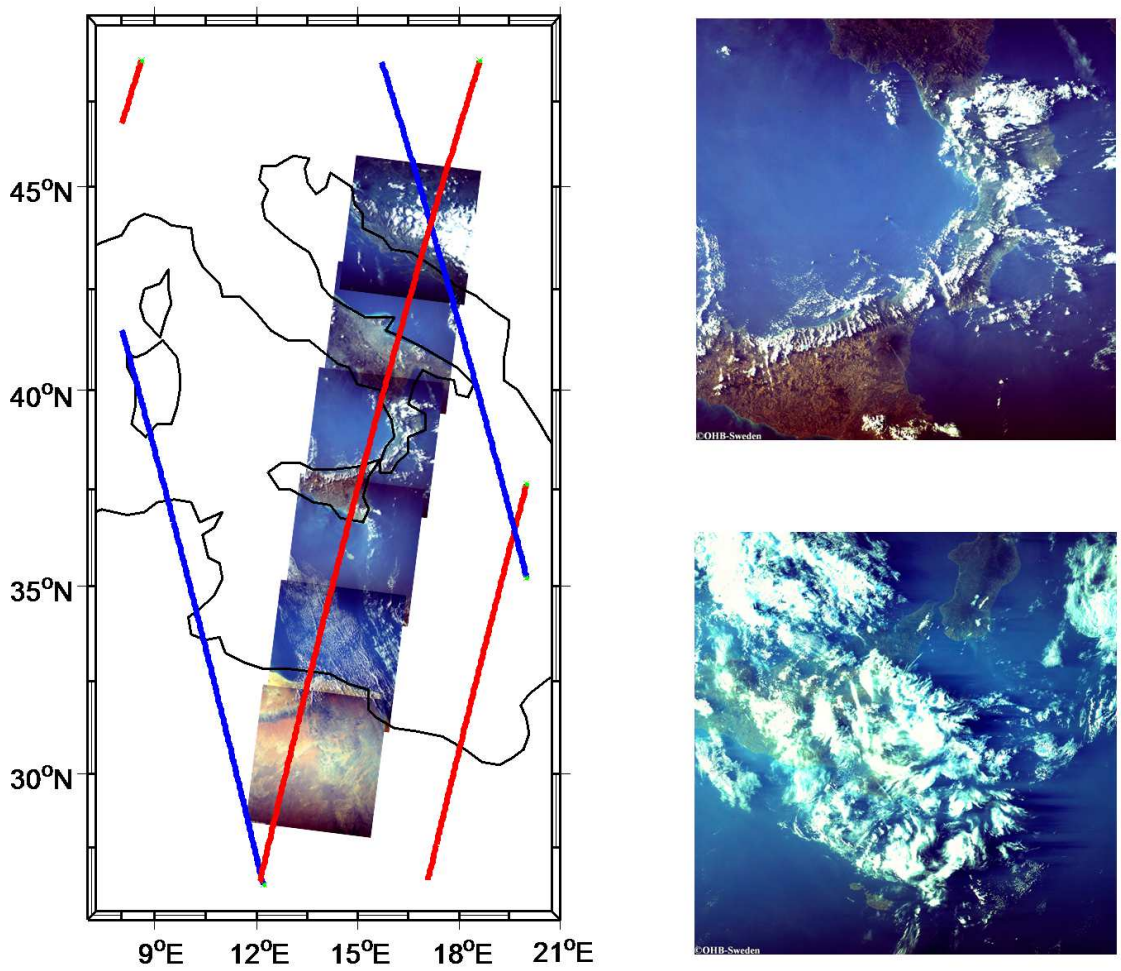

Figure 7.1.: Remote sensing activity planning (left). Volcanoes Etna and Stromboli as imaged on 10th of August (top) and on 15th of August (bottom) 2011. Images courtesy of OHB Sweden.

7.1. The AOK In-Flight Experiment

7.1.1. Experiment Requirements

Table 7.1 summarises the AOK experiment requirements described in detail in [98].

Table 7.1.: AOK experiment requirements

Requirement	**Description**
Functional	Autonomous orbit control of the LAN by means of along-track and anti-along-track velocity increments based on on-board GPS navigation system
Performance	Control accuracy of the LAN of 10 m (1σ standard deviation)
System	Impulsive orbital maneuvers performed by hydrazine propulsion system. Total Δv budget of 0.5 m/s with a resolution of 1 mm/s*
Operations	5 days open-loop commissioning phase and 25 days closed-loop AOK operations
Initial and final states	Initial state inherited from the previous experiment slots. The LAN will be kept within 10 m from a predefined profile based on the actual orbit
Attitude guidance	MANGO spacecraft body axes aligned with the local orbital frame with GPS antenna used in zenith pointing
Constraints	Orbit control maneuvers should be performed exclusively by AOK. The time slot allocated for the experiment is 1 month
*At AOK experiment start the Δv resolution was 0.4 mm/s	

7.1.2. Reference Orbit

The RO of the AOK experiment was generated once at the beginning of the operations using as initial state the position and velocity vector of MANGO at 01:00 UTC on 18th of July 2011 as estimated by the GPS based POD process at GSOC/DLR [83]. The orbit is the product of a numerical orbit propagation over one month. GRACE GGM01S Earth gravitational field model up to 70x70 degree and order has been used and the numerical integrator employed is the Dormand-Prince, a member of the Runge-Kutta family of ODE solvers [4]. The RO is split in blocks to be uploaded on-board the satellite periodically. Each uploaded block has a validity of about 3.2 days corresponding to the available on-board buffer which contains the GPS time

of the first reference LAN, 50 reference LAN values, and 50 semi-major axis values at the ascending node, consecutive in time. The semi-major axis values are used for atmospheric drag on-board estimation. Each block is generated in such a way to ensure about 8 hours time overlap with the contiguous ones. This RO upload strategy allows the exploitation of 3 of the available 3.2 days of each block ensuring at the same time the availability of more than 4 consecutive passes for the upload or on-board activation of a new block. The possibility of generating blocks with different time overlaps gives a great flexibility in the scheduling and re-scheduling of RO uploads. When a new RO block is copied in the control software buffer, the AOK's controller memory is deleted. The controller can thus maneuver only at the fourth ascending node from the new RO block activation as it needs four ascending nodes to re-build its memory and thus to have enough information to compute a new maneuver. The AOK software has the functionality of on-board RO propagation. The RO is propagated on-board using a GRACE GGM01S 20x20 gravitational field model and an initial state given by the on-board navigation despite of the results of Sec. 3.2 which would recommend the use of a GRACE GGM01S 40x40 (or higher) and an uploaded POD initial state for the control requirements of the AOK experiment. This limitation was imposed by the available on-board CPU resources and by the fact that the TCs interfaces could not be changed any more when the results of the analyses of Sec. 3.2 were confirmed.

7.1.3. Sequence of Events

Table 7.2 and Fig. 7.2 summarise the sequence of events of the entire AOK experiment. On 18th July at 10:20 UTC during orbit 5729 AOK was activated. The first block of RO has been uploaded to the satellite during the previous pass. A commissioning phase of 4 days was required to verify that the AOK control software was working properly in all its functionalities. In this phase the orbit controller was in open-loop meaning that the orbital maneuvers were computed but not executed and the MANGO satellite was thus flying in free motion. The closed-loop phase of 26 days started on 22nd of July at 12:35 UTC and was divided in three sub-phases. In the first 5 days of the closed-loop phase, maneuvers were issued to acquire the RO and thus bring the LAN deviation into the control window starting from a value of 300 m built up dur-

ing the commissioning phase from an initial deviation of about 120 m. A 3.5 day controller tuning phase from the 27th to the 30th of July was required to evaluate the correct values of the controller's settings for the fine control. Finally the fine orbit control phase started on the 30th of July and lasted until the end of the experiment. The RO blocks were always uploaded to

Table 7.2.: AOK experiment sequence of events

Task	Orbit	Start	End	Duration [days]
AOK Commissioning Phase	5727	18 Jul 08:30	22 Jul 12:35	4.17
RO generation	5727	18 Jul 08:30	18 Jul 09:30	0.04
GOD performance parameters and solo mode	5728	18 Jul 08:4	18 Jul 08:45	0
Switch to AOK mode	5729	18 Jul 10:20	18 Jul 10:20	0
Update AOK TCs	5729	18 Jul 10:20	18 Jul 10:20	0
RO_1 upload	5729	18 Jul 10:20	18 Jul 10:20	0
RO_1 active	5729	18 Jul 11:00	21 Jul 16:00	3.21
Upload of RO_2, RO_3 and RO_4	5756	20 Jul 07:25	20 Jul 07:25	0
Start of TANGO branches override procedure	5758	20 Jul 10:40	20 Jul 10:40	0
DVS_1 - U.S.A. and Canada	5758	20 Jul 12:11	20 Jul 12:31	0.01
DVS_2 - Europe	5760	20 Jul 17:31	20 Jul 17:51	0.01
DVS_3 - U.S.A	5773	21 Jul 13:11	21 Jul 13:31	0.01
RO_2 active	5775	21 Jul 16:00	22 Jul 12:35	0.86
AOK Closed-loop	5788	22 Jul 12:35	16 Aug 12:30	25
RO_2 active	5788	22 Jul 12:35	24 Jul 02:41	1.59
Closed-loop TC procedure upload and activation	5788	22 Jul 12:35	22 Jul 12:35	0
RO_3 active	5811	24 Jul 03:30	27 Jul 02:21	2.95
RO_4 active	5854	27 Jul 03:00	30 Jul 02:00	2.96
DVS_4 - Utah U.S.A.	5773	27 Jul 12:30	27 Jul 12:50	0.01
Upload of RO_5, RO_6 and RO_7	5872	28 Jul 08:40	28 Jul 08:40	0
RO_5 active	5897	30 Jul 03:00	02 Aug 06:40	3.15
Disable RO_6	5933	01 Aug 14:30	01 Aug 14:30	0
Upload and activation of RO_6	5943	02 Aug 07:05	05 Aug 09:40	3.11
Disable RO_7	5975	04 Aug 12:15	04 Aug 12:15	0
DVS_5 - Europe	5978	04 Aug 17:32	04 Aug 17:42	0.01
Upload and activation of RO_7	5988	05 Aug 10:02	08 Aug 07:39	2.9
DVS_6 - Sicilia	5992	05 Aug 16:52	05 Aug 17:02	0.01
Upload and activation of RO_8	6030	08 Aug 08:00	11 Aug 07:18	2.97
DVS_7 - Cleveland volcano	6031	08 Aug 10:39	08 Aug 10:39	0
DVS_8 - Chile	6034	08 Aug 16:11	08 Aug 16:21	0.01
DVS_9 - Etna volcano	6064	10 Aug 16:52	10 Aug 17:02	0.01
Upload and activation of RO_9	6073	11 Aug 07:40	12 Aug 08:19	1.03
DVS_10 - Turkey	6078	11 Aug 16:14	11 Aug 16:24	0.01
DVS_11 - South Europe	6079	11 Aug 17:49	11 Aug 17:59	0.01
AOK on-board propagation mode	6088	12 Aug 08:40	16 Aug 12:30	4.16
On board propagation TC	6088	12 Aug 08:40	12 Aug 08:40	0
DVS_12 - Turkey	6092	12 Aug 15:33	12 Aug 15:43	0.01
DVS_13 - South Europe	6093	12 Aug 17:12	12 Aug 17:22	0.01
DVS_14 - Etna volcano	6136	15 Aug 16:52	15 Aug 17:02	0.01
DVS_15 - Australia	6145	16 Aug 08:06	16 Aug 08:16	0.01
End of AOK experiment	6148	16 Aug 12:30	16 Aug 12:30	0

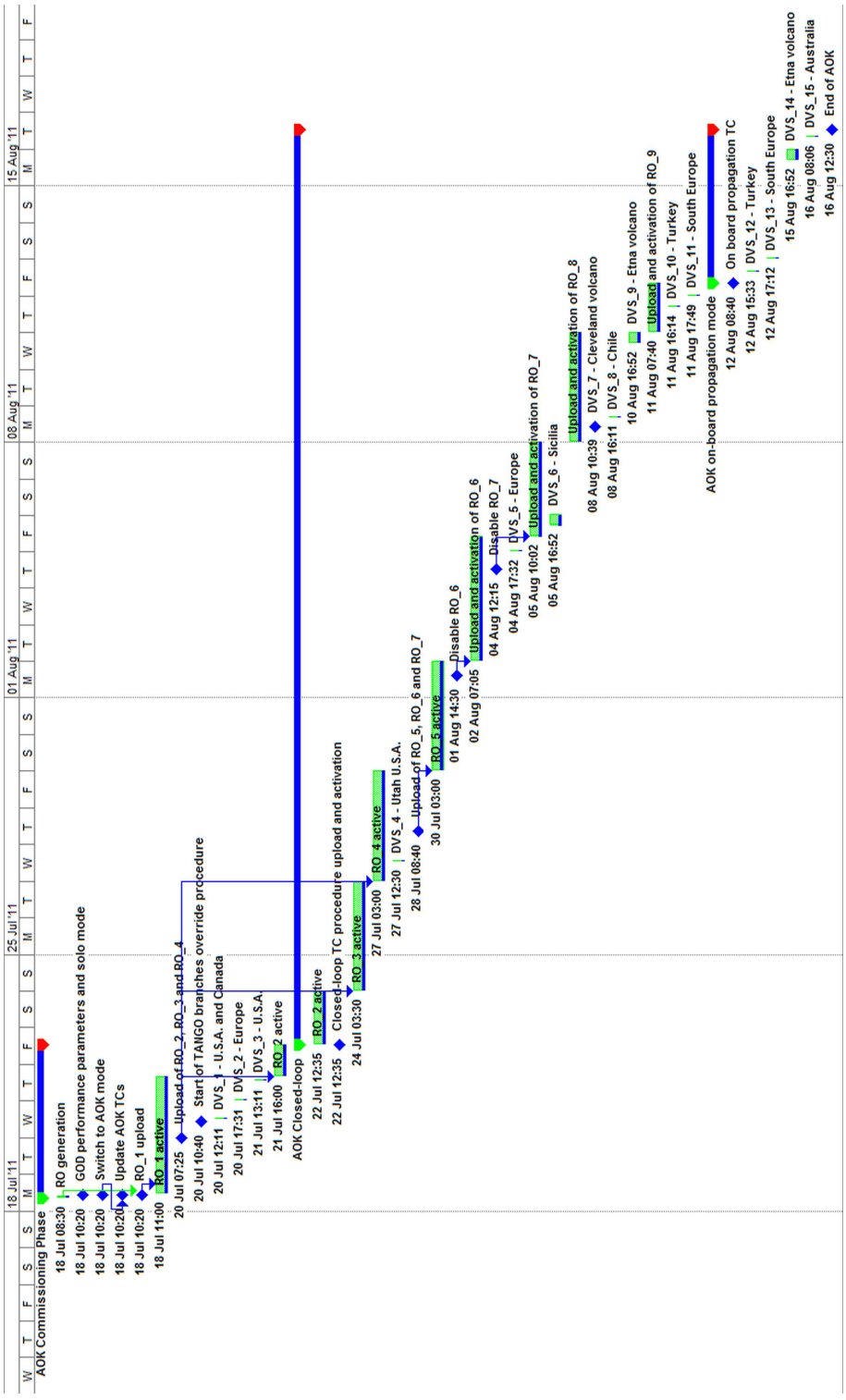

Figure 7.2.: AOK experiment sequence of events

the satellite and stored as time tagged telecommands (TTTCs) in the on-board memory. Each stored RO block had an activation time flag indicating when it had to be copied into the AOK software RO buffer. On 12th August, 4 days before the end of the experiment, AOK was put in on-board RO propagation mode. In the next sections the different experiment phases are described in detail.

7.1.4. Commissioning and RO Acquisition Phases

Fig. 7.3 shows the difference between the MANGO's real and reference semi-major axis and LAN and the magnitude of the along-track maneuvers during the experiment commissioning and reacquisition phases. The legend notations POD and AOK in Fig. 7.3 indicate that the satellite state as estimated respectively by the ground based and on-board navigation system has been used for the computation of Δa and ΔL. It can thus be assumed that the points noted as POD represent the real situation at each ascending node pass (at least with an accuracy of the sub-decimetre level) while the points noted with AOK represent what the on-board controller actually determined on-board the spacecraft as the position accuracy available on-board MANGO was about 2 m (1 σ) during the entire experiment [84]. The accuracy of the on-board estimation of the semi-major axis and therefore of Δa is instead 4 m (1σ) as it comes from a combination of the accuracies of position and velocity. This fact has a significant impact on the orbit control performance. An error of about 2 mm/s is introduced in the computation of the orbital maneuvers (Eq. (4.5)) by a 4 m error in the estimation of Δa. This fact has a significant impact on the orbit control efficiency as in the ideal case the Δvs required to keep ΔL in a control window of ± 10 m in steady-state have a range of 2 to 8 mm/s. The navigation accuracy is indeed the most important cost factor of the control Δv budget. This important consideration had already been identified in the numerical simulations performed during the system validation. In Fig. 7.4 (top) the plots of the accuracy of the on-board estimation of the semi-major axis and of the Δa as estimated on-board and ground based have been superposed. The error of the semi-major axis' on-board estimation is included as noise in the on-board estimation of Δa and consequently in the computation of the maneuvers. The only significant event during the commissioning phase was the auto-transition to on-board reference propagation mode. In order

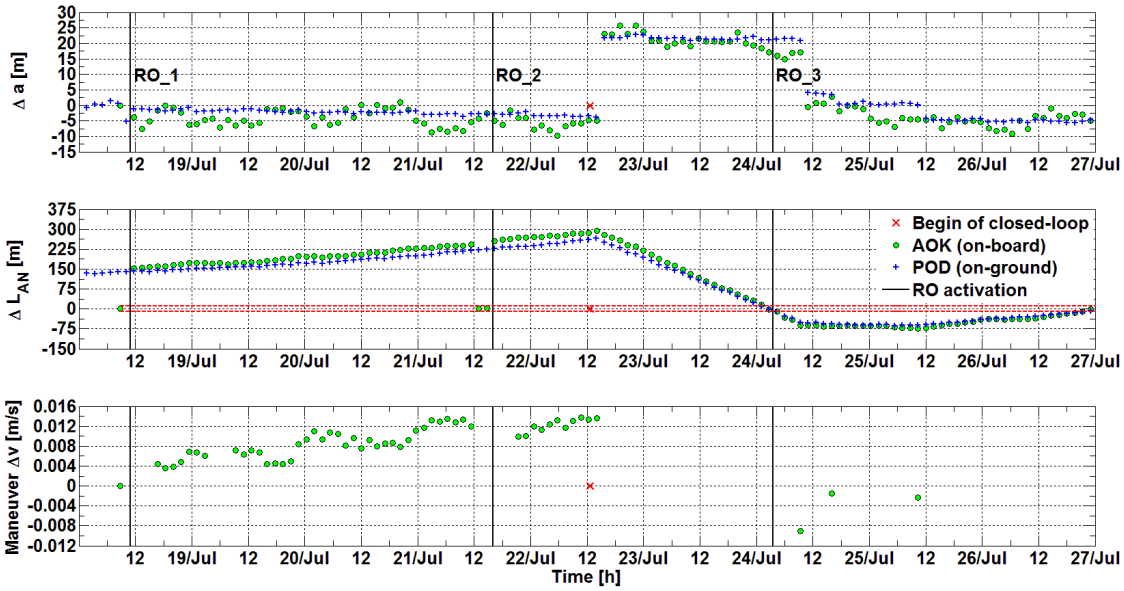

Figure 7.3.: Semi-major axis deviation (top), LAN deviation (middle), computed orbital maneuvers (bottom)

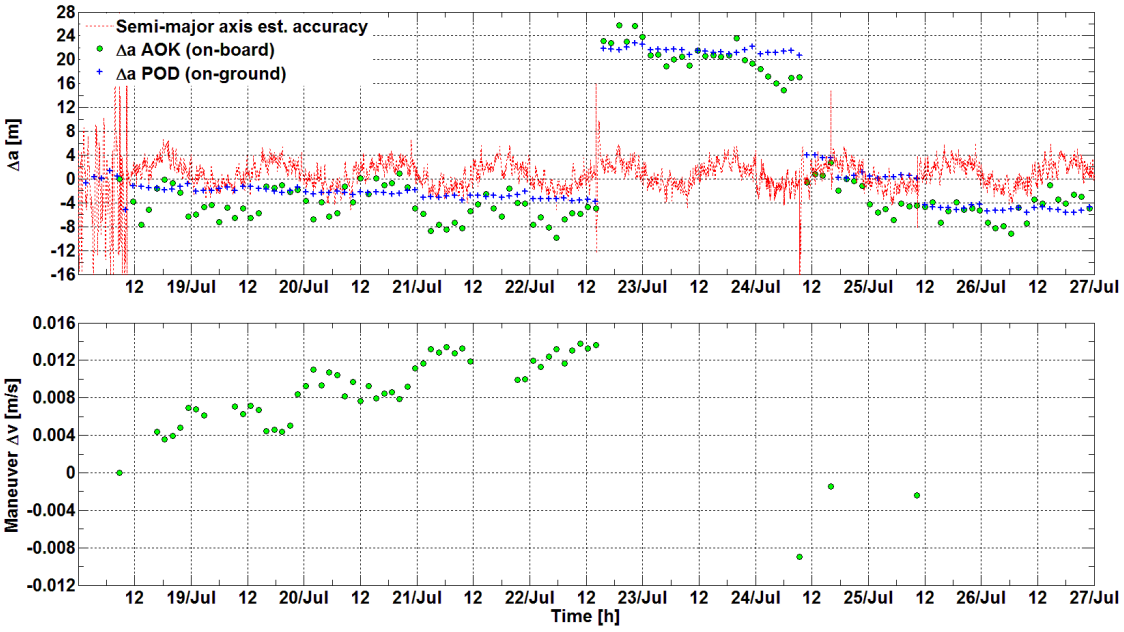

Figure 7.4.: Semi-major axis deviation and on-board estimation accuracy (top). Orbital maneuvers (bottom)

to test this functionality, the on-board activation of RO_2 was scheduled after the expiration of the validity of RO_1 and this triggered the auto-transition to on-board reference propagation mode that was at that time enabled.

As the controller was in closed-loop it was set up by TC to bring the LAN deviation from 300 m to 10 m in 1.5 days and an along-track Δv of +0.0136 m/s was executed. As shown in Fig. 7.3 the commanded RO acquisition maneuver was very accurate and the value of ΔL_{AN} was actually reduced to 10 m after 1.5 days. In this case the on-board navigation accuracy had little influence on the accuracy of the maneuver as the required Δa_c was about 30 m. The counter-maneuver (anti-along-track) that was expected to be executed just after passing the -10 m threshold, was instead executed with a delay of four orbits due to a mistake in the operations planning. In fact just 30 minutes before the time the controller would have commanded the counter-maneuver, RO_3 was activated on-board by TTTC and the maneuver execution was possible only after 4 ascending node passes from the new RO block activation (see Sec. 7.1.2). The result was that when the -0.009 m/s counter-maneuver was issued, the LAN deviation had a value of -60 m. A correction maneuver of -0.0015 m/s that brought Δa to 0.0 m was executed 4 orbits after the counter-maneuver. The controller was then set up to execute a RO reacquisition maneuver as the natural motion that would have brought ΔL_{AN} back in the control window was considered to be too slow when taking into consideration the remaining time available for the AOK experiment. The value of the new RO acquisition maneuver was -0.0024 m/s. The total Δv spent during the RO acquisition phase was 0.0265 m/s.

7.1.5. Control Tuning Phase

Once the LAN deviation value was brought into the control window, a 3.5 day control tuning phase was required to determine the best AOK controller settings. The maneuver duty cycle was 4 orbits for positive as well as for negative maneuvers. This means that the minimum allowed time between two consecutive maneuvers commanded was to be 4 orbits. This limitation, despite the degradation in the control performance, helped to understand the main factors for the control accuracy in the actual orbital perturbations forces environment. Fig. 7.5 shows clearly that the navigation error plays a fundamental role in the control accuracy performance espe-

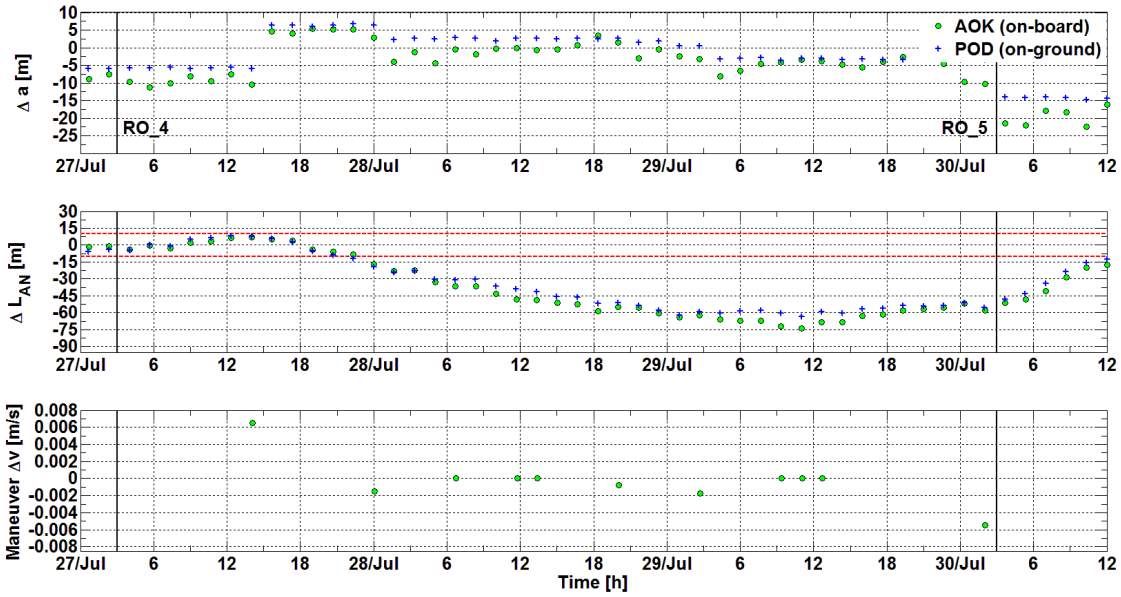

Figure 7.5.: Semi-major axis deviation (top), LAN deviation (middle), maneuvers (bottom)

cially in the presence of small atmospheric drag (see Appendix D). It can be noticed in Fig. 7.5 that the value of Δa on 28th at about 00:00 UTC computed using the on-board navigation was smaller than the actual one (POD). As a consequence the maneuver commanded was smaller than that required to bring the value of Δa to 0.0 m in order to stop the evolution of ΔL_{AN} towards larger (in magnitude) negative values. In this phase the controller was not allowed to perform RO acquisition maneuvers and this means that by its logic it could command only positive maneuvers for positive Δa to bring its value to 0.0 m. Thus a new correction maneuver was not issued until 20:00 UTC on 28th July. This delay was due in large part to the fact that AOK could see a negative or null value of Δa despite the real one was positive and in smaller part to the 4 orbits duty cycle that prevented issuing a maneuver at 16:40 UTC. The result was that at the time the new corrective maneuver was executed the value of ΔL_{AN} was already -50 m. On 29th of July, AOK was again set up to command RO acquisition maneuvers and the value of ΔL_{AN} was brought back into the control window. Two important lessons were learned during the control tuning phase. The first was that the duty cycle to be imposed for anti-along-track maneuvers had to be only 1 orbit. In this way the possibility of poor accuracy of an anti-along-track maneuver could be compensated by the freedom given to the on-board controller to make

small corrections at each orbit. The second lesson learned was the confirmation that a small decay rate of the semi-major axis implies a slow dynamics of the near parabolic evolution of the ΔL_{AN}. The impact of the on-board navigation accuracy on the control performance was less significant in case of positive ΔL as in this case maneuvers are issued for either positive or negative values of Δa. The total Δv spent during the control tuning phase was 0.016 m/s.

7.1.6. Fine Control Phase - On-ground Generated Reference Orbit

On 30$^{\text{th}}$ of July, as the RO acquisition was completed, the fine control phase officially started and lasted until the end of the AOK experiment. Table 7.3 collects the values of the most significant controller's parameters during this experiment phase. The largest maneuver allowed (Δv_{MAX})

Table 7.3.: AOK controller settings during the fine control phase

TC	**Value**
Δv_{MAX} [m/s]	0.008
ΔL_{MAX} [m]	5
ΔL_{min} [m]	-5
T_{d+} [s]	15000
T_{d-} [s]	5000
Maneuver delay [s]	120
On-board RO auto-transition	0

was set to 0.008 m/s as a base value and was later increased to 0.01 m/s. In case AOK issues a Δv maneuver whose magnitude is larger than Δv_{MAX}, the maneuver is not executed and AOK resets. The LAN control window was imposed to be ± 5 m in order to allow the controller enough time to maintain the ΔL_{AN} absolute value within the required 10 m. The imposed duty cycle for along-track maneuvers was 15000 s so that AOK was allowed to issue a positive Δv maneuver every 3 orbits. The imposed duty cycle for anti-along-track maneuvers was 5000 s. In this way AOK was allowed to command maneuvers at each orbit for negative ΔL_{AN}'s. The maneuver delay was imposed to be 120 s and no auto-transition to on-board RO generation was allowed in case of expiration of the validity of the uploaded on-board RO. Fig. 7.6 depicts the control tracking error during the fine control phase with ground based generated RO. In this steady-state control phase a regular maneuver cycle cannot be identified. This lack of

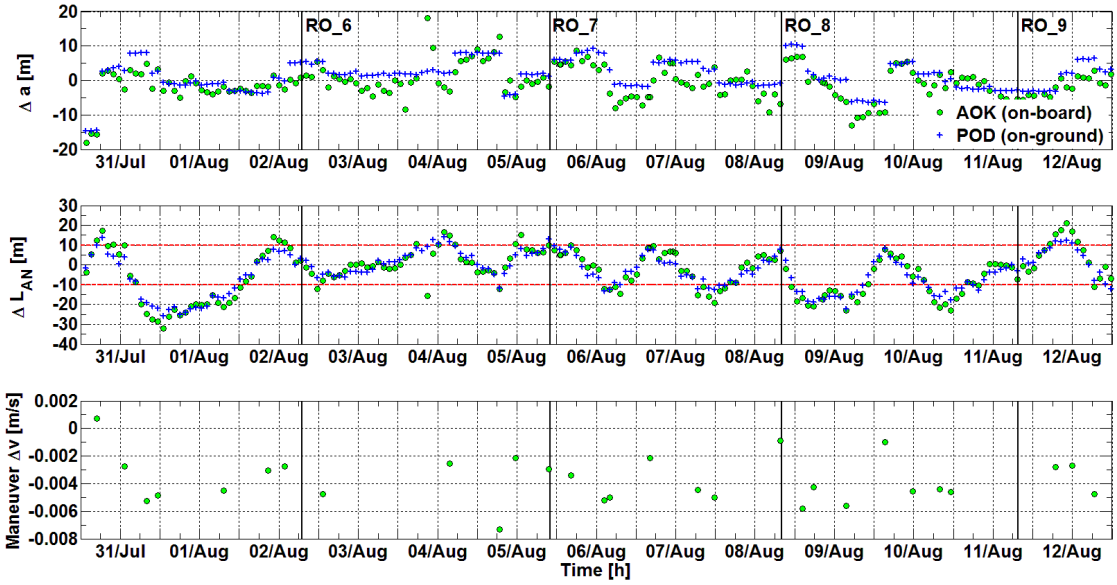

Figure 7.6.: Semi-major axis deviation (top), LAN deviation (middle), orbital maneuvers (bottom)

determinism is due to the fact that with a ± 10 m control window the noise in the estimation of Δa due to the on-board navigation accuracy is not negligible with respect to the order of magnitude of the Δa_c required for the control. The on-board estimation of da/dt by means of data-fitting was not exploited by the controller regularly as expected due to implementation issues related to the re-initialization of the Δa filtering buffer and Eq. (4.17) was employed more often for the on-board estimation of the atmospheric drag. Table 7.4 collects the most significant control statistics during this phase. The minimum value of Δv is defined here as its minimum absolute value. The 10 m (1 σ standard deviation) LAN control requirement is fully satisfied. During this entire steady-state fine control phase the magnitude of the maneuvers issued was 0.002 to 0.004 m/s with peaks of 0.006 to 0.008 m/s. The total Δv spent during the control tuning phase was 0.0857 m/s.

Table 7.4.: Most significant control statistics

Parameter	**Min**	**Max**	**Mean**	σ	**RMS**
ΔL_{AN} (POD) [m]	-25.9	14.1	-3.6	9.0	10.2
Δv [m/s]	0.0006	0.0094	0.0005	0.0034	0.0034
Man. cycle [h]	1.7	38.4	11	8.3	13.7

7.1.7. Fine Control Phase - On-board Generated Reference Orbit

On the 12th of August AOK was put in an on-board generated RO mode for the last 4 days section of the experiment. As the RO was propagated on-board using a GRACE GGM01S 20x20 gravitational field model (Sec. 7.1.2), the goal of this experiment phase was to validate this software functionalities more than a comparison of the control performance with on-board and ground-based RO generation. Fig. 7.7 depicts the control tracking error with respect to the on-board RO. The controller settings of Table 7.3 were maintained. At the moment AOK is set in on-board RO propagation mode, its propagator takes as initial state the first valid navigation state given by the on-board navigation filter. Table 7.5 collects the most significant control statistics during this phase in which the total Δv spent was 0.0065 m/s.

Table 7.5.: Most significant control statistics

Parameter	**Min**	**Max**	**Mean**	σ	**RMS**
ΔL_{AN} (POD) [m]	-23.2	14.0	-9.3	11.7	14.9
Δv [m/s]	0.0008	0.003	-0.0007	0.003	0.003
Man. cycle [h]	8.3	76.7	33.3	37.7	50.3

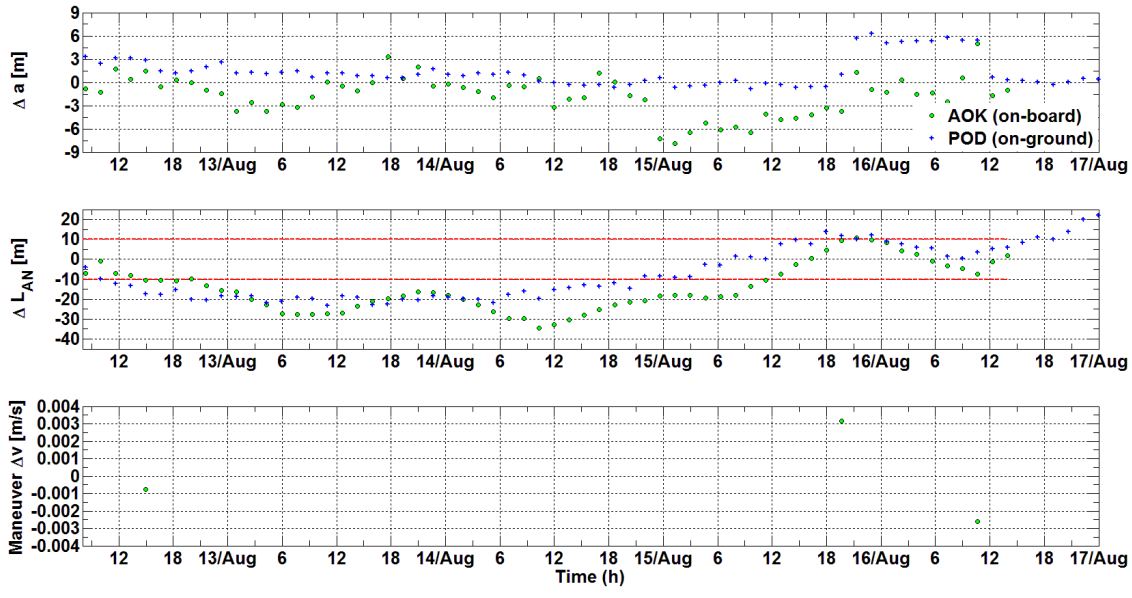

Figure 7.7.: Semi-major axis deviation (top), LAN deviation (middle), orbital maneuvers (bottom)

7.1.8. Overall AOK Experiment Review

Control

Fig. 7.8 gives an overview of the most significant control parameters during the experiment's different phases described in detail in the previous sections. Table 7.6 collects the Δv budget pertaining to each experiment phase and to the entire experiment. The Δv_{NETTO} is the sum of the Δvs with their signs. The total amount of maneuver Δv spent for the accomplishment of the AOK experiment was 0.1347 m/s corresponding to 27% of the allocated Δv budget (Table 7.1). The flight results of the AOK experiment have been compared to the numerical simulations performed during the system validation phase confirming the high degree of realism of the simulations results [75, 73].

Navigation

Before the start of the experiment new settings were uploaded by TC for MANGO's GPS-based on-board navigation filter. MANGO's navigation filter was set up to have the best performances after the evaporation of the PRISMA formation.

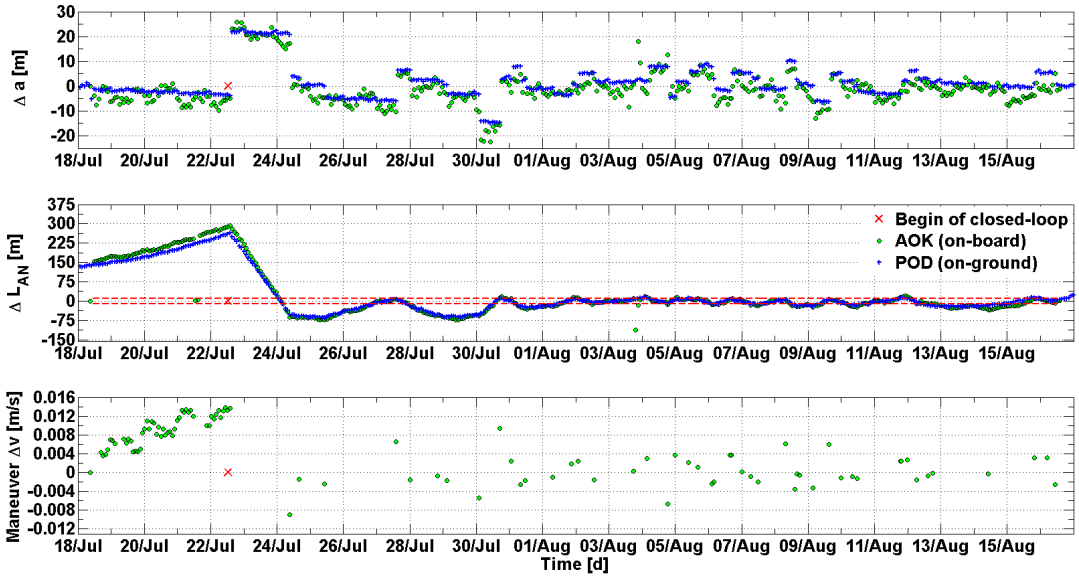

Figure 7.8.: Semi-major axis deviation (top), LAN deviation (middle), orbital maneuvers (bottom)

Table 7.6.: Maneuver $\mathbf{\Delta v}$ budget

Experiment Phase	$\lvert\mathbf{\Delta v}\rvert_{\mathbf{min}}\,[\mathrm{m/s}]$	$\lvert\mathbf{\Delta v}\rvert_{\mathbf{MAX}}\,[\mathrm{m/s}]$	$\mathbf{\Delta v_{NETTO}}[\mathrm{m/s}]$	$\lvert\mathbf{\Delta v}\rvert_{\mathbf{TOT}}\,[\mathrm{m/s}]$
Commissioning	0.0015	0.0137	0.0008	0.0265
RO acquisition	0.0007	0.0065	-0.0030	0.0160
Fine control - uploaded RO	0.0006	0.0094	0.0160	0.0857
Fine control - on-board RO	0.0008	0.003	-0.0002	0.0065
Entire experiment	0.0006	0.0137	0.0136	0.1347

TANGO was put in safe mode at a safe distance and the formation geometry configured with collision avoidance criteria [143,146]. Fig. 7.9 depicts the accuracy of the on-board estimated absolute position during the entire experiment. The navigation accuracy is evaluated in local orbital frame (R axis in radial, N anti-cross-track and T along-track oriented) with respect to the POD products that are accurate at the sub-decimetre level. The effect of the inclusion of the executed orbital maneuvers on the navigation accuracy can be noticed in Fig. 7.9 especially on the radial component. During the entire experiment the on-board estimated semi-major axis had an average accuracy of 4 m (1σ) as can be appreciated in Fig. 7.10. The spikes in the plot of Fig. 7.10 are well correlated with the execution of orbital maneuvers. The only significant event during the AOK control tuning phase was an outlier in the navigation accuracy on 28$^{\text{th}}$ of July at about 17:00 UTC (Fig. 7.9).

Two on-board navigation problems are to be reported during the fine-control experiment phase (Fig. 7.9). The first one, that took place on 3$^{\text{rd}}$ August at about 13:45 UTC, was a loss of track of GPS satellites. This problem was initiated by excessive pseudo-range values that trigger in the Phoenix GPS receiver's logic a progressive loss of signals. The on-board navigation filter could thus not perform the GPS measurements update for about 60 minutes and went in orbit propagation mode. This event had no major consequences on the navigation accuracy. AOK went in idle state only for 2 minutes as in such cases the idle state is triggered. At the moment of the ascending node at 14:20 UTC, AOK kept working despite the on-board navigation was degraded and this caused a degradation in the estimation of Δa but no degradation in the estimation of ΔL_{AN} as shown in Fig. 7.6. This event had no consequences on the control as at the moment it occurred the value of ΔL_{AN} was inside the control window and no maneuver was to be issued. The second on-board navigation problem, which caused a major degradation

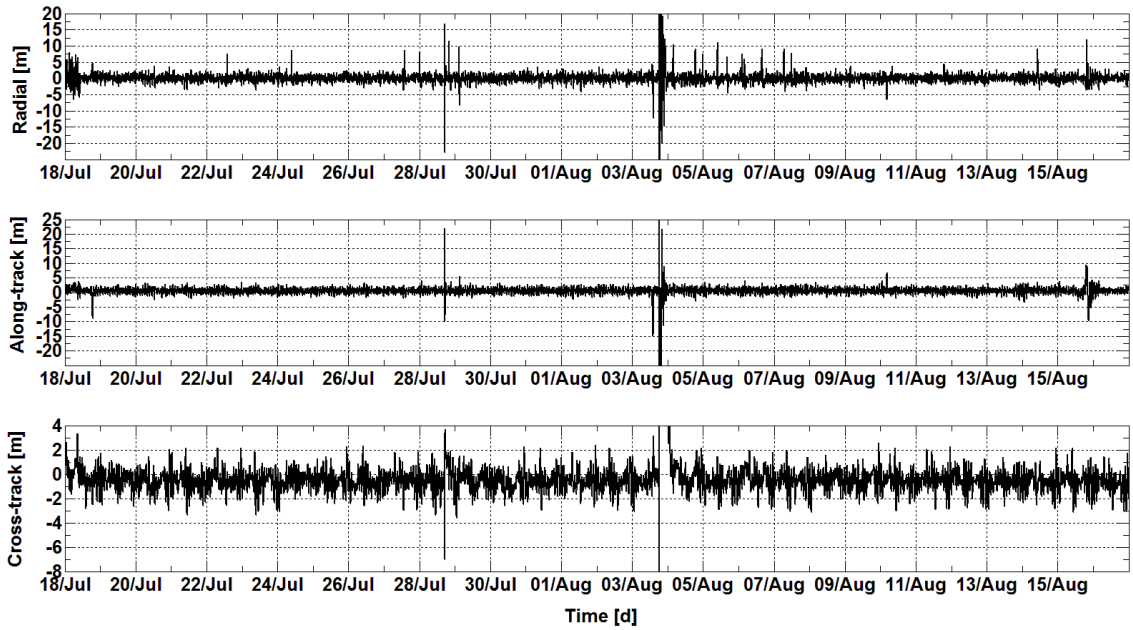

Figure 7.9.: Accuracy of the on-board estimated position in RTN

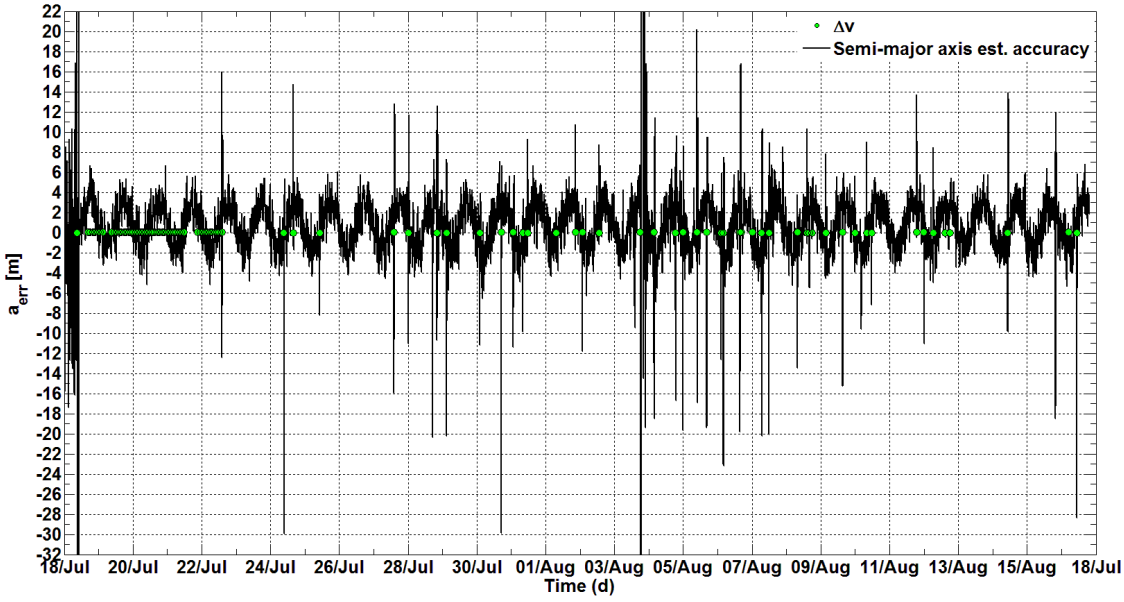

Figure 7.10.: Accuracy of the on-board estimation of the semi-major axis

in the navigation accuracy for 30 minutes, took place on 3rd August at 18:24:40 UTC and ended at about 20:45 UTC. In this case the estimation of Δa and ΔL_{AN} made by AOK were considerably degraded as can be noticed in Fig. 7.8 where outliers show up in the plots in that date. This event was a Singular Event Upset (SEU) most probably due to corrupted GPS receiver data possibly caused by an ongoing geomagnetic storm (see Appendix D). As this occurrence was not detected as a navigation problem by the on-board navigation filter, AOK had no protection from it but no wrong maneuver was issued as the navigation SEU occurred inside a maneuver duty cycle. Nevertheless AOK would have commanded an auto-reset not issuing any maneuver as the computed Δv would have had the order of magnitude of 0.06 m/s far larger than the maximal allowed Δv (Δv_{MAX} in Table 7.3) set to 0.008 m/s. Setting Δv_{MAX} to the smallest possible value compatible with the LAN control window amplitude is indeed one of the ways to avoid or at least restrain the catastrophic effect of a wrong orbital maneuver due to a navigation SEU. It is interesting to notice that though the Phoenix is a Commercial Off The Shelf (COTS) GPS receiver that has no proper protection to the space electromagnetic environment, its performance is in some cases superior to space proofed GPS receivers [113].

8. Conclusions

The main purpose of this research is the analysis, development and implementation of a precise autonomous orbit control system for a spacecraft in low Earth orbit. The study of this topic stems from the author's persuasion that in the near future this technology will be exploited on a routine basis for the precise orbit maintenance of remote sensing satellites very high resolution optical systems and synthetic aperture radars. The discussion is carried out through the thesis' chapters in a step-wise way from the parametrization used to model the problem, through the theoretical achievements and their practical implementation. One of the milestones of this work is the realization of a flight-ready space-borne autonomous orbit control system which has been integrated into the PRISMA technology demonstration mission and has been validated in flight.

8.1. Discussion

8.1.1. A Qualitative Cost Analysis

Starting from the assumption that the autonomous orbit control technology is now mature to be used on a routine basis, a major driver in choosing whether a ground-based or an on-board orbit control system is its cost. At this stage, only a qualitative cost analysis is possible since the data about the four autonomous orbit control experiments of Table 1.3 cannot represent a significant statistics. The cost of an orbit control system is mainly determined by the control accuracy required and its reliability. The control accuracy $e_c = e_c(e_n, e_m, e_{dy})$ depends on the navigation accuracy e_n, the maneuvers errors e_m and the dynamic model uncertainties e_{dy} which increase when the spacecraft's altitude h decreases. It is assumed here that the accuracy

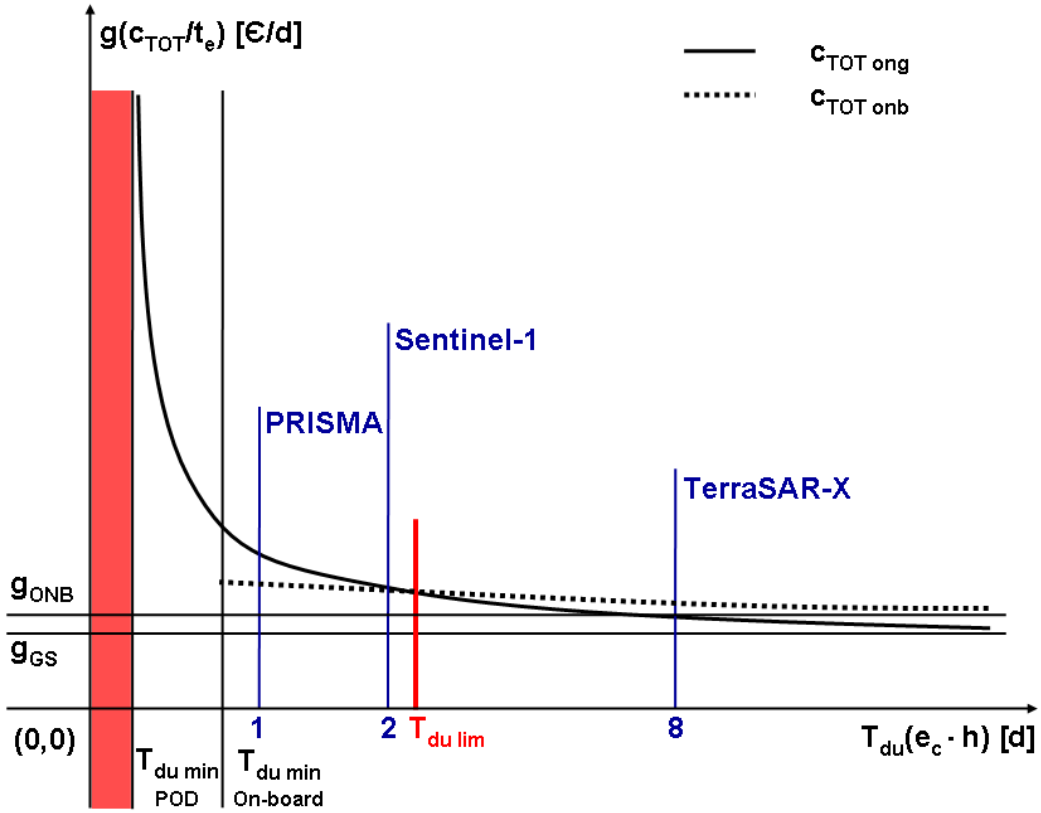

Figure 8.1.: Ground-based vs on-board orbit control systems cost

of the control cannot be better than that of the navigation i.e. it is always $e_m \geq e_n$. The value of e_c required at a certain altitude h, determines the value of the maneuvers duty cycle $T_{du} = T_{du}(e_c \cdot h)$. The total cost of the control system can be expressed as $c_{TOT}(T_{du}) = c_i + c_{OPS} + c_p$ where c_i, c_{OPS} and c_p are respectively the implementation, operations and performance cost. The performance cost c_p quantifies the additional on-board thrusters' fuel consumption which results from a non-optimal computation of the maneuvers. An optimal computation of the orbital maneuvers will yield therefore $c_p = 0$. In general it can be stated that the development and implementation costs $c_{i_{onb}}$ of an on-board orbit control software are larger than the costs $c_{i_{ong}}$ required by the realization on-ground ($c_{i_{onb}} > c_{i_{ong}}$). This is due to the greater effort for the implementation, validation and testing of a on-board control software compliant with all the standard safety criteria. The operations costs $c_{OPS_{ong}}$ of a ground-based orbit control system are instead larger than those of a on-board system ($c_{OPS_{ong}} > c_{OPS_{onb}}$). Finally the

availability of an optimal maneuvers' computation process on-ground will result in a smaller fuel consumption ($c_{p_{onb}} > c_{p_{ong}}$). Fig. 8.1 depicts the result of this qualitative cost analysis. The function $g = g(c_{TOT}/t_e)$ represents the orbit control system cost considering also its total exploitation time t_e during the mission lifetime. The two curves $c_{TOT_{ong}}$ and $c_{TOT_{onb}}$ are plotted as a function of T_{du} assuming that the orbit control system is exploited continuously during the entire mission lifetime. The value g_{ONB} represents the sum of the cost g_{GS} required for the implementation of the ground segment and the implementation of the autonomous control flight software. The cost g_{GS} is required irrespective of the control type. Assuming that a POD process cannot be implemented on-board and that $e_m \geq e_n$, $T_{du_{min}}$ represents the minimum duty cycle and thus the minimum value of e_c achievable with the available navigation accuracy. The value of $c_{TOT_{ong}}$ and $c_{TOT_{onb}}$ tends asymptotically respectively to g_{GS} and g_{ONB} by increasing the value of T_{du}. This is justified by the assumption that for an infinite value of T_{du} there are no operations costs required for the orbit control. The cost $c_{TOT_{ong}}$ of the ground-based orbit control system is supposed to increase asymptotically by decreasing the value of e_c since the smaller is the value of T_{du}, the larger is the number of ground station contacts and work time required. The function $c_{TOT_{onb}}$ increases by decreasing the value of T_{du} as well. This is due to the fact that the on-board maneuvers' computation error increases by increasing the navigation error (Sec. 7.1.4). The three missions PRISMA [73], Sentinel-1 [121] and TerraSAR-X [44] are inserted in the cost analysis of Fig. 8.1 considering their duty cycle which is respectively about 1, 2 (TBC) and 8 days, for required control accuracies of 10, 50 and 250 m at the altitudes of 700, 700 and 400 km respectively. For values of T_{du} smaller than $T_{du_{lim}}$ an autonomous orbit control system is the more convenient option. The on-board control options is considered more convenient for a mission like Sentinel-1 assuming that this technology is nowadays ready to be used on a routine basis.

8.1.2. Achievements of this Research

This thesis work represents a step forward in the theoretical formalization and implementation of an on-board orbit maintenance system. Autonomous orbit control finds its natural exploitation in the frame of low-Earth-orbit missions which require strict constraints on the maximum

allowed deviation of the real from the nominal spacecraft's ground track and altitude. This technology has nowadays reached a sufficient level of maturity to be applied routinely to such space programs. The research must proceed now towards the definition of a general and rigorous formalization of the models and control requirements and the study of new control methods.

The analytical approach developed from the state-of-the-art uses the so called operation parameters as controlled quantities. The operational parameters lack of the rigorous, general and compact mathematical formalization of a coordinates system. For this reason a new parametrization, the relative Earth-fixed elements, has been introduced. The problem of the autonomous absolute orbit control can in fact be formalized as a specific case of two spacecraft in formation in which one, the reference, is virtual and affected only by the Earth's gravitational field. The relative Earth-Fixed elements describe the relative motion of the real and reference sub-satellite points on the Earth surface and can be mapped directly into relative orbital elements with a coordinates transformation. This approach allows the direct translation of absolute orbit control requirements in terms of relative orbit control. The methods developed for the formation-keeping can thus be used for the orbit control of a single satellite. This formalization allows also the straightforward use of modern control theory numerical techniques for orbit control. Indeed, a bridge between the worlds of control theory and orbit control is built by this formalization. As a demonstration, a linear and a quadratic optimal regulators have been designed and tested. The state-space representation has been used for the mathematical formulation of the problem. The system to be controlled has been described by means of a linear dynamic model including the J_2 zonal coefficient of the Earth's gravitational field and the atmospheric drag perturbation force. These two numerical control methods have been compared, by means of numerical simulations, with the analytical algorithm.

The main difference between these methods is that the maneuvers' computation by the analytical controller is based on a long term orbit prediction whereas the linear regulators compute the control actions with a pure feedback logic based on the values of the control gains. The accuracy of the orbit model plays therefore a critical role in the implementation of the analytical controller. For the implementation of the numerical feedback regulators, the critical issue is not the prediction accuracy of the model but its reliability in defining the stability conditions of

the closed-loop system in the determination of the gains. The analytical controller has demonstrated in-flight to be robust, cost-effective and capable of very good control accuracies. With the on-board availability of an accurate orbit model, this type of analytical controller has an optimal control performance in terms of accuracy and costs, and a deterministic maneuvers cycle whose duration depends on the size of the control window. On the other hand, the numerical regulators have a simpler flight software implementation and an enhanced flexibility given by the possibility of varying the type of on-board controller simply by uploading to the spacecraft different gain configurations. The type of control of these feedback systems is in fact entirely determined by the type and value of the gains.

This research presents the most advanced to date demonstration of a complete guidance, navigation and control system for autonomous absolute orbit control. The implementation of this system for the PRISMA mission has been described in detail. The AOK experiment on the PRISMA mission, which was executed successfully from the 18$^{\text{th}}$ of July to the 16$^{\text{th}}$ of August 2011, has validated in flight the analytical orbit control algorithm developed in this thesis (Sec. 4.1). Using GPS-based absolute navigation data, the on-board controller commanded thruster activations in the orbital frame to autonomously control the satellite's longitude of ascending node within a predefined window. The main performance requirement of the experiment was a control accuracy of the longitude of ascending node of 10 m (1σ standard deviation). The control accuracy requirement was fulfilled. The navigation accuracy has shown to be the most important cost factor of the control Δv budget as highlighted also by the numerical simulations performed during the system validation. The maneuvers' execution error had a mean value of about 5% during the experiment and did not cause any degradation on the control accuracy. This on-board orbit control system can compute a maneuver only once every orbit at the ascending node and the on-orbit place for the execution of a maneuver can be imposed by telecommand with the value of the maneuver time delay from the ascending node pass time. For this reason it can be concluded that an autonomous orbit controller of this type could be fully compatible with the optimal planning of missions with very demanding payload activity and strict orbit control requirements. The main differences with respect to the experiment carried on by Demeter (Sec. 1.2.2), the most similar performed in the past, are the extremely tight re-

quirements, a better on-board navigation accuracy, the structure of the GNC architecture which has separated orbit control and navigation software modules installed in the spacecraft's on-board computer, and the possibility of on-board RO generation. The better control performance achieved during the AOK experiment can be attributed to the better navigation performance and to the available provision of small velocity increments (in the order of magnitude of 1 mm/s) by the spacecraft's thrusters.

The flight software development and testing platform at DLR (Chapter 6), developed in the frame of the PRISMA mission, has demonstrated to be a powerful and reliable simulation tool for the design and validation of the orbit control software. The high degree of realism of the numerical simulations is also emphasized by comparing the numerical results of Fig. 5.5 and Table 5.5 for AOK with the flight results of Fig. 7.8 and Table 7.6. The final maneuver budget of the numerical simulation is 0.09 m/s whereas that of the in-flight experiment is 0.13 m/s. This values are comparable considering that during the in-flight experiment the RO acquisition was from an initial LAN deviation of 300 m and that a calibration phase preceded the fine control phase. The simulation results obtained for the test scenario of TerraSAR-X (Table C.1) can be compared with the flight data as well. The simulation foresees orbital maneuvers of about 0.017 m/s with a maneuver cycle of about 10 days whereas the flight data shows a mean maneuvers' value of 0.01 m with a mean maneuver cycle of about 7 days. The more cost-effective performance of the orbit control system of TSX is due to the fact that the value of the maneuvers computed on-ground is the output of an optimization process which has the availability of space environment data collected on the long period, the most precise navigation data and practically no constraints on the computational resources.

8.2. Future Work

The theoretical and practical achievements of this research can certainly be considered an important milestone in the road-map to precise autonomous absolute orbit control. Many technical challenges have been faced and overcome in the development, implementation and operations of the PRISMA mission and the execution of the flight dynamics experiments. From this starting

point some new research paths can be opened.

The mathematical formalization can be further developed. The final goal should be to use the same formalization for the analytical and numerical methods. Indeed starting from the following equation, derived from Eqs. (2.28), (2.30) and (A.5), which relates the REFE and the velocity increments in the orbital frame, the absolute orbit control can be defined as a constrained optimization problem.

$$\boldsymbol{\delta F} = \mathbf{TB}\boldsymbol{\Delta v} \tag{8.1}$$

$$\mathbf{T}(u) = \frac{1}{n}\begin{pmatrix} 2\tau(\alpha-1) & \tau[-3\overline{u}+4\beta] & \dfrac{(\tau\cos i_{\mathcal{R}}-1)\beta}{\sin i_{\mathcal{R}}} + \tau\sin u\left(\dfrac{1}{\tan i_{\mathcal{R}}} - \dfrac{1}{\tan i}\right) \\ 2\sin i_{\mathcal{R}}(\alpha-1) & \sin i_{\mathcal{R}}[-3\overline{u}+4\beta] & \cos i_{\mathcal{R}}\beta + \sin u\left(\cos i_{\mathcal{R}} - \dfrac{\sin i_{\mathcal{R}}}{\tan i}\right) \\ \beta & 2[1-\alpha] & 0 \end{pmatrix} \tag{8.2}$$

where $\tau = (|\omega_E - \dot{\Omega}_{\mathcal{R}}|/n)\sqrt{1-(\sin u \sin i)^2}$, $\alpha = \sin\overline{u}\sin u + \cos\overline{u}\cos u$ and $\beta = \sin\overline{u}\cos u - \cos\overline{u}\sin u$.

The constraints of this problem are the specific mission orbit's requirements. Each type of requirement can be formalized with a linear combination of the relative Earth-fixed elements. The closed analytical solutions of the problem identify the optimal on-orbit place, direction and number of maneuvers. The numerical regulators can also be designed by means of Eqs. (8.1)-(8.2) using the REFE as states.

The design of a predictive control system using the virtual formation model could join the deterministic behaviour of an analytical algorithm and the flexibility of a numerical regulator. For the realization of a performing system, the prediction capability of the on-board analytical model has to be improved and eventually replaced by a numerical propagator.

The analytical algorithm validated on PRISMA, can be considered a ready-to-fly tool for autonomous orbit control. Nevertheless, the experience gained during the autonomous orbit keeping experiment on PRISMA, was invaluable for the identification of major improvements for the control performances and the operations. The on-board navigation filter can be tuned to reach the meter level accuracy on the estimation of the semi-major axis. One of the improvements should regard the prediction model used by the PRISMA on-board absolute orbit control

software which should include, in addition to the semi-major axis' decay rate, the rate of change of the orbit's inclination. The on-board estimation of the semi-major axis' decay rate should be improved eventually with the inclusion of on-ground estimated perturbation environment parameters (e.g. solar fluxes, geomagnetic indices, etc.) which could be uploaded periodically to the spacecraft. The effect of the navigation errors on the maneuvers computation can be reduced by using a smooth and filtering technique similar to that used for the on-board estimation of the semi-major axis' decay rate. By using a 70x70 Earth's gravitational field model, and eventually the third body perturbation, in the on-board orbit propagator, the RO could be generated on-board without any loss of accuracy. The PRISMA control software could be easily further developed also for the control of the orbit's eccentricity and inclination. Some improvements to ease the ground operations for the software monitoring concern also the on-board RO management and the telemetry.

A further development is also the combination of autonomous absolute and relative orbit control. As a first step the DLR's autonomous formation and orbit maintenance systems on PRISMA could be made to work at the same time. The results of the numerical simulation performed for the evaluation of the formation behaviour are promising. A big step forward would be then the mathematical formalization of the problem and the minimization of the fuel consumption by an optimal allocation of the absolute and relative control tasks among the two spacecraft.

A. Linearized Orbit Model

A.1. Model Matrices

A.1.1. Gravity Field

$$\tilde{\mathbf{A}}_{\mathbf{g}} = \frac{3}{4}\left(\frac{R_E}{a}\right)^2 \frac{nJ_2}{(1-e^2)^2} \begin{pmatrix} 0 \\ -(5\cos^2 i - 1)e_y \\ (5\cos^2 i - 1)e_x \\ 0 \\ -2\cos i \\ 5\cos^2 i - 1 + (3\cos^2 i - 1)\sqrt{1-e^2} \end{pmatrix} + \begin{pmatrix} 0 \\ 0 \\ 0 \\ 0 \\ 0 \\ n \end{pmatrix} \tag{A.1}$$

$$\mathbf{A}_{\mathbf{g}} = \mathbf{J}_{\mathbf{A}_{\mathbf{g}}}(\boldsymbol{\kappa}) = \frac{3}{4}\left(\frac{R_E}{a}\right)^2 \frac{nJ_2}{(1-e^2)^2} \begin{pmatrix} 0 & 0 & 0 & 0 & 0 & 0 \\ a_{g_{21}} & a_{g_{22}} & a_{g_{23}} & a_{g_{24}} & 0 & 0 \\ a_{g_{31}} & a_{g_{32}} & a_{g_{33}} & a_{g_{34}} & 0 & 0 \\ 0 & 0 & 0 & 0 & 0 & 0 \\ a_{g_{51}} & a_{g_{52}} & a_{g_{53}} & a_{g_{54}} & 0 & 0 \\ a_{g_{61}} & a_{g_{62}} & a_{g_{63}} & a_{g_{64}} & 0 & 0 \end{pmatrix} - \begin{pmatrix} 0 & \dots & 0 \\ \vdots & \ddots & \vdots \\ (3n/2a)a_{\mathcal{R}} & \dots & 0 \end{pmatrix} \tag{A.2}$$

$$a_{g_{21}} = \frac{7a_{\mathcal{R}}}{2a}(5\cos^2 i - 1)e_y \qquad a_{g_{22}} = -\frac{4(5\cos^2 i - 1)}{(1-e^2)}e_x e_y$$

$$a_{g_{23}} = -(5\cos^2 i - 1)\left[\frac{4e_y^2}{(1-e^2)} + 1\right] \qquad a_{g_{24}} = 10e_y \sin i \cos i$$

$$a_{g_{31}} = -\frac{7a_{\mathcal{R}}}{2a}(5\cos^2 i - 1)e_x \qquad a_{g_{32}} = (5\cos^2 i - 1)\left[\frac{4e_x^2}{(1-e^2)} + 1\right]$$

$$a_{g_{33}} = \frac{4(5\cos^2 i - 1)}{(1-e^2)}e_x e_y \qquad a_{g_{34}} = -10e_x \sin i \cos i$$

$$a_{g_{51}} = \frac{7a_{\mathcal{R}}\cos i}{a \sin i_{\mathcal{R}}} \qquad a_{g_{52}} = -\frac{8e_x \cos i}{(1-e^2)\sin i_{\mathcal{R}}}$$

$$a_{g_{53}} = -\frac{8e_y \cos i}{(1-e^2)\sin i_{\mathcal{R}}} \qquad a_{g_{54}} = \frac{2\sin i}{\sin i_{\mathcal{R}}}$$

$$a_{g_{61}} = -\frac{7a_{\mathcal{R}}}{2a}\left[5\cos^2 i - 1 + (3\cos^2 i - 1)\sqrt{1-e^2}\right]$$

$$a_{g_{62}} = \frac{e_x}{(1-e^2)}\left[4(5\cos^2 i - 1) + 3(3\cos^2 i - 1)\sqrt{1-e^2}\right]$$

$$a_{g_{63}} = \frac{e_y}{(1-e^2)}\left[4(5\cos^2 i - 1) + 3(3\cos^2 i - 1)\sqrt{1-e^2}\right]$$

$$a_{g_{64}} = -2(5 + 3\sqrt{1-e^2})\sin i \cos i$$

A.1.2. Atmospheric Drag

$$\tilde{\mathbf{A}}_{\mathbf{d}} = -\frac{A}{m} C_D \rho \begin{pmatrix} \sqrt{\mu a} \\ (e_x + \cos u)\sqrt{\mu/a} \\ (e_y + \sin u)\sqrt{\mu/a} \\ 0 \\ 0 \\ 0 \end{pmatrix} \tag{A.3}$$

$$\mathbf{A}_{\mathbf{d}} = \mathbf{J}_{\mathbf{A}_{\mathbf{d}}}(\boldsymbol{\kappa}) = \frac{A}{m} C_D \rho \begin{pmatrix} a_{d_{11}} & 0 & 0 & 0 & 0 & 0 \\ a_{d_{21}} & a_{d_{22}} & 0 & 0 & 0 & a_{d_{26}} \\ a_{d_{31}} & 0 & a_{d_{33}} & 0 & 0 & a_{d_{36}} \\ 0 & 0 & 0 & 0 & 0 & 0 \\ 0 & 0 & 0 & 0 & 0 & 0 \\ 0 & 0 & 0 & 0 & 0 & 0 \end{pmatrix} \tag{A.4}$$

$$a_{d_{11}} = -\frac{1}{2a_{\mathcal{R}}}\sqrt{\frac{\mu}{a}} \qquad a_{d_{21}} = \frac{1}{2} n (e_x + \cos u) a_{\mathcal{R}} \qquad a_{d_{22}} = -\sqrt{\frac{\mu}{a}} \qquad a_{d_{26}} = \sqrt{\frac{\mu}{a}} \sin u$$

$$a_{d_{31}} = \frac{1}{2} n (e_y + \sin u) a_{\mathcal{R}} \qquad a_{d_{33}} = -\sqrt{\frac{\mu}{a}} \qquad a_{d_{36}} = -\sqrt{\frac{\mu}{a}} \cos u$$

A.1.3. Control Matrix

$$\mathbf{B} = \frac{1}{n\Delta t}\begin{pmatrix} 0 & 2 & 0 \\ \sin u & 2\cos u & 0 \\ -\cos u & 2\sin u & 0 \\ 0 & 0 & \cos u \\ 0 & 0 & \sin u \\ -2 & 0 & -\sin u/\tan i \end{pmatrix} \quad , \quad \Delta t = 1s \tag{A.5}$$

A.2. Characteristic Polynomial

$$|s\mathbf{I} - \mathbf{A}| = s^6 + p_1 s^5 + p_2 s^4 + p_3 s^3 + p_4 s^2 = 0 \tag{A.6}$$

$$p_1 = -a_{11} + a_{22} + a_{33}$$

$$p_2 = a_{11}(a_{22} + a_{33}) + a_{22}a_{33} - a_{26}a_{62} - a_{36}a_{63} - a_{23}a_{32}$$

$$p_3 = a_{26}(a_{62}a_{33} - a_{63}a_{32}) + a_{36}(a_{63}a_{22} - a_{23}a_{62}) - a_{11}(a_{22}a_{33} - a_{26}a_{62} - a_{36}a_{63} - a_{23}a_{32})$$

$$p_4 = -a_{11}[a_{26}(a_{62}a_{33} - a_{63}a_{32}) + a_{36}(a_{63}a_{22} - a_{23}a_{62})]$$

A.2.1. Near Circular Orbits

In case $e \approx 0$

$$|s\mathbf{I} - \mathbf{A}| = s^3(s - a_{11})[\, s^2 - (a_{22} + a_{33})s + a_{22}a_{33} - a_{26}a_{62} - a_{36}a_{63} - a_{23}a_{32}\,] = 0 \tag{A.7}$$

$$s_1 = s_2 = s_3 = 0 \qquad s_4 = -\frac{\beta}{2}\sqrt{\frac{\mu}{a}} \tag{A.8}$$

$$s_5 = -\beta\sqrt{\frac{\mu}{a}} - \alpha(5\cos^2 i - 1)j \qquad s_6 = -\beta\sqrt{\frac{\mu}{a}} + \alpha(5\cos^2 i - 1)j \tag{A.9}$$

A.2.2. Near Circular Orbits and no Drag

In case $e \approx 0$ and the atmospheric drag perturbation force is not considered ($a_{11} = 0$, $a_{26} = 0$, $a_{36} = 0$)

$$|s\mathbf{I} - \mathbf{A}| = s^4[\, s^2 - (a_{22} + a_{33})s + a_{22}a_{33} - a_{23}a_{32}\,] = 0 \tag{A.10}$$

$$s_1 = s_2 = s_3 = s_4 = 0 \qquad s_5 = -\alpha(5\cos^2 i - 1)j \qquad s_6 = +\alpha(5\cos^2 i - 1)j \tag{A.11}$$

A.3. Transfer Function

$$(s\mathbf{I} - \mathbf{A})^{-1} = \frac{1}{|s\mathbf{I} - \mathbf{A}|} \cdot \begin{pmatrix} a^*_{11} & 0 & 0 & 0 & 0 & 0 \\ 0 & a^*_{22} & a^*_{23} & 0 & 0 & a^*_{26} \\ 0 & a^*_{32} & a^*_{33} & 0 & 0 & a^*_{36} \\ 0 & 0 & 0 & a^*_{44} & 0 & 0 \\ 0 & 0 & 0 & 0 & a^*_{55} & 0 \\ 0 & a^*_{62} & a^*_{63} & 0 & 0 & a^*_{66} \end{pmatrix} \tag{A.12}$$

$$\begin{aligned}
a^*_{11} =& s^6 - (a_{11} + a_{22} + a_{33})s^5 + [\, a_{11}(a_{22} + a_{33}) + a_{22}a_{33} - a_{26}a_{62} - a_{36}a_{63} - a_{23}a_{32}\,]s^4 + \\
&+[\, a_{26}(a_{62}a_{33} - a_{63}a_{32}) + a_{36}(a_{63}a_{22} - a_{23}a_{62}) - a_{11}(a_{22}a_{33} - a_{26}a_{62} - a_{36}a_{63} - a_{23}a_{32})\,]s^3 + \\
&-a_{11}[\, a_{26}(a_{62}a_{33} - a_{63}a_{32}) + a_{36}(a_{63}a_{22} - a_{23}a_{62})\,]s^2 \\
a^*_{22} =& s^6 - (a_{11} + a_{22} + a_{33})s^5 + [\, a_{33}(a_{11} + a_{22}) + a_{11}a_{22} - a_{36}a_{63}\,]s^4 + \\
&+[\, a_{36}a_{63}(a_{11} + a_{22}) - a_{11}a_{22}a_{33}\,]s^3 - a_{11}a_{22}a_{36}a_{63}s^2 \\
a^*_{23} =& -a_{23}a_{32}s^4 + a_{32}(a_{11}a_{23} - a_{26}a_{63})s^3 + a_{11}a_{32}a_{26}a_{63}s^2 \\
a^*_{26} =& -a_{26}a_{62}s^4 + a_{62}(a_{11}a_{26} + a_{26}a_{33} - a_{23}a_{36})s^3 - a_{11}a_{62}(a_{26}a_{33} - a_{23}a_{36})s^2 \\
a^*_{32} =& -a_{23}a_{32}s^4 + a_{23}(a_{11}a_{32} - a_{36}a_{62})s^3 + a_{11}a_{23}a_{36}a_{62}s^2
\end{aligned}$$

$$a^*_{33}=s^6-(a_{11}+a_{22}+a_{33})s^5+[\,a_{22}(a_{11}+a_{33})+a_{11}a_{33}-a_{26}a_{62}\,]s^4+$$
$$+[\,a_{26}a_{62}(a_{11}+a_{33})-a_{11}a_{22}a_{33}\,]s^3-a_{11}a_{33}a_{26}a_{62}s^2$$

$$a^*_{36}=-a_{36}a_{63}s^4+a_{63}(a_{11}a_{36}+a_{22}a_{36}-a_{26}a_{32})s^3-a_{11}a_{63}(a_{26}a_{32}-a_{22}a_{36})s^2$$

$$a^*_{44}=s^6-(a_{11}+a_{22}+a_{33})s^5+[\,a_{11}(a_{22}+a_{33})+a_{22}a_{33}-a_{26}a_{62}-a_{36}a_{63}-a_{23}a_{32}\,]s^4+$$
$$+[\,a_{36}(a_{22}a_{63}-a_{23}a_{62})+a_{26}(a_{33}a_{62}-a_{32}a_{63})-a_{11}(a_{22}a_{33}-a_{26}a_{62}-a_{36}a_{63}-a_{23}a_{32})\,]s^3$$
$$-a_{11}[\,a_{36}(a_{22}a_{63}-a_{23}a_{62})+a_{26}(a_{33}a_{62}-a_{32}a_{63})\,]s^2$$

$$a^*_{55}=s^6-(a_{11}+a_{22}+a_{33})s^5+[\,a_{11}(a_{22}+a_{33})+a_{22}a_{33}-a_{26}a_{62}-a_{36}a_{63}-a_{23}a_{32}\,]s^4$$
$$+[\,a_{36}(a_{22}a_{63}-a_{23}a_{62})+a_{26}(a_{33}a_{62}-a_{32}a_{63})-a_{11}(a_{22}a_{33}-a_{26}a_{62}-a_{36}a_{63}-a_{23}a_{32})\,]s^3$$
$$-a_{11}[\,a_{36}(a_{22}a_{63}-a_{23}a_{62})+a_{26}(a_{33}a_{62}-a_{32}a_{63})\,]s^2$$

$$a^*_{62}=-a_{26}a_{62}s^4+a_{26}(a_{11}a_{62}+a_{33}a_{62}-a_{32}a_{63})s^3-a_{11}a_{26}(a_{33}a_{62}-a_{32}a_{63})s^2$$

$$a^*_{63}=-a_{36}a_{63}s^4+a_{36}(a_{11}a_{63}+a_{22}a_{63}-a_{23}a_{62})s^3-a_{11}a_{36}(a_{23}a_{62}-a_{22}a_{63})s^2$$

$$a^*_{66}=s^6-(a_{11}+a_{22}+a_{33})s^5+[\,a_{11}(a_{22}+a_{33})+a_{22}a_{33}-a_{23}a_{32}\,]s^4-a_{11}(a_{22}a_{33}-a_{23}a_{32})s^3$$

B. Navigation Accuracy in Numerical Simulations

Figures B.1 and B.2 and Tables B.1 and B.2 show the accuracy of the on board estimated absolute position in the RTN orbital frame and of the orbital elements in the realistic simulations scenario.

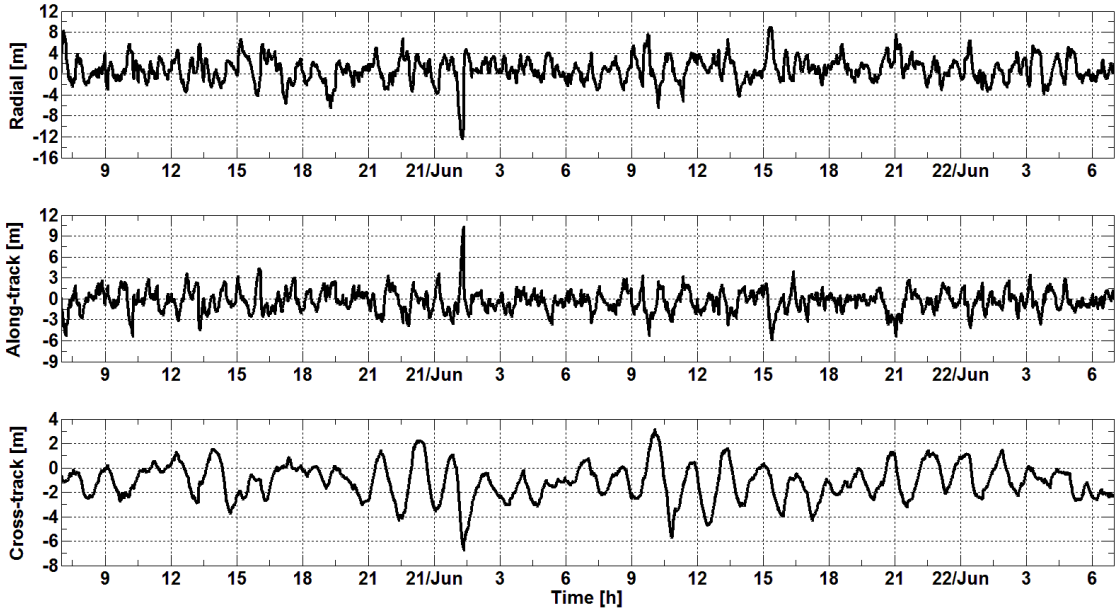

Figure B.1.: Accuracy of the on-board estimated position in RTN

Table B.1.: Navigation error - Position and velocity in RTN

	R [m]	T [m]	N [m]	Pos. 3D [m]	v_R [m/s]	v_T [m/s]	v_N [m/s]	Vel. 3D [m/s]
Mean	0.86	-0.30	-1.13	3.04	$3{\cdot}10^{-5}$	$-3.5{\cdot}10^{-5}$	$-2.3{\cdot}10^{-5}$	$4.35{\cdot}10^{-3}$
σ	2.32	1.51	1.42	1.60	$3{\cdot}10^{-3}$	$3.7{\cdot}10^{-3}$	$2{\cdot}10^{-3}$	$2.7{\cdot}10^{-3}$
RMS	2.47	1.54	1.81	3.43	$3{\cdot}10^{-3}$	$3.7{\cdot}10^{-3}$	$2{\cdot}10^{-3}$	$5.1{\cdot}10^{-3}$

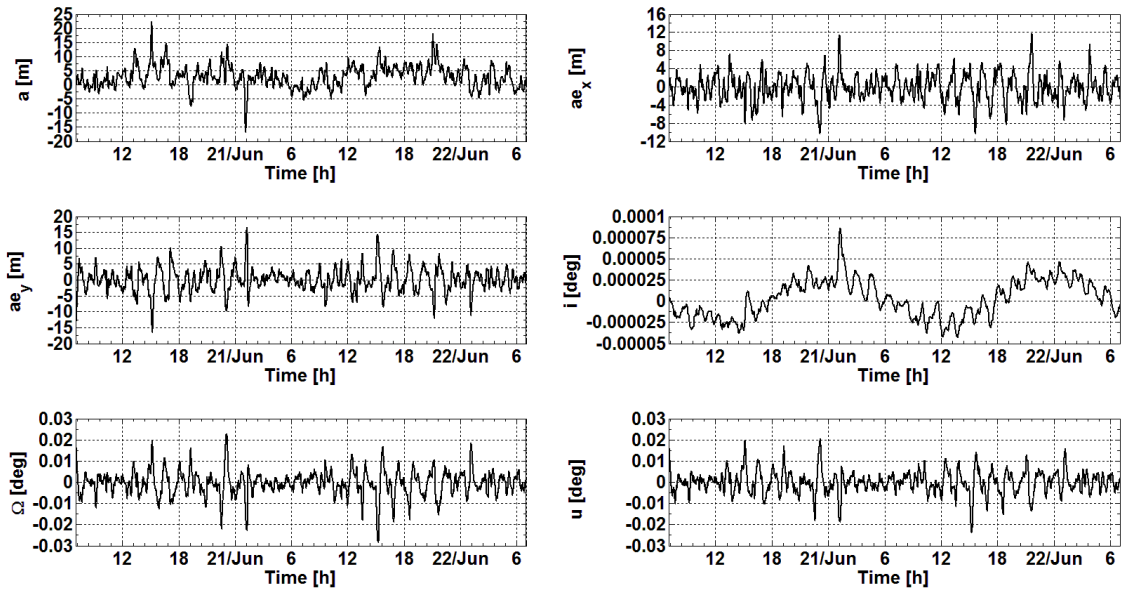

Figure B.2.: Accuracy of the on-board estimated orbital elements

Table B.2.: Navigation error - Orbital elements

	a [m]	ae_x [m]	ae_y [m]	i [deg]	Ω [m]	u [deg]
Mean	2.78	-0.18	0.01	$3{\cdot}10^{-6}$	$-3.8{\cdot}10^{-4}$	$2.7{\cdot}10^{-5}$
σ	3.94	2.99	3.71	$2.2{\cdot}10^{-5}$	$6.1{\cdot}10^{-3}$	$5.6{\cdot}10^{-3}$
RMS	4.82	2.99	3.71	$2.2{\cdot}10^{-5}$	$6.1{\cdot}10^{-3}$	$5.6{\cdot}10^{-3}$

C. Numerical Simulations of Combined Autonomous Absolute and Relative Orbit Control

This chapter is dedicated to the analysis of the combined autonomous absolute and relative control of a two spacecraft formation in LEO using different types of on-board feedback control. One of the two spacecraft keeps its orbit's parameters within the control windows imposed around nominal values which characterize a reference orbit. The other spacecraft controls instead the relative motion. A distributed control tasks assignment over time is suggested in order to keep the mass of the two spacecraft as similar as possible. With this approach the differential drag, and thus the fuel consumption, can be minimized and the mission lifetime maximized. The autonomous formation control is meant to meet the payload requirements and to keep the required formation geometry safe from a collision risk. The collision avoidance criterion used is the maintenance of a (anti-)parallel alignment of the relative eccentricity and inclination vectors [143,146]. In this context the autonomous control has an added value as it allows a prompt reaction to unexpected events. The secular non-keplerian perturbation forces acting on both satellites alter the nominal formation configuration. The most critical change is the clockwise drift of the relative eccentricity vector $\boldsymbol{\delta e}$ that tends to the perpendicular of the relative inclination vector $\boldsymbol{\delta i}$, thus increasing the collision risk. As a consequence, the formation must be controlled to maintain the predefined orientation of the two vectors. A ground-based control has to regularly keep the formation configuration by commanding small orbit correction maneuvers. In most cases the ground station contacts are limited due to the geographic position of the sta-

tion and the costs for contact time. A ground station placed at a middle latitude allows about two scheduled contacts every twelve hours for a LEO satellite. Only the availability of a polar ground station guarantees a contact at each orbit. While this limitation is usually not critical for single satellite operations, the visibility constraints determine the achievable orbit control accuracy for a LEO formation if a ground based approach is chosen. An autonomous relative orbit control system can provide a robust formation keeping improving the control performance as the orbital maneuvers are planned and executed more frequently. The combination of autonomous absolute and relative orbit control can thus enhance the overall control performance, reactivity in case of contingency and reduce the ground support efforts and costs.

Analytical and numerical control methods have been considered. The overall strategy is verified using the TerraSAR-X/TanDEM-X formation (Sec. 1.5) as case study. This is the typical LEO remote sensing mission which could take advantage of the autonomous orbit control discussed here. In the simulations, run over 30 days, the absolute orbit of spacecraft TSX is controlled by the AOK analytical controller (Sec. 4.1 and 7) or an in-plane linear regulator (Sec. 4.3.1). These absolute orbit control methods are combined with the autonomous relative analytical controller validated with the SAFE experiment [92,143] on the PRISMA mission. The initial state of Table 3.9 has been used for TSX. The relative initial state of TDX is $(\delta a, a\delta e_x, a\delta e_y, a\delta i_x, a\delta i_y, a\delta u) = (0, 0, 300, 0, -400, 0)$ m in compliance with the collision risk minimization criteria of parallel/anti-parallel eccentricity and inclination vectors [143-145]. The goal of the relative control is to keep this initial safe formation geometry. The simulation parameters and the physical properties of TSX and TDX, considered identical spacecraft, are collected in Table 3.8. No navigation or actuator errors are included in the numerical simulations.

C.1. SAFE Closed-Form Analytical Control

Depending on the required orbit control accuracy, along-track, radial and cross-track maneuvers (in the form of single or double pulses) are executed at regular time intervals in a deterministic fashion according to the following solutions [92].

An arbitrary correction of the relative inclination vector $\boldsymbol{\delta i}$ can be realized through a single cross-track maneuver of size Δv_N at location u_m, given by

$$\Delta v_N na \|\boldsymbol{\delta i}_{aft} - \boldsymbol{\delta i}_{bef}\| = na\|\Delta\boldsymbol{\delta i}\| \quad \text{at} \quad u_m = \arctan(\Delta\delta i_y/\Delta\delta i_x) \tag{C.1}$$

where the superscripts aft and bef denote relative orbital elements immediately before and after the maneuver under consideration. Eq. (C.1) represents the minimum delta-v solution for out-of-plane control.

The minimum delta-v solution for in-plane control provides an arbitrary correction of the remaining relative orbital elements according to the following double-impulse scheme

$$\Delta v_{T_1} = na(\Delta\delta a + \|\Delta\boldsymbol{\delta e}\|)/4 \quad \text{at} \quad u_{m_1} = \arctan(\Delta\delta e_y/\Delta\delta e_x) \tag{C.2}$$

$$\Delta v_{T_2} = na\Delta\delta a/2 \quad \text{at} \quad u_{m_2} = u_{m_1} + \pi \tag{C.3}$$

where along-track maneuvers in flight or anti-flight direction are separated by a half-orbit (the subscripts 1 and 2 indicate the first and second maneuvers of the same pair). Here, $\Delta\delta a$ and $\Delta\boldsymbol{\delta e}$ represent the desired corrections computed before the execution of the each individual maneuver of the pair.

An alternative approach for in-plane control is based on the execution of radial maneuvers separated by a half-orbit given by

$$\Delta v_{R_1} = na(\Delta\delta\lambda + \|\Delta\boldsymbol{\delta e}\|)/2\ ,\ \Delta v_{T_1} = na(\Delta\delta a/4) \quad \text{at} \quad u_{m_1} = \arctan(\Delta\delta e_y/\Delta\delta e_x) \tag{C.4}$$

$$\Delta v_{R_2} = -na\Delta\delta\lambda/2 \quad , \quad \Delta v_{T_2} = na\Delta\delta a/2 \quad \text{at} \quad u_{m_2} = u_{m_1} + \pi \tag{C.5}$$

The choice of the most appropriate in-plane control strategy, i.e. the usage of Eqs. (C.2)-(C.3) or Eqs. (C.4)-(C.4) is mission and application dependant. Pairs of tangential-only maneuvers ensure minimum propellant consumption, but when used for routine formation-keeping, cause unintentional drifts in along-track direction due to the continuous corrections of the semi-major axis. Pairs of radial maneuvers do not affect the semi-major axis and can realize smaller corrections of the relative orbital elements, due to the double delta-v consumption and the consequent

longer burn times. The autonomous formation control (AFC) software module used during the SAFE experiment on PRISMA features two modes: the closed-loop along-track mode (CL-T) based on Eqs. (C.2)-(C.3) and the closed-loop radial mode (CL-R) based on Eqs. (C.4)-(C.4). CL-T is mainly used for large reconfigurations in along-track directions in rendezvous scenarios, whereas CL-R is preferred to accurately control the formation for tight reconfigurations at short separations in fly-around and inspection phases.

C.2. Combination of the AOK and SAFE Analytical Controllers

C.2.1. AOK Absolute Orbit Control

Figures C.1 and C.2 show the ROE and REFE (computed at the ascending node), and the along-track control maneuvers Δv_T executed by spacecraft TSX in case the orbit control system is designed with the algorithms of Eq. (4.2) (AOK control). The control window is $\delta L_{\lambda_{MAX}} = \pm 250$ m. The same general considerations of Sec. 5.2 and Chap. 6 about AOK's features are valid here.

Fig. C.2 shows that the control of δL_λ is characterized by a strict determinism. Three along-

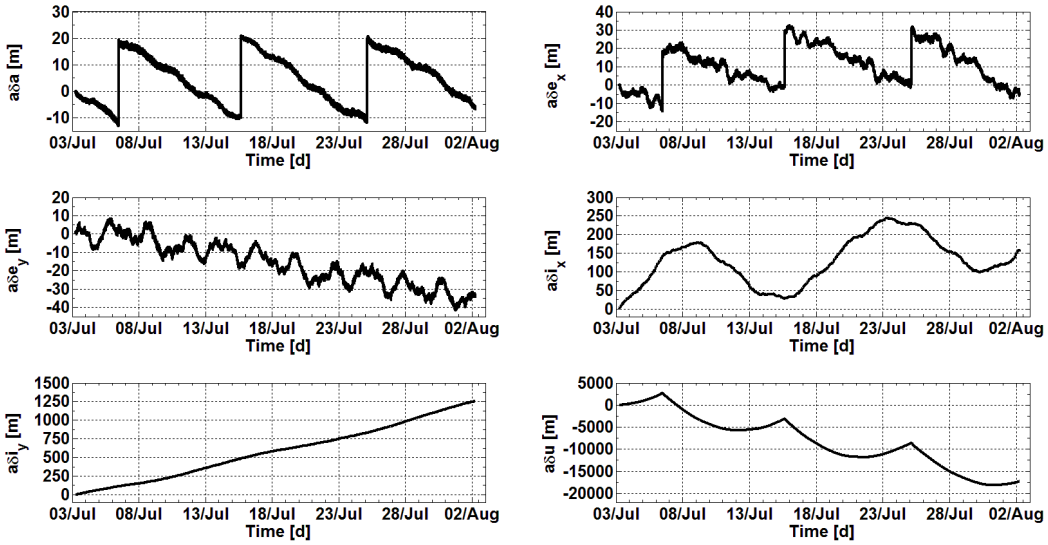

Figure C.1.: Relative orbital elements (AOK)

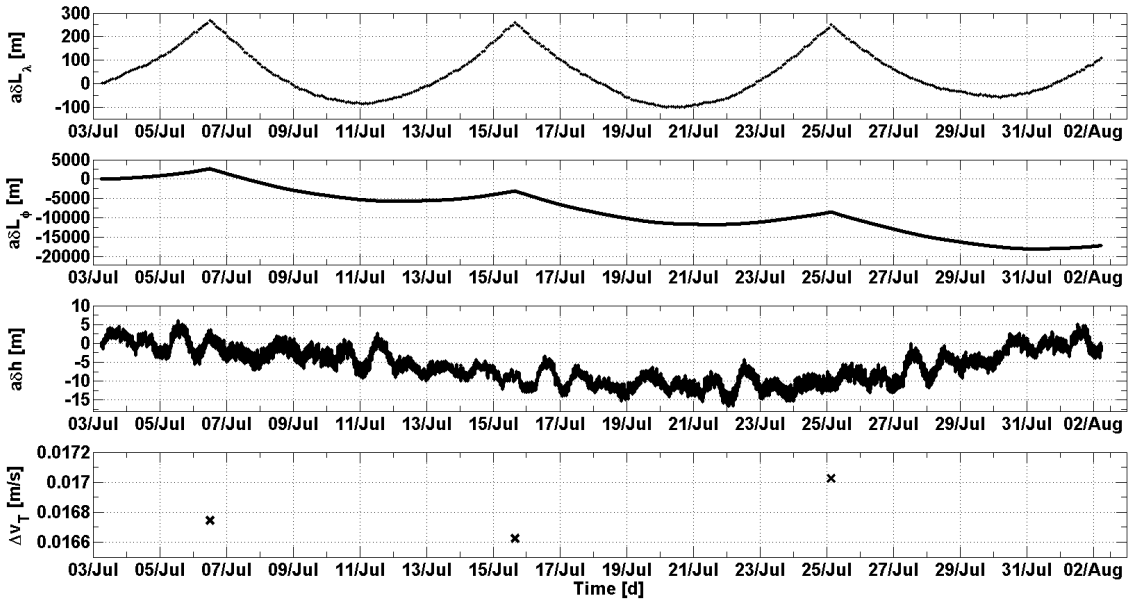

Figure C.2.: Relative Earth-fixed elements and executed orbital maneuvers - AOK

track maneuvers of about 0.17 m/s are executed with a maneuver cycle of 8 days. The vertices of the parabolas which characterize the time evolution of δL_λ are not placed in proximity of the lower bound of the control window at -250 m. This is due to the fact that the long term prediction of $\delta L_\lambda = k_1 \delta i_y + k_2 \delta L_\varphi$ (Eqs. (2.31)-(2.33)) on which the maneuvers' computation is based, does not include the contribution of δi_x to the variation of δi_y (see Eqs. (2.11), (4.2), (2.28) and (4.26)) but only that of δa. This approximation of the model used by the AOK control system is highlighted by this test case in which the control cycle is 8 days. Indeed the weight of the contribution of δi_x to the variation of δL_λ increases with the duration of the maneuver cycle. Table C.1 collects the control performance and the maneuver budget. The total Δv spent is 0.05 m/s.

Table C.1.: Control performance and maneuver budget of AOK control

$\boldsymbol{\delta L}$ **[m]**	**Min**	**Max**	**Mean**	σ	**RMS**
$\boldsymbol{\delta L_\lambda}$	-101.97	269.71	40.87	100.31	108.31
$\boldsymbol{\delta L_\varphi}$	-17938.72	2688.1	-8074.03	5923.36	10013.8
$\boldsymbol{\delta L_h}$	-16.63	6.11	-6.15	4.65	7.71
$\boldsymbol{\Delta}$**v [m/s]**	**Min**		**Max**		**TOT**
$\boldsymbol{\Delta v_T}$	0.01663		0.01703		0.0504

C.2.2. SAFE Relative Control

Figures C.3 and C.4 show the ROE and REFE of TDX with respect to TSX when the absolute orbit of TSX is controlled by the AOK controller and the relative orbit of TDX is controlled by the SAFE controller working in along-track mode (Eqs. (C.2)-(C.3)). The REFE are computed at the ascending node. The control window of δe and δi are respectively 5 m and 2 m. The control is characterized by a strict determinism with an in-plane maneuver cycle of 6 hours during the steady-state phases as can be observed in Fig. C.5. Only one out-of-plane maneuver of 0.002 m/s is executed when δi_y exceeds the maximum allowed deviation of 2 m. The SAFE controller reacts to the absolute orbit control maneuvers of TSX which causes a sudden change of δa, δe_x and δe_y and re-acquires the formation configuration in about 1.5 days. Table C.2 collects the statistical quantities of the values assumed by δL_λ, δL_φ and δL_h during the steady-state phase between the 7$^{\text{th}}$ and 15$^{\text{th}}$ of July. The quantity δL_{err} indicates the difference between the actual and the nominal values of the on-ground baseline $\delta L = \sqrt{\delta L_\lambda^2 + \delta L_\varphi^2}$ formed by the spacecraft TSX and TDX. The control accuracies of δL_λ, δL_φ and δL_h in the steady-state phase are respectively 1.5, 168 and 6 m. The total Δv spent for the formation keeping during the simulation time of one month is 0.4 m/s. Fig. C.6 shows the time evolution of the on-ground

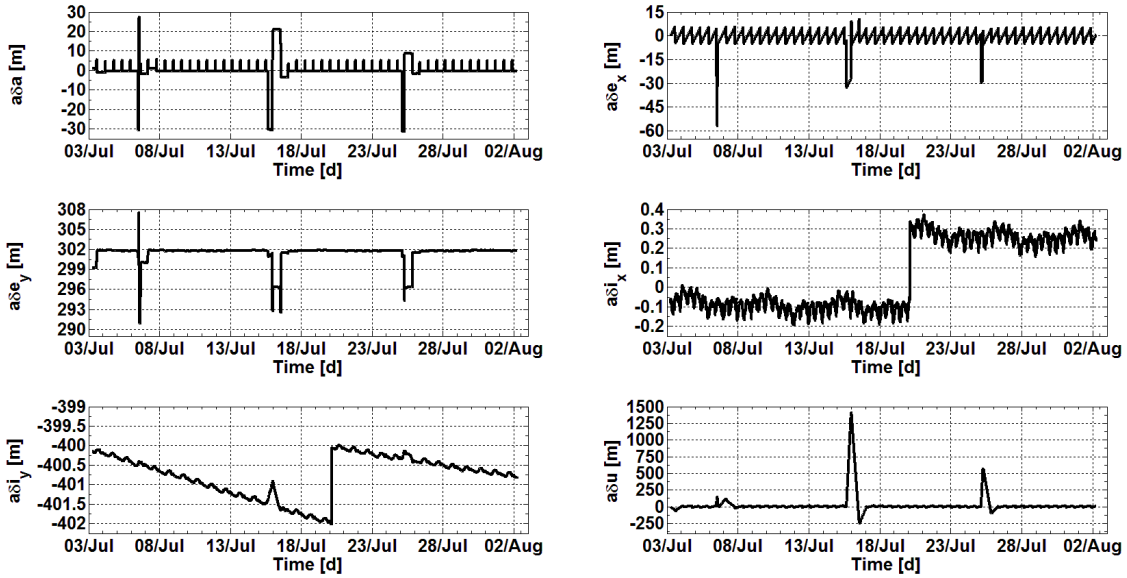

Figure C.3.: Relative orbital elements AFC-AOK

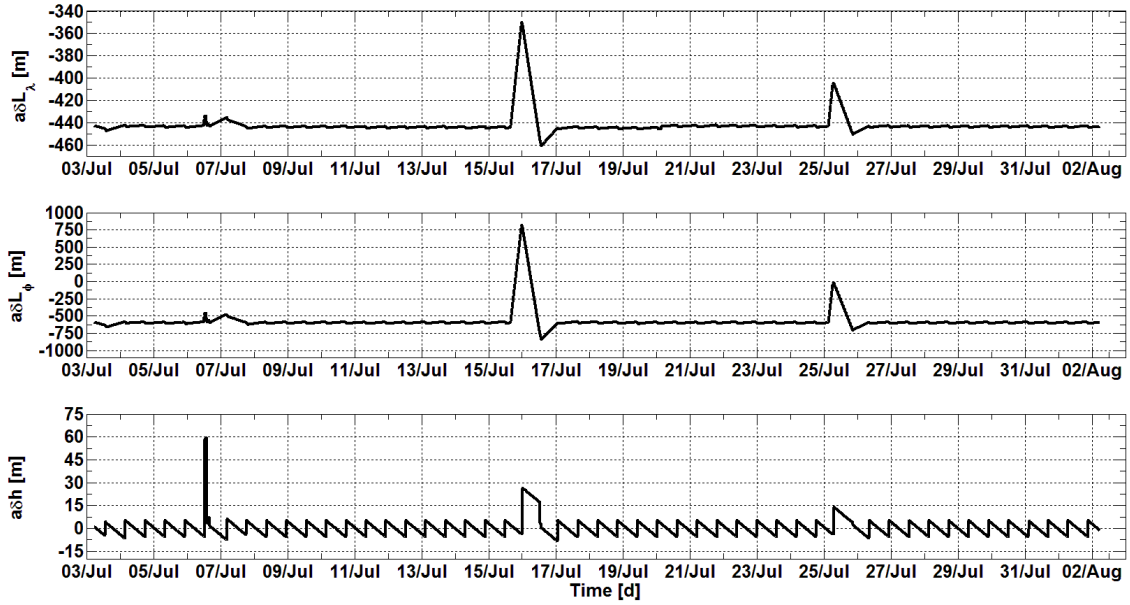

Figure C.4.: Relative Earth-fixed elements AFC-AOK

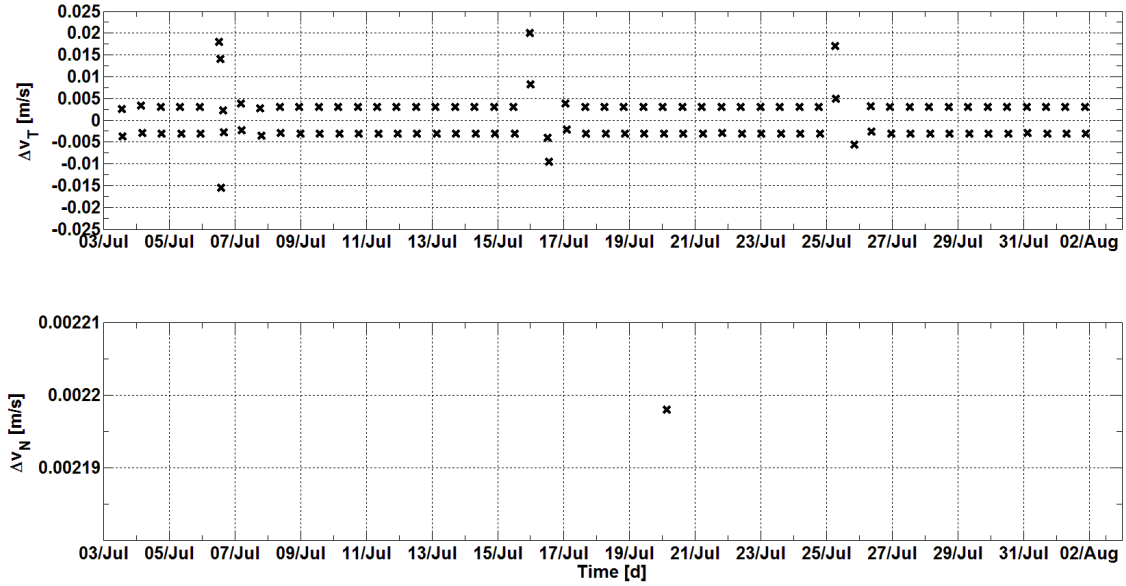

Figure C.5.: Executed formation control maneuvers AFC-AOK

baseline δL computed at the ascending node. The baseline, controlled with an accuracy of 7 m (1 σ) has a nominal value of 742 m and reaches a minimum and maximum length of respectively 400 and 950 m during the formation re-acquisition phases.

Table C.2.: Control performance and maneuver budget of AFC relative control

δL [m]	Min	Max	Mean	σ	RMS
δL_λ	-445.35	-442.99	-444.14	0.51	444.14
δL_φ	-845.89	821.31	-573.96	148.32	592.81
δL_h	-8.44	59.55	0.58	5.21	5.25
δL_{err}	-9.1	16.15	3.71	6.01	7.06
Δv [m/s]	Min		Max		TOT
Δv_T	-0.0155		0.0201		0.3997
Δv_N	0		0.0022		0.0022

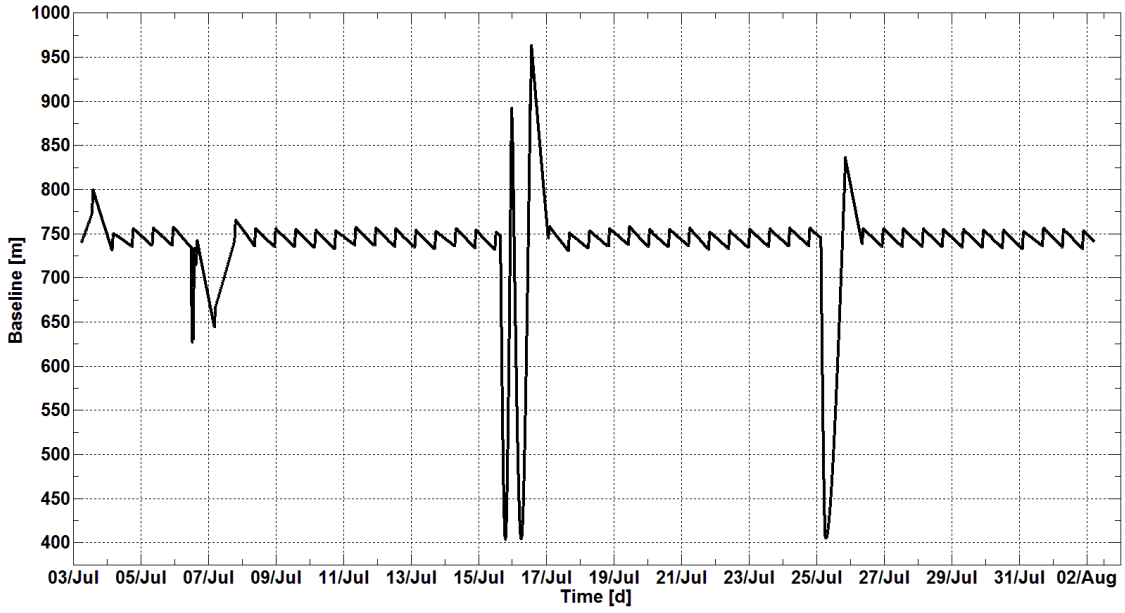

Figure C.6.: Earth-fixed baseline TSX-TDX

C.3. Combination of Linear and SAFE Controllers

C.3.1. Linear Absolute Orbit Control

Figures C.7 and C.8 show the ROE and REFE (computed at the ascending node), and the along-track control maneuvers Δv_T executed by spacecraft TSX in case the orbit control system is the linear regulator of Eq. (4.40). The maneuver duty cycle is 24 hours and the parameters for the calculation of the gains are $a\delta L_{\lambda_{MAX}} = 30$, $a(\delta L_\lambda/dt)_{MAX} = 30/(86400)$, $(\Delta v_{T_{MAX}})_{\delta L} = 0.004$ and $(\Delta v_{T_{MAX}})_{\delta L/dt} = 0.001$. Unlike the case of spacecraft MANGO (Fig. 5.4), the

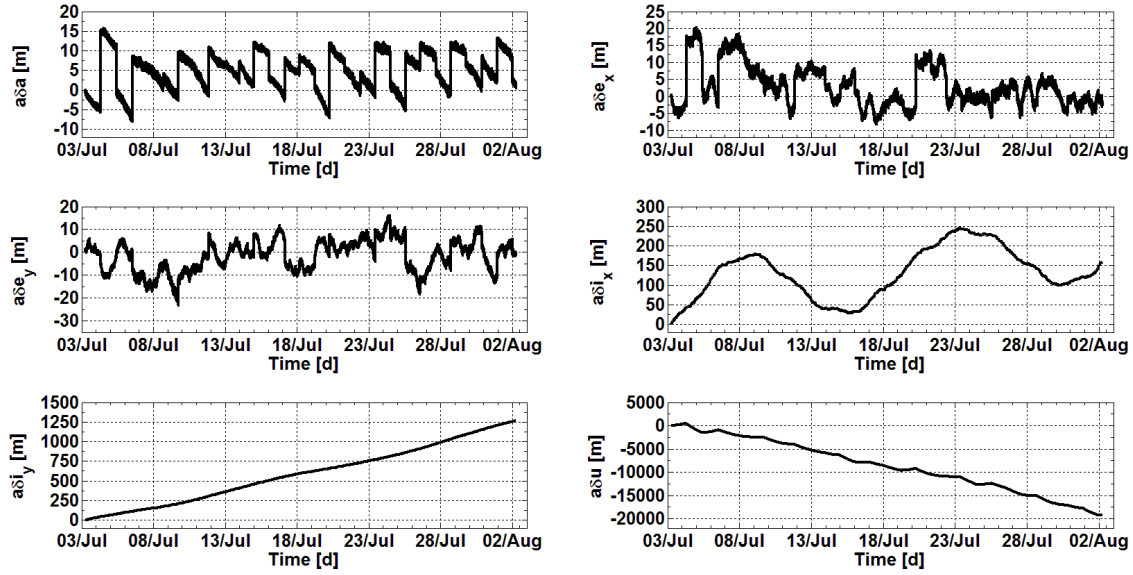

Figure C.7.: Relative orbital elements - Linear regulator

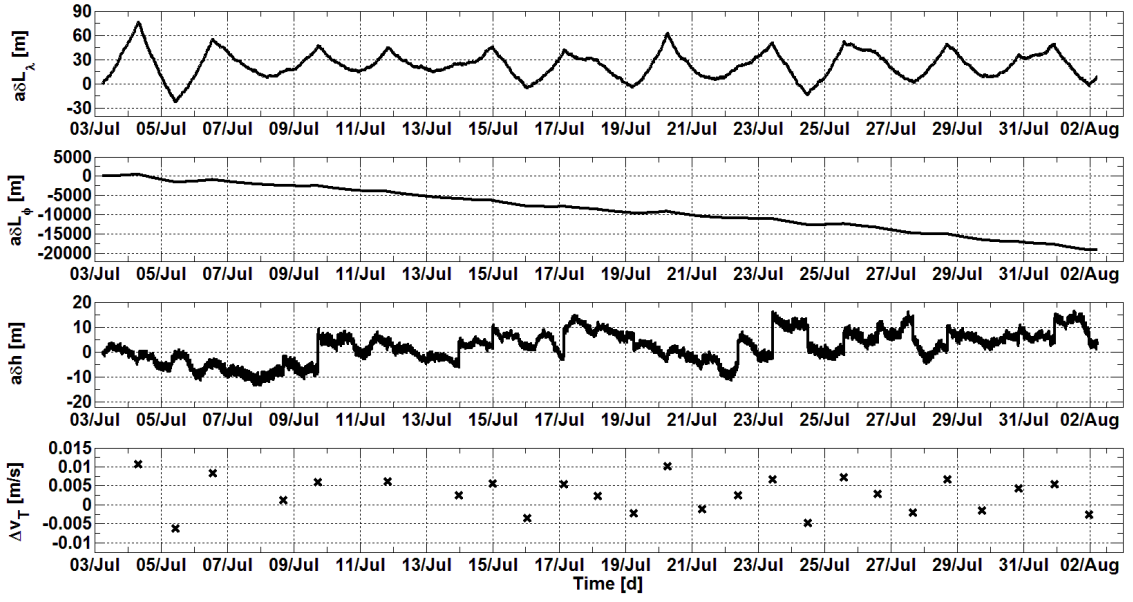

Figure C.8.: Relative Earth-fixed elements and executed orbital maneuvers - Linear regulator

maneuver placement rule of Eq. (4.43) is effective in controlling the components of the relative eccentricity vector because at the altitude of TSX the solar radiation pressure perturbation force is weaker and the spacecraft flies in a frozen eccentricity orbit. Table C.3 collects the control

performance and the maneuver budget. The total Δv spent is 0.12 m/s.

Table C.3.: Control performance and maneuver budget of in-plane linear control

δL [m]	Min	Max	Mean	σ	RMS
δL_λ	-22.6	76.44	23.42	16.07	28.41
δL_φ	-19108.0	505.68	-8562.02	5533.0	10194.23
δL_h	-13.33	16.59	1.85	6.07	6.34
Δv [m/s]	Min		Max		TOT
Δv_T	-0.0062		0.0108		0.1189

C.3.2. SAFE Relative Control

Figures C.9 and C.10 show the ROE and REFE of TDX with respect to TSX when the absolute orbit of TSX is controlled by the linear regulator and the relative orbit of TDX is controlled by the SAFE controller working in along-track mode (Eqs. (C.2)-(C.3)). The REFE are computed at the ascending node. The control window of δe and δi are respectively 5 m and 2 m. The lack of determinism in the absolute orbit control of TSX is reflected by the relative control as can be observed comparing the absolute and relative orbit maneuvers displayed in Figures C.8 and C.11.

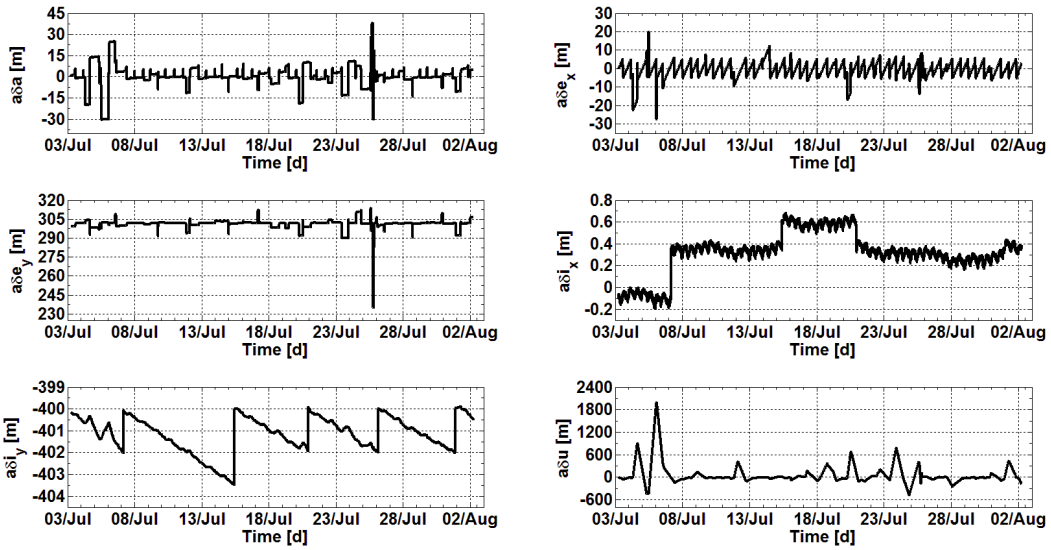

Figure C.9.: Relative orbital elements SAFE-Linear

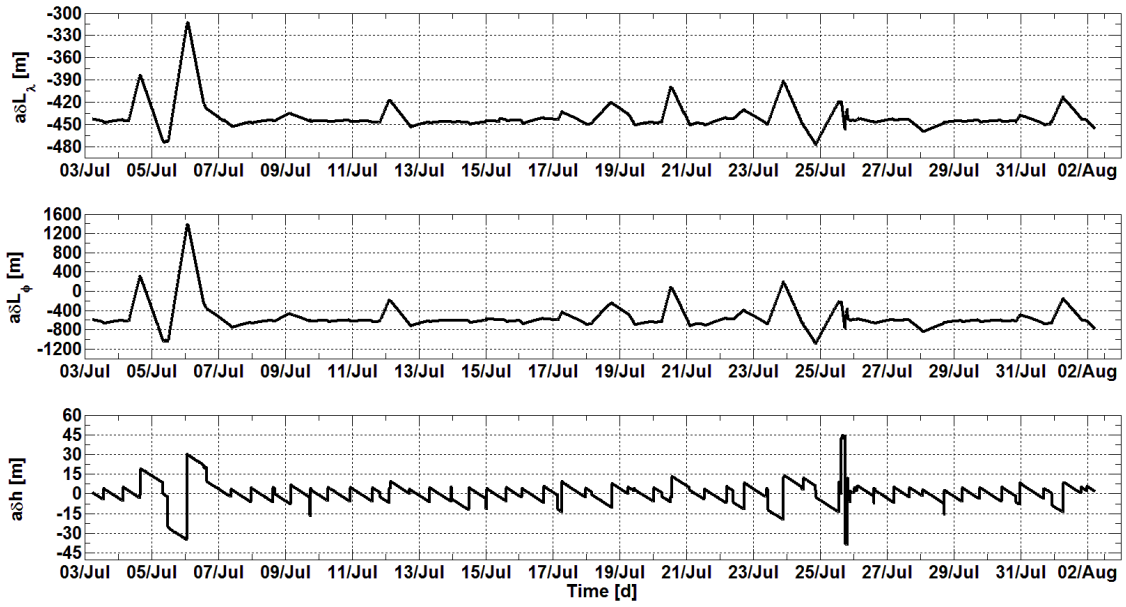

Figure C.10.: Relative Earth-fixed elements AFC-Linear

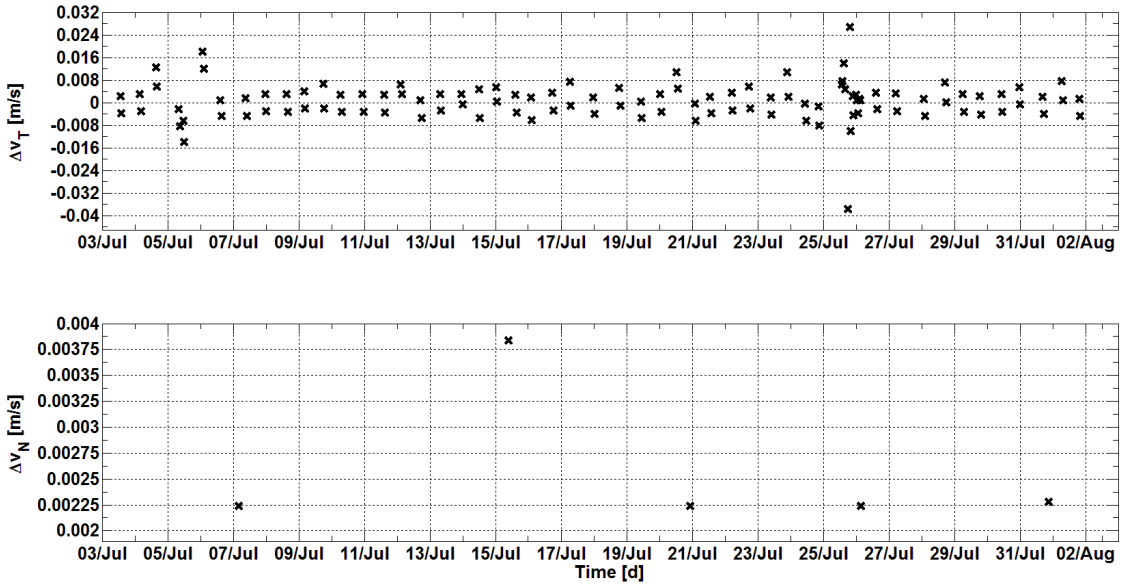

Figure C.11.: Executed formation control maneuvers AFC-Linear

The SAFE control system has to react to the orbital maneuver commanded by the linear regulator on-board TSX once per day. Table C.4 collects the statistical quantities of the values assumed by δL_λ, δL_φ, δL_h and δL_{err} during the entire simulation. The control accuracies

of δL_λ, δL_φ and δL_h are respectively 21, 340 and 10 m. The baseline is controlled with an accuracy of 134 m (1 σ) and reaches a minimum and maximum length of respectively 400 and 1400 m. The total Δv spent is 0.53 m/s.

Table C.4.: Control performance and maneuver budget of AFC relative control

$\boldsymbol{\delta L}$ **[m]**	**Min**	**Max**	**Mean**	σ	**RMS**
$\boldsymbol{\delta L_\lambda}$	-477.38	-312.3	-439.62	18.39	440.0
$\boldsymbol{\delta L_\varphi}$	-1089.65	1383.03	-528.86	276.17	596.62
$\boldsymbol{\delta L_h}$	-38.64	44.94	0.4	8.42	8.43
$\boldsymbol{\delta L_{err}}$	-338.72	676.17	-12.56	133.9	134.48
$\boldsymbol{\Delta}$**v [m/s]**	**Min**		**Max**		**TOT**
$\boldsymbol{\Delta v_T}$	-0.0377		0.0269		0.5166
$\boldsymbol{\Delta v_N}$	0		0.0038		0.0128

D. AOK Experiment Appendix

D.1. Orbit Perturbation Forces Environment

The AOK experiment was conducted in condition of minimum solar magnetic activity as it took place during the first phase of solar cycle 24 started in 2008. The small mean value of index F10.7 in comparison with other solar cycle phases can be appreciated in Fig. D.1. The F10.7 index is a measure of the solar radio flux per unit frequency at a wavelength of 10.7 cm near the peak of the observed solar radio emission while Kp summarizes the global level of geomagnetic activity. The F10.7 and Kp indices' values are a good reference in evaluating the variation of the atmospheric drag that is the main perturbation force at the altitude of MANGO. In fact the increase of the atmospheric drag is well correlated with solar Ultra Violet (UV) output and additional atmospheric heating that occurs during geomagnetic storms. For this reason most drag models use the radio flux at 10.7 cm wavelength as a proxy for solar UV flux while Kp is the index commonly used as a surrogate for short-term atmospheric heating due to geomagnetic storms. In general $F10.7 > 250$ and $Kp \geq 6$ result in detectably increased drag on LEO spacecraft. Fig. D.2 shows the evolution of solar flux indices F10.7 and Kp during the AOK experiment. A peak in the value of index F10.7 can be noticed in the first days of August when a geomagnetic storm took place as a consequence of the unleashing of M class flares by three sunspots. An analysis of MANGO's free motion was done during the AOK experiment preparation phase, in order to quantify the influence of the orbit perturbation forces environment on the decay of the semi-major axis and the consequent increase rate of the LAN during the AOK experiment. POD ephemerides of TANGO have been used for the analysis as TANGO, whose orbit is almost identical to that of MANGO, is actually in free motion not

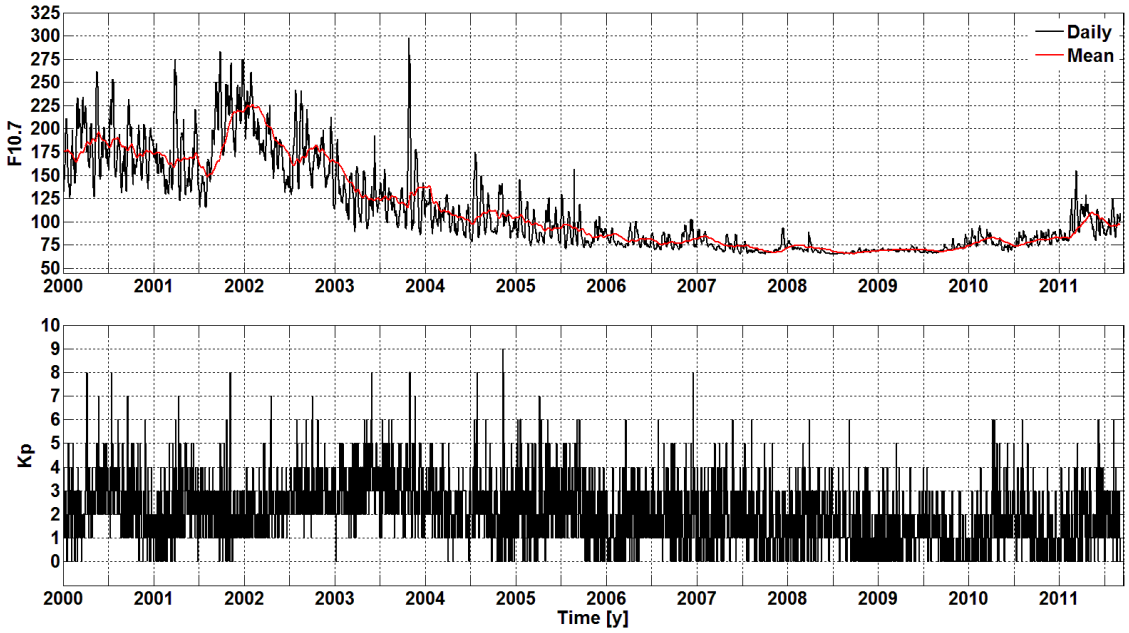

Figure D.1.: Solar flux indices F10.7 and Kp from January 2000 to September 2011

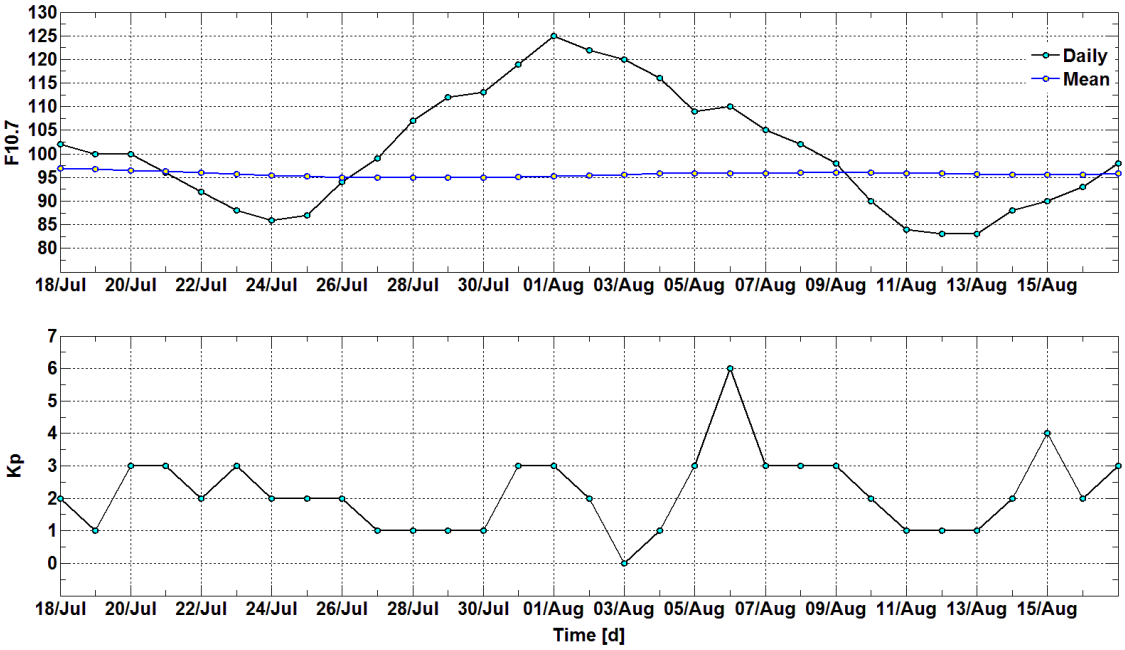

Figure D.2.: Solar flux indices F10.7 and Kp during the AOK experiment

having any orbit control capability. The POD ephemerides have been compared with a reference orbit propagated with a GRACE GGM01S 70x70 gravity field model with initial state TANGO's POD state as on 20th of June at 06:00:00 GPS time. The period considered was from 20th of June to the 18th of July in order to exploit the most accurate TANGO's POD products as after the 18th of July TANGO's GPS receiver was switched on only for one orbit each day. The results of this analysis are showed in Sec. 3.3.1

D.2. DVS Camera Activities

Digital Video System (DVS) activities have played an important role in the frame of the AOK experiment. They represent the practical demonstration of the possibility of remote sensing activities with an autonomous orbit control system. Referring to Table 7.2 the most relevant data-takes for the experiment are those made during the fine control phase starting from the 30th of July. Each of these DVS data-takes includes 14 shots taken in 10 minutes over about 5000 km on Earth. The DVS activities were planned by means of a routine that receives in input the region and time window of interest and gives in output the times of the data-takes possibilities with the respective ground tracks. Two main exercises were performed in planning the DVS data-takes. The first one was the periodical monitoring on a site of geological interest as an active volcano. Fig. 7.1 (left) shows the planning of such a data-take (red tracks are during the daylight). The main objective was the volcano Etna and its imaging was placed in the middle of the available ground track. The activation of the DVS camera for this data-takes (DVS_6 and DVS_9) was scheduled on 10th and 15th of August. The result is shown in Fig. 7.1 (right) where in the picture on top the plumes from volcanoes Etna and Stromboli can be noticed. The second exercise was the complete coverage of a certain area of interest by different data-takes in a limited time frame. This was done with DVS_5, DVS_6, DVS_11 and DVS_13 for South Europe and the result is shown in Fig. D.3.

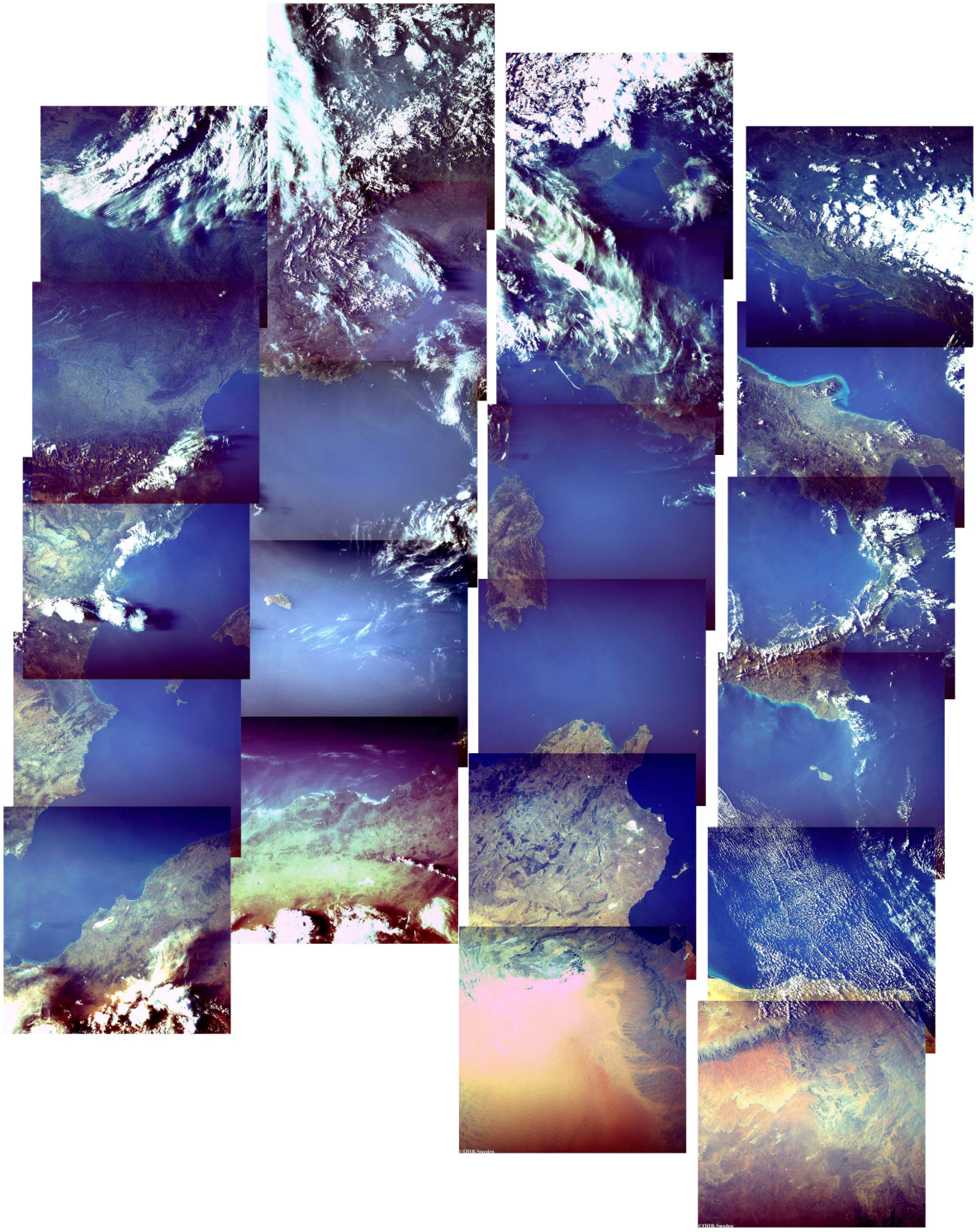

Figure D.3.: South Europe from 4th to 12th of August. Images courtesy of OHB Sweden.

D.3. The PRISMA Formation During the AOK Experiment

D.3.1. TANGO's Navigation

MANGO's on-board navigation system was designed to work in complete absence of TANGO's navigation data during the AOK experiment. Nevertheless it was decided to switch on TANGO's GPS receivers for one orbit each day. This was an operational compromise to keep the inter-satellite link MANGO - TANGO as long as possible and to have the possibility to get TANGO's GPS data to be input in the POD process, without jeopardizing the correct course of the AOK experiment. In fact if the GPS interface (GIF) receives both MANGO and TANGO messages, then it assumes that the navigation system works in duo mode. It tries thus to provide the latest set of synchronous valid GPS measurements from both satellites. If for some reason like receiver hick-up, ISL data gaps, etc. TANGO or MANGO messages are delayed or absent, then GIF provides alternatively TANGO or MANGO measurements depending on what has been done at the previous step. This improves the data diversity and coverage in duo mode, but if GOD is in solo mode it can cause a degradation of the quality of the GIF output leading to artificial data gaps and missed measurements updates. A navigation issue detected and solved in the first two days of the AOK experiment was caused by the fact that MANGO's was steadily receiving information about the GPS antenna used by TANGO. But as TANGO, in safe mode, was continuously tumbling, there was a GPS antenna switch about every 6 min. This antenna switch caused an interruption of 90 sec (3 GOD calls) in the measurement update of GOD at a rate of about 6 min. This behaviour is due to a protection mechanism to improve the robustness of the navigation in case of antenna switches on MANGO and/or TANGO. This problem was completely solved with the upload of the TANGO branches override procedure on the 20^{th} of July. As depicted in Fig. D.4, this procedure commanded to TANGO to hold the same information about which GPS antenna was used also in case of GPS antenna switches. The correct information about TANGO's GPS antennas switches was delivered only when TANGO's GPS receiver was on as this information is required by the POD process.

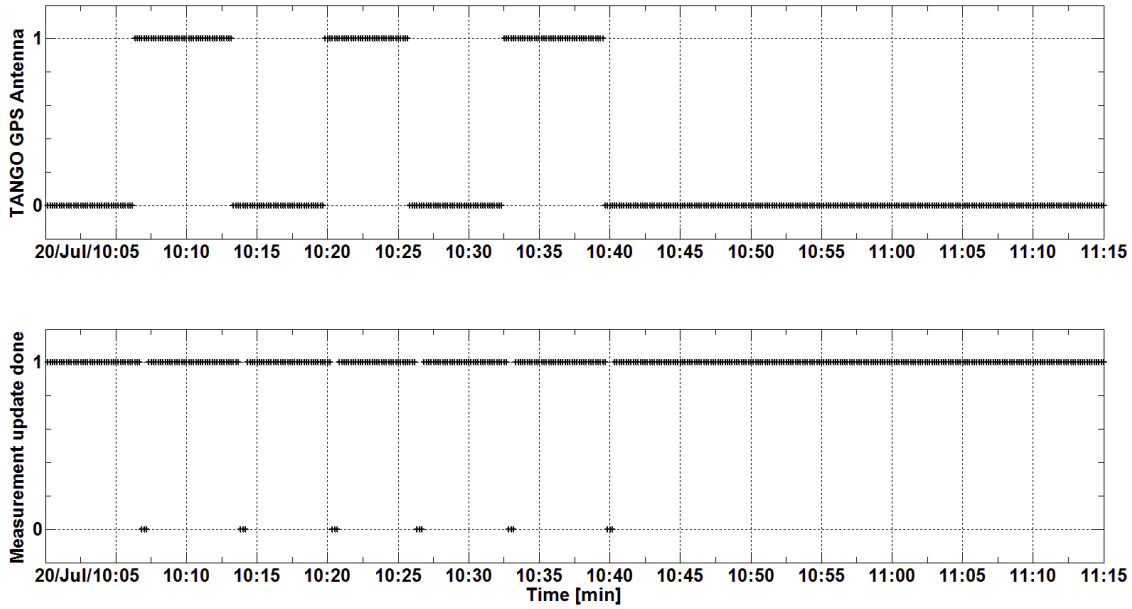

Figure D.4.: TANGO's GPS antennas switch (top) and GOD measurement update status (bottom)

D.3.2. MANGO - TANGO Relative Motion

Table D.3.2 collects the requested and actual MANGO - TANGO relative initial state required for the start of the AOK experiment. These requested initial conditions were meant to have TANGO drifting away from MANGO in the direction of the velocity due to the 2 m $a\delta a$ with an initial safe along-track separation of about 3000 m. The relative eccentricity and inclination vector had to be parallel as collision avoidance criteria (Ref. 143). Fig. D.5 shows the relative position MANGO - TANGO in the RTN orbital frame during the acquisition phase of the initial relative state for AOK experiment. Figures D.6 and D.7 show the corresponding relative orbital elements and relative eccentricity and inclination vectors. Fig. D.8 shows the relative position

Rel. Orbital Elements	$\mathbf{a\delta a[m]}$	$\mathbf{a\delta e_x[m]}$	$\mathbf{a\delta e_y[m]}$	$\mathbf{a\delta i_x[m]}$	$\mathbf{a\delta i_y[m]}$	$\mathbf{a\delta u[m]}$
Requested	2.0	0.0	-300.0	0.0	-400.0	-3000.0
Actual	2.9	-58.0	-272.0	-36.0	-396.0	-3205.0

Table D.1.: Requested and actual MANGO - TANGO relative initial state for the AOK experiment

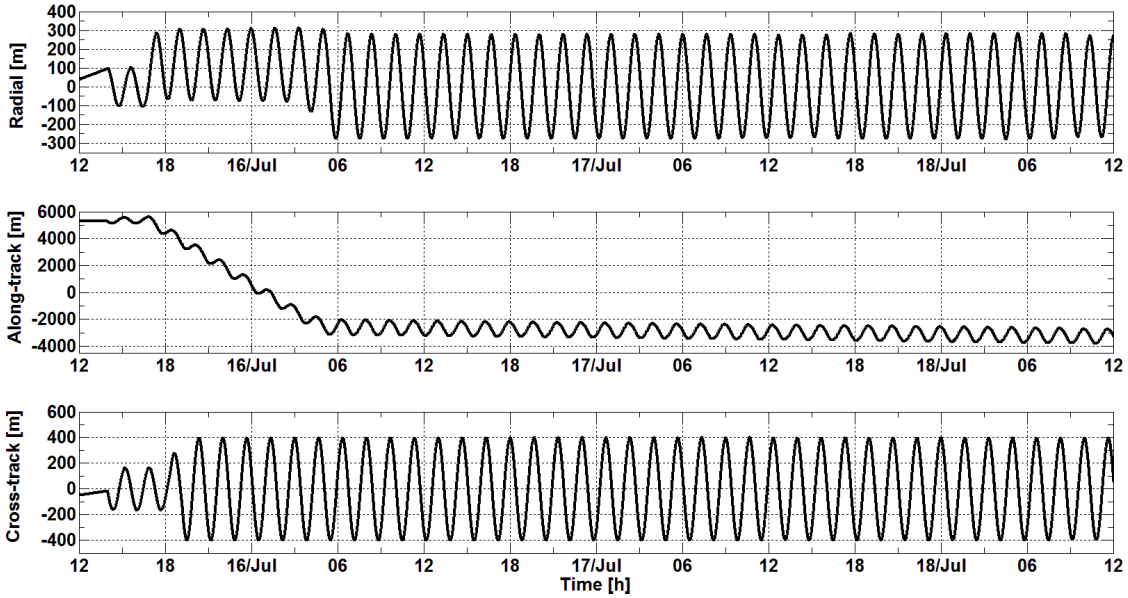

Figure D.5.: Relative position MANGO - TANGO in the RTN orbital frame during the acquisition phase of the initial relative state for AOK experiment

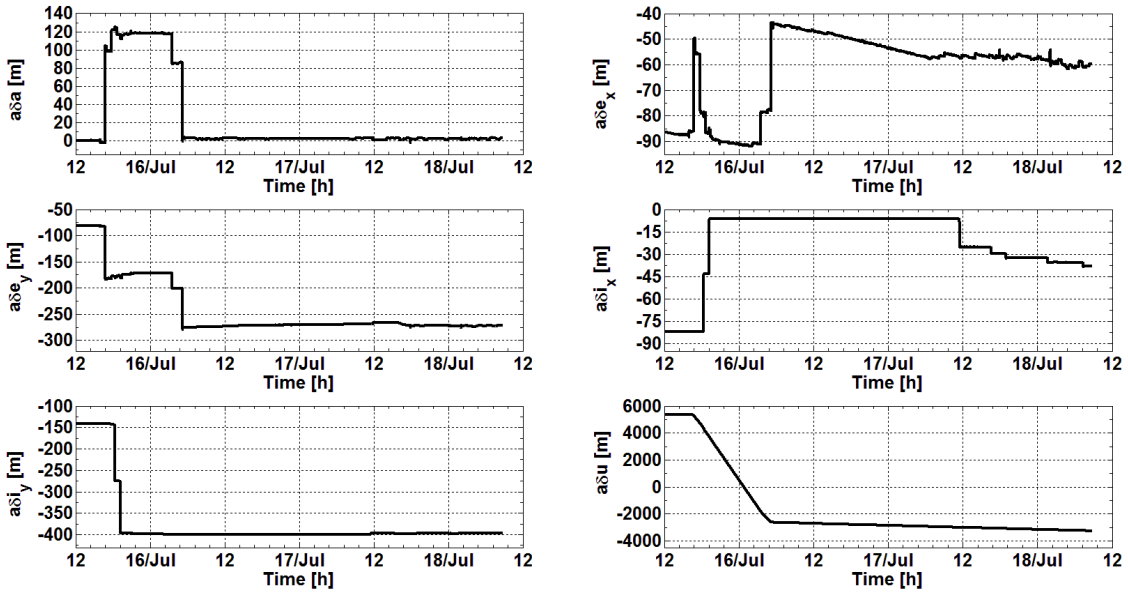

Figure D.6.: Relative orbital elements MANGO - TANGO during the acquisition phase of the initial relative state for AOK experiment

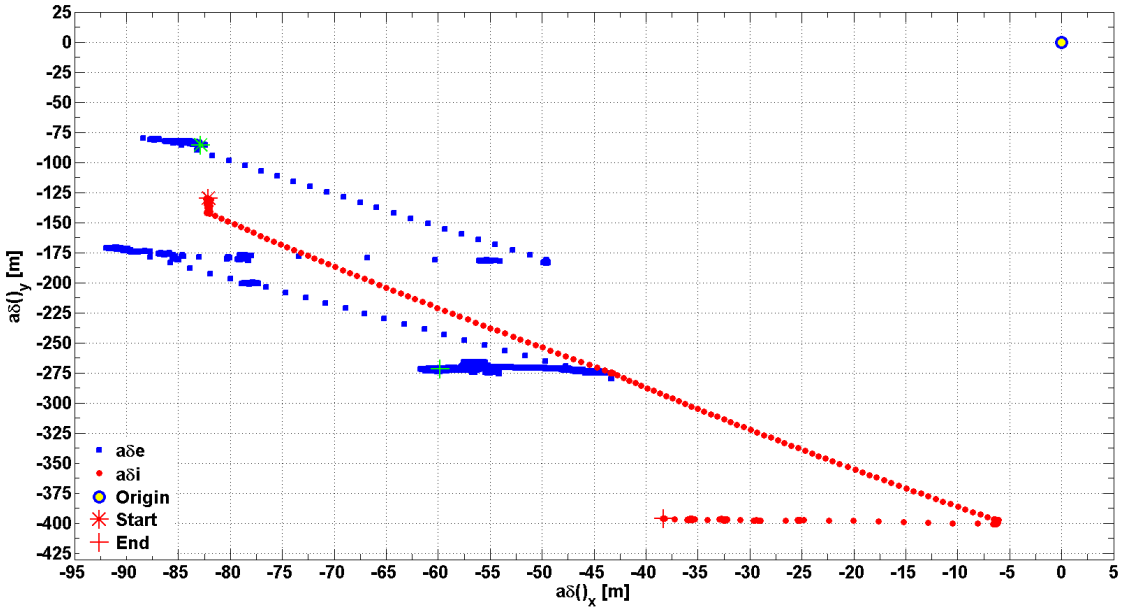

Figure D.7.: Relative eccentricity and inclination vectors MANGO - TANGO during the acquisition phase of the initial relative state for AOK experiment

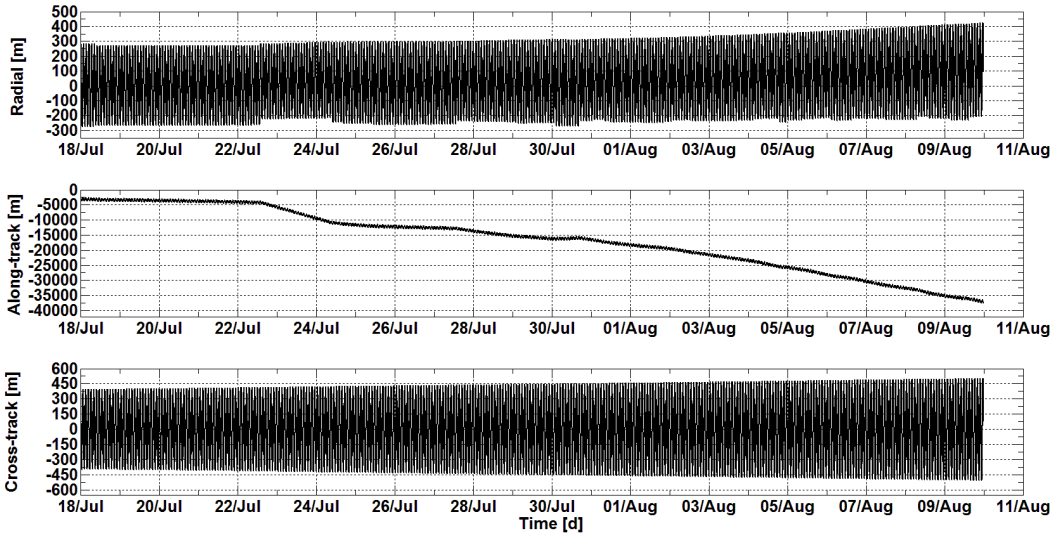

Figure D.8.: Relative position MANGO - TANGO in the RTN orbital frame during the AOK experiment

MANGO - TANGO during the AOK experiment up to the moment the GPS receiver on-board TANGO was switched off on 10^{th} of August. The sudden increase of the relative drift rate

in the along-track-direction on 22^{nd} of July after the beginning of the 1.5 days reacquisition maneuver can be appreciated as well as the return to a smaller drift rate after the execution of the counter-maneuver by AOK.

Bibliography

BOOKS

[1] Bate, R.R., Mueller, D.D., and White, J.E., “Fundamentals of Astrodynamics”, Dover Publications, 1971, ISBN:0-486-60061-0.

[2] Chao, C.,“Applied Orbit Perturbation and Maintenance”, AIAA, Reston, VA, USA, 2005, ISBN:1-884989-17-9.

[3] Micheau, P.,“Spaceflight Dynamics, Vol. I, Chap. Orbit Control Techniques for LEO Satellites”, Toulouse, France, Cepadues-Editions, 1995, ISBN:2-85428-376-7.

[4] Montenbruck, O., and Gill, E.,“Satellite Orbits - Model, Methods and Applications”, Springer Verlag, Heidelberg, Germany, 2000, ISBN:3-540-67280-X.

[5] Schaub, H., and Junkins, J. L.,“Analytical Mechanics of Space Systems”, AIAA Education Series, Reston, VA, USA, 2003, ISBN:1-56347-563-4.

[6] Vallado, D.A.,“Fundamentals of Astrodynamics and Applications”, Microcosm Press and Kluwer Academic Publishers, 2001, ISBN:1-881883-12-4.

[7] Wertz, J.R.,“Mission Geometry: Orbit and Constellation Design and Management”, Microcosm Press and Kluwer Academic Publishers, 2001, ISBN:1-881883-07-8.

[8] Kaula, W.M.,“Theory of Satellite Geodesy: Applications of Satellites to Geodesy”, Dover Publications, Inc., Mineola, New York, 2000, ISBN:0-486-41465-5

[9] Friedland, B.,“Control System Design - An Introduction to State-space Methods”, McGraw Hill, 1986, ISBN:0-486-44278-0.

[10] Kirk, D. E.,“Optimal Control Theory - An Introduction”, Dover Publications, 1970, ISBN-10:0-486-43484-2.

[11] Pagani, C.D., and Salsa, S.,“Analisi Matematica - Volumi 1 e 2”, Masson editore, 1992.

ORBIT MODELS

Analytical Models

[12] Brouwer, D.,“Solution of the Problem of Artificial Satellite Theory Without Drag”, *The Astronomical Journal*, Vol. 64, No. 1274, pp. 378-397, 1959, doi:10.1086/107958.

[13] Brouwer, D., and Hori, G.I.,“Theoretical evaluation of atmospheric drag effects in the motion of an artificial satellite”, *The Astronomical Journal*, Vol. 66, No. 5, pp. 193-225, 1961, doi:10.1086/108399.

[14] Coffey, S.L., and Deprit, A.,“Third-Order Solution to the Main Problem of Satellite Theory”, *AIAA Journal of Guidance, Control, and Dynamics*, Vol. 5, No. 4, pp. 366-371, July-Aug., 1982, doi:10.2514/3.56183

[15] Deprit, A.,“The Main Problem of Artificial Satellites to Order Four”, *AIAA Journal of Guidance, Control, and Dynamics*, Vol. 4, No. 2, pp. 201-206, March-April 1981, doi:10.2514/3.56072.

[16] Hintz, G.R.,“Survey of Orbit Element Sets”, *AIAA Journal of Guidance, Control, and Dynamics*, Vol. 31, No. 3, pp. 785-790, May-June 2008, doi:10.2514/1.32237.

[17] Kaula, W.M.,“Development of the lunar and solar disturbing functions for a close satellite”, *The Astronomical Journal*, Vol. 67, No. 5, pp. 300-303, 1962, doi:10.1086/108729.

[18] Kozai, Y.,“The Motion of a Close Earth Satellite”, *The Astronomical Journal*, Vol. 64, pp. 367-377, Nov. 1959, doi:10.1086/107957.

[19] Kozai, Y.,“Second-order solution of artificial satellite theory without air drag”, *The Astronomical Journal*, Vol. 67, No. 7, pp. 446-461, Nov. 1962, doi:10.1086/108753.

[20] Kozai, Y.,“Second-order solution of artificial satellite theory without air drag”, *The Astronomical Journal*, Vol. 67, pp. 446-461, Nov. 1962, doi:10.1086/108753.

[21] Liu, J.,“Satellite Motion about an Oblate Earth”, *AIAA Journal*, Vol. 12, pp. 1511-1516, November 1974, doi:10.2514/3.49537.

[22] Walter, H. G.,“Conversion of osculating orbital elements into mean elements”, *Astronomical Journal*, Vol. 72, No. 8, pp. 994-997, Oct. 1967, doi:10.1086/110374.

Frozen Orbits

[23] Aorpimai, M. and Palmer, P.L.,“Analysis of Frozen Conditions and Optimal Frozen Orbit Insertion”, *AIAA Journal of Guidance, Control, and Dynamics*, Vol. 26, No. 5, pp. 786-793, 2003, doi:10.2514/2.5113.

[24] Coffey, S.L., Deprit, A., and Deprit, E.,“Frozen orbits for satellites close to an Earth-like planet”, *Journal of Celestial Mechanics and Dynamical Astronomy*, Vol. 59, Issue 1, pp 37-72, May 1994, doi:10.1007/BF00691970.

[25] Lara, M., Deprit, A., and Elipe, A.,“Numerical continuation of families of frozen orbits in the zonal problem of artificial satellite theory”, *Celestial Mechanics and Dynamical Astronomy*, Vol. 62, Issue 2, pp. 167-181, June 1995, doi:10.1007/BF00692085.

[26] Pinto Mesquita Pardal, P.C., Koiti Kuga, H., and Vilhena de Moraes, R.,“Study of Orbital Elements on the Neighbourhood of a Frozen Orbit”, *Journal of Aerospace Engineering, Sciences and Applications*, Vol. 1, No. 2, pp. 23-32, May-Aug. 2008, ISSN 2236-577X.

[27] Schrama, E.J.O.,“Frozen orbits and their application in satellite altimetry”, *Satellite Altimetry in Geodesy and Oceanography - Lecture Notes in Earth Sciences*, Vol. 50, pp. 443-452, 1993, doi:10.1007/BFb0117934.

[28] Smith, J.,“Analysis and application of frozen orbits for the TOPEX mission”, Proceedings of the *AIAA/AAS Astrodynamics Conference*, AIAA-86-2069-CP, 18-20 Aug., 1986, Williamsburg, VA, USA, doi:10.2514/6.1986-2069.

Sun-synchronous Orbits

[29] Docherty, S.Y., and Macdonald, M.,“Analytical Sun-Synchronous Low-Thrust Orbit Maneuvers”, *AIAA Journal of Guidance, Control, and Dynamics*, Vol. 35, No. 2, pp. 681-686, March-April 2012, doi:10.2514/1.54948.

[30] Macdonald, M., McKay, R., Vasile, M., and Bosquillon de Frescheville F.,“Extension of the Sun-Synchronous Orbit”, *AIAA Journal of Guidance, Control, and Dynamics*, Vol. 33, No. 6, pp. 1935-1939, November-December 2010, doi:10.2514/1.49011.

Repeat Track Orbits

[31] Aorpimai, M., and Palmer, P.L.,“Repeat-Groundtrack Orbit Acquisition and Maintenance for Earth-Observation Satellites”, *AIAA Journal of Guidance, Control, and Dynamics*, Vol. 30, No. 3, pp. 654-659, 2007, doi:10.2514/1.23413.

[32] D’Amico, S., Arbinger, C., Kirschner, M., and Campagnola, S.,“Generation of an Optimum Target Trajectory for the TerraSAR-X Repeat Observation Satellite”, Proceedings of the *18th International Symposium on Space Flight Dynamics, ISSFD 2004*, Munich, Germany, 11-15 October 2004.

[33] Klinkrad, H.,“Orbit characteristics of the first ESA remote sensing satellite ERS-1”, Proceedings of the *36th IAF, International Astronautical Congress*, 7-12 Oct., 1985.

[34] Lara, M., and Russell, R.P.,“Fast design of repeat ground track orbits in high-fidelity geopotentials”, *The Journal of the Astronautical Sciences*, Vol. 56, Issue 3, pp 311-324, 2008, doi:10.1007/BF03256555.

[35] Lara, M.,“Repeat Ground Track Orbits of the Earth Tesseral Problem as Bifurcations of the Equatorial Family of Periodic Orbits”, *Celestial Mechanics and Dynamical Astronomy*, Vol. 86, Issue 2, pp. 143-162, June 2003, doi:10.1023/A:1024195900757.

[36] Lara, M., Blesa, F., Elipe, A., and Soriano, M.A.,"An efficient method for searching periodic orbits in Earth observation missions", *International Journal of Remote Sensing*, Vol. 24, No. 15, pp. 3149-3161, 2003, doi:10.1080/0143116021000021233.

[37] Vtipil, S.D., and Newman, B.,"Determining an Earth Observation Repeat-Ground-Track Orbit for an Optimization Methodology", *AIAA Journal of Spacecraft and Rockets*, Vol. 49, No. 1, pp. 157-164, Jan.-Feb. 2012, doi:10.2514/1.A32038.

[38] Xiaofeng, F., Meiping, W., and Tang, Y.,"Design and Maintenance of Low-Earth Repeat-Groundtrack Successive-Coverage Orbits", *AIAA Journal of Guidance, Control, and Dynamics*, Vol. 35, No. 2, pp. 686-691, March-April 2012, doi:10.2514/1.54780.

Coverage Orbit Design

[39] Abdelkhalik, O., and Mortari, D.,"Two-Way Orbits", *Celestial Mechanics and Dynamical Astronomy*, Vol. 94, No. 4, pp. 399-410, April 2006, doi:10.1007/s10569-006-9001-5.

[40] Flandrin, J.C.,"Statistical method for ground and sky coverage calculation", *Acta Astronautica*, Vol. 12, Issue 10, pp. 731-739, Oct. 1985, doi:10.1016/0094-5765(85)90089-X.

[41] Sengupta, P., Vadali, S.R., and Alfriend, K.T.,"Satellite Orbit Design and Maintenance for Terrestrial Coverage", *AIAA Journal of Spacecraft and Rockets*, Vol. 47, No. 1, pp. 177-187, Jan.-Feb. 2010, doi:10.2514/1.44120.

ORBIT CONTROL

[42] Arbinger, C., and D'Amico, S.,"Impact of Orbit Prediction Accuracy on Low Earth Remote Sensing Flight Dynamics Operations", Proceedings of the *18th International Symposium on Space Flight Dynamics, ISSFD 2004*, Munich, Germany, 11-15 October 2004.

[43] Bhat, R.S., Shapiro, B.E., Frauenholz, R.B., and Leavitt, R.K.,"TOPEX/Poseidon Orbit Maintenance for the First Five Years", Proceedings of the *13th AAS/GSFC International Symposium on Space Flight Mechanics*, AAS 98-379, pp. 973-988, 11-15 May 1998, Greenbelt, MD, USA.

[44] D'Amico, S., Kirschner, M., and Arbinger, C.,"Precise Orbit Control of LEO Repeat Observation Satellites with Ground-in-the-Loop", Tech. Rep. DLR-GSOC TN 04-05, Deutsches Zentrum für Luft und Raumfahrt, Oberpfaffenhofen, Germany, 2004.

[45] Frauenholz, R.B., Bhat, R.S, Shapiro, B.E., and Leavitt, R.K.,"Analysis of the TOPEX/Poseidon Operational Orbit: Observed Variations and Why", *AIAA Journal of Spacecraft and Rockets*, Vol. 35, No. 2, pp. 212-224, 1998, doi:10.2514/2.3312.

[46] Rosengren, M.,"High-accuracy orbit control for the ERS spacecraft", Proceedings of the *12th International Symposium on Space Flight Dynamics*, pp. 417-424, 2-6 June 1997, Darmstadt, Germany, edited by T.-D. Guyenne, ESA SP-403.

[47] Rosengren, M.,"ERS-1 - An Earth Observer that exactly follows its Chosen Path", ESA Bulletin number 72, pp. 76-82, Nov. 1992.

[48] Rudolph, A., Kuijper, D.,Ventimiglia, L., Garcia Matatoros, M.A., and Bargellini, P.,"Envisat Orbit Control - Philosophy, Experience and Challenge", Proceedings of the *2004 Envisat and ERS Symposium*, ESA SP-572, 6-10 Sep. 2004, Salzburg, Austria.

AUTONOMOUS ORBIT CONTROL

Theory

[49] Bonaventure, F., Baudry, V., Sandre, T., and Gicquel, A.-H.,"Autonomous Orbit Control for Routine Station Keeping on a LEO Mission", Proceedings of the *23rd International Symposium on Space Flight Dynamics*, 29 Oct.-2 Nov., 2012, Pasadena Convention Center, CA, USA.

[50] Collins, J.T., Dawson, S.D., and Wertz, J.R.,"Autonomous Constellation Maintenance System", Proceedings of the *10th Annual AIAA/USU Conference on Small Satellites*, 1996, North Logan, UT, USA.

[51] Dawson, S.D., Early, L.W., Potterveld, C.W., and Königsmann, H.J.,“Low-cost Autonomous Orbit Control about Mars: initial Simulation Results”, *Acta Astronautica*, Vol. 45, No. 4-9, p. 475-482, 1999, doi:10.1016/S0094-5765(99)00167-8.

[52] De Florio, S., D’Amico, S., and Radice, G.,“The Virtual Formation Method for Precise Autonomous Absolute Orbit Control”, *Journal of Guidance, Control and Dynamics*, doi:10.2514/1.61575.

[53] De Florio, S., D’Amico, S., and Radice, G.,“Precise Autonomous Orbit Control in Low Earth Orbit”, Proceedings of the *AIAA/AAS Astrodynamics Specialist Conference and Exhibit*, 13-16 Aug. 2012, Minneapolis, MN, doi:10.2514/6.2012-4811.

[54] Galski, R. L., Orlando, V., and Kuga, H. K.,“Autonomous Orbit Control Procedure, Using a Simplified GPS Navigator, Applied to the CBERS Satellite”, *16th International Symposium on Spaceflight Dynamics, ISSFD 2001*, Pasadena, CA, USA, 2001.

[55] Galski, R. L., and Orlando, V.,“Autonomous Orbit Control Procedure, Using a Simplified GPS Navigator and a new Longitude Phase Drift Prediction Method, Applied to the CBERS Satellite”, *Journal of Aerospace Engineering, Sciences and Applications*, Vol. IV, No 3, Jul.-Sep. 2012, doi 10.7446/jaesa.0403.05.

[56] Garulli, A., Giannitrapani, A., Leomanni, M., and Scortecci, F.,“Autonomous Low-Earth-Orbit Station-Keeping with Electric Propulsion”, *Journal of Guidance, Control and Dynamics*, Vol. 34, No. 6, pp. 1683-1693, Nov.âĂŞDec. 2011, doi:10.2514/1.52985.

[57] Julien, E., and Lamy, A.,“Out-of-plane Autonomous Orbit Control”, *Journal of Aerospace Engineering, Sciences and Applications*, Vol. 4, No. 3, pp. 28-40, 2012, ISSN:2236-577X.

[58] Königsmann, H.J., Collins, J.T., Dawson, S., and Wertz, J.R.,“Autonomous Orbit Maintenance System”, *Acta Astronautica*, Vol. 39, No. 9-12, pp. 977âĂŞ985, 1996, doi:10.1016/S0094-5765(97)00084-2.

[59] Kudryavtsev, S., and Gill, E.,“Autonomous Orbit Control of Remote Sensing Spacecraft using Spaceborne GPS Receivers’, Tech. Rep. DLR-GSOC-TN-00-06, DLR/GSOC, Deutsches Zentrum für Luft und Raumfahrt, Oberpfaffenhofen, Germany, 2000. = ""

[60] Orlando, V., and Micheau, P.,“Autonomous Orbit Control for Phased LEO Satellites”, Proceedings of the *11th IAS-International Astrodynamics Symposium jointly held with the 20th ISTS-International Symposium on Space Technology and Science*, p. 143-148, Nagaragawa Convention Center, Gifu, Japan, May 19-25 1996, ISBN 9784990050009.

[61] Orlando, V., and Kuga, H. K.,“A Survey of Autonomous Orbit Control Investigations at INPE”, Proceedings of the *17th International Symposium on Space Flight Dynamics, ISSFD 2003*, Moscow, Russia, June 16-20, 2003.

[62] Wertz, J.R., Gurevich, G.,“Applications of Autonomous On-board Orbit Control”, Proceedings of the *11th AAS/AIAA Space Flight Mechanics Meeting*, AAS 01-238, Feb. 11-15, 2001, Santa Barbara, CA, USA.

[63] Wertz, J.R., Sarzi-Amade, N., Shao, A., Taylor, C., and Van Allen R.E.,“Moderately Elliptical Very Low Orbits (MEVLOs) as a Long-Term Solution to Orbital Debris”, Proceedings of the *26th Annual AIAA/USU Conference on Small Satellites*, SSC12-IV-6, 13-16 Aug., 2012, Logan, Utah, USA.

[64] Wertz, J.R., Collins, J.T., Dawson, S.D., Königsmann, H.J., and Potterveld, C.W.,“Autonomous Constellation Maintenance”, Proceedings of the *IAF Workshop on Satellite Constellations*, 18-19 Nov. 1997, Toulouse, France.

Missions - UoSAT-12 and TacSat

[65] Gurevich, G., Bell, R., Wertz, J.R.,“Autonomous On-board Orbit Control: Flight Results and Applications”, Proceedings of the *AIAA 2000 Conference and Exposition*, AIAA 2000-5226, Sept. 19 - 21, 2000, Long Beach, CA, USA, doi: 10.2514/6.2000-5226.

[66] Plam, Y., Allen, R. V., Wertz, J.R., and Bauer, T.,“Autonomous Orbit Control Experience

on TacSat-2 using Microcosm's Orbit Control Kit (OCK)", *31st Annual AAS Guidance and Control Conference*, Breckenridge, Colorado, USA, 1-6 Feb. 2008.

Missions - Demeter

[67] Duchevet, F., and Lamy, A.,"DEMETER: Experience Feedback on Operations with an Autonomous Orbit Control Demonstrator", Proceedings of the *SpaceOps 2008 Conference*, 12-16 May 2008, Heidelberg, Germany, doi:10.2514/6.2008-3238.

[68] Lamy, A., and Charmeau, M.-C.,"Performance of the Autonomous Orbit Control of the DEMETER Satellite", Proceedings of the *AIAA/AAS Astrodynamics Specialist Conference and Exhibit*, 5-8 Aug. 2002, Monterey, CA, USA, doi:10.2514/6.2002-4906.

[69] Lamy, A., Charmeau, M.-C., Laurichesse, D., Grondin, M., and Bertrand, R.,"Experiment of autonomous Orbit Control on the Demeter Satellite", Proceedings of the *18th International Symposium on Space Flight Dynamics*, pp. 327-333, 11-15 October 2004, Munich, Germany.

[70] Lamy, A., Charmeau, M.-C., and Laurichesse, D.,"Experiment of autonomous Orbit Control on the Demeter Satellite: In-flight Results and Perspectives", Proceedings of the *AIAA/AAS Astrodynamics Specialist Conference and Exhibit*, Keystone, CO, 21-24 Aug. 2006, Chapter doi:10.2514/6.2006-6681

[71] Lamy, A., Julien, E., and Flamenbaum, D.,"Four Year Experience of Operational Implementation of Autonomous Orbit Control: Lessons Learned, Feedback and Perspectives", Proceedings of the *21st International Symposium on Space Flight Dynamics*, 2009, Toulouse, France.

Missions - PRISMA/AOK

[72] De Florio, S., and D'Amico, S.,"The Precise Autonomous Orbit Keeping Experiment on the Prisma Mission", *The Journal of the Astronautical Sciences*, Vol. 56, No. 4, Oct.-Dec. 2008, pp. 477-494.

[73] De Florio, S., D'Amico, S., and Radice, G.,"Flight Results of the Precise Autonomous Orbit Keeping Experiment on the Prisma Mission", *AIAA Journal of Spacecraft and Rockets*, Vol. 50, No. 3, pp. 662-674, May 2013, doi:10.2514/1.A32347.

[74] De Florio, S., D'Amico, S., and Radice, G.,"Operation Concept of the Precise Autonomous Orbit Keeping Experiment on the PRISMA Mission", *8th IAA Symposium on Small Satellites for Earth Observation*, International Academy of Astronautics, IAA-B8-0513P, Berlin, 4-8 April 2011.

[75] De Florio, S.,"Operations Concept of the Precise Autonomous Orbit Keeping Experiment on the PRISMA Mission", Tech. Rep. PRISMA-DLR-OPS-55, DLR/GSOC, Deutsches Zentrum für Luft und Raumfahrt, Oberpfaffenhofen, Germany, March 2011.

Patents

[76] Montenbruck, O., Eckstein, M., and Werner, W.,"Apparatus for Orbit Control of at Least Two Co-located Geostationary Satellites", U.S. Patent 5506780, 9 Apr. 1996.

[77] Wertz, J.R.,"Satellite Orbit Maintenance System", U.S. Patent 5687084, 11 Nov. 1997.

[78] Parvez, S.A., and Xing, G.-Q.,"Autonomous Orbit Control with Position and Velocity Feedback Using Modern Control Theory", U.S. Patent 6089507, 18 Jul. 2000.

[79] Reckdahl, K., and Sauer, B.,"Closed-loop Spacecraft Orbit Control", U.S. Patent 6439507 B1, 27 Aug. 2002.

[80] Eyerly, B.N.,"Spacecraft Orbit Control Using Orbit Position Feedback", U.S. Patent 6508438 B2, 21 Jan. 2003.

MISSIONS

[81] Schreier, G., and Dech, S.,"High resolution earth observation satellites and services in the next decade - a European perspective", *Acta Astronautica*, Vol. 57, Issues 2-8, pp. 520-533, July-Oct. 2005, doi:10.1016/j.actaastro.2005.03.029.

Prisma

[82] Anflo, K., and Möllerberg, R.,“Flight demonstration of new thruster and green propellant technology on the PRISMA satellite”, *Acta Astronautica*, Vol. 65, Issues 9-10, pp. 1238-1249, 2009, doi:10.1016/j.actaastro.2009.03.056.

[83] Ardaens, J.-S., D’Amico, S., and Montenbruck, O.,“Final Commissioning of the Prisma GPS Navigation System”, *Journal of Aerospace Engineering, Sciences and Applications*, Vol. 4, No. 3, pp. 104-118, Jul.-Sep. 2012, doi:10.7446/jaesa.0403.10.

[84] Ardaens, J.-S., D’Amico, S., and Montenbruck, O.,“Flight Results from the PRISMA GPS-Based Navigation”, Proceedings of the *5th ESA Workshop on Satellite Navigation Technologies, NAVITEC 2010*, 8-10 Dec. 2010, Noordwijk, The Netherlands.

[85] Ardaens, J.-S., Montenbruck, O., and D’Amico, S.,“Functional and Performance Validation of the PRISMA Precise Orbit Determination Facility”, Proceedings of the *ION International Technical Meeting*, pp. 490-500, 25-27 Jan. 2010, San Diego, CA, USA.

[86] Bodin, P., Larsson, R., Nilsson, F., and Chasset, C.,“PRISMA: An In-Orbit Test Bed for Guidance, Navigation, and Control Experiments”, *AIAA Journal of Spacecraft and Rockets*, Vol. 46, No. 3, pp. 615-623, May-June 2009, doi:10.2514/1.40161.

[87] Bodin, P., Noteborn, R., Larsson, R., and Chasset, C.,“System Test Results from the GNC Experiments on the PRISMA In-Orbit Test Bed”, *Acta Astronautica*, Vol. 68, 7-8, , pp. 862-872, 2011, doi:10.1016/j.actaastro.2010.08.021.

[88] Bodin, P., Noteborn, R., Larsson, R., Karlsson, T., D’Amico, S., Ardaens, J.-S., Delpech, M., and Berges, J.-C.,“The Prisma Formation Flying Demonstrator: Overview and Conclusions from the Nominal Mission”, Proceedings of the *35th Annual AAS Guidance And Control Conference*, AAS 12-072, 3-8 Feb. 2012, Breckenridge, CO, USA, ISBN 978-0-87703-585-5.

[89] D’Amico, S., Bodin, P., Delpech, M., and Noteborn, R.,“PRISMA”, *Distributed Space*

Missions for Earth System Monitoring - Space Technology Library, Vol. 31, pp. 599-637, Ed. Springer New York, 2013, doi:10.1007/978-1-4614-4541-8_21.

[90] D'Amico, S., Ardaens, J.-S., and De Florio, S.,"Autonomous Formation Flying based on GPS - PRISMA Flight Results", *Acta Astronautica*, Vol. 82, No. 1, pp. 69.79, Jan. 2013, doi:10.1016/j.actaastro.2012.04.033.

[91] D'Amico, S., and Larsson, R.,"Navigation and Control of the PRISMA Formation: In-Orbit Experience", *Journal of Mechanics Engineering and Automation*, 2012, 2(5):312-320 (2012).

[92] D'Amico, S., Ardaens, J.-S., and Larsson, R.,"Spaceborne Autonomous Formation Flying Experiment on the PRISMA Mission", *AIAA Journal of Guidance, Control and Dynamics*, vol.35, no.3, pp 834-850, 2012, doi:10.2514/1.55638.

[93] D'Amico, S., De Florio, S., Larsson, S., and Nylund, M.,"Autonomous Formation Keeping and Reconfiguration for Remote Sensing Spacecraft", Proceedings of the *21st International Symposium on Space Flight Dynamics, ISSFD 2009*, 28 Sep.-2 Oct., 2009, Toulouse, France.

[94] D'Amico, S., Ardaens, J.-S., and Montenbruck, O.,"Navigation of Formation Flying Spacecraft using GPS: the PRISMA Technology Demonstration", Proceedings of the *22nd International Technical Meeting of The Satellite Division of the Institute of Navigation - ION GNSS 2009*, pp. 1427-1441, 22-25 Sep., 2009, Savannah International Convention Center, Savannah, GA, USA.

[95] D'Amico, S., and Montenbruck, O.,"GPS-Based Relative Navigation during the Separation Sequence of the PRISMA Formation", Proceedings of the *AIAA Guidance, Navigation and Control Conference and Exhibit*, AIAA 2008-6661, 18-21 Aug. 2008, Honolulu, Hawaii, USA, doi:10.2514/6.2008-6661.

[96] De Florio, D'Amico, S., and Ardaens, J.-S.,"Flight Results from the Autonomous Naviga-

tion and Control of Formation Flying Spacecraft on the PRISMA Mission", Proceedings of the *61st International Astronautical Congress*, IAC-10.C1.5.12, 2010, Prague, CZ.

[97] Gill E., D'Amico, S., and Montenbruck, O.,"Autonomous Formation Flying for the PRISMA Mission", *AIAA Journal of Spacecraft and Rockets*, Vol. 44, No. 3, May-June 2007, doi:10.2514/1.23015.

[98] Gill, E., "Requirements for DLR's Contributions to PRISMA", Tech. Rep. PRISMA-DLR-REQ-31, DLR/GSOC, Deutsches Zentrum für Luft und Raumfahrt, Oberpfaffenhofen, Germany, 2005.

[99] Grönland, T.-A., Rangsten, P., Nese, M., and Lang, M.,"Miniaturization of Components and Systems for Space using MEMS-technology", *Acta Astronautica*, Vol. 61, Issues 1-6, pp. 228-233, 2007, doi:10.1016/j.actaastro.2007.01.029.

[100] Harr, J., Delpech, M., Lestarquit, L., and Seguela, D.,"RF Metrology Validation and Formation Flying Demonstration by Small Satellites âĂŞ The CNES Participation on the PRISMA Mission", Proceedings of the *4S Symposium Small Satellites, Systems and Services*, ESA SP-625, 2006.

[101] Larsson, R., Mueller, J., Thomas, S., Jakobsson, B., and Bodin, P.,"Orbit Constellation Safety on the PRISMA In-Orbit Formation Flying Test Bed", Proceedings of the *3rd International Symposium on Formation Flying, Missions and Technologies*, ESA SP-654, 2008.

[102] Montenbruck, O., Delpech, M., Ardaens, J.-S., Delong, N., D'Amico, S., and Harr, J.,"Cross-Validation of GPS and FFRF-based Relative Navigation for the Prisma Mission", Proceedings of the *4th ESA Workshop on Satellite Navigation Technologies, NAVITEC 2008*, 10-12 Dec. 2008, Noordwijk, The Netherlands.

[103] Montenbruck, O., Gill, E., and Markgraf, M.,"Phoenix-XNS - A Miniature Real-Time Navigation System for LEO Satellites", Proceedings of the *3rd ESA Workshop on Satellite Navigation User Equipment Technologies, NAVITEC 2006*, 11-13 Dec. 2006, Noordwijk.

[104] Markgraf, M., Montenbruck, O., Santandrea, S., and Naudet, J.,"Phoenix-XNS Navigation System On-board the PROBA-2 Spacecraft - First Flight Results", Proceedings of the *4S Symposium Small Satellites, Systems and Services*, 31 May-4 June 2010, Madeira, Portugal.

[105] Montenbruck, O., and Markgraf, M.,"User's Manual for the Phoenix GPS Receiver", Tech. Rep. GTN-MAN-0120, DLR/GSOC, Deutsches Zentrum für Luft und Raumfahrt, Oberpfaffenhofen, Germany, 2008.

[106] Persson, S., Veldman, S., and Bodin, P.,"PRISMA - A formation flying project in implementation phase", *Acta Astronautica*, Vol. 65, No. 9-10, pp. 1360-1374, 2009, doi:10.1016/j.actaastro.2009.03.067.

[107] Persson, S., D'Amico, S., and Harr, J.,"Flight Results from PRISMA Formation Flying and Rendezvous Demonstration Mission", Proceedings of the *61st International Astronautical Congress*, IAC-10-B4.2.9, 2010, Prague, CZ.

[108] Spirent,"SimREMOTE USER MANUAL", DGP00792AAA, Spirent Communication, 2006.

[109] Thevenet, J.-B., and Grelier, T.,"Formation Flying Radio-Frequency metrology validation and performance: The PRISMA case", *Acta Astronautica*, Vol. 82, No. 1, pp. 2-15, Jan. 2013, doi:10.1016/j.actaastro.2012.07.034.

TerraSAR-X/TanDEM-X

[110] Arbinger, C., D'Amico, S., and Eineder, M.,"Precise Ground-In-the-Loop Orbit Control for Low Earth Observation Satellites", Proceedings of the *18th International Symposium on Space Flight Dynamics, ISSFD 2004*, Munich, Germany, 11-15 October 2004.

[111] Ardaens, J.-S., and D'Amico, S.,"Spaceborne Autonomous Relative Control System for Dual Satellite Formations", *AIAA Journal of Guidance, Navigation and Control*, Vol. 32, No. 6, pp. 1859-1870, Nov.-Dec. 2009, doi:10.2514/1.42855.

[112] Ardaens, J.-S., and Fischer, D.,“TanDEM-X Autonomous Formation Flying System: Flight Results”, *Journal of Mechanics Engineering and Automation*, Vol. 2, No. 5, pp. 332-339, May 2012, ISSN 2159-5283 (online).

[113] D’Amico, S., Ardaens, J.-S., and Fischer, D.,“Early Flight Results from the TanDEM-X Autonomous Formation Flying System”, *4th International Conference on Spacecraft Formation Flying Missions and Technologies*, St-Hubert, Quebec, Canada, 18-20 May 2011.

[114] Kahle, R., Kazeminejad, B., Kirschner, M., Yoon, Y., Kiehling, R., and D’Amico, S.,“First in-orbit Experience of TerraSAR-X Flight Dynamics Operations”, Proceedings of the *20th International Symposium on Space Flight Dynamics, ISSFD 2007*, 24-28 Sep. 2007, Annapolis, USA.

[115] Kahle, R., Schlepp, B., and Kirschner, M.,“TerraSAR-X/TanDEM-X Formation Control - First Results from Commissioning and Routine Operations”, *Journal of Aerospace Engineering, Sciences and Applications*, Vol. 3, No. 2, pp. 16-27, May-Aug. 2011, ISSN:2236-577X.

[116] Montenbruck, O., Kahle, R., D’Amico, S., and Ardaens, J.-S.“Navigation and Control of the TanDEM-X Formation”, *The Journal of the Astronautical Sciences*, Vol. 56, No. 3, Jul.-Sept. 2008, pp. 341-357.

[117] Wermuth, M., Hauschild A., Montenbruck, O. and Kahle, R.,“TerraSAR-X precise orbit determination with real-time GPS ephemerides”, *Advances in Space Research*, Vol. 50, No. 5, pp. 549-559, 2012, doi:10.1016/j.asr.2012.03.014.

Sentinel-1

[118] Attema, E., Bargellini, P., and Edwards, P.,“Sentinel-1 the Radar Mission for GMES Operational Land and Sea Services”, *ESA Bulletin 131*, Aug. 2007.

[119] Attema, E., Snoeij, P., Davidson, M., Floury, N., Levrini, G., Rommen, B., and Rosich, B.,“The European GMES Sentinel-1 Radar Mission”, Proceedings of the *Geoscience and*

Remote Sensing Symposium, 2008 IEEE International, IGARSS 2008, Vol.1, pp. I94-I97, 7-11 July 2008, doi:10.1109/IGARSS.2008.4778801.

[120] Attema, E., Davidson, M., Snoeij, P., Rommen, B., and Floury, N.,"Sentinel-1 mission overview", Proceedings of the *Geoscience and Remote Sensing Symposium, 2009 IEEE International, IGARSS 2009*, Vol.1, pp. I36-I39, 12-17 July 2009, doi:10.1109/IGARSS.2009.5416921.

[121] Martin, M.A., Shurmer, I., and Marc, X.,"Sentinel-1: Operational Approach to the Orbit Control Strategy", Proceedings of the *23rd International Symposium on Space Flight Dynamics*, 29 Oct.-2 Nov., 2012, Pasadena Convention Center, CA, USA.

ON-BOARD SOFTWARE

Model Based Design

[122] Ahmadian, M., Nazari, Z., Nakhaee, N., and Kostic, Z.,"Model Based Design and SDR", Thecnical note, Sundance Multiprocessor Technology, 2009.

[123] Edfors, A.,"PRISMA ASW Subsystem Description", Technical Report PRISMA Phase B Study, Swedish Space Corporation, 2005.

[124] Eickhoff, J., Falke, A., and Röser, H.-P.,"Model-based design and verificationâĂŤState of the art from Galileo constellation down to small university satellites", *Acta Astronautica*, Vol. 61, Issue 1-6, pp. 383-390, 2007, doi:10.1016/j.actaastro.2007.01.027.

[125] Eickhoff, J., Hendricks, R., and Flemmig, J.,"Model-based development and verification environment", Proceedings of the *54th International Astronautical Congress*, 29 Sept.-3 Oct. 2003, Congress Centre, Bremen, Germany, doi:10.2514/6.IAC-03-U.3.07.

[126] Gaisler, J.,"The LEON Processor UserâĂŹs Manual", Version 2.3.7, Gaisler Research, 2001.

[127] MathWorks,"The Simulink manual, Writing S-Functions", Version 6, 2002.

[128] Olsson, T., and Edfors, A.,“Model-Based On-board Software Design: the Prisma Case Study”, Proceedings of the *DASIA 2006 - Data Systems in Aerospace conference*, 22-25 May, 2006, Berlin, Germany, ESA SP-630. European Space Agency, 2006. Published on CDROM., p.43.1, BC:2006ESASP.630E..43O.

[129] “RTEMS C UserÂŠs Guide. Edition 4.6.5, for RTEMS 4.6.5”, On-Line Applications Research Corporation (OAR), http://www.rtems.com, 2003.

Flight-software Testing

[130] Bodin, P., Nylund, M., and Battelino, M.,“SATSIM - A real-time multi-satellite simulator for test and validation in formation flying projects”, *Acta Astronautica*, Vol. 74, May-June 2012, pp. 29-39, doi:10.1016/j.actaastro.2011.11.015.

[131] D’Amico, S., De Florio, S., and Yamamoto, T.,“Offline and Hardware-in-the-loop Validation of the GPS-based Real-Time Navigation System for the PRISMA Formation Flying Mission”, Proceedings of the *3rd International Symposium on Formation Flying, Missions and Technology*, ESA/ESTEC, ESA SP-654, Noordwijk, The Netherlands, 23-25 April 2008.

[132] De Florio, S., and D’Amico, S.,“First Tests of the PRISMA Flight Software on LEON2 Board”, Tech. Rep. PRISMA-DLR-TN-14, DLR/GSOC, Deutsches Zentrum für Luft und Raumfahrt, Oberpfaffenhofen, Germany, March 2007.

[133] De Florio, S., and D’Amico, S.,“Max-Path Unit Tests of the PRISMA Flight Software v. 6.0.0”, Tech. Rep. PRISMA-DLR-TN-17, DLR/GSOC, Deutsches Zentrum für Luft und Raumfahrt, Oberpfaffenhofen, Germany, March 2007.

[134] Gill, E., and D’Amico, S.,“Architectural Design of DLR’s Flight Software for the PRISMA Mission”, Tech. Rep. PRISMA-DLR-ADD-31, DLR/GSOC, Deutsches Zentrum für Luft und Raumfahrt, Oberpfaffenhofen, Germany, Dec. 2005.

[135] De Florio, S., Gill, E., D’Amico, S., and Grillenberger, A.,“Performance Comparison of Microprocessors for Space-based Navigation Applications”, Proceedings of the *7th IAA*

Symposium on Small Satellites for Earth Observation, IAA-B7-0915P, 4-8 May 2009, Berlin, Germany.

[136] Persson, S., Noteborn, R., D'Amico, S., Harr, J., and Delpech, M.,"The Validation and Testing of the PRISMA Formation Flying Project", Proceedings of the *59th International Astronautical Congress*, IAC-08.B4.2.2, 2008, Glasgow, Scotland, UK.

SPACECRAFT FORMATION FLYING

[137] Alfriend, K.T., Vadali, S. R., Gurfil, P., How, J. P., and Breger, L. S.,"Spacecraft Formation Flying - Dynamics, control and navigation", Elsevier Astrodynamics Series, 2010, ISBN:978-075-068533-7.

[138] Alfriend, K.T., Schaub, H., and Gim, D.W.,"Gravitational Perturbations, Nonlinearity and Circular Orbit Assumption Effects on Formation Flying Control Strategies", Proceedings of the *AAS Rocky Mountain Guidance and Control Conference*, AAS 00-012, Feb. 3-7, 2000, Breckenridge, CO, USA.

[139] Breger, L., and How, J.P.,"Gauss's Variational Equation-Based Dynamics and Control for Formation Flying Spacecraft", *Journal of Guidance, Control and Dynamics*, Vol. 30, No. 2, MarchâĂŞApril 2007, pp. 437-448, doi:10.2514/1.22649.

[140] Carter, T.E.,"State Transition Matrices for Terminal Rendezvous Studies: Brief Survey and New Example", *Journal of Guidance, Control and Dynamics*, Vol. 21, No. 1, Jan.-Feb. 1998, pp. 148-155, doi:10.2514/2.4211.

[141] Carter, T.E., and Humi, M.,"Clohessy-Wiltshire Equations ModiÂŐfied to Include Quadratic Drag", *Journal of Guidance, Control and Dynamics*, Vol. 25, No. 6, Nov.-Dec. 2002, pp. 1058-1063.

[142] Clohessy, W.H., and Wiltshire, R.S.,"Terminal Guidance System for Satellite Rendezvous", *Journal of Aerospace Sciences*, Vol. 27, No. 9, pp. 653-658, 1960, doi:10.2514/8.8704.

[143] D'Amico, S.,"Autonomous Formation Flying in Low Earth Orbit", PhD thesis, Technische Universiteit Delft, 2010. ISBN 978-90-5335-253-3.

[144] D'Amico, S., and Montenbruck, O.,"Proximity Operations of Formation-Flying Spacecraft Using an Eccentricity/Inclination Vector Separation", *Journal of Guidance, Control and Dynamics*, Vol. 29, No. 3, pp. 554-563, May-June 2006.

[145] De Florio S., and D'Amico, S.,"Collision Risk Assessment for Co-orbiting Spacecraft", Tech. Rep. DEOS-DLR-TN-02, DLR/GSOC, Deutsches Zentrum für Luft und Raumfahrt, Oberpfaffenhofen, Germany, May 2010.

[146] De Florio, S., D'Amico, S., and Radice, G.,"Combined Autonomous Absolute and Relative Orbit Control in Low Earth Orbit", Proceedings of the *5th International Conference on Spacecraft Formation Flying Missions and Technologies*, No. 40096, 29-31 May, 2013, Munich, Germany.

[147] De Vries, J.P.,"Elliptic Elements in Terms of Small Increments of Position and Velocity Components", *AIAA Journal*, Vol. 1, No. 11, pp. 2626-2629, 1963, doi:10.2514/3.2124.

[148] Eckstein M.C., Rajasingh C.K., and Blumer P.,"Colocation strategy and collision avoidance for the geostationary satellites at 19 degrees west", Proceedings of the *CNES International Symposium on Space Flight Dynamics*, 6-10 Nov., 1989, Toulouse, France.

[149] Geller, D.K.,"Orbital Rendezvous: When Is Autonomy Required?", *Journal of Guidance, Control and Dynamics*, Vol. 30, No. 4, pp. 974-981, Jul.-Aug. 2007, doi:10.2514/1.27052.

[150] Gurfil, P., and Kholshevnikov, K.V.,"Manifolds and Metrics in the Relative Spacecraft Motion Problem", *Journal of Guidance, Control and Dynamics*, Vol. 29, No. 4, 2006,, pp. 1004-1010, doi: 10.2514/1.15531.

[151] Gurfil, P.,"Generalized Solutions for Relative Spacecraft Orbits under Arbitrary Perturbations", *Acta Astronautica*, Vol. 60, No. 2, pp. 61-78, 2007, doi:10.1016/j.actaastro.2006.07.013.

[152] Hamel, J.-F.,and de Lafontaine, J.,"Neighboring Optimum Feedback Control Law for Earth-Orbiting Formation-Flying Spacecraft", *Journal of Guidance, Control and Dynamics*, Vol. 32, No. 1, pp. 290-299, Jan.-Feb. 2009, doi:10.2514/1.32778.

[153] Hughes, S.P.,"General Method for Optimal Guidance of Spacecraft Formations", *Journal of Guidance, Control and Dynamics*, Vol. 31, No. 2, pp. 414-423, March-Apr. 2008, doi:10.2514/1.23731.

[154] Lee, D., Cochran, J.E., and Jo, J.H.,"Solutions to the Variational Equations for Relative Motion of Satellites", *Journal of Guidance, Control and Dynamics*, Vol. 30, No. 3, pp. 669-678, May-June 2007, doi:10.2514/1.24373.

[155] Montenbruck, O., Kirschner, M., D'Amico, S., and Bettadpur, S.,"E/I-vector separation for safe switching of the GRACE formation", *Aerospace Science and Technology*, Vol. 10, No. 7, pp. 628-635, 2006, doi:10.1016/j.ast.2006.04.001.

[156] Palmer, P., and Halsall, M.,"Designing Natural Formations of Low-Earth-Orbiting Satellites", *Journal of Guidance, Control and Dynamics*, Vol. 32, No. 3, pp. 860-868, May-June 2009, doi:10.2514/1.39631.

[157] Sabol, C., Burns, R., and McLaughlin, C.A.,"Satellite Formation Flying Design and Evolution", *Journal of Spacecraft and Rockets*, Vol. 38, No. 2, pp. 270-278, March-Apr. 2001.

[158] Schaub, H., Alfriend, K.,"Impulsive Feedback Control to Establish Specific Mean Orbit Elements of Spacecraft Formations", *AIAA Journal of Guidance, Control and Dynamics*, Vol. 24, No. 4, pp.739-745, Jul.-Aug. 2001.

[159] Schaub, H.,"Relative Orbit Geometry through Classical Orbit Element Differences", *AIAA Journal of Guidance, Control and Dynamics*, Vol. 27, No. 5, Sept.-Oct., 2004, pp. 839-848, doi:10.2514/1.12595.

[160] Sengupta, P., Vadali, S.R., and Alfriend, K.T.,"Averaged Relative Motion and Applications to Formation Flight Near Perturbed Orbits", *AIAA Journal of Guidance, Control and Dynamics*, Vol. 31, No. 2, pp. 258-272, March-Apr. 2008, doi:10.2514/1.30620.

[161] Sengupta, P., and Vadali, S.R.,"Relative Motion and the Geometry of Formations in Keplerian Elliptic Orbits", *AIAA Journal of Guidance, Control and Dynamics*, Vol. 30, No. 4, pp. 953-964, Jul.-Aug. 2007, doi:10.2514/1.25941.

[162] Sengupta, P., Sharma, R., and Vadali, S.R.,"Periodic Relative Motion Near a Keplerian Elliptic Orbit with Nonlinear Differential Gravity", *AIAA Journal of Guidance, Control and Dynamics*, Vol. 29, No. 5, pp. 1110-1121, Sep.-Oct. 2006, doi:10.2514/1.18344.

[163] Vadali, S.R.,"Model for Linearized Satellite Relative Motion About a J2-Perturbed Mean Circular Orbit", *Journal of Guidance, Control and Dynamics*, Vol. 32, No. 5, pp. 1687-1691, Sep.-Oct. 2009, doi:10.2514/1.42955.

[164] Vaddi, S.S., Vadali, S.R. and Alfriend, K.T.,"Formation Flying: Accommodating Nonlinearity and Eccentricity Perturbations", *Journal of Guidance, Control and Dynamics*, Vol. 26, No. 2, pp.214-223, March-Apr. 2003.

[165] Vaddi, S.S., Alfriend, K.T., Vadali, S.R., and Sengupta, P.,"Formation Establishment and Reconfiguration Using Impulsive Control", *Journal of Guidance, Control and Dynamics*, Vol. 28, No. 2, pp. 262-268, March-Apr. 2005.

[166] Yamanaka, K., and Ankersen, F.,"New State Transition Matrix for Relative Motion on an Arbitrary Elliptical Orbit", *Journal of Guidance, Control and Dynamics*, Vol. 25, No. 1, pp. 60-66, Jan.-Feb. 2002.

Web Pages

[167] Prisma mission blog:http://www.prismasatellites.se

[168] Swedish Space Corporation:http://www.sscspace.com

[169] DLR - German Aerospace Center:http://www.dlr.de

[170] DLR/GSOC's Space Flight Technology Department:http://www.weblab.dlr.de/rbrt/

[171] TerraSAR-X:http://www.dlr.de/dlr/en/desktopdefault.aspx/tabid-10380/568_read-435/

[172] TanDEM-X:http://dlr.de/dlr/en/desktopdefault.aspx/tabid-10388/574_read-425/